SLAC – 316
UC – 34C
(T/E)

PROCEEDINGS OF THE WORKSHOP ON ELECTRONUCLEAR PHYSICS WITH INTERNAL TARGETS STANFORD LINEAR ACCELERATOR CENTER JANUARY 5–8, 1987

Edited by R. G. Arnold and R. C. Minehart

Stanford Linear Accelerator Center
Stanford University
Stanford, California 94305

May 1987

Prepared for the Department of Energy
under contract number DE-AC03-76SF00515

Printed in the United States of America. Available from the National Technical Information Service, U.S. Department of Commerce, 5285 Port Royal Road, Springfield, Virginia 22161. Price: Printed Copy A11, Microfiche A01.

Workshop Organizing Committee

R. G. Arnold, Chairman	American University
K. Van Bibber	LLNL
F. S. Dietrich	LLNL
T. W. Donnelly	MIT
A. K. Kerman	MIT
S. E. Koonin	CalTech
S. Kowalski	MIT
R. D. McKeown	CalTech
R. C. Minehart	University of Virginia
E. Moniz	MIT
B. E. Norum	University of Virginia
S. E. Rock	American University
J. E. Spencer	SLAC
J. P. Vary	Iowa State University

Forward

The Workshop on Electronuclear Physics with Internal Targets was held at SLAC on January 5-8, 1987. The idea for this workshop grew out of interest among physicists at SLAC and MIT/Bates who have been exploring the possibilities for internal targets in the PEP ring at SLAC and in a proposed stretcher ring at MIT/Bates. The aim of the workshop was to bring together physicists from these groups and from other laboratories and universities to discuss the new physics that could be made accessible with internal targets, and to share information on recent developments in internal target technology, on the impact of internal targets on ring operation, and on the detector requirements. The workshop was sponsored by NPAS, the program of Nuclear Physics at SLAC, and it was attended by more than 100 physicists from the U.S., Canada, Europe, and Japan.

The workshop sessions began with two days of invited talks followed by two days of shorter presentations organized by the chairmen of four Working Groups. Written versions of all the plenary talks and all but four of the Working Group talks are presented here. The table of contents closely follows the meeting agenda. One talk on the agenda was not presented orally, but the written version by J. Fay and M. Macri is included here. Also included are two papers contributed for the proceedings that were not on the agenda.

Use of low density internal gas targets in high current circulating electron beams offers a number of unique features that would open up several new areas for electronuclear physics research. A primary advantage is the possibility for detection of multiple particles in the final state using large acceptance detectors. In addition a variety of nuclei can be produced in the form of polarized gas with high polarization and sufficient density and purity to give useful counting rates in high current circulating beams. Polarized targets will allow unique measurements of the spin dependence in a variety of electromagnetic interactions, and large acceptance detectors will make possible a large class of measurements of nuclear structure and reaction mechanisms not practical with external beams and thick targets. Finally it may also be possible to produce beams of polarized electrons and arrange for longitudinal polarization at the target. With polarized electrons and polarized targets, a number of fundamental measurements of nuclear and nucleon spin structure might be possible that would otherwise be impossible using external beams.

Future developments of the internal target method for electron beams will benefit from and be stimulated by work planned or under way for numerous other internal and external beams around the world. At the workshop we heard about previous internal target work for the proton beams at Fermilab and CERN. The requirements for the large acceptance detectors will be similar to other detector systems in use today or planned, for example, at CEBAF. The unique physics made accessible by this technique will be complementary to that now under investigation or planned for fixed target beams at SLAC, MIT/Bates, Fermilab, CERN, and CEBAF. There was considerable interest expressed at the workshop in pursuing future work on ideas for internal target experiments at electron

rings. It is possible that if these developments continue there will emerge a new subfield of experimental research exploring a wide range of topics in nuclear and nucleon structure.

We would like to express our thanks to all the speakers and authors of the papers presented here for their efforts in advancing our understanding of these topics. We also want to thank those people who helped organize the meetings and produce the proceedings: the Organizing Committee and the Working Group Chairmen for arranging the speakers and planning the program; Lynn Hanlon, Lesia Machicao, and Nina Adelman, the Conference Secretariat, who worked behind the scenes and smoothly operated the front desk; Kevin Johnston and Lucy Yuen who masterfully converted the manuscripts into this proceedings.

R. G. Arnold R. C. Minehart
May 1987

Contents

Session I
Chairman: F. S. Dietrich

Session II
Chairman: J. S. McCarthy

Session III
Chairman: G. A. Peterson

Session IV

Chairman: C. F. Williamson

Working Group I

Physics with Multi-Arm Detectors and Nucleon Targets
Chairmen: R. G. Arnold and S. J. Brodsky

Working Group II

Physics with Multi-Arm Detectors and Nuclear Targets
Chairmen: S. E. Rock and J. P. Vary

Working Group III

Physics with 4π Detectors

Chairmen: S. E. Koonin and K. Van Bibber

Working Group IV

Physics with Polarized Beams and Targets

Chairmen: T. W. Donnelly and B. E. Norum

Contributed Papers

FROM THE HADRONIC PHOTON AT $Q^2=0$ TO HARD SCATTERING AT SPACE-LIKE Q^2

T. Sloan

University of Lancaster
Physics Department
Lancaster, LA1 4YB, England

Introduction

Real photons ($Q^2=0$) show much larger cross sections for the production of hadrons than would be expected if they interacted only electromagnetically. In contrast the scaling behaviour in deep inelastic scattering shows that the space-like virtual photons scatter from point-like nucleon constituents (quarks) without any form factor effects. Thus space-like virtual photons behave as pure electromagnetic probes whereas real photons behave more like hadrons.

In real photoproduction ($Q^2=0$) a large cross section for the production of ρ° mesons is observed which is ~9 times the cross section for ω meson production. These observations led to the formulation of the vector meson dominance model (VMD) for the interactions of real photons[1]. In this model the cross section for the photoproduction of vector mesons V is written as;

$$\left(\frac{d\sigma}{dt}\right)_{\gamma p \to Vp} = f_V^2 \left(\frac{d\sigma}{dt}\right)_{Vp \to Vp}$$

where f_V represents the coupling constant between the photon and vector meson and $\left(\frac{d\sigma}{dt}\right)_{Vp\to Vp}$ is the elastic scattering cross section for the vector meson V. The ratio of the coupling constants is expected to be

$$f_\rho^2 : f_\omega^2 : f_\phi^2 : f_{J/\psi}^2 : f_\nu^2 = 9:1:2:8:2$$

from SU(3) symmetry (quark charges).

Clearly there is a substantial difference between the behaviour of real photons and that of virtual photons at higher Q^2. In this paper, I shall attempt to trace the evolution of the hadron-like behaviour of the photon at $Q^2=0$ to its electromagnetic behaviour at larger space-like Q^2.

Exclusive Vector Meson Production at High Energies

Exclusive vector meson production is the process

$$\gamma^* + p \to V + p$$

where γ^* is a real ($Q^2=0$) or a virtual (finite negative Q^2) photon in electron or muon deep inelastic scattering. Experimental data at high energies are available on exclusive ρ° and ϕ^2 and J/ψ production[3]. Figure 1 shows the total cross sections as a function of Q^2. It can be seen from this figure that the ratio of $\sigma_\rho:\sigma_\phi:\sigma_{J/\psi}$ is tending towards the values 9:2:8 as Q^2 increases i.e. the values expected from the photon coupling to the quark charges.

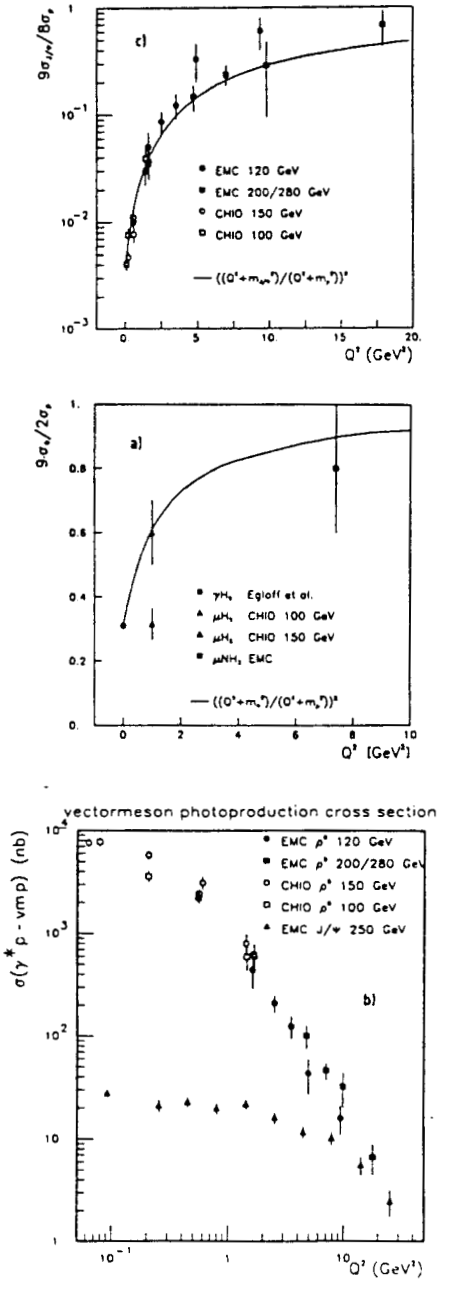

Fig. 1

a) The ratio $9\sigma(\phi)/2\sigma(\rho)$, b) The cross sections sections for elastic ρ° and J/ψ production.
c) The ratio $9\sigma(J/\psi)/8\sigma(\rho)$ as a function of Q^2.

In the generalised vector dominance model[1], assuming ρ° dominance and neglecting off diagonal terms, the cross section for exclusive ρ° production at higher Q^2 should follow the form

$$\sigma(Q^2) = \sigma(Q^2=0)\,\frac{m_\rho^4}{(Q^2+m_\rho^2)^2}\,[1+\varepsilon\xi^2\frac{Q^2}{m_\rho^2}] \qquad (1)$$

where m_ρ is the mass of the ρ° meson, ε is the ratio of the longitudinal to transverse virtual photon fluxes and $\xi^2Q^2/m_\rho^2=R$, the ratio of the production cross sections of longitudinally and transversely polarised virtual photons ($R=\sigma_L/\sigma_T$).

In real photoproduction ($Q^2=0$) of ρ° mesons s channel helicity is observed to be conserved[1], i.e. transverse photons produce ρ°'s in a helicity ± 1 state in the s channel frame (which gives a pure $\sin^2\theta$ angular distribution of the decay pions). If s channel helicity were conserved at higher Q^2 any longitudinal photon contribution would give a $\cos^2\theta$ component to the angular distribution. The EMC observed[2] that the ρ°'s are produced with almost a pure $\cos^2\theta$ angular distribution at high Q^2, and that the $\sin^2\theta$ component falls rapidly with Q^2. From fits to the angular distribution assuming s channel helicity conservation this group deduce that the parameter ξ^2 should be 0.4 ± 0.1. Figure 2 shows the measured cross section for exclusive ρ° production as a function of Q^2. The solid curve (dashed curve) shows the generalised vector dominance model prediction (eqn. 1) with $\xi^2=0.4$ ($\xi^2=0.0$). It is clear that the data prefer the value $\xi^2=0.0$ and exclude the value $\xi^2=0.4$. Thus generalised vector meson dominance with s channel helicity conservation does not describe the data at high Q^2.

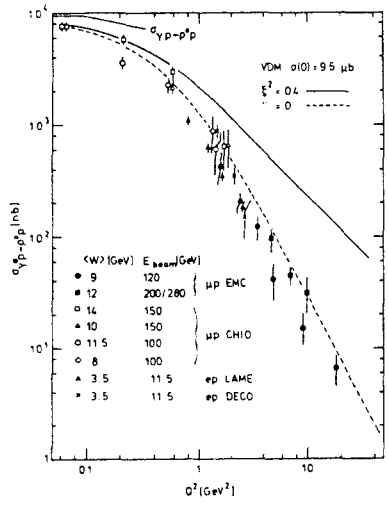

Fig. 2

ρ° photoproduction cross section versus Q^2. The smooth curves show the VMD predictions (equation 1) with $\xi^2=0$ and $\xi^2=0.4$.

The EMC have measured independently (from the incident muon energy dependence) the value of $R=\sigma_L/\sigma_T=-0.4^{+0.9}_{-0.4}$ by combining their data with the measurements of the CHIO group, each extrapolated to $Q^2=2$ GeV². This shows that exclusive ρ° production is mainly by transversely polarised virtual photons. Projecting out the observed $\sin^2\theta$ and $\cos^2\theta$ components from the decay pion angular distributions would imply a value $R=2.7\pm0.5$ at $Q^2=2$ GeV² if s channel helicity were conserved. Comparing these two values of R one concludes that s channel helicity is no longer conserved at larger Q^2 i.e. exclusive ρ° photoproduction occurs mainly from transverse (helicity $\pm$ 1) photons and the ρ°'s are produced mainly in a helicity 0 state.

Could the generalised vector meson dominance picture work with s channel helicity flip? Equation (1) shows that as Q^2 becomes large the expected cross section ratio $\sigma_\rho:\sigma_\phi:\sigma_{J/\psi}$ (large Q^2) $=\sigma_\rho m_\rho^4:\sigma_\phi m_\phi^4:\sigma_{J/\psi} m_{J/\psi}^4$ ($Q^2=0$)$=9:1:0.75$. The value of these ratios observed at $Q^2=15$ GeV² are $9:1.6\pm0.4:5.6\pm1.0$ and are inconsistent with this picture. Thus the generalised vector dominance model with or without s channel helicity conservation fails to describe the data at higher Q^2. However, the observed ratios are tending to the values expected (9:2:8) from the electromagnetic coupling of the virtual photon to the quark charges.

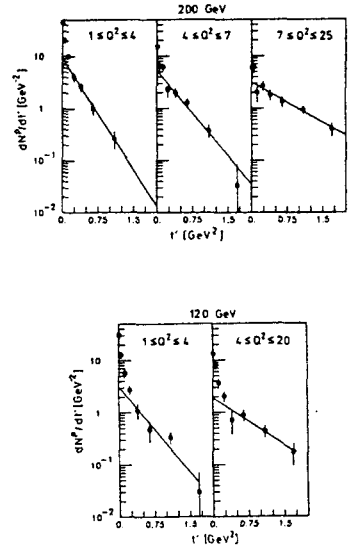

Fig. 3

The exclusive ρ° yields as a function of $t'=|t-t_{min}|$ in different Q^2 bins from an ammonia (mainly nitrogen) target

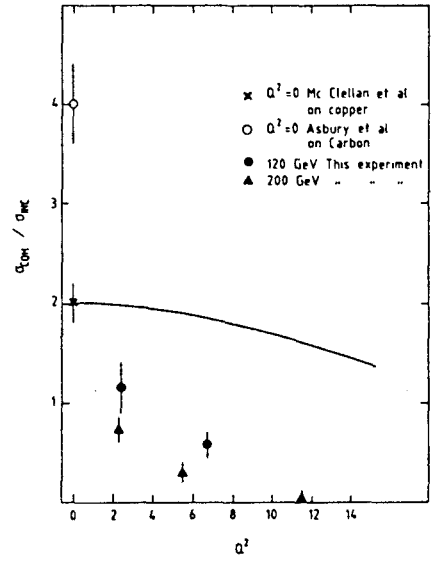

Fig. 4

The ratio of the total coherent to incoherent cross sections from nitrogen as a function of Q^2. The smooth curve shows the expected decrease due to the increase of t_{min} with Q^2.

Figure 3 shows the measured $t'(=t-t_{min})$ dependence[2] for exclusive ρ^0 production from an ammonia (mainly nitrogen) target. The sharp peak at small t is due to coherent production smeared by experimental resolution. The smooth curves are fits of the form $e^{-bt'}$ outside the coherent region ($t'<0.2$). Figure 3 shows that the value of b decreases rapidly with Q^2. This indicates that at higher Q^2 exclusive ρ^0 production is dominated by a hard scattering mechanism. The exponentials in fig. 3 were extrapolated under the coherent peak to measure the ratio of the coherent to incoherent cross sections. Figure 4 shows that this ratio decreases with Q^2. Such behaviour can be understood from the failure of s channel helicity conservation at high Q^2. In the forward direction, by angular momentum conservation, the helicity flip of the ρ^0 implies that the nucleon spin must also flip. Such spin flip amplitudes cannot contribute to coherent production since the final state of the nucleus changes.

The coherent cross section ratio decreases approximately as $1/Q^2$. Presumably such a cross section is due to the residual diffractive (i.e. vector meson dominance type) behaviour. A $1/Q^2$ dependence indicates that such behaviour is a higher twist mechanism.

Nuclear Shadowing of Photons[4]

This is studied by measuring the A dependence of the total hadronic photoabsorption cross section $\sigma_{\gamma A}$ where A is the atomic mass number. For any nucleus we define

$$A_{eff} = \frac{A\sigma_{\gamma A}}{(Z\sigma_{\gamma p}+N\sigma_{\gamma n})}$$

where $\sigma_{\gamma p}$ and $\sigma_{\gamma n}$ are the free proton and neutron cross sections and Z and N are the number of protons and neutrons in the nucleus. This is parameterised by

$$\frac{A_{eff}}{A} = A^{\epsilon}$$

Such a parameterisation fits imperfectly the pion-nucleus cross section variation with a value $\epsilon\sim-0.14$. However, it will suffice for the less precise photon data.

For real photons ($Q^2=0$) of energy $\nu\gtrsim10$ GeV, ϵ is found to be approximately independent of ν with a value of about -0.07. This indicates partial shadowing of real photons. The data are well represented by a model which assumes that the photon has a point-like cross section as well as a part interacting as in the vector meson dominance model[5].

There are several experiments with have contributed data on shadowing at finite Q^2 in charged lepton scattering[6,10]. Splitting these data into different Q^2 ranges and plotting ϵ as a function of $x=Q^2/2M\nu$, trends appear in the measurements. Here x is the fraction of the momentum of the nucleon carried by a struck parton in the quark parton model. Figure 5 shows ϵ as a function of x for the low Q^2 range[6,7] ($Q^2<1$). The measurements show that shadowing turns off smoothly as x increases (i.e. ν decreases) as would be expected in the model used to describe the real photoproduction data. Figure 6 shows the ratio of Aeff/A ($=\sigma_{\gamma A}/A\sigma_{\gamma N}$, where N is the average of the proton and neutron cross sections) for carbon and iron or copper for intermediate Q^2[8], $Q^2<4$ GeV^2 and high Q^2[10] $Q^2>2$ GeV^2. The data of [9] has been omitted from this plot because the two experiments neither agree with each other or with the other measurements[8] in the same Q^2 range. At $x>0.1$ the ratio decreases with x. This effect is known as the EMC effect. For $x<0.1$ the ratio decreases and tends to show shadowing i.e. the ratio tends to a value <1.

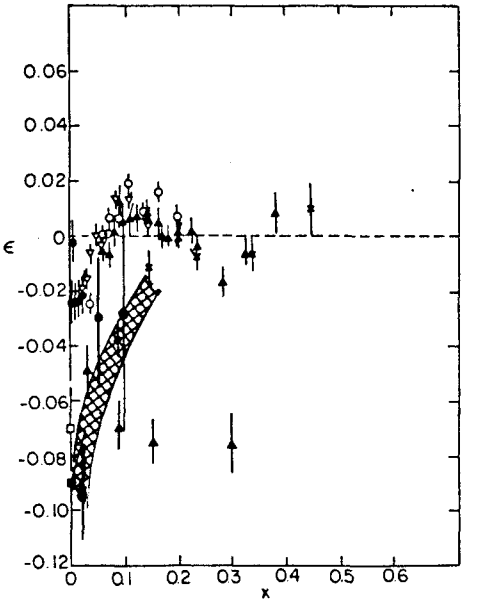

Fig. 5

The parameter ϵ as a function of x for low Q^2 data the hatched region shows the range of variation of the data of[6] and the points are the data of [7].

Many theoretical models exist to explain the EMC effect at high x[11]. There are three models of the contributing mechanisms in the region $x\lesssim0.2$. The model of Brodsky, Close and Gunion[5] predicts that shadowing occurs at small x, but that it dies uniformly with Q^2. This model does not predict antishadowing at $x\sim0.15$, as indicated by the data.

The presence of pions in the nucleus has been used to predict the antishadowing excess at $x\sim0.15$[12]. In this model the nucleon structure function in the nucleus is given by

$$F_2^A(x) = \int_x^A f_N(z)\, F_2^N(\tfrac{x}{z})dz + \int_X^A f_\pi(z)\, F_2^\pi(\tfrac{x}{z})dz$$

where F_2^N and F_2^π are the structure functions and f_N, f_π are the fractional momentum distributions of the nucleon and pion in the nucleus respectively. The increase of the ratio in fig. 6 above unity at $x\sim0.15$ is ascribed to the excess pion content and the decrease below unity at large x to momentum conservation. The shadowing at small x is not predicted and is ascribed to a separate process e.g. the Brodsky, Close and Gunion mechanism.

A parton model of shadowing and antishadowing was developed by Nicholaev and Zacharov[13]. They postulate that soft partons (e.g. gluons) can fuse to produce harder partons. Thus the tiny x region, $x\lesssim A^{-\frac{1}{3}}\, m_\pi/m_N$ (where m_π and m_N are the pion and nucleon

masses), in deep inelastic scattering is depleted as there are fewer soft partons which accrete at x~0.15, giving an excess in this region. In this model the ratios will be approximately Q^2 independent.

At present the data are too few and too imprecise to separate these two pictures. It will be necessary to measure the Q^2 dependence of the ratio in fig. 6 in the tiny x region to understand the detailed mechanisms in the shadowing region.

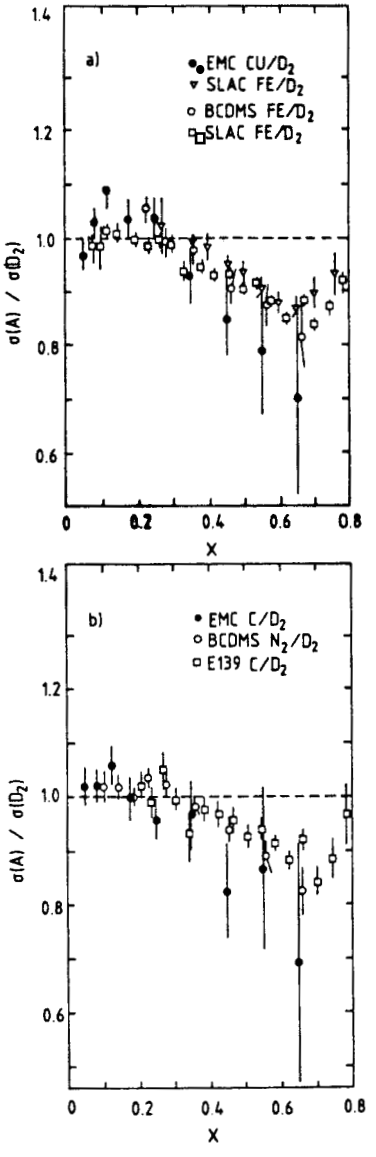

Fig. 6

The ratio of the cross section for deep inelastic scattering per nucleon from a) iron or copper b) carbon to that from deuterium at high and intermediate values of Q^2

Conclusions

In exclusive vector meson production in deep inelastic scattering, the vector meson dominance picture dies away and the production mechanism becomes a hard scattering process at $Q^2 \gtrsim 1$ GeV^2. The virtual photon has been demonstrated to behave as a pure electromagnetic probe. In shadowing in nuclei there are indications for the electromagnetic behaviour of the photon but the picture is still somewhat confused. There is a need to measure the Q^2 dependence of the shadowing region at very small x in order to better understand the processes involved.

I would like to thank the organisers of the NPAS Workshop at SLAC for their hospitality. I should also like to thank Per Grafström for helpful discussions.

References

1. For a review see T.H. Bauer, R.D. Spital, D.R. Yennie and F.M. Pipkin, Rev. Mod. Phys. 50, 261 vol. 2 (1978).
2. CHIO, W.D. Schambroom et al., Phys. Rev. D26, 1 (1982);
   EMC, J.J. Aubert et al., Phys. Lett. 161B, 203 (1985);
   EMC, K. Mönig, Diplom Thesis, Univ. of Wuppertal WUD 86-10.
3. BFP, T. Markiewicz, Ph.D. Thesis (Lawrence Berkeley Laboratory);
   EMC, J.J. Aubert et al., Nucl. Phys. B213, 1 (1983).
4. For a review, see G. Grammer Jr. and J.D. Sullivan, Electromagnetic Interactions of Hadrons, vol. 2 edited by A. Donnachie and G. Shaw (Published by Plenum Press, 1978).
5. S.J. Brodsky, F.E. Close and J. Gunion, Phys. Rev. D6, 177 (1972).
6. J. Franz et al., (.08<Q^2<1 GeV^2) Z. Phys. C10, 105 (1981);
   G. Huber et al., (.075<Q^2<1. GeV^2) Z. Phys. C2, 279 (1979);
   J. Bailey et al., (0.1<Q^2<0.3 GeV^2) Nucl. Phys. B151, 367 (1979).
7. J. Eickmeyer et al., (Q^2~0.1 GeV^2) Phys. Rev. Letts. 36, 289 (1976).
8. S. Stein et al., Phys. Rev. D12, 1884 (1975);
   W.R. Ditzler et al., Phys. Letts. 57B 201 (1975)
9. M. May et al., Phys. Rev. Letts. 35 407 (1975);
   M. Miller et al., Phys. Rev. D24, 1 (1981).
10. SLAC-E139, R.G. Arnold et al., Phys. Rev. Letts. 52, 722 (1984).
    EMC. P.R. Norton, Talk at 23rd Int. Conf. on High Energy Physics, Berkeley, 1986.
    BCDMS CERN preprint EP/87-13.
    BCDMS G. Bari et al., Phys. Lett 163B, 282, (1985).
11. O. Nachtmann, Proc. 11th Int. Conf. on Neutrino Physics and Astrophysics, Nordkirchen, Dortmund, (1984) p.405;
    N.N. Nikolaev, Oxford Universtiy preprint TP 58/84 (1984);
    C.H. Llewellyn-Smith, Proc. PANIC, Heidelberg 1984 eds. B. Povh and G.zu Putlitz, Nucl. Phys. A434 35c (1985);
    A. Krzywicki, Proc. 11th Europhysics Conf. "Nuclear Physics with Electromagnetic Probes", Paris 1985 eds. A. Gerard and C. Samour, Nucl. Phys. A446 135c (1985).
    J. Dias de Deus, Int. Conf. on High Energy Physics, Bari 1985 eds. L. Nitti and G. Preparata p.571.
12. E. Berger, ANL-HEP-CP-86-103 (ANL Preprint).
13. N.H. Nicholaev and V.I. Zacharov, Phys. Lett. 55B 397 (1975).

TESTING QUANTUM CHROMODYNAMICS IN ELECTROPRODUCTION*

STANLEY J. BRODSKY

Stanford Linear Accelerator Center
Stanford University, Stanford, California 94305

Introduction

Deep inelastic lepton nucleon scattering has been one of the key testing grounds of QCD over the past two decades. Measurements of the nucleon and nuclear structure functions have not only tested the short-distance properties of the theory, (such as the scaling properties of structure functions and their logarithmic evolution with momentum transfer), but they have also illuminated the nonperturbative bound state structure of the nucleon and nuclei in terms of their quark and gluon degrees of freedom. For the most part, this information has been obtained from single-arm inclusive experiments where only the recoil lepton was detected.

One of the important potential advantages of an internal target facility in an electron storage ring as discussed in this workshop is that the entire final state of electroproduction can be measured in coincidence with the scattered electron with close to 4π acceptance. In the case of the PEP ring ($E(e^{\pm}) \sim 15$ GeV), measurements can be performed above the onset of Bjorken scaling. Both polarized and unpolarized hydrogen and nuclear targets may be feasible, and eventually even polarized electron beams may be available. High precision comparisons between electron and positron scattering would allow the study of higher order QED and electroweak interference effects. The asymmetry in the cross sections for $e^{\pm}p \to e^{\pm}\gamma X$ can be sizeable,[1] providing a sum rule for the cube of the charges of the quarks in the target.

At the most basic level, Bjorken scaling of deep inelastic structure functions implies the production of a single quark jet, recoiling against the scattered lepton. The spectator system–the remnant of the target remaining after the scattered quark is removed–is a colored $\bar{3}$ system. (See fig. 1.) According to QCD factorization, the recoiling quark jet, together with the gluonic radiation produced in the scattering process, produces hadrons in a universal way, independent of the target or particular hard scattering reaction. This jet should be identical to the light quark jets produced in e^+e^- annihilation. In contrast, the hadronization of the spectator system depends in detail on the target properties. Unlike the quark jet, the leading particles of the target spectator system do not evolve and thus should not depend on the momentum transfer Q^2 [at fixed $W^2 = (q+p)^2$]. At present we do not have a basic understanding of the physics of hadronization, although phenomenological approaches, such as the Lund string model, have been successful in parameterizing many features of the data.

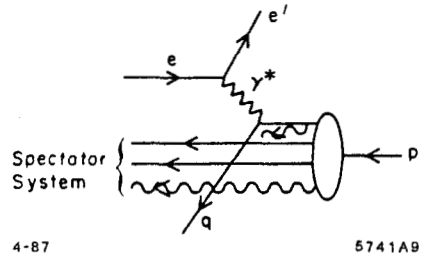

Fig. 1. Struck quark and spectator systems in electroproduction.

* Work supported by the Department of Energy, contract DE-AC03-76SF00515.

At a more detailed level, the features of the standard leading twist description are modified by coherent or nonperturbative effects. For example, higher twist–power-law suppressed contributions arise when two or more quarks recoil against the scattered lepton. At high energies, the quark jet does not change its state or hadronize over a distance scale proportional to its energy. Thus inelastic or absorptive processes cannot occur inside a nucleus–at least for the very fast hadronic fragments. We will discuss this target length condition[2,3] in more detail below. Nevertheless, a nuclear target can provide an essential tool for studying the detailed features of jet hadronization since the fast fragments are expected to scatter elastically in the nuclear medium, and the slow particles can interact inelastically and shower inside the nucleus. A review of the QCD predictions for jet hadronization can be found in Berger's contribution[4] to this workshop.

Many of the novel features expected in QCD are also apparent in QED. It is thus often useful to keep a QED analog in mind, replacing the target by a neutral atom such as positronium. Even in QED where there is no confinement, one expects in certain kinematic regions significant corrections to the Bjorken scaling associated with positron or electron knockout, in addition to the logarithmic evolution of the QED structure functions associated with induced photon radiation. For example, at low Q^2, the interference between amplitudes where different constituents are struck become important. Near threshold, where charged particles emerge at low relative velocities, there are strong Coulomb distortions, as summarized by the Sommerfeld[5] factor. In QCD these have their analog in a phenomena called "jet coalescence"[6] which we discuss in a later section. The Coulomb distortion factor must be included if one wants to maintain duality between the inelastic continuum and a summation over exclusive channels in electroproduction.

My main emphasis is this talk, however, is in the study of exclusive channels in electroproduction. It is clearly interesting to study how the summation of such channels yields the total inelastic cross section. More important, each individual exclusive channel can provide detailed information on basic scattering mechanisms in QCD and how the scattered quarks and gluons recombine into hadrons. In certain cases such as Compton scattering and meson electroproduction, we can study new aspects of the light cone expansion for the product of two currents, thus extending the renormalization group analysis into a new domain.[7] The diffractive production of vector mesons at high Q^2 can test the basic composition of the Pomeron in QCD. Further, as we discuss in the next section, measuring exclusive reactions inside a nuclear target allows the study of "color transparency",[8,9] the "formation zone",[2] and other novel aspects of QCD.

Exclusive Channels in Electroproduction

In high momentum transfer inclusive reactions, the underlying quark and gluon scattering processes lead directly to jet production in the final state, To leading order in $1/Q^2$, the cross sections and jet hadronization can be understood at the probabilistic level. In contrast, in *exclusive* electroproduction processes, one studies quark and gluon scattering and their reformation into hadrons at the *amplitude* level. Exclusive reactions thus depend in detail on the composition of the hadron wavefunctions themselves.

There is now an extensive literature, both experimental and theoretical, describing the features of large momentum transfer exclusive reactions. The QCD predictions are based on a factorization theorem[10-14] which separates the non-perturbative physics of the hadron bound states from the hard scattering amplitude which controls the scattering of the constituent quarks and gluons from the initial to final directions. This is illustrated for the proton form factor in fig. 2. Electroproduction of exclusive channels provides one of the most valuable testing ground of this QCD formalism, since the incoming photon provides a probe of variable spacelike mass directly coupling to the hard-scattering amplitude.

It has been known since 1970 that a theory with underlying scale-invariant quark-quark interactions leads to dimensional counting rules[15] for large momentum transfer exclusive processes; e.g. $F(Q^2) \sim (Q^2)^{1-n}$ where n is the minimum number of quark fields in the hadron. QCD is such a theory; the factorization formula leads to nucleon form factors of the form:[16]

$$G_M(Q^2) = \left[\frac{\alpha_s(Q^2)}{Q^2}\right]^2 \sum_{n,m} a_{nm} \left(\ell n \frac{Q^2}{\Lambda^2}\right)^{-\gamma_n - \gamma_m} \times \left[1 + O(\alpha_s(Q)) + O\left(\frac{1}{Q}\right)\right]$$

The first factor, in agreement with the quark counting rule, is due to the hard scattering of the three valence quarks from the initial to final nucleon direction. Higher Fock states lead to form factor contributions of successively higher order in $1/Q^2$. The logarithmic corrections derive from an evolution equation[10,16] for the nucleon distribution amplitude. The γ_n are the computed anomalous dimensions, reflecting the short distance scaling of three-quark composite operators. The results hold for any baryon to baryon vector or axial vector transition amplitude that conserves the baryon helicity. Helicity non-conserving form factors should fall as an additional power of $1/Q^2$. Measurements of the transition form factor to the $J = 3/2$ $N(1520)$ nucleon resonance are consistent with $J_z = \pm 1/2$ dominance, as predicted by the helicity conservation rule.[17] It is very important to explicitly verify that $F_2(Q^2)/F_1(Q^2)$ decreases at large Q^2. The angular distribution decay of the $J/\Psi \to p\bar{p}$ is consistent with the QCD prediction $\lambda_p + \lambda_{\bar{p}} = 0$.

The normalization constants a_{nm} in the QCD prediction for G_M can be evaluated from moments of the nucleon's distribution amplitude $\phi(x_i, Q)$. There are extensive on-going theoretical efforts computing constraints on this nonperturbative input directly from QCD. The pioneering QCD sum rule analysis of Chernyak and Zhitnitskii[12] provides constraints on the first few moments of $\phi(x, Q)$. Using as a basis the polynomials which are eigenstates of the nucleon evolution equation, one gets a model representation of the nucleon distribution amplitude, as well as its evolution with the momentum transfer scale.

The QCD sum rule analysis predicts a surprising feature: strong flavor asymmetry in the nucleon's momentum distribution. The computed moments of the distribution amplitude imply that 65% of the proton's momentum in its 3-quark valence state is carried by the u-quark which has the same helicity as the parent hadron. (See fig. 3.) A recent comprehensive re-analysis by King and Sachrajda[18] has now confirmed the Chernyak and Zhitnitskii form in its essential details. In addition, Dziembowski and Mankiewicz[19] have recently shown that the asymmetric form of the CZ distribution amplitude can apparently be derived from a rotationally-invariant CM wavefunction transformed to the light cone using a Melosh-type boost of the quark spinors. The transverse size of the valence wavefunction is found to be significantly smaller than the mean radius of the proton–averaged over all Fock states. This was predicted in ref. 10. Dziembowski and Mankiewicz also show that the perturbative QCD contribution to the form factors dominates over the soft contribution (obtained by convoluting the non-perturbative wave functions) at a scale $Q/N \approx 1$ GeV, where N is the number of valence constituents. Similar criteria were also derived in ref. 20. Results of the similar Jacob and Kisslinger[21] analysis of the pion form factor are shown in fig. 4. Claims[22] that a simple overlap of soft hadron wavefunctions could fit the form factor data were based on wavefunctions which violate rotational symmetry in the CM.

A detailed phenomenological analysis of the nucleon form factors for different shapes of the distribution amplitudes has been given by Ji, Sill, and Lombard-Nelsen.[23] Their results show that the CZ wavefunction is consistent with the sign and

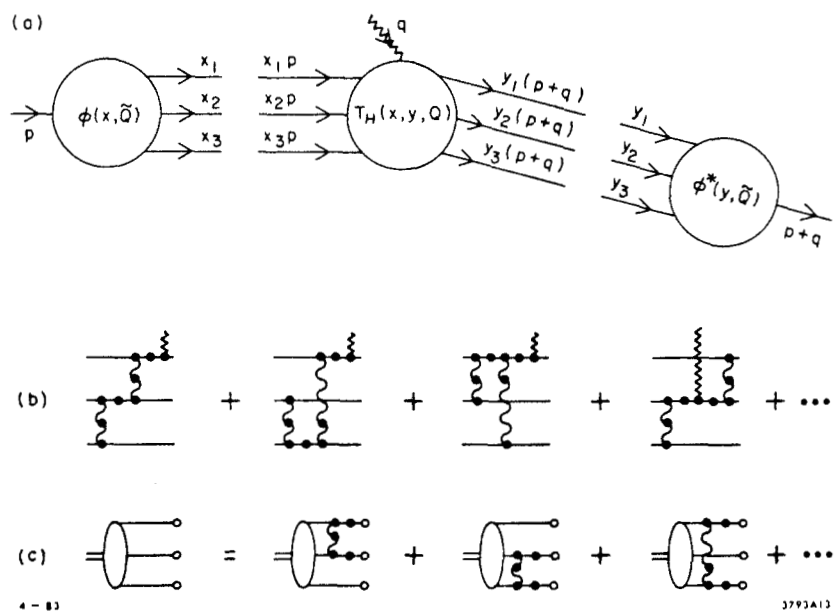

Fig. 2. Factorization of the nucleon form factor at large Q^2 in QCD.

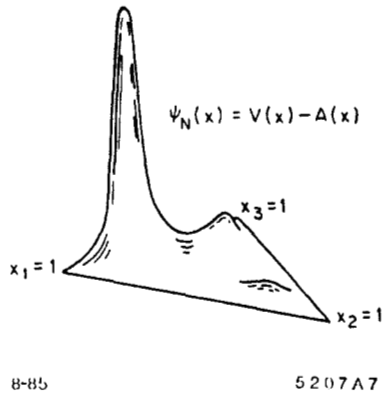

Fig. 3. QCD sum rule prediction for the proton distribution amplitude.

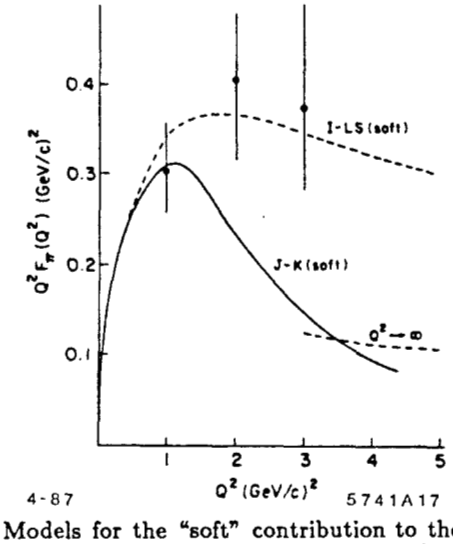

Fig. 4. Models for the "soft" contribution to the pion form factor. The Isgur-Llewellyn-Smith prediction[22] is based on a wavefunction with Gaussian fall-off in transverse momentum but power-law falloff at large x. The Jacob-Kisslinger prediction[21] is based on a rotationally symmetric form in the center of mass frame. The perturbative QCD contribution calculated with CZ[12] distribution amplitudes is consistent with the normalization and shape of the data for $Q^2 > 1$ GeV^2.

magnitude of the proton form factor at large Q^2 as recently measured by the American University/SLAC collaboration.[24] (See fig. 5.) The fact that the correct normalization emerges is a non-trivial test of the distribution amplitude shape; for example, the if the proton wavefunction has a non-relativistic shape peaked at $x_i \sim 1/3$ then one obtains the wrong sign for the nucleon form factor. Furthermore symmetrical distribution amplitudes predict a much too small magnitude for $Q^4 G_M^p(Q^2)$ at large Q^2. Gari and Stefannis[25] have developed a useful model for the nucleon form factors which incorporates the CZ distribution amplitude predictions at high Q^2 together with VMD constraints at low Q^2. Their analysis predicts sizeable values for the neutron electric form factor at intermediate values of Q^2. (See fig. 6.)

Measurements of the two-photon exclusive processes $\gamma\gamma \to \pi^+\pi^-$ and K^+K^- are in excellent agreement with the perturbative QCD predictions. The data[26] (see fig. 7) extend out to invariant mass squared 10 GeV^2, a region well beyond any significant contribution from soft contributions.

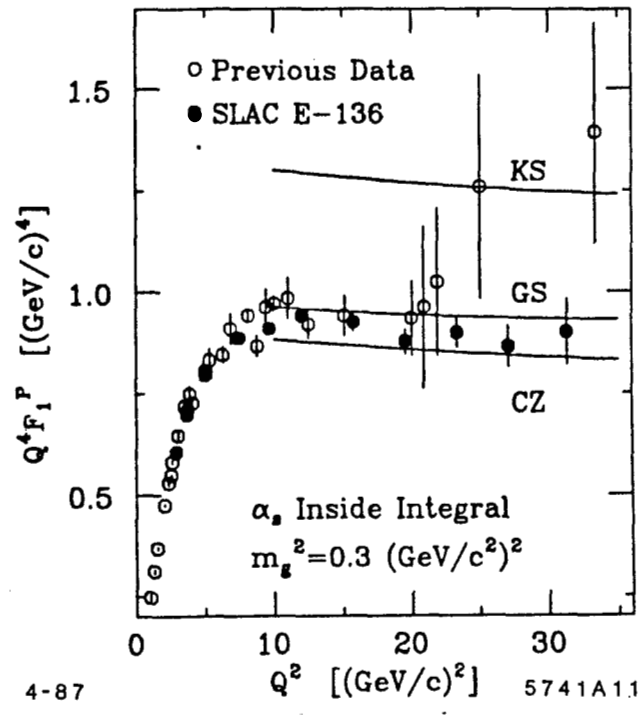

Fig. 5. Comparison of perturbative QCD predictions and data for the proton form factor. The calculation, based on the CZ QCD sum rule distribution amplitude, is from ref. 23. The prediction depends on the use of the running coupling constant as a function of the exchanged gluon momentum. The data are from ref. 24.

Nevertheless, one can question[22] with the consistency of the perturbative QCD analysis, particularly for baryon reactions at moderate momentum transfer:

1. The perturbative analysis of the baryon form factor and large angle hadron-hadron scattering depends on the suppression of the endpoint regions $x_i \sim 1$ and pinch singularity contributions. This suppression occurs automatically in QCD due to Sudakov form factors, as has been shown by Mueller[11] based on the all-orders analysis of the vertex function by Sen.[27] Since these analyses require an all-orders resummation of the vertex corrections, they cannot be derived by standard renormalization group analysis. In this sense the baryon and large angle scattering results are considered less rigorous than the results from analysis of the meson form factor and the $\gamma\gamma$ production of meson pairs.[28]
2. The magnitude of the proton form factor is sensitive to the $x \sim 1$ dependence of the proton distribution amplitude, where non-perturbative effects could be important. The CZ asymmetric distribution amplitude, in fact, emphasizes contributions from the large x region. Since non-leading corrections are expected when the quark propagator scale $Q^2(1-x)$ is small, relatively large Q^2 is required to clearly test the perturbative QCD predictions. A similar criterion occurs in the analysis of corrections to QCD evolution in deep inelastic lepton scattering. Dziembowski and Mankiewicz[19] claim that one can consistently fit low energy phenomena (the nucleon magnetic moments), the measured high momentum transfer hadron form factors, and the CZ distribution amplitudes with a self-consistent ansatz for the quark wavefunctions.

A complete derivation of the nucleon form factors at all momentum transfers would require a calculation of the entire set of hadron Fock wavefunctions. (See fig. 8.) This is the

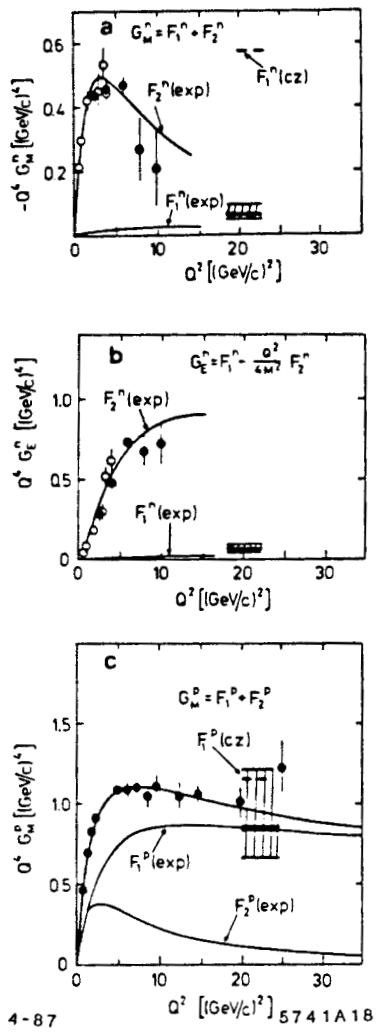

Fig. 6. Predictions for the nucleon form factors assuming VMD at low Q^2 and perturbative QCD at high Q^2. From ref. 25.

goal of the "discretized light-cone quantization" approach[29] for finding the eigen-solutions of the QCD Hamiltonian quantized at equal light cone time $\tau = t + z/c$. using a discrete basis. Thus far results have been obtained for the spectrum and wavefunctions for QED and Yukawa field theories in one-space and one-time dimension. The structure function of the lowest mass bound state in QED[1+1] as a function of a scaled coupling constant is shown in fig. 9.

Color Transparency

The QCD analysis of exclusive processes depends on the concept of a Fock state expansion of the nucleon wavefunction, projected onto the basis of free quark and gluon Fock states. The expansion is done at equal time on the light-cone and in the physical light-cone gauge. At large momentum transfer the lowest particle-number "valence" Fock component with all the quarks within an impact distance $b_\perp \leq 1/Q$ controls the form factor at large Q^2. Such a Fock state component has a small color dipole moment and thus interacts only weakly with hadronic or nuclear matter.[8,9] Thus if elastic electron-scattering is measured as a quasi-elastic process inside a nucleus, one predicts negligible final state interactions in the target as Q becomes large. Integrating over Fermi-motion, one predicts[20] that the differential cross section is additive in the number of nucleons in the nucleus. A test of this novel effect, "color transparency", has recently been carried out at

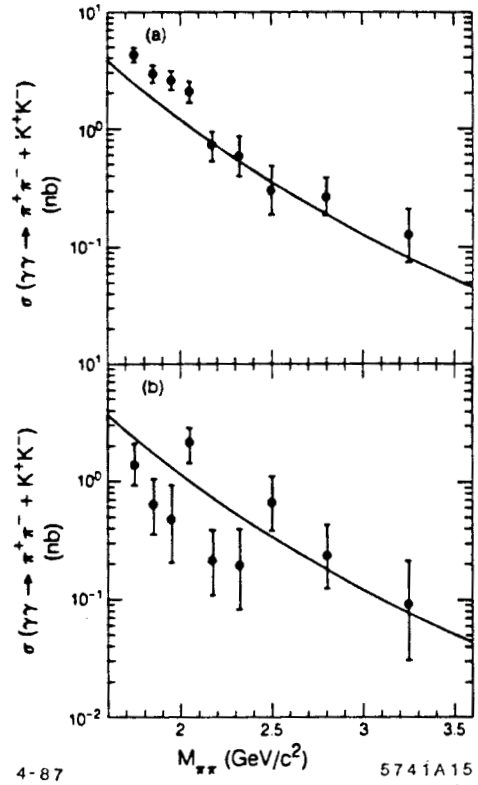

Fig. 7. Measurements[26] of exclusive two-photon reactions compared with the perturbative QCD predictions of ref. 28. The predictions are nearly independent of the shape of the meson distribution amplitudes.

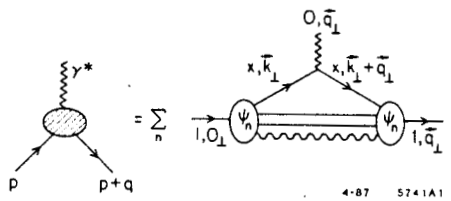

Fig. 8. Representation of electoweak hadron form factors in the light-cone formalism. The sum is over all charged quark lines and all Fock states ψ_n.

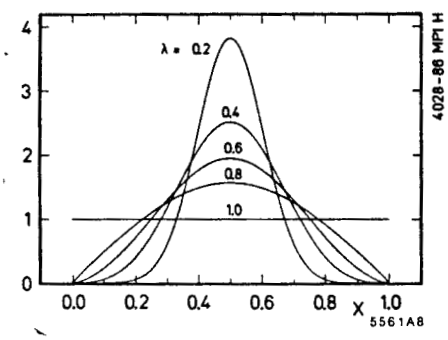

Fig. 9. The structure function of the lowest mass bound state for QED in 1+1 space-time dimensions, as calculated in the DLCQ formalism.[30]

Brookhaven for large momentum transfer elastic pp scattering in nuclear targets by a BNL-Columbia collaboration.[31] The initial results are consistent with diminished absorptive cross sections at large momentum transfer. If these preliminary results are verified they could provide a striking confirmation of the perturbative QCD predictions.

The strong spin-asymmetries seen in elastic p-p scattering[32] and the oscillations of the data modulating the predicted dimensional counting rule power-law fall-off[33] suggest possible resonant interference effects with the perturbative amplitude. [See also ref. 34.] These features evidentially cannot be explained in terms of the simplest QCD perturbative contributions.[35] (See fig. 10.) It is interesting to speculate whether one is observing an interference with pinch singularity contribution[34] or di-baryon resonances associated with the "hidden color" degrees of freedom of the six-quark state.[36] Since the resonant contributions are not coupled to small valence Fock states, one could expect significant final state corrections at energies where the resonances are important. Thus color transparency can be used to distinguish mechanisms for hadron scattering.

In the case of nucleon transition form factors measurable in inelastic electron nucleon scattering, the magnitude of the final state interactions should depend on the nature of the excited baryon. For example final state resonances which are higher orbital qqq states should have large color final state interactions.

Perhaps the most dramatic application of color transparency is to the QCD analysis of the deuteron form factor at large momentum transfer.[20,43] A basic feature of the perturbative QCD formalism is that the six-quark wavefunction at small impact separation controls the deuteron form factor at large Q^2. Thus even a complex six-quark state can have negligible final state interactions in a nuclear target–provided it is produced in a large momentum transfer reaction. One thus predicts that the "transparency ratio" $\frac{d\sigma}{dt}[eA \to ed(A-1)] / \frac{d\sigma}{dt}[ed \to ed]$ will increase with momentum transfer. The normalization of the effective number of deuterons in the nucleus can be determined by single-arm quasi-elastic scattering.

Other experimental tests of the reduced amplitude formalism are discussed in a later section.

Diffractive Electroproduction Channels

As a further example of the richness of the physics of exclusive electroproduction consider the "diffractive" channel $\gamma^* p \to \rho^0 p$. At large momentum transfer, QCD factorization for exclusive amplitudes applies, and we can write each helicity amplitude in the form:[10]

$$M_{\gamma^* p \to \rho^0 p}(s,t,q^2) = \int \prod dx_i \; T_H(x_i, p_T^2, \theta_{cm}, q^2)$$

$$\times \phi^\dagger_{\rho^0}(x_i, p_T)\phi^\dagger_p(x_i, p_T)\phi_p(x_i, p_T) \; .$$

This represents the convolution of the distribution amplitudes $\phi(x,Q)$ for the ingoing and outgoing hadrons with the quark-gluon hard scattering amplitude $T_H(\gamma^* + (qqq)_p \to (q\bar{q})_{\rho^0} + (qqq)_p)$ for the scattering of the quarks from the initial to final hadron directions. Since T_H involves only large momentum transfer, it can be expanded in powers of $\alpha_s(Q^2)$. The distribution amplitudes $\phi(x_i, p_T)$ only depend logarithmically on the momentum transfer scale, as determined from the meson and baryon evolution equations. As we discussed above, the functional dependence of the meson and baryon distribution amplitudes can be predicted from QCD sum rules. A surprising feature of the Chernyak and Zhitnitsky analysis[12] of the distribution amplitude of helicity-zero mesons is the prediction of a double-hump shape of $\phi_M(x,Q)$ with a minimum at equal

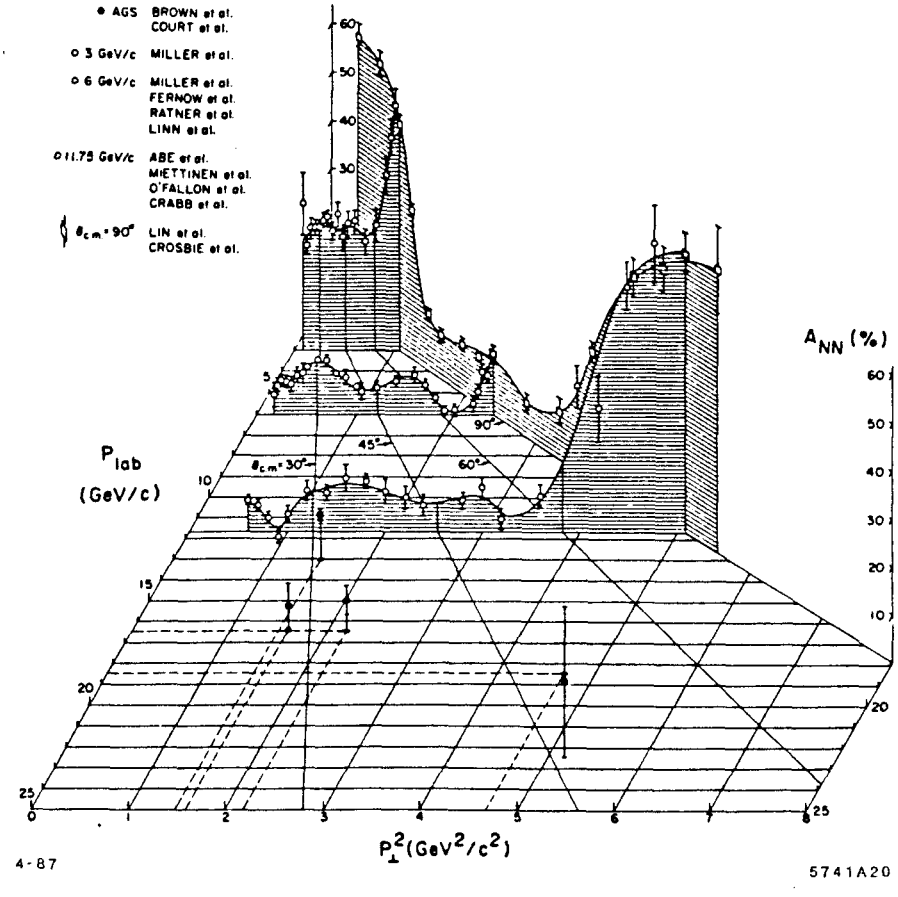

Fig. 10. Spin asymmetry for polarized pp elastic scattering. From ref. 32.

partition of the light-cone momentum fractions. (See fig. 11.) This result has now been confirmed in a lattice gauge theory calculation of the pion distribution amplitude moments by Martinelli and Sachrajda.[37] Similar conclusions also emerge from the wavefunction ansatz of Dziembowski and Mankiewicz.[19]

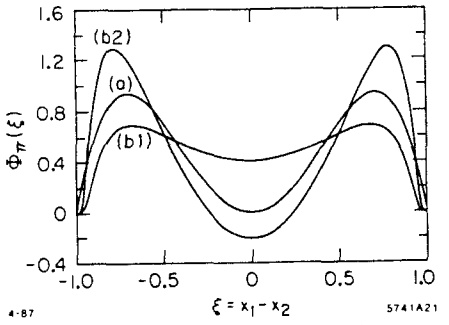

Fig. 11. Theoretical predictions for the pion distribution amplitude.

The main dynamical dependence of the electroproduction amplitude is determined by T_H. To leading order in $\alpha_s(p_T^2)$, T_H can be calculated from minimally-connected tree graphs; power counting predicts

$$T_H = \frac{e\alpha_s^3(p_T^2)}{(p_T^5)}\, f\left(\theta_{cm}, \frac{Q^2}{p_T^2}\right)$$

and thus

$$\frac{d\sigma}{dt}\,(\gamma^* p \to \rho p) \sim \frac{\alpha\alpha_s^6(p_T^2)}{(p_T^2)^7}\, F\left(\theta_{cm}, \frac{Q^2}{p_T^2}\right)$$

to leading order in $1/p_T^2$ and $\alpha_s(p_T^2)$. This prediction is consistent with the dimensional counting rule $d\sigma/dt \sim s^{2-n} f(\theta_{cm})$ where $n = 9$ is the total number of initial and final fields. The scaling laws hold for both real and virtual photons. As shown in fig. 12, the data[38] for $\gamma p \to \pi^+ n$ are consistent with the QCD scaling law prediction.

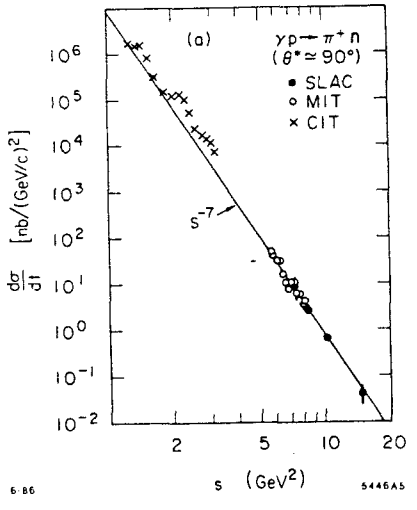

Fig. 12. Comparison of pion photoproduction data[38] at $\theta_{cm} = \pi/2$ with the quark counting rule prediction.

The leading contributions at large momentum transfer in QCD satisfy hadron helicity conservation[17]

$$\lambda_p = \lambda_{p'} + \lambda_\rho\ .$$

This selection rule is an important test of the vector coupling of the gluon in QCD. The result is independent of the photon helicity! Furthermore, the leading behavior comes from the "point-like" Fock component of the photon. The vector-meson-dominance contribution corresponds to the $q\bar{q}$ state where the constituent momenta are restricted to be collinear to the photon. This region gives a power-law suppressed $(1/p_T^2)^8$ contribution to the cross section at fixed θ_{cm}.

The dependence on the photon mass in exclusive electroproduction amplitudes in QCD occurs through the scaling variable Q^2/p_T^2. Thus for $Q^2 \ll p_T^2$, the transverse photon electroproduction amplitudes are predicted to be insensitive to Q^2. This is in striking consequence to the vector meson dominance picture, which predicts a universal $1/(1 + Q^2/m_\rho^2)$ dependence in the amplitude. Furthermore, since only the point-like component of the photon is important at large p_T, one expects no absorption of the initial state photon as it penetrates a nuclear target. The reaction $\gamma^* n \to \pi^- p$ is a particularly interesting test of color transparency since the dependence on photon mass and momentum transfer can be probed.

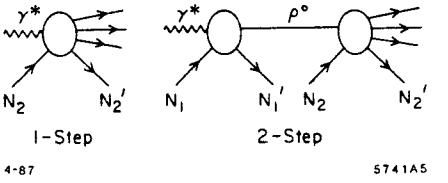

Fig. 13. Conventional description of nuclear shadowing of low Q^2 virtual photon nuclear interactions. The 2-step amplitude is opposite in phase to the direct contribution on nucleon N_2 because of the diffractive vector meson production on upstream nucleon N_1.

The conventional theory[39] of shadowing of photon interactions is illustrated in fig. 13. At large Q^2 the two-step amplitude is suppressed and the shadowing effect becomes negligible. This is the basis for a general expectation that shadowing of nuclear structure functions is actually a higher-twist phenomena, vanishing with increasing Q^2 at fixed x. [A recent analysis on shadowing in electroproduction by Qiu and Mueller[40] based on internucleon interactions in the gluon evolution equation in a nucleus suggests that shadowing is a higher twist effect, but decreases slowly as Q^2 increases.] Thus we predict simple additivity for exclusive electroproduction in nuclei

$$\overline{\frac{d\sigma}{dt}}\,(\gamma^* A \to \rho^0 N(A-1)) = A\,\frac{d\sigma}{dt}\,(\gamma^* N \to \rho^0 N)$$

to leading order in $1/p_T^2$. (The bar indicates that the cross sections are integrated over the nucleon Fermi motion.) This is another application of color transparency. What is perhaps surprising is that the prediction holds for small Q^2, even $Q^2 = 0$! Note that the leading contribution in $1/p_T^2$ (all orders in $\alpha_s(p_T^2)$) comes from the $\gamma \to q\bar{q}$ point-like photon coupling in T_H where the relative transverse momentum of the $q\bar{q}$ are of order p_T. Thus the "impact" or transverse size of the $q\bar{q}$ is $1/p_T$, and such a "small" color dipole has negligible strong interactions in a nucleus. The final state proton and ρ^0 also couple in leading order to Fock components which are small in impact space, again having minimal initial or final state interactions. If this additivity and absence of shadowing is verified, it will also be important to explore the onset of conventional shadowing and absorption as p_T^2 and Q^2 decrease.

Electroproduction of Diffractive Channels

Exclusive processes such as virtual Compton scattering, $\gamma^* p \to \gamma p$ and ρ^0 electroproduction $\gamma^* p \to \rho^0 p$ play a special role in QCD as key probes of "pomeron" exchange and its possible basis in terms of multiple-gluon exchange.[7] At large photon energy, the diffractive amplitudes are dominated by $J = 1$ Regge singularities.

Recent measurements of $\gamma^* p \to \rho^0 p$ by the EMC group[41] using the high energy muon beam at the SPS show three unexpected features: (1) The ρ^0 is produced with zero helicity at $Q^2 \geq 1$ GeV^2; (2) the falloff in momentum transfer becomes remarkably flat for $Q^2 \geq 5$ GeV^2; and (3) the integrated cross section falls as $1/Q^4$.

The most surprising feature of the EMC data is the very slow fall-off in t for the highest Q^2 data. (See fig. 14.) Using the parameterization $e^{bt'}$, $t' = |t - t_{min}|$, the slope for $7 \leq Q^2 \leq 25$ GeV^2, $E_L = 200$ GeV data is $b \sim 2$ GeV^{-2}. If one assumes Pomeron factorization, then the fall-off in momentum transfer to the proton should be at least as fast as the square of the proton form factor,[42] representing the probability to keep the scattered proton intact. (See fig. 15(b).) The predicted slope for $|t| < 1.5$ GeV^2 is $b \sim 3.4$ GeV^{-2}, much steeper than the EMC data. The background due to inelastic effects is estimated by the EMC group to be less than 20% in this kinematic domain.

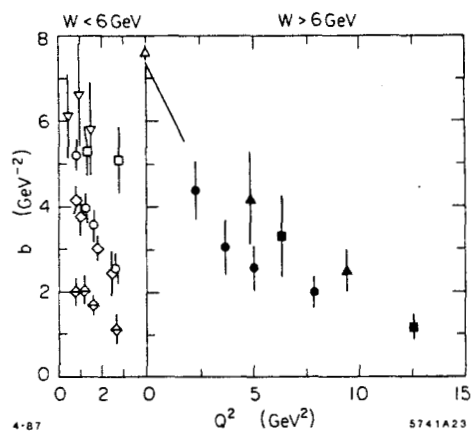

Fig. 14. The slope parameter b for the form $d\sigma/dt = Ae^{bt'}$ fit to the EMC data (ref. 41) for $\mu p \to \mu \rho^0 p$ for $|t'| \leq 1.5$ GeV^2.

In the vector meson dominance picture one expects: (1) dominantly transverse ρ polarization (s-channel helicity conservation); (2) fall-off in t similar to the square of the proton form factor (Pomeron factorization); and (3) a $1/Q^2$ asymptotic fall-off when longitudinal photons dominate.

The physics of electroproduction is quite different in QCD. At large $Q^2 \gg p_T^2$ diffractive channels take on a novel character.[7] (See fig. 15(c).) The transverse momentum k_T in the upper loop connecting the photon and ρ^0 is of order the photon mass scale, $k_T \sim Q$. (Other regions of phase space are suppressed by Sudakov form factors). Thus just as in deep inelastic inclusive scattering, the diffractive amplitude involves the proton matrix element of the product of operators near the light-cone. In the case of virtual Compton scattering $\gamma^* p \to \gamma p'$, one measures product of two electromagnetic currents. Thus one can test an operator product expansion similar to that which appears in deep inelastic lepton-nucleon scattering, but for non-forward matrix elements. In such a case the upper loop in fig. 15(c) can be calculated using perturbative methods. The ρ enters through the same distribution

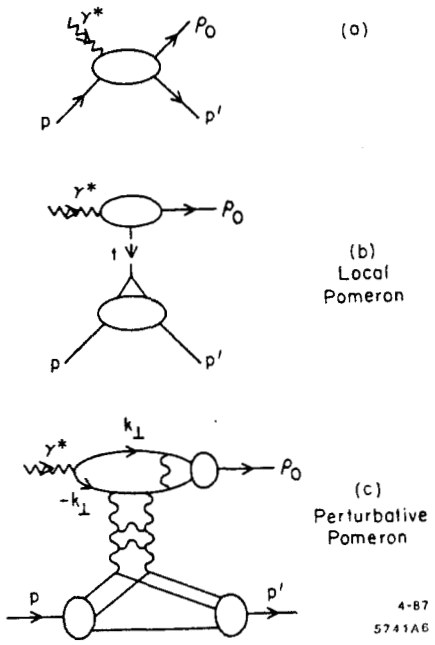

Fig. 15. (a) Diffractive electroproduction of vector mesons. (b) Local pomeron contribution coupling to one quark. (c) Perturbative pomeron contribution. For large transverse momentum $k_t^2 \approx Q^2$ two-gluon exchange contributions are dominant.

amplitude that appears in large momentum transfer exclusive reactions. Since the gauge interactions conserve helicity, this implies $\lambda_\rho = 0$, $\lambda_p = \lambda_p'$ independent of the photon helicity. The predicted canonical Q^2 dependence is $1/Q^4$, which is also consistent with the EMC data.

Since the EMC data is at high energy ($E_\gamma = 200$ GeV, $s \gg p_T^2$) one expects that the vector gluon exchange diagrams dominate quark-exchange contributions. One can show that the virtuality of the gluons directly coupled to the $\gamma \to \rho$ transition is effectively of order Q^2, allowing a perturbative expansion. The effect is a known feature of the higher Born, multi-photon exchange contributions to massive Bethe Heitler processes in QED.[6]

The dominant exchange in the t-channel should thus be the two-gluon ladder shown in fig. 15(c). This is analogous to the diagrams contributing to the evolution of the gluon structure function. If each gluon carries roughly half of the momentum transfer to different quarks in the nucleon, then the fall-off in t can be significantly slower than that of the proton form factor, since in the latter case the momentum transfer to the nucleon is due to the coupling to one quark. This result assumes that the natural fall-off of the nucleon wavefunction in transverse momentum is Gaussian rather than power-law at low momentum transfer.

In the case of quasi-elastic diffractive electroproduction in a nuclear target, we expect neither shadowing of the incident photon nor final state interactions of the outgoing vector meson at large Q^2 (color transparency).

Thus ρ^0 electroproduction and virtual Compton scattering can give essential information on the nature of diffractive (pomeron exchange) processes. Data at all energies and kinematic regions are clearly essential.

Exclusive Nuclear Processes in QCD

One of the most elegant areas of application of QCD to nuclear physics is the domain of large momentum transfer exclusive nuclear processes. Rigorous results have been given by Lepage, Ji and myself[43] for the asymptotic properties of the

deuteron form factor at large momentum transfer. The basic factorization is shown in fig. 16. In the asymptotic $Q^2 \to \infty$ limit the deuteron distribution amplitude, which controls large momentum transfer deuteron reactions, becomes fully symmetric among the five possible color-singlet combinations of the six quarks. One can also study the evolution of the "hidden color" components (orthogonal to the np and $\Delta\Delta$ degrees of freedom) from intermediate to large momentum transfer scales; the results also give constraints on the nature of the nuclear force at short distances in QCD. The existence of hidden color degrees of freedom further illustrates the complexity of nuclear systems in QCD. It is conceivable that six-quark d^* resonances corresponds to these new degrees of freedom may be found by careful searches of the $\gamma^* d \to \gamma d$ and $\gamma^* d \to \pi d$ channels.

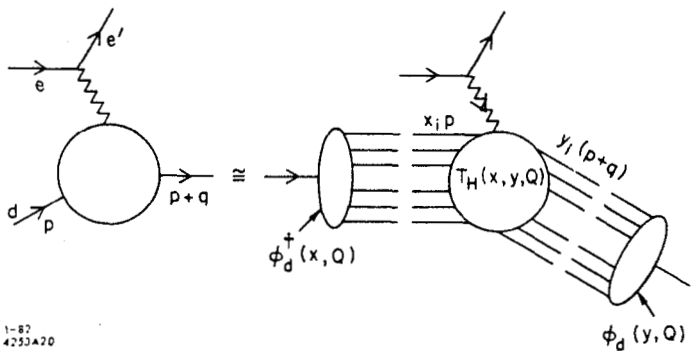

Fig. 16. Factorization of the deuteron form factor at large Q^2.

The QCD analyses suggests a consistent way to eliminate the effects of nucleon compositeness in exclusive nuclear reactions.[20,44] The basic observation is that for vanishing nuclear binding energy $\epsilon_d \to 0$, the deuteron can be regarded as two nucleons sharing the deuteron four-momentum. The $\gamma^* d \to np$ amplitude then contains two factors representing the probability amplitude for the proton and neutron to remain intact after absorbing momentum transfers

$$\hat{t} = (p_p - \tfrac{1}{2} p_d)^2 \quad \text{and} \quad \hat{u} = (p_n - \tfrac{1}{2} p_d)^2 .$$

The "reduced" amplitude

$$m_r(\gamma^* d \to np) = \frac{\mathcal{M}(\gamma^* d \to np)}{F_{1N}(\hat{t}) F_{1N}(\hat{u})}$$

is predicted to have the same fixed angle scaling behavior as $\gamma^* M \to q\bar{q}$; i.e., the nucleons are reduced to point particles. We thus predict

$$\frac{\frac{d\sigma}{d\Omega_{cm}}(\gamma^* d \to np)}{F_{1N}^2(\hat{t}) F_{1N}^2(\hat{u})} \sim \frac{f(\Omega_{cm})}{(p_T^2)^2}$$

to leading order in $1/p_T^2$.

The analogous analysis (see fig. 17) of the deuteron form factor as defined in

$$\frac{d\sigma}{dt}(\ell d \to \ell d) = \left.\frac{d\sigma}{dt}\right|_{point} |F_d(Q^2)|^2$$

yields a scaling law for the reduced form factor

$$f_d(Q^2) \equiv \frac{F_d(Q^2)}{F_{1N}\left(\frac{Q^2}{4}\right) F_{1N}\left(\frac{Q^2}{4}\right)} \sim \frac{1}{Q^2}$$

i.e., the same scaling law as a meson form factor. As shown in fig. 18, this scaling is consistent with experiment for $Q^2 = p_T^2 \gtrsim$ 1 GeV^2. There is also evidence for reduced amplitude scaling for $\gamma d \to pn$ at large angles and $p_T^2 \gtrsim 1$ GeV^2. (see fig. 19). We thus expect similar precocious scaling behavior to hold for $\bar{p}d \to \pi^- p$ and other $\bar{p}d$ exclusive reduced amplitudes. In each case the incident and outgoing hadron and nuclear states are predicted to display color transparency, i.e. the absence of initial and final state interactions if they participate in a large momentum transfer exclusive reaction.

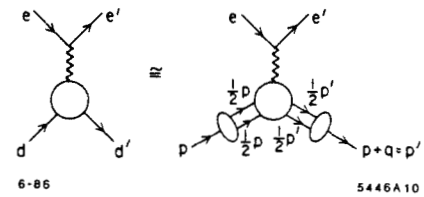

Fig. 17. Application of the reduced amplitude formalism to the deuteron form factor at large momentum transfer.

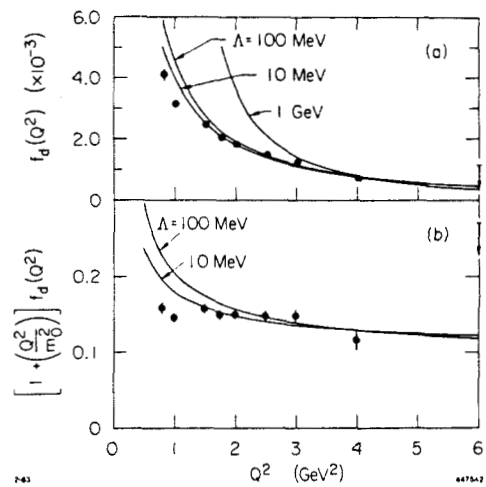

Fig. 18. Scaling of the deuteron reduced form factor. The data are summarized in ref. 20.

Electroproduction: A General View

The factorization formula[45]

$$\frac{d\sigma(AB \to CX)}{d^3p_c/E_c} \cong \sum_{ab,cd} \int_0^1 dx_a \int_0^1 dx_b \int_0^1 \frac{dx_c}{x_c^2}$$

$$\times G_{a/A}(x_a,Q) G_{b/B}(x_b,Q) \tilde{G}_{C/c}(x_c,Q)$$

$$\times \delta(s'+t'+u') \frac{s'}{\pi} \frac{d\sigma}{dt'}(ab \to cd)$$

for the inclusive production processes $AB \to CX$ has general validity in gauge theory. The systems A, B, C can be leptons, photons, hadrons, or nuclei. The primary subprocess in electroproduction is $eq \to eq$. The electron structure function $G_{e/e}(x,Q)$ automatically provides the (leading logarithmic) QED radiative corrections. The energy distribution of the beam itself plays the role of the non-perturbative or initial structure function. (See fig. 20(b).) The subprocess $\gamma^* q \to gq$ corresponds to photon-induced two-jet production. (See fig. 20(a).) This subprocess dominates reactions in which

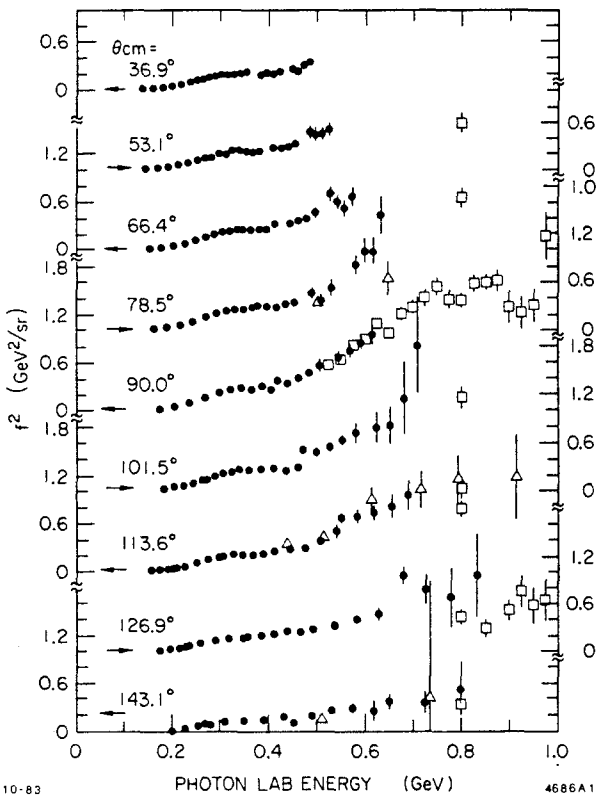

Fig. 19. Scaling of the reduced amplitude for deuteron electrodisintegration. The data are summarized in ref. 44.

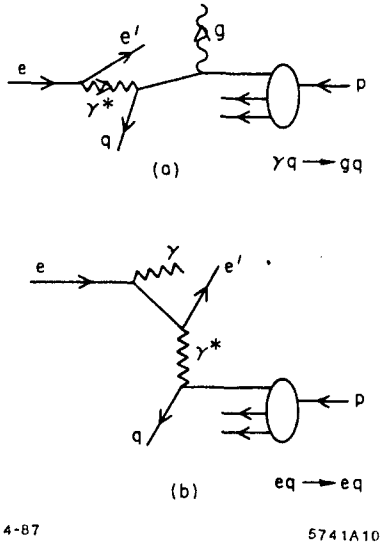

Fig. 20. Application of gauge theory factorization to electroproduction. (a) The $\gamma q \to gq$ subprocess produces hadron jets at high p_T. (b) The $eq \to eq$ produces one quark jet and one recoil electron jet at high p_T. The QED radiative corrections are incorporated into the electron and photon QED structure functions.

the large transverse momentum trigger is a hadron rather than the scattered lepton. Thus one sees that conventional deep inelastic $eq \to eq$ scattering subprocess is just one of the several modes of electroproduction.

The dominant contribution to the meson semi-inclusive cross section is predicted by QCD factorization to be due to jet fragmentation from the recoil quark and spectator diquark jets. When the momentum transfer is in the intermediate range $1 \lesssim Q^2 \lesssim 10$ GeV^2, several other contributions for meson production are expected to become important in $eN \to e'MX$. These include:

(1) Higher twist contributions to jet fragmentation:

$$\frac{dN_\pi}{dz} = D_{\pi/q}(z,Q^2) \cong A(1-z)^2 + \frac{C}{Q^2} \qquad (z \to 1) \; .$$

The scaling term reflects the behavior of the pion fragmentation function at large fractional momentum ($z \to 1$) as predicted by perturbative QCD (one-gluon exchange). (See fig. 21(a).) The C/Q^2 term[46] is computed from the same perturbative diagrams. For large z where this term dominates, we predict that the deep inelastic cross section will be dominantly longitudinal rather than transverse $R = \sigma_L/\sigma_T > 1$.

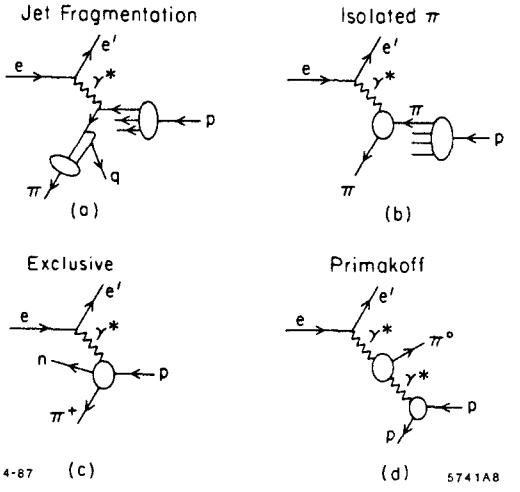

Fig. 21. QCD contributions to pion electroproduction. (a) Jet fragmentation, including leading and $1/Q^2$ higher twist contributions. (b) Isolated pion contributions at order $1/Q^4$. (c) Exclusive production. (d) Primakoff contribution.

(2) "Direct" meson production. Isolated pions may also be created by elastic scattering off of an effective pion current: (See fig. 21(b).)

$$\frac{d\sigma}{dQ^2 dx_\pi} = G_{\pi/p}(x_\pi) \left.\frac{d\sigma}{dQ^2}\right|_{e\pi \to e\pi}$$

$$\left.\frac{d\sigma}{dy dQ^2}\right|_{e\pi \to e\pi} = \frac{4\pi\alpha^2}{(Q^2)^2} |F_\pi(Q^2)|^2 (1-y) \; .$$

Here $y = q \cdot p / p_e \cdot p$. In the case of a nuclear target, one can test for non-additivity of virtual pions due to nuclear effects, as predicted in models[47] for the EMC effect[41] at small x_{Bj}. Jaffe and Hoodbhoy[48] have shown that the existence of quark exchange diagrams involving quarks of different nucleons in the nucleus invalidates general applicability of the simplest convolution formulae conventionally used in such analyses. The $G_{\pi/p}(x,Q)$ structure function is predicted to behave roughly as $(1-x)^5$ at large x, as predicted from spectator quark counting rules.[15,45] Applications of these rules to other off-shell nucleon processes are discussed in refs. 20 and 49.

(3) Exclusive Channels. (See fig. 21(c).) The mesons can of course be produced in exclusive channels; e.g. $\gamma^* p \to \pi^+ n$, $\gamma^* p \to \rho^0 p$. Pion electroproduction extrapolated to $t = m_\pi^2$ provides our basic knowledge of the pion form factor at spacelike Q^2. With the advent of the perturbative QCD analyses of

large momentum transfer exclusive reactions, predictions can be given over the whole range of large t and Q^2. We discussed some of the features of ρ^0 electroproduction above.

(4) Another possible meson production channel is Primakoff production $\gamma^*\gamma \to \pi^0$, etc., identifiable from very low target recoil events. (See fig. 21(d).) Such measurements would allow the determination of the $\gamma \to \pi^0$ transition form factor. This quantity, combined with the QCD analysis of the pion form factor leads to a method to determine the QCD running coupling constant $\alpha_s(Q^2)$ solely from exclusive measurements.[28]

The above examples make it clear that complete final state measurements are necessary for separating the various production channels; detailed study of meson electroproduction can yield valuable information concerning basic issues in QCD.

Higher Twist Contributions to Deep Inelastic Scattering

One of the most difficult aspects of electroproduction phenomenology is the separation of logarithmic scaling violations predicted by QCD evolution from the scale violations induced by power law corrections. The lack of a full understanding of these higher twist terms has prevented the extraction of reliable values of the QCD scale Λ_{QCD} from the data. As we have noted above, shadowing behavior in nuclei is likely associated with higher twist contributions. In addition, it is not clear whether ordinary Regge behavior of the inelastic lepton scattering cross section, which is a valid parameterization at fixed Q^2, persists into the scaling region or whether it is associated with higher twist dynamical effects. The fact that the non-singlet structure functions obey additive sum rules suggests that Regge behavior is absent in leading twist.

In some cases the higher twist effect corresponds to coherent many-particle processes which potentially could be identified by study of the final state. As an example, consider the processes illustrated in fig. 22. At intermediate Q^2 and $x = x_{Bj} \sim 1$ the cross section has the simplified form

$$\frac{d\sigma}{dQ^2 dx} = \frac{4\pi\alpha^2}{Q^4}\left[A(1-x)^3 + B(1-x)\left(\frac{1}{Q^2}\right)^2 + C(1-x)^{-1}\left(\frac{1}{Q^2}\right)^4\right].$$

The three terms correspond to lepton scattering off of one, two, or three quarks, respectively. The power in $1/Q^2$ increases with the number of active quarks: $(Q^2)^{2(n_A-1)}$ The power in $(1-x)$ counts the number of spectators required to stop as $x \to 1$: $(1-x)^{2n_s-1}$. The "diquark" term gives a large σ_L contribution.[46] The analogous structure in the pion structure function has been confirmed in the Drell-Yan reaction $\pi N \to \mu^+\mu^- X$ at large x.[46] The relative normalization of the power-law suppressed terms is uncertain, although the model calculations based on tree-graph gluon exchange diagrams performed by Blankenbecler, Gunion, and Nason[50] suggests very large coefficients B and C. If this is true for the physical situation, then the existence of such terms would make it very difficult to isolate the logarithmic corrections to scaling, except at very high momentum transfers–where unfortunately the sensitivity to the numerical value of Λ_{QCD} is small. Internal target experiments may be able to confirm the different contributions by studies of the recoil and spectator systems as functions of Q^2 and x together with separation of σ_L and σ_T.

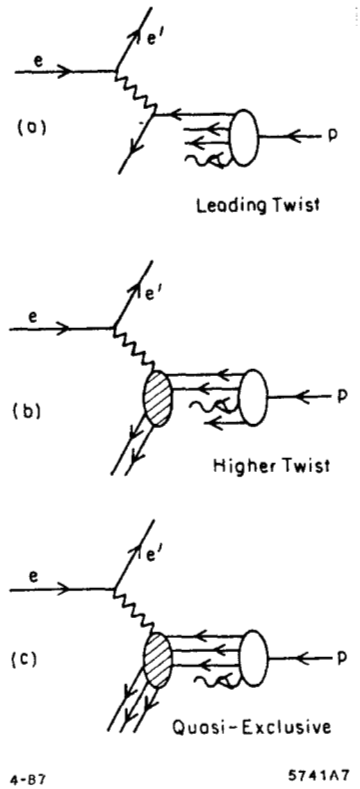

Fig. 22. Leading and higher twist contributions to deep inelastic lepton scattering due to multiparticle hard scattering subprocesses.

Formation Zone Phenomena in Deep Inelastic Scattering

One of the remarkable consequences of QCD factorization for inclusive reactions at large p_T is the absence of inelastic initial or final state interactions of the high energy particles in a nuclear target. Since structure functions measured in deep inelastic lepton scattering are essentially additive (up to the EMC deviations), factorization implies that the $q\bar{q} \to \mu^+\mu^-$ subprocesses in Drell-Yan reactions occurs with equal effect on each nucleon throughout the nucleus. At first sight this seems surprising since one expects energy loss from inelastic initial state interactions.

In fact, potential inelastic reactions such as quark or gluon bremsstrahlung induced in the nucleus which could potentially decrease the incident parton energy (illustrated in fig. 23) are suppressed by coherence if the quark or gluon energy (in the laboratory frame) is large compared to the target length:

$$E_q > \mu^2 L_A$$

Here μ^2 is the difference of mass squared that occurs in the initial or final state collision. This phenomenon has its origin in studies of QED processes by Landau and Pomeranchuk. The QCD analysis is given by Bodwin, Lepage and myself.[2] Elastic collisions, however, are still allowed, so one expects collision broadening of the initial parton transverse momentum. Recent measurements of the Drell-Yan process $\pi A \to \mu^+\mu^- X$ by the NA-10 group[51] at the CERN-SPS confirm that the cross section for muon pairs at large transverse momentum is increased in a tungsten target relative to a deuteron target. (See fig. 24). Since the total cross section for lepton-pair production scales linearly with A (aside from relatively small EMC-effect corrections), there must be a corresponding decrease of the ratio

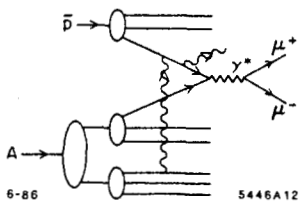

Fig. 23. Induced radiation from the propagation of an anti-quark through a nuclear target in massive lepton production. Such inelastic interactions are coherently suppressed at parton energies large compared to a scale proportional to the length of the target.

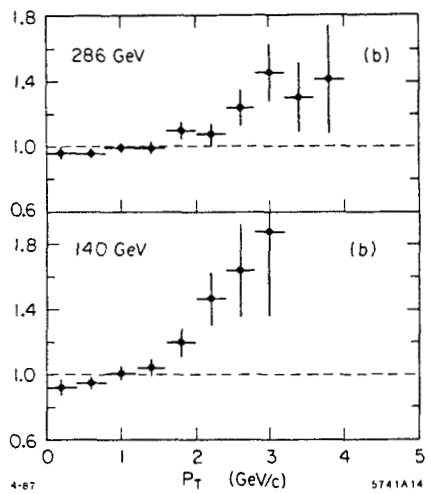

Fig. 24. The ratio $\sigma(\pi^- W \to \mu^+\mu^- X)/\sigma(\pi^- D \to \mu^+\mu^- X)$ as a function of the pair transverse momentum. From ref. 51.

of the differential cross section at low values of the di-lepton transverse momentum. This is also apparent in the data.

These results have striking implications for the interaction of the recoil quark jet in deep inelastic electron-nucleus scattering. For the quark (and gluons) satisfying the length condition, there should be no extra radiation induced as the parton traverses the nucleus. Thus gluon radiation of the type illustrated in fig. 25 should be suppressed. However, low energy gluons, emitted in the deep inelastic electron-quark collision, can suffer radiative losses, leading to cascading of soft particles in the nucleus. It is clearly very important to study this phenomena as a function of recoil quark energy and nuclear size.

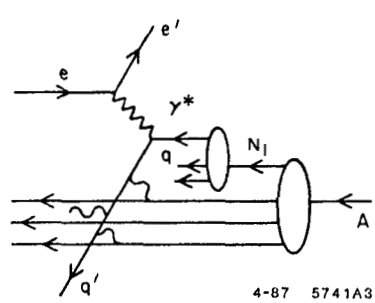

Fig. 25. Propagation of the struck quark through a nuclear target. Induced gluon radiation (inelastic final state interactions) is suppressed at high quark energies. Elastic scattering in the final state however is not suppressed.

It should be emphasized that the absence of inelastic initial or final state collisions for high energy partons does not preclude collision broadening due to elastic initial or final state interactions. The elastic corrections are unitary to leading order in $1/Q$ and do not effect the normalization of the deep inelastic cross section. Thus we predict that the mean square transverse momentum of the recoil quark and its leading particles will increase as $A^{1/3}$.

The transverse momentum of the recoil quark reflects the intrinsic transverse momentum of the nucleon wavefunction. The EMC effect[41] implies that quarks in a nucleus have smaller average longitudinal momentum than in a nucleon. (See fig. 26.) Independent of the specific physical mechanism underlying the EMC effect, the quarks in a nucleus would also be expected to have smaller transverse momentum. This effect can counteract to a certain extent the collision broadening of the outgoing jet.

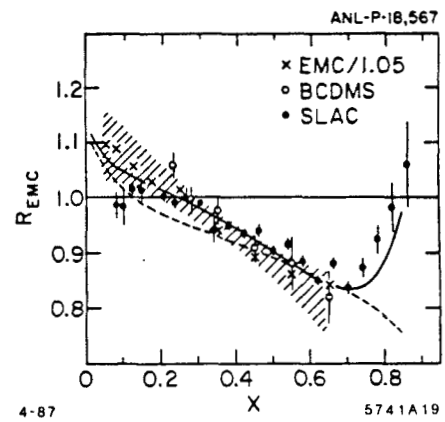

Fig. 26. Ratio of nuclear and nucleon structure functions. The theoretical curves are from the pion current calculation of Berger and Coester, ref. 47.

Unlike the struck quark the remnant of the target system does not evolve with the probe momentum Q. However, since the quantum numbers of the spectator system is $\bar{3}$ in color, nonperturbative hadronization must occur. Since the transverse momentum of the leading particles in the spectator jet is not affected by the QCD radiative corrections, it more closely reflects the intrinsic transverse momentum of the hadron state.

It is also interesting to study the behavior of the transverse momentum of the quark and spectator jets as a function of x_{Bj}. For $x_{Bj} \sim 1$, the 3-quark Fock state dominates the reaction. If the valence state has a smaller transverse size[10] than that of the nucleon, averaged over all of its Fock components, then we expect an increase of $\langle k_\perp^2 \rangle$ in that regime. Evidence for a significant increase of $\langle k_\perp^2 \rangle$ in the projectile fragmentation region at large quark momentum fractions has been reported by the SFM group[52] at the ISR for $pp \to$ dijet $+X$ reactions.

Diffraction Channels and Nuclear Structure Function Non-Additivity

One unusual source of non-additivity in nuclear structure functions (EMC effect) are electroproduction events at large Q^2 and low x which nevertheless leave the nucleus completely intact $x < (1/ML_A)$. In the case of QED, analogous processes such as $\gamma^* A \to \mu^+\mu^- X$ yield nuclear-coherent contributions which scales as $A_{eff} = Z^2/A$. (See fig. 27(a).) Such processes contribute to the Bjorken-scaling, leading-twist cross section.[53] In QCD we expect[54] the nuclear dependence to be less than additive for the analogous gluon exchange contributions (see fig. 27(b)) because of their diffractive coupling to the nucleus. One can identify nuclear-coherent events contributions by observing a rapidity gap between the produced particles and the

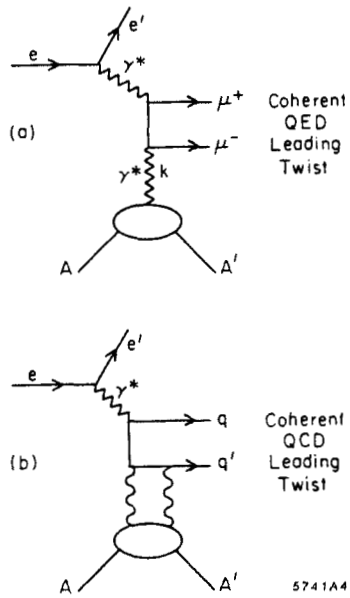

Fig. 27. Leading twist contributions to deep inelastic lepton-nucleus scattering that leave the target intact. (a) QED example. (b) QCD example.

recoiling target. An interesting question is how the gluon momentum fraction sum rule is modified by the diffractive contributions.

Studying "Jet-Coalescence" in Electroproduction

What happens if two jets overlap in phase-space? Certainly independent fragmentation of the jets will fail because of coherent effects. For example, in QED there are strong final state interactions when two charged particles are produced at low relative velocity. In the case of particles of opposite charge $Z_1 e, -Z_2 e$, the QED Born cross sections are corrected by the factor[5] :

$$\sigma = \sigma_0 \frac{2\pi Z_1 Z_2 \alpha / v}{1 - exp(2\pi Z_1 Z_2 \alpha / v)}$$

which increases the cross section dramatically at low relative velocity v. We expect similar effects in QCD when two jets can coalesce to attractive color channels ($Z_1 Z_2 \alpha \to C_F \alpha_s$ for $q\bar{q}$ color singlets). In the case of electroproduction, the low relative velocity enhancements provide a simple estimate of the increase of the $ep \to eX$ cross section at low values of $W^2 = (q+p)^2$, beyond that given by simple duality arguments.

Gunion, Soper and I[6] have recently proposed this jet coalescence mechanism as an explanation of the observed leading particle correlations seen in charm hadroproduction experiments and the anomalously large cross section[55] observed at the SPS for $\Sigma^- N \to A^+(csu)X$ at large x_L. [The hyperon momentum was 135 GeV/c.] In the case of heavy quark electroproduction *e.g.* $\gamma^* g \to s\bar{s}, c\bar{c}$, one predicts an enhancement of the cross section when the produced quark is at low rapidity relative to the target fragmentation region. The correction to the rate, integrated over relative rapidity, is found to vanish only as a single inverse power of the heavy quark mass, and thus may give significant corrections to charm production rates and distributions.

Summary

Electroproduction at intermediate energies on an internal target in a storage ring such as PEP could allow the study of many fundamental phenomena in QCD:

(a) A primary goal is the channel-by-channel reconstruction of the final state in electoproduction in order to understand in detail the final state hadronization of both the quark and nucleon spectator jets in a regime where Bjorken scaling is manifest. Such studies can also provide checks on the effect of the higher-twist coherent contributions to electroproduction cross sections. The hadronization of the target jet is a still largely unexplored phenomenon.

(b) The dynamics of individual exclusive electroproduction amplitudes can be probed as a function of all kinematic energy and angle variables including the virtual photon's mass and polarization. As we have discussed here, such processes can often be analyzed systematically in perturbative QCD, providing detailed checks on both QCD dynamics and hadron wavefunctions. The diffractive reactions also allow the study of the non-forward matrix elements of the same operator product entering the near the light-cone analysis of deep inelastic structure functions.

(c) A nuclear target provides a unique probe of short-distance QCD dynamics. The basic subprocesses can be studied in a background nuclear field. In particular, one wants to study the sources of nonadditivity in the nuclear target channel by channel. This includes tests of various shadowing mechanisms, effects of modification of mesonic degrees of freedom, the predicted "color transparency" of quasi-exclusive amplitudes at large momentum transfer inside a nucleus, and the propagation of quark jets through the nuclear medium. Further, as discussed in ref 20, one can use large x measurements to probe nuclear matter in the far off-shell domain. We also note that exclusive channels which involve the scattering of light nuclei at high momentum transfer probe the NN interaction at short distances.

(d) Given sufficient luminosity, internal target experiments could allow the study of strange and charm particle electroproduction near threshold. By comparing electron and positron beam experiments, one can probe[1] virtual Compton scattering; the sum of the quark charges cubed can be obtained from the ratio of the $e^{\pm}p \to e^{\pm}\gamma + X$ cross sections. Polarized proton and nuclear targets allow the study of detailed effects of spin via correlations with final state properties. The combination of polarized target and polarized electron beams allow measurements of the spin dependent structure functions and their sum rules,[56] checks of helicity selection rules, and the separation of different electroproduction channels.

Although there has been extensive of many aspects of electroproduction over the past decade, there are still many phenomena not fully explored. The distinction between logarithmic and power-law scale breaking effects is still in a confused state. Shadowing, diffraction, the interrelation with vector meson dominance, the structure of the (non-evolved) spectator jet system, Regge behavior in non-singlet structure functions, and other phenomena at the boundary between perturbative and non-perturbative effects, all are central topics in hadron and nuclear dynamics, ideally studied in electroproduction.

References

1. S.J. Brodsky, J.F. Gunion and R.L. Jaffe Phys. Rev. **D6**, 2487 (1972).
2. S.J. Brodsky, G.T. Bodwin and G.P. Lepage, in the Proc. of the Volendam Multipart. Dyn. Conf., 1982, p. 841; Proc. of the Banff Summer Inst., 1981, p. 513. This effect is related to the formation zone principle of L. Landau and I. Pomeranchuk, Dok. Akademii Nauk SSSR **92**, 535,735 (1953).
3. G.T. Bodwin, Phys. Rev. **D31**, 2616 (1985); G.T. Bodwin, S.J. Brodsky and G.P. Lepage, ANL-HEP-CP-85-32-mc (1985), presented at 20th Rencontre de Moriond, Les Arcs, France, March 10-17, 1985.
4. E. Berger, ANL-HEP-PR-87-45 and references therein.

5. A. Sommerfeld, *Atombau and Spektallinen* (Vieweg, Braunschweig, 1939).
6. S.J. Brodsky, J.F. Gunion and D. Soper, SLAC-PUB-4193 (1987).
7. S.J. Brodsky and A.H. Mueller, in preparation.
8. A.H. Mueller, Proc. of the Moriond Conf., 1982.
9. S.J. Brodsky, XIII Int. Symp. on Multiparticle Dynamics, 1982.
10. G.P. Lepage and S.J. Brodsky, Phys. Rev. **D22**, 2157 (1980); G.P. Lepage, S.J. Brodsky, T. Huang and P.B. Mackenzie, CLNS-82/522, published in the Proc. of the Banff Summer Institute, 1981.
11. A.H. Mueller, Phys. Rept. **73**, 237 (1981).
12. V.L. Chernyak and I.R. Zhitnitskii, Phys. Rept. **112**, 1783 (1984); Xiao-Duang Xiang, Wang Xin-Nian and Huang Tao, BIHEP-TH-84, 23 and 29 (1984).
13. A.V. Efremov and A.V. Radyushkin, Phys. Lett. **94B**, 245 (1980).
14. S.J. Brodsky, Y. Frishman, G.P. Lepage and C. Sachrajda, Phys. Lett. **91B**, 239 (1980).
15. S.J. Brodsky and G.R. Farrar, Phys. Rev. Lett. **31**, 1153 (1973); Phys. Rev. **D11**, 1309 (1975).
16. S.J. Brodsky and G.P. Lepage, Phys. Rev. **D23**, 1152 (1981); S.J. Brodsky, G.P. Lepage and S.A.A. Zaidi, Phys. Rev. **D23**, 1152 (1981).
17. S.J. Brodsky and G.P. Lepage, Phys. Rev. **D24**, 2848 (1981).
18. I.D. King and C.T. Sachrajda, SHEP-85/86-15 (1986), p. 36.
19. Z. Dziembowski and L. Mankiewicz, Warsaw University preprint (1986).
20. S.J. Brodsky and B.T. Chertok, Phys. Rev. Lett. **37**, 269 (1976); Phys. Rev. **D114**, 3003 (1976).
21. O.C. Jacob and L.S. Kisslinger, Phys. Rev. Lett. **56**, 225 (1986).
22. N. Isgur and C.H. Llewellyn Smith, Phys. Rev. Lett. **52**, 1080 (1984).
23. C-R Ji, A.F. Sill and R.M. Lombard-Nelsen, SLAC-PUB-4068 (1986).
24. R.G. Arnold *et al.*, SLAC-PUB-3810 (1986).
25. M. Gari and N. Stefanis, Phys. Lett. **B175**, 462 (1986), M. Gari and N. Stefanis, preprint RUB-TPII-86-21 (1986).
26. J. Boyer *et al.*, Phys. Rev. Lett. **56**, 207 (1986).
27. A. Sen, Phys. Rev. **D24**, 3281 (1981).
28. S.J. Brodsky and G.P. Lepage, Phys. Rev. **D24**, 1808 (1981). The next to leading order evaluation of T_H for these processes is given by B. Nezic, Ph.D. Thesis, Cornell Univ. (1985).
29. H.C. Pauli and S.J. Brodsky, Phys. Rev. **D32**, 1993 (1985); Phys. Rev. **D32**, 2001 (1985).
30. T. Eller, H.C. Pauli and S.J. Brodsky, Phys. Rev. **D35**, 1493 (1987).
31. S. Heppelmann, DPF Meeting, Salt Lake City (1987).
32. A.D. Krisch, UM-HE-86-39 (1987).
33. A.W. Hendry, Phys. Rev. **D10**, 2300 (1974).
34. J.P. Ralston and B. Pire, Phys. Rev. Lett. **57**, 2330 (1986).
35. S.J. Brodsky, C.E. Carlson and H.J. Lipkin, Phys. Rev. **D20**, 2278 (1979); H.J. Lipkin, private communication.
36. C.-R. Ji and S.J. Brodsky, Phys. Rev. **D34**, 1460; **D33**, 1951; **D33**, 1406; **D33**, 2653 (1986); Phys. Rev. Lett. **55**, 2257 (1985).
37. G. Martinelli and C.T. Sachrajda, CERN-TH-4637/87 (1987). The results are based on the method of S. Gottlieb and A.S. Kronfeld, Phys. Rev. **D33**, 227 (1986); A.S. Kronfeld and D.M. Photiadis, Phys. Rev. **D31**, 2939 (1985).
38. R.L. Anderson *et al.*, Phys. Rev. Lett. **30**, 627 (1973).
39. S.J. Brodsky and J. Pumplin, Phys. Rev. **182**, 1794 (1969); S.J. Brodsky, F.E. Close and J.F. Gunion, Phys. Rev. **D6**, 177 (1972).
40. A.H. Mueller and J. Qui, Nucl. Phys. **B268**, 427 (1986); J. Qui, preprint CU-TP-361.
41. J.J. Aubert *et al.*, Phys. Lett. **123B**, 275 (1983); For a recent review see E.L. Berger and F. Coester, ANL-HEP-PR-87-13 (to be published in Ann. Rev. of Nucl. Part. Sci.).
42. A. Donnachie and P.V. Landshoff, Phys. Lett. **185B**, 403 (1987).
43. S.J. Brodsky, C.-R. Ji and G.P. Lepage, Phys. Rev. Lett. **51**, 83 (1983).
44. S.J. Brodsky and J.R. Hiller, Phys. Rev. **C28**, 475 (1983).
45. J.F. Gunion, S.J. Brodsky and R. Blankenbecler, Phys. Rev. **D8**, 287 (1973); Phys. Lett. **39B**, 649 (1972); D. Sivers, S.J. Brodsky and R. Blankenbecler, Phys. Reports **23C**, 1 (1976). Extensive references to fixed angle scattering are given in this review.
46. E.L. Berger and S.J. Brodsky, Phys. Rev. **D24**, 2428 (1981).
47. E.L. Berger and F. Coester, ANL-HEP-PR-87-13 (1987).
48. P. Hoodbhoy and R.L. Jaffe, Phys. Rev. **D35**, 113 (1987); R.L. Jaffe, CTP #1315 (1985).
49. I.A. Schmidt and R. Blankenbecler, Phys. Rev. **D15**, 3321 (1977).
50. J.F. Gunion, P. Nason and R. Blankenbecler, Phys. Rev. **D29**, 2491 (1984); Phys. Lett. **117B**, 353 (1982).
51. K. Freudenreich, Zurich, NA-10 collaboration.
52. H.G. Fischer, presented at the Leipzig Conference, 1984.
53. G. Alexander, E. Gotsman and U. Maor, Phys. Lett. **161B**, 384 (1985).
54. S.J. Brodsky and M. Soldate, unpublished.
55. S.F. Biagi *et al.*, Z. Phys. **C28**, 175 (1985).
56. R.L. Jaffe, MIT-CTP-1445 (1987).

A SPACE-TIME ANALYSIS OF MUO-PRODUCED HADRONIC SHOWERS

Jorge G. Morfín
Fermi National Laboratory
Batavia, IL 60510

Abstract

Hadron showers, produced by high energy muons interacting on various targets, have been analysed for evidence of a space-time structure of parton fragmentation by the European Muon Collaboration. Target-dependent multiplicity ratios and Bose-Einstein interference phenomena both yield information on this subject.

Introduction

What I will be discussing in this presentation is the latest step in the process which has taken the concept of partons from being a theoretical explanation[1] for a surprising experimental result to a particle in its own right. While it is true that the unconfined parton has not yet been detected, the characteristics of the parton have been fairly well defined through experimentation[2]. By studying the space-time development of a high energy muo-produced hadron shower, we are trying to answer two more fundamental questions about the nature of the quark. First, what is the quark-nucleon crosssection? Second, when does the struck quark start fragmenting into hadrons? Since the relevant distances and time intervals will turn out to be relatively large we will have opportunity to briefly look at the problem of quark confinement. Furthermore, we will see that a study of nuclear effects becomes not only very intriguing but crucial to answering the above two questions. As experimental references I will concentrate on the results of the European Muon Collaboration (EMC), which used muons of energy 100 - 300 GeV on various targets, and the Tevatron Muon Experiment[3] (TMC), scheduled to start running this spring at Fermi National Laboratory with 600 GeV muons. It is not coincidental that the primary goal of the TMC is a high statistics analysis of these nuclear effects.

Experimentally we are trying to determine what happens between the time a muon is detected as entering the experimental target and a shower of hadrons emerges. The process can be divided into three stages:

1. The muon transfers a fraction of its energy to a parton.
2. The parton travels through the nuclear medium and hadronizes.
3. The hadrons continue the passage through the target material and emerge.

Stage 1 covers such topics as the hadronic nature[4] of the photon which mediates the deep inelastic interactions (to be covered in these proceedings by T. Sloan) and the measurement of the nucleon structure function[5]. These results tell us the probability with which we will interact with a quark of a given flavor and what fraction of the total nucleon's momentum will be carried by the quark. Stage 3 has been studied for many years and is covered well by references[6] dealing with the passage of a particle through matter. Naturally stage 3 phenomena also includes hard final state scatters which would take us back to stage 2 ... etc.

Kinematics

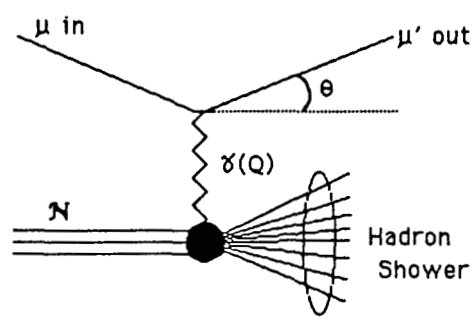

Fig 1. Feynman Graph representation of deep inelastic muon scattering

In discussing the phenomena of deep inelastic scattering, there are standard kinematic variables that are most helpful in characterising the interaction. If the incoming muon has energy E

while the scattered muon has energy E' and scattering angle θ then the amount of 4-momentum transferred to the struck quark is:

$$Q^2 = 4EE'\sin^2 \theta/2 = -q^2$$

and the transferred energy is

$$\upsilon = E - E' .$$

The ratio of the 4-momentum transferred to the energy transferred is a measure of the fraction of the total nucleon momentum carried by the struck quark, as first formulated by Bjorken;

$$x_{Bj} = Q^2 / 2M\upsilon.$$

The hadronic shower is described by the effective mass of the shower

$$W^2 = M^2 + 2M\upsilon - Q^2,$$

and individual hadrons within the shower are characterized by the ratio of the hadron's energy to the total energy transferred to the hadron system

$$z = p / p_{max} = E_h / \upsilon.$$

Finally, Feynman-x relates a hadron's 3-momenta to the 3-momentum of the photon propagator, and the rapidity of a hadron is a measure of it's direction relative to the photon propagator's direction;

$$x_F = \frac{P_L^*}{(P_L^*)_{max}}$$

$$Y = 0.5 \ln \frac{E + P_L}{E - P_L}$$

Survey of Theoretical Ideas: A-Dependent Multiplicity Distributions

The significance of a space-time analysis of high energy processes as well as the basic ideas were summarized by Bjorken[7] in several fundamental reports from the mid 70's. He pointed out the importance of long time intervals and large distances which had been hinted at earlier by Landau and colleagues[8]. At the time, the emission of hard hadrons was postulated to be a tail effect of a bremsstrahlung-type process of soft hadron emission. In this case, the distance required for the hadron to form in the lab is simply the time/distance for the quark to fragment to the hadron in the quark rest frame - a distance of ≈ $1/m_h$ - boosted by its Lorentz factor (E_h / m_h) into the lab. This hypothesis was consistent with the observed[9] absence of intra-nuclear cascading of high energy hadrons since if E_h / m_h^2 > nuclear size, the hadron is **formed <u>outside</u> of the nuclear matter.**

A series of increasingly complex models followed these early concepts. They attempt to describe the behavior of leading hadrons with large z (or x_F):

<u>Dar and Takagi[10]</u> -- postulated that the leading quark either escapes completely or is entirely absorbed in a single interaction. With a **quark**-nucleon cross section (σ_{qN}) of 13 mb they were able to successfully describe the existing data as shown in Fig 2.

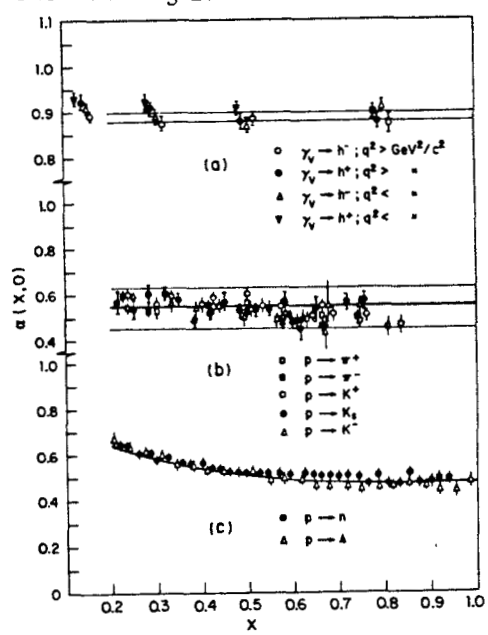

Fig. 2 The predictions of reference 10 (solid lines) compared to various experimental results.

<u>Nilsson, Andersson and Gustafson[11]</u> -- The quark can interact more than once, transferring energy to a nucleon each time, before finally fragmenting. They needed a value of σ_{qN} = 20 mb to fit the data as in Fig 3.

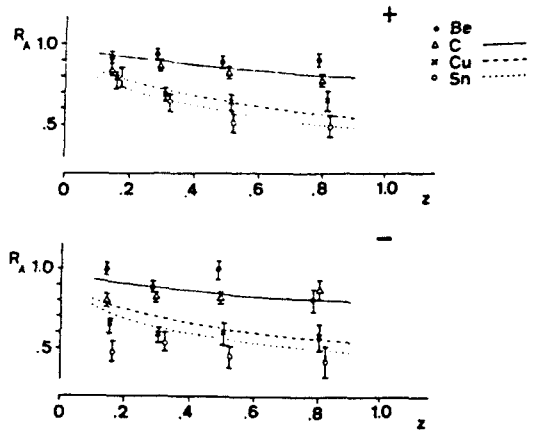

Fig. 3 The predictions of reference 11 compared to the positive and negative particles from the data of reference 17.

Bialas and Bialas[12] -- This model was relatively sophisticated in that it contained multiple elastic and inelastic quark - nucleon scattering. A separate analysis of the longitudinal and transverse hadron momentum spectra yielded information on σ_q^{inel} and σ_q^{tot} respectively.

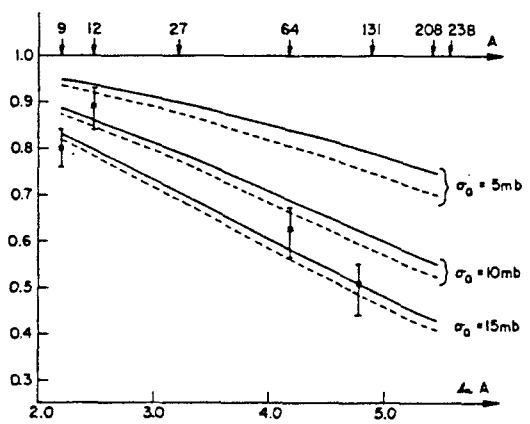

Fig. 4 The A-dependence of the ratio of hadronic yields from nuclei and H_2 for different values of the total quark-nucleon cross section. The data are from reference 17.

Bialas[13] -- This was the first model to stress the simple idea of measuring the A-dependence of the multiplicity of *different* leading hadrons. If it is the same, the intermediate state which escapes the nucleus is a quark. Bialas also stressed the importance of the interplay between σ_q and the formation length τ_q --> h.

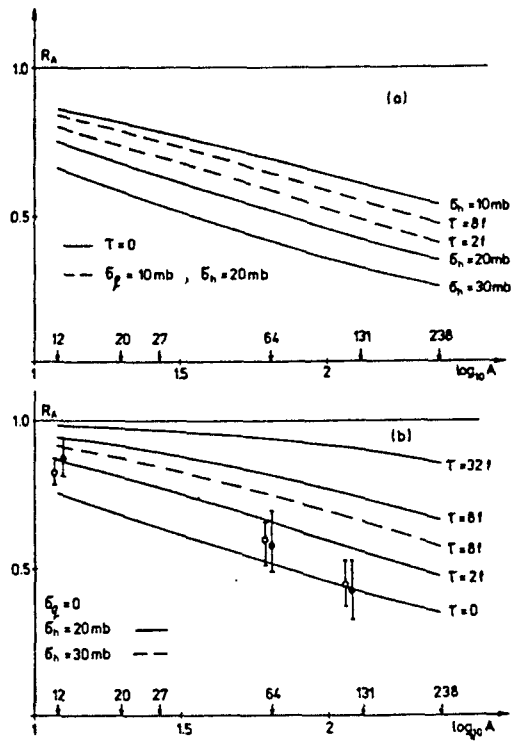

Fig. 5 The ratio of multiplicities from nucleus A versus H_2 for various values of the formation length and the quark nucleon cross section. The data are from reference 17.

Nikolaev[14] -- A very sophisticated model which uses a nuclear transport equation combined with the concept of formation length to predict multiplicity distributions for deep inelastic and photoproduced hadron showers.

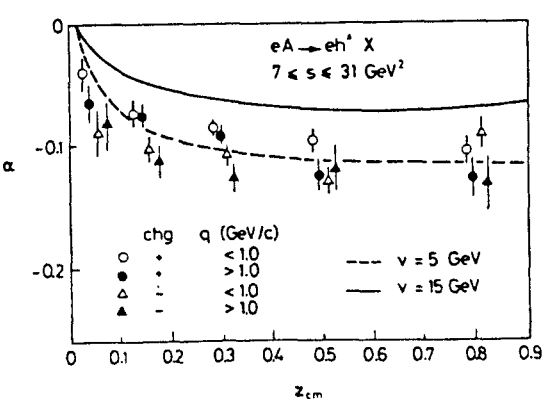

Fig. 6 The predicted behavior of α, the exponent of A^{α}, vs z in the cm system and compared to the data of reference 17.

Bialas and Chmaj[15] -- introduced an alternative definition of formation length by postulating that fragmentation may be similar to the decay of the quark into a hard hadron. In this case, the formation length is $\tau = \upsilon / m_q^2$ where the quark life-time has been assumed to be $\approx 1 / m_q$. If this is the case, then the formation length should be Q^2 dependent. Fig. 7.

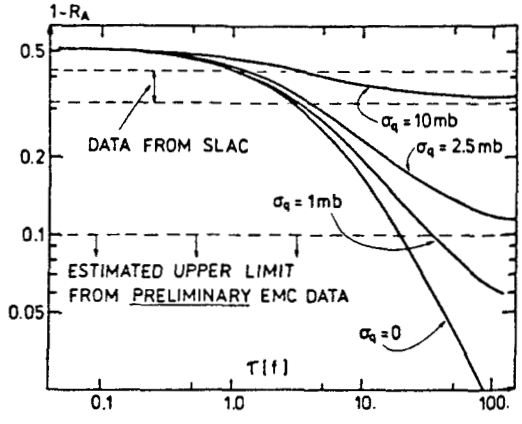

Fig. 7 The ratio of hadrons produced on copper and H_2 versus the formation length for various values of the quark nucleon cross section. The data are from reference 17 and early EMC results.

QCD Models[16] -- The application of QCD to the space-time development of hadron showers does not appreciably change the basic scale invariant parton model predictions we have just outlined.

One common thread which binds all of the models which we have discussed and which has guided our planning of the Tevatron Muon Collaboration is that

To determine the validity of the various ideas contained in these models, a measurement of the A-DEPENDENCE of the hadron shower characteristics is crucial!!

Experimental Results: A-Dependent Multiplicity Distributions

The EMC experiment was not the first to study leptoproduced hadron showers. There have been electron and neutrino as well as earlier muon experiments which have studied lepton-nucleus scattering. However, the earlier experiments were handicapped by a lack of statistics and/or a low and limited energy range. Except for the SLAC results[17] using a 20.5 GeV electron beam with statistics of 10000 events per target, the earlier experiments were limited to 600 ($<E_\upsilon> \approx 20$ GeV) and 3100 ($<E_\upsilon> \approx 200$ GeV) event neutrino[18,19] experiments and an 88 event muon ($E_\mu = 150$ GeV) emulsion experiment[20].

The European Muon Collaboration, running without a vertex detector, took data with Carbon and Copper targets[21] and compared it with earlier data[22] using a hydrogen target. The main thrust of this phase of the experiment was to study the ratios of multiplicity distributions of hadrons produced off of these different nuclei. Examined was the ratio of differential multiplicity distributions

$$R_{A_1/A_2}(z) = \left(\frac{1}{N_\mu}\frac{dn}{dz}\right)_{A_1} / \left(\frac{1}{N_\mu}\frac{dn}{dz}\right)_{A_2}$$

and, to emphasize any nuclear effects on the leading hadrons, the ratio of integrated z distributions

$$\bar{R}_{A_1/A_2}(z_{min}) = \int_{z_{min}}^{1.0} dz \left(\frac{1}{N_\mu}\frac{dn}{dz}\right)_{A_1} / \int_{z_{min}}^{1.0} dz \left(\frac{1}{N_\mu}\frac{dn}{dz}\right)_{A_2}$$

Kinematic Cuts and Data Sample

To keep acceptance corrections small and consistent for the different nuclear runs, the following kinematic cuts were made on all samples;

$$Q^2 > 5.0 \text{ GeV}^2$$
$$\upsilon > 50.0 \text{ GeV}$$
$$x_{Bj} > 0.02$$
$$W^2 > 25.0 \text{ GeV}^2$$
$$P_{had} > 6.0 \text{ GeV} \quad .$$

After these cuts had been made, the following sample sizes were used in the final analysis:

Nucleus	E_μ	Events	$\langle W^2 \rangle$	$\langle \upsilon \rangle$	$\langle Q^2 \rangle$	$\langle x \rangle$
Hydrogen	120 GeV	9.0 K	121 GeV^2	71 GeV	12 GeV^2	.10
Hydrogen	280	9.8 K	174	108	29	.15
Carbon	200	13.9 K	186	110	21	.11
Copper	200	10.4 K	188	112	21	.11

The differences between the hydrogen and heavier nuclei samples arose since the Carbon and Copper runs were performed at a different time with a somewhat altered spectrometer.

Analysis

Since the analysis concentrates on the ratios of hadronic distributions from the three targets, it is the *differences* in the corrections which are crucial. For the acceptance corrections it was determined that at high z the acceptance during hydrogen running was twice as high as for the heavy nucleus runs. For the radiative corrections, the C and Cu data had to be corrected for coherent radiative processes in addition to the corrections which had been applied to the hydrogen sample. This amounted to, at most, a 5% correction to the Cu data in the lowest x range. The only other correction required to account for the difference between hydrogen and the heavier nuclei is a compensation for hadronic interactions with other nuclei of the target. Absorption or the creation of secondaries modified produced multiplicities. Using Monte Carlo techniques the maximum correction was found to be < 5%. **Note that after this correction the results correspond to zero target length.**

Results

The overall average multiplicities are 1.58 ± .02 for Carbon and 1.69 ±.02 for Copper. This represents an increase of 7% ± 2%(statistical) ± 3%(systematic) which is hardly significant. A more detailed look at the multiplicities is shown in the following figure. Even at this level there is no difference between the carbon and copper data.

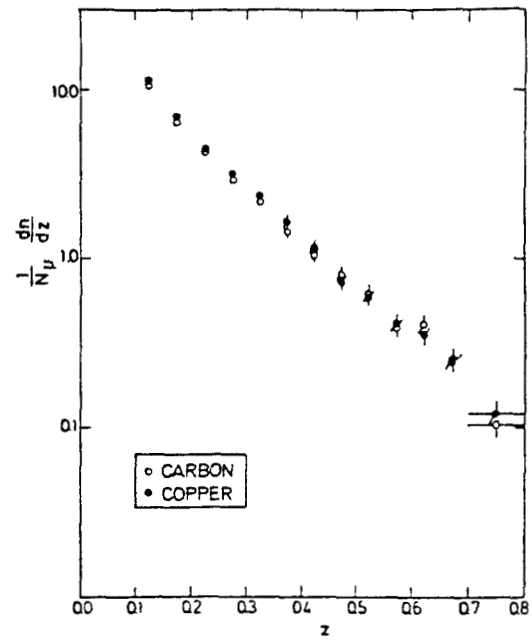

Fig. 8 shows the charged hadron multiplicity as a function of z for C and Cu.

To see if the multiplicities are dependent on the energy transferred to the struck parton, the data has been divided into three υ bins; $50 < \upsilon < 70$ GeV, $70 < \upsilon < 90$ GeV, and $\upsilon > 90$ GeV. The results are shown in Fig. 9.

The average multiplicity ratios for leading ($z>0.5$) hadrons in the three υ bins is:

Ratio	$50<\upsilon<70$	$70<\upsilon<90$	$\upsilon>90$ GeV
Cu/C	.78±.13±.05	1.27±.20±.10	1.04±.12±.14
C/H_2	1.07±.13±.17	0.77±.12±.11	1.16±.12±.20
Cu/H_2	0.84±.12±.14	0.97±.14±.13	1.20±.12±.20

The overall trend of the υ-dependence is a depletion of leading hadrons and an overall broadening of hadron showers at low υ in Cu compared to C and H_2.

There is a similar although statistically less significant effect when we look at the x_{Bj} dependence of the multiplicities. We find a depletion of leading hadrons and a broadening of the hadron showers at large x. Since $x = Q^2/2M\upsilon$ we are probably seeing a reflection of the previously mentioned υ dependence in the x-distribution.

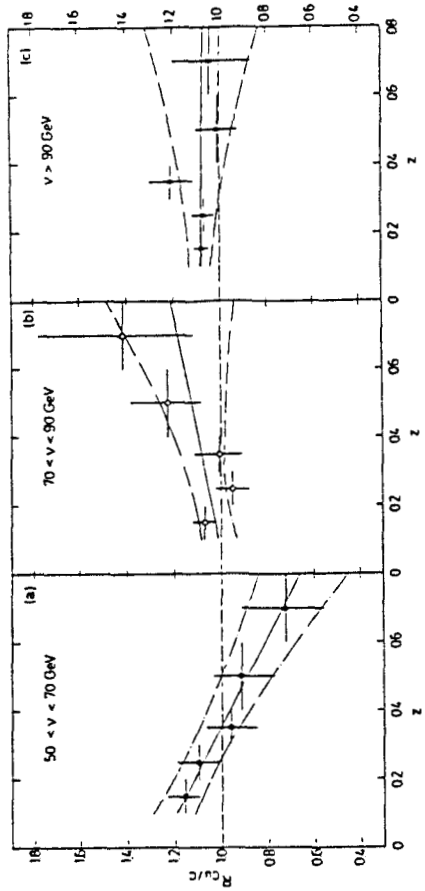

Fig. 9 The ratio of copper and carbon multiplicities as a function of z in three different virtual gamma energy bins. The solid lines are linear fits to the data and the dashed lines are the 1 sd limits.

We can combine these EMC results with the earlier SLAC[17] results for $3 < \upsilon < 17$ GeV.

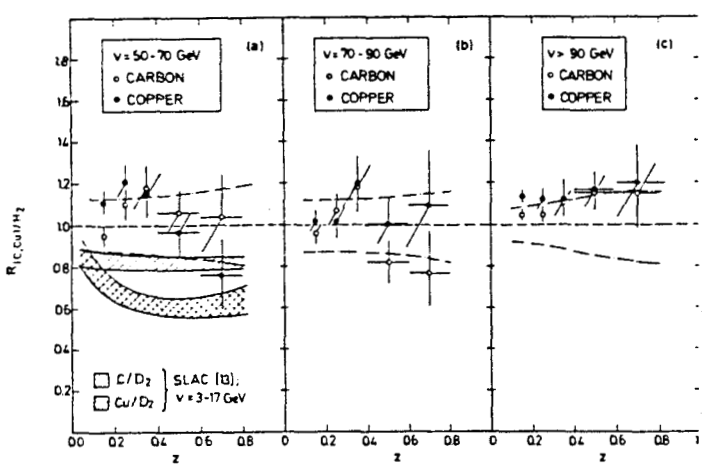

Fig. 10 The ratio of multiplicity distributions from EMC and the low energy SLAC results plotted together.

The nuclear effects are much more pronounced at the low SLAC values of υ. Assuming that the effect depends only on υ (not on Q^2), the model of Bialas[13] can be used to fit the two υ ranges (roughly $3 < \upsilon < 180$ GeV) of the SLAC and EMC results. Using the measured ratios of C:Cu <1.25 (2 s.d) by EMC at $\langle\upsilon\rangle \approx 100$ GeV and C:Cu > 1.17 by the SLAC group at $\langle\upsilon\rangle = 8$ GeV, and expressing the formation length τ as

$$\tau(\text{fm}) = \delta(\text{fm/GeV}) * \upsilon(\text{GeV})$$

then Fig. 11 shows the region in the δ-σ_{qN} plane allowed by the two results.

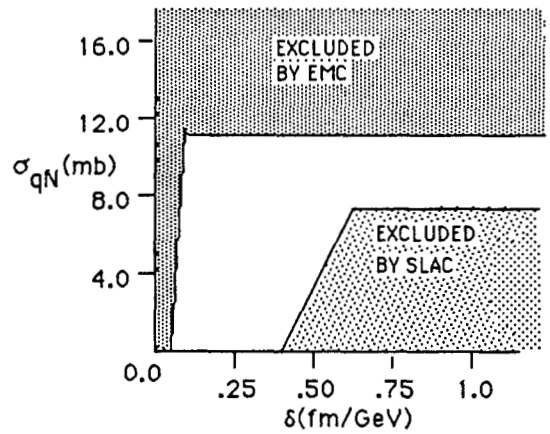

Fig. 11 Allowed region in the δ-σ_{qN} plane by both the SLAC and EMC results using Bialas' model.

It can be seen that the SLAC results favor smaller values of δ while the EMC results exclude $\delta = 0$. Cross sections larger than ≈ 10 mb are excluded by the EMC results. It should be quite obvious that much more exact data at all values of υ are necessary before further model dependent interpretation is possible.

Conclusions: A-Dependent Multiplicity Distributions

There is a depletion of leading particles and a broadening of hadron jets at low υ with increasing A of the target. Analysis of the EMC and SLAC results in terms of the Bialas model implies that τ, the formation length, is υ dependent and comparable to the size of the nucleus ($r_C = 2.7$ fm and $r_{Cu} = 4.8$ fm) and the quark-nucleon cross section would have to be less than 10 mb.

Improvements expected from the Tevatron Muon Experiment

Following is a list of the major improvements we expect from the upcoming Tevatron experiment on nuclear targets compared to the recently completed EMC heavy target experiment:

1. Increase statistics by an order of magnitude
2. Improved acceptance for high-z particles.
3. Various A targets will be exposed in the same run to the same muon energy distribution resulting in reduced systematic errors.
4. There will be a factor > 2 larger kinematic range which should allow finer binning in υ and a measurement of the Q^2 dependence of the formation length τ.
5. Much better particle identification (i.e. K/π separation from 1 to 120 GeV) should improve the chance of measuring τ and σ_{qN} for different hadrons.

The Bose-Einstein Effect: Introduction

I am sure we all recall studying the difference between Fermi statistics and Bose-Einstein statistics in Quantum Mechanics and, perhaps, thinking that this will never apply to much that we would be doing professionally. This next method for studying the development of a hadron shower is a vindication of the hours invested in studying Bose-Einstein!

A method to use Bose-Einstein interference to determine the spatial extent of an object was first proposed by Hanbury-Brown and Twiss[23] in the mid 50's to determine the diameter of stellar objects using photon interferometry. Several years later, and unaware of the Hanbury-Brown Twiss work, G. Goldhaber and colleagues[24] noticed a distinct difference between the rate of like-charge and unlike-charge pion pairs as a function of the opening angle between the pions. After a month of contemplation they interpreted this result in terms of the Bose-Einstein effect for pions and were able to obtain a quantitative fit to their data by symmeterizing the two pion wave functions for like pions. In the intervening years the analysis has become much more sophisticated[25] and high statistics experiments now use correlation densities to extract the effect. Defining the one and two particle densities

$$\rho(p_1) = \frac{1}{\sigma}\frac{d\sigma}{dp_1}$$

$$\rho(p_1,p_2) = \frac{1}{\sigma}\frac{d^2\sigma}{dp_1 dp_2}$$

respectively, the two body correlation coefficient is given by

$$C_2 = \frac{\rho(p_1, p_2)}{\rho(p_1)\,\rho(p_2)}$$

To remove kinematic and dynamic correlations not associated with the Bose-Einstein effect, ratios are taken between a like-sign experimental density and a reference sample density which should not have any Bose-Einstein correlations,

$$R_0^{Like} = \frac{\rho(p_1, p_2)}{\rho_0(p_1, p_2)}$$

The quantity $(R_0{}^{Like} - 1)$ is the **Fourier transform of the space-time distribution of the particle source.**[26]

The important thing for experimentalists is that the consequences of the Bose-Einstein effect should be an enhancement of n(>1) identical boson final states compared to a final state composed of n dissimilar bosons. Using the parameterization chosen by the EMC collaboration[27], if $\Delta p = p_i - p_j$ is the difference of the 4-momenta of two like sign pions, then the ratio of like-sign pairs to non-interfering pairs can be expressed as

$$1 = 1 + \lambda \exp(-\tilde{M}^2 R^2)$$

with $\tilde{M}^2 = -(\Delta p)^2$ the square of the difference of the pions 4-momenta and **R is the rms size of the pion source!** The factor λ is necessary to compensate for coherently produced pions.

The Bose-Einstein Effect: EMC Results

The European Muon Collaboration's full spectrometer (with streamer chamber and associated vertex detectors) was used to study the Bose-Einstein effect in muoproduced hadronic showers. Using 280 GeV muons on a H_2 target, a sample of events was collected which survived the

following kinematic cuts:

$$Q^2 > 4\ GeV^2$$
$$4 < W < 20\ GeV$$
$$20 < \upsilon < 260\ GeV$$
$$y < 0.9$$
$$\theta_{\mu'} > 0.75^\circ \quad .$$

After further resolution associated cuts, the final sample consisted of 17,343 events.

Since only **50%** of the hadrons were identified, it was assumed that all negative hadrons were pions. This was justified by the Lund Monte Carlo results which showed that the ratio $\pi : K : P$ was 80 : 9 : 11. Furthermore, within the hadronic shower all particles had to have momentum measurements with $\Delta P/P < 20\%$ and, most significantly, all accepted tracks had to be measurable in the streamer chamber. This last requirement effectively limited the particles to $x_F < 0.2$ which is relatively low momentum particles. Under these conditions the following combinations were found

126,000 $(\pi^+\pi^-)$ combinations

60,000 $(\pi^+\pi^+)$ combinations
38,300 $(\pi^-\pi^-)$ combinations
98,300 like sign pion pairs

Results

The most difficult task in the analysis is separating the Bose-Einstein Effect from elementary kinematic and dynamic correlations. The standard technique, mentioned above, is to form ratios of the like-sign pairs--$\rho(p_1,p_2)$--to pairs where the Bose-Einstein effect should be absent--$\rho_0(p_1,p_2)$. In the EMC analysis three reference groups were formed:

REF 1 — $(\pi^+\pi^-)$ combinations from the same event in which a like-sign pair was found,

REF 2 — $(\pi^+\pi^-)$ combinations from the same event but with transverse momentum from random pions within the event,

REF 3 — LIKE combinations constructed from random tracks from various events.

The LIKE/REF ratios as a function of $\tilde{M}^2$ are shown in Fig. 12a. There is an increase in the ratio as $\tilde{M}^2$ approaches 0, but there is an inconsistency in the shapes as well as the overall normalization of the three curves. This is an indication that there are still dynamical or kinematical correlations that remain uncompensated in the ratios. The next step in eliminating these non-interfering correlations involves the use of the Lund Monte Carlo[28] which does not contain interference effects. Subjecting the Monte Carlo events to the same cuts as the data the ratio LIKEMC/REFMC is formed. Again it is seen--Fig. 12b--that there is a disagreement in shape and normalization between the three ratios which must arise from residual dynamic and/or kinematic correlations. In an attempt rid the sample of these correlations, a "ratio of ratios" is formed resulting in the curves shown in Fig. 12c.

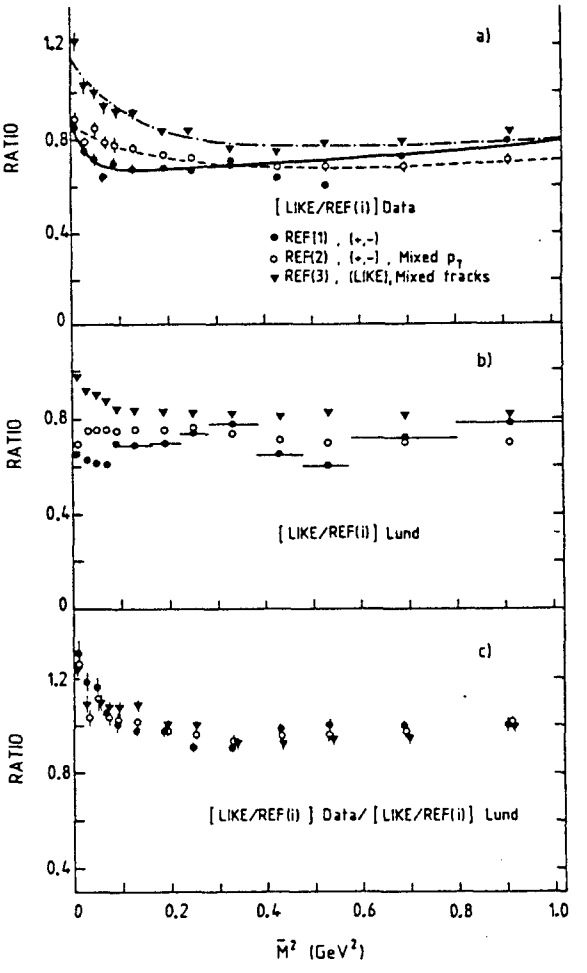

Fig. 12 Ratios as a function of the difference in the 4-momenta of the pion pairs. a) ratio of LIKE to REF(i) as defined above, b) the same ratios when using the Lund Monte Carlo results and c) the ratio of ratios a) and b).

The results now show a trend which is similar in both shape and magnitude indicating that the non-interfering correlations have been more successfully removed. A fit to $\tilde{M}^2$ and λ yields the following values, using the double ratios, for the three reference samples

	R(fm)	λ	χ^2 (12 DF)
REF 1	0.84 ± 0.03	1.08 ± 0.10	12.4
REF 2	0.66 ± 0.01	0.60 ± 0.06	12.2
REF 3	0.46 ± 0.03	0.73 ± 0.06	20.3

The results still depend on the reference sample which indicates that there are some correlations that have not been removed from the LIKE sample. Berger and his colleagues have shown[29] how intertwined the Bose-Einstein and resonance correlations can be.

Conclusion

The EMC analysis continues in an attempt to extract the shape of the pion emission region and the details can be found in reference 27. The EMC group comes to the conclusions that;

1. The Bose-Einstein interference effect has been seen in muoproduced like-sign pion pairs,
2. The results are consistent with a **spherically** shaped pion emission region, and
3. The radius of the emission region is **0.46 < R < 0.84 fm** and the suppression factor is $0.6 < \lambda < 1.0$.

These results are approximately consistent with almost every other experiment, regardless of energy or target, which has attempted the analysis. This, as well as the *spherical* nature of the emission region, tends to go against intuition and might indicate that there is something not consistent with either the method and/or the interpretation of the results of the Bose-Einstein analysis.

Critique

No one doubts the validity of Bose-Einstein statistics so that there should indeed be an interference effect that would enhance the number of "similar" bosons. However, aside from the difficulty of extracting the signal due to interference from the non-interfering correlations, the question of interpretation of the result is quite crucial.

The method used by the EMC and others, which involves describing the pion emission region with a single spatial variable R, is realistic in only a very few situations[30]. There is obviously no directional information in R so the data can only be described by this form if the source density of the emission region depends only on the length of the 4-vector difference between the two pions. Furthermore, and most telling, the 4-momentum difference of any pair of pions as well as the "shape" of the source has to depend on the frame in which they are being evaluated. Fig. 13 illustrates this by indicating a pair of pions which have identical 4-vectors in a frame where the current and target fragment sources are moving in opposite directions with respect to each other. Upon boosting to the lab they are no longer "identical pions". This, of course, implies that if lab momenta are used to search for identical pion pairs, there is no way that the resulting pion source size can be a measure of the **total emission (current + target fragments) region!** It is, at best, a measure of the spatial extent of either current fragment sources or target fragment sources. Even this interpretation is not necessarily correct if there is an ordered momentum/space-time correlation, as postulated by Bjorken and incorporated by the successful Lund Monte Carlo, so that particles with similar momentum have been emitted at **neighboring** space-time points in the evolution of the hadronic shower!

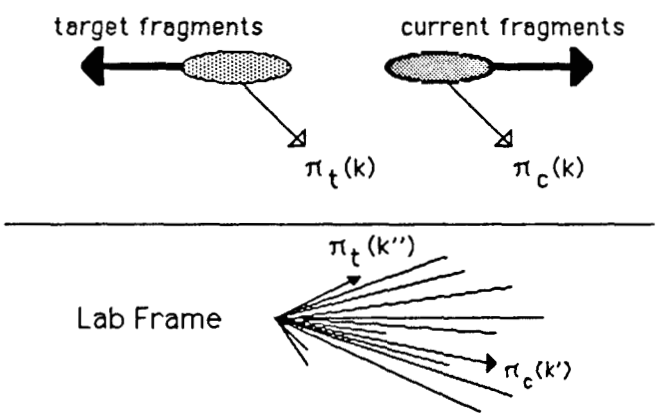

Fig. 13 Identical pion in one frame are not identical pions in all frames.

There have been attempts[30,31], particularly in the interpretation of e^+e^- Bose-Einstein analyses, to determine whether currently acceptable hadronization models, such as the Lund-type string model, might yield the results found by almost all Bose-Einstein analyses including the EMC result. Both of the references find consistency between string model predictions and the experimental results that the emission region is "spherical" and the associated length is of the order of 1 fm. However, this length has little to do with the spatial extent of the source of all particles in the shower.

The TMC will take a much more critical look at the method and interpretation of Bose-Einstein interference effects. Much improved particle identification, improved momentum resolution and increased kinematical range should allow Bose-Einstein analyses in more than one reference frame and off various targets.

Overall Conclusion

The topic of the space-time development of a hadron shower, although of fundamental importance, has barely progressed beyond the most elementary level of experimental investigation. The concepts of quark-nucleon cross sections and hadron formation lengths are still more philosophical than scientific quantities. There is a need for carefully controlled, high statistics measurements of hadron multiplicities off a variety of nuclear targets and over a wide kinematic range before a quantified knowledge of the space-time structure of a hadronic shower can be claimed. This need will be answered by the upcoming Tevatron Muon Collaboration which will begin taking data at Fermilab in the very near future. A second experiment, preferably covering lower energies than this Tevatron experiment, would be extremely useful in answering the questions posed in this presentation.

References

1. R. P. Feynman, Photon-Hadron Interactions, W. A. Benjamin, New York, 1972.
2. T. Sloan, Recent Results in Deep Inelastic Scattering, CERN EP/86-111, August, 1986.
3. Muon Scattering with Hadron Detection at the Tevatron, Fermilab Experiment 665.
4. T. Sloan, Recent Results in Deep Inelastic Scattering, CERN EP/86-111, August, 1986.
5. J. J. Aubert et al., Nucl. Phys B272 , 158 (1979).
6. E. Segrè, Nuclei and Particles, W. A. Benjamin, New York, 1964.
7. J. D. Bjorken, SLAC-PUB-1756, May 1976.
8. L. D. Landau, Izv. Acad. Nauk. SSSR 17, 31 (1953).
9. W. Busza, Acta Phys. Pol. B8 , 333 (1977).
10. A. Dar and F. Takagi, Phys. Rev. Lett. 44, 768 (1980).
11. G. Nilsson, B. Andersson and G. Gustafson, Phys. Lett. 83B, 379 (1979).
12. A. Bialas and E. Bialas, Phys. Rev. D21, 675 (1980).
13. A. Bialas, Acta Phys. Pol. B11, 475 (1980).
14. N. N. Nikolaev, Z. Phys. C 5, 291 (1980).
15. A. Bialas and T. Chmaj, Phys. Lett. 133B, 241 (1983).
16. S. J. Brodsky, SLAC-PUB-2970, September 1982. A. H. Mueller, Topics in High Energy Perturbative QCD Including Interactions with Nuclear Matter, Proc. XVIIth Rencontre de Moriond, Les Arcs, 1982.
17. L. S. Osborne et al., Phys. Rev. Lett. 40, 1624 (1978).
18. J. P. Berge et al., Phys. Rev. D18, 3905 (1978).
19. H. Deden et al., Nucl. Phys. 198B, 365 (1982).
20. L. Hand et al., Z. Phys. C 1, 139 (1979).
21. A. Arvidson et al., Nucl. Phys. B246, 381 (1984).
22. J. J. Aubert et al., Phys. Lett. 114B, 373 (1982).
23. R. Hanbury-Brown and R. Q. Twiss, Philos. Mag. 45, 663 (1954).
24. G. Goldhaber et al., Phys. Rev. Lett. 3, 181 (1959).
25. G. Goldhaber, LBL Preprint 19417 (1985).
26. G. Goldhaber et al., Phys. Rev. 120, 300 (1960).
27. M. Arneodo et al., CERN-EP/86-42, April 1986.
28. G. Ingelman et al., Nucl. Phys. B206, 239 (1982).
29. E. L. Berger et al., Phys. Rev. D15, 206 (1977).
30. M. G. Bowler, Z. Phys. C 29, 617 (1985).
31. B. Andersson and W. Hofmann, Phys. Lett. 169B, 1986)

THE NUCLEAR RESPONSE AT MEDIUM ENERGY*

T. W. Donnelly†

Center for Theoretical Physics
Laboratory for Nuclear Science
and Department of Physics
Massachusetts Institute of Technology
Cambridge, Massachusetts 02139 U.S.A.

Abstract

The use of internal targets to investigate the nuclear response at medium energies is discussed with emphasis being placed on what can be learned by employing polarized targets to study "electromagnetic spin physics." The importance of having longitudinally polarized electrons is stressed. Both single-arm and coincidence reactions are discussed and contrasted with similar studies involving final-state polarimetry using external beams and targets. Conclusions are drawn concerning practical implications for polarized internal target experiments.

Introduction

The discussions here center around what can be learned about the nuclear response at medium energy by exploiting polarization degrees of freedom: polarized electrons, polarized targets and measurement of final-state polarizations. As we shall see in the closing comments, there are only a very few special cases in which it is practical to use polarized targets with external beams of electrons, whereas with the extremely high current which can be obtained in electron storage/stretcher rings it becomes feasible to contemplate using (low density) *internal polarized targets*. Consequently, the main focus in the present context is placed on reactions of this sort, with or without having polarized electrons as well. In certain cases, the same or possibly complementary information can be obtained using unpolarized targets but measuring some final-state polarization; these are noted in the following discussions.

Two classes of reactions are considered, the first being single-arm (inclusive) studies of the type

$$e + \vec{A} \rightarrow e' + X$$
$$\vec{e} + \vec{A} \rightarrow e' + X \ ,$$

in which a (possibly polarized) electron is scattered from a polarized target and the scattered electron is detected. The products of the reaction, X, are presumed not to be detected. Of course, from the kinematics of the electron scattering it is possible to specify the total energy of the final state and, when this is a discrete nuclear level (such as the ground state itself in elastic scattering), the word "exclusive" is frequently used. However, here we presume no knowledge of the final-state polarization, no knowledge of the final-state decay branching (even for a discrete state it can, say, γ-decay with several branches) and no knowledge of the specifics of how the various open channels are populated when above particle emission threshold (for example, the relative weightings of proton knockout, neutron knockout, two-nucleon knockout, pion production, etc.).

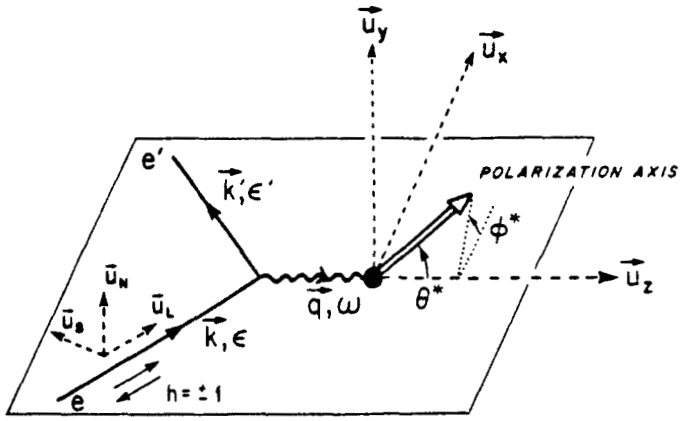

Fig. 1: Single-arm electron scattering from polarized targets including the possibility of having longitudinally polarized electrons (helicity $h = \pm 1$), $\vec{A}(\vec{e},e')$. The target polarization axis is specified by the angles (θ^*,ϕ^*) as shown.

The second class of reactions considered here are then the more exclusive coincidence reactions, for instance of the type

$$e + \vec{A} \rightarrow e' + x + X$$
$$\vec{e} + \vec{A} \rightarrow e' + x + X \ ,$$

where, in addition to detecting the scattered electron, a particle x in the final state is also detected. Again, the rest, X, is not detected. These particular cases can be termed exclusive-1 reactions (or alternatively semi-inclusive reactions). There are also exclusive-2, -3, $\cdots$ reactions in which 2, 3, $\cdots$ particles are detected in coincidence with the scattered electron; here we restrict our attention only to the simplest class of exclusive-1 or double-arm coincidence reactions.

For either of the two general classes we may or may not assume that the electron is polarized. The kinematics are specified in Fig. 1. Here, an electron with 3-momentum $\vec{k}$ and energy ϵ is scattered through an angle θ_e to be detected with 3-momentum $\vec{k}'$ and energy ϵ'. The 3-momentum transfer is

*This work is supported in part by funds provided by the U. S. Department of Energy (D.O.E.) under contract # DE-AC02-76ER03069.

†Alexander von Humboldt Foundation Senior U.S. Scientist Award holder.

Typeset in TEX by Roger L. Gilson.

$\vec{q} = \vec{k} - \vec{k}'$ with magnitude $q = |\vec{q}|$ and the energy transfer is $\omega = \epsilon - \epsilon'$. The 4-momentum transfer $q_\mu q^\mu = \omega^2 - q^2$ is space-like (≤ 0). In general, we may consider coordinate systems fixed by the electron momenta so that $\vec{u}_L$ is along $\vec{k}$, $\vec{u}_N$ is normal to the electron scattering plane and $\vec{u}_S = \vec{u}_N \times \vec{u}_L$, with a similar form labelled L', N', S' going with the scattered electron. Here $L \leftarrow$ longitudinal, $N \leftarrow$ normal, $S \leftarrow$ sideways (as used in hadron scattering). The cross section may be broken down into specific projections, $\sigma^{P'P}$, where $P = L, N$ or S and $P' = L', N'$ or S'. We are specifically interested in the Extreme Relativistic Limit (ERL) in which $\gamma = \epsilon/m_e >> 1$ and $\gamma' = \epsilon'/m_e >> 1$ and so where terms of order γ^{-1} or γ'^{-1} can safety be neglected (*i.e.* in all but a few very specific circumstances such as when $\theta_e < \gamma^{-1}$). In the ERL we find that[1]

$$\sigma^{P'P} \sim \begin{cases} O(1) & \text{for } P'P = L'L \\ O(\gamma^{-1} \text{ or } \gamma'^{-1}) & \text{for } P'P \neq L'L \end{cases} ,$$

and so we practically only need to consider *longitudinally polarized electrons* having helicities $h = \pm 1$ and $h' = \pm 1$. Furthermore, the scattering process is *helicity conserving* to $O(\gamma^{-1} \text{ or } \gamma'^{-1})$, $h' = h$ and so the information obtained using an incident longitudinally polarized electron beam is the same as that obtained by measuring the longitudinal polarization of the scattered electron. We only consider the former as they are trivially related.

The polarized electron cross section in this case may be written

$$\sigma^h = \Sigma + h\Delta \ , \tag{1}$$

where the helicity averaged cross section

$$\Sigma = \frac{1}{2}\left(\sigma^{+1} + \sigma^{-1}\right) \tag{2a}$$

is obtained using unpolarized beams and where determination of the helicity difference cross section

$$\Delta = \frac{1}{2}\left(\sigma^{+1} - \sigma^{-1}\right) \tag{2b}$$

requires the use of longitudinally polarized electrons. There are then two general classes of responses to be addressed. Note that in the very low energy case (electron energy $\sim m_e$; or equivalently muon energy $\sim m_\mu$, which may have some application for muon scattering), when terms of $O(\gamma^{-1} \text{ or } \gamma'^{-1})$ are also considered, then transverse polarizations and helicity flips become accessible and Eq. (1) needs to be extended.[1] The practical implications of requiring longitudinally polarized electrons for internal target studies are important and will have a non-negligible impact on the facility requirements (see the talk by B. Norum at this workshop).

We may now proceed with a discussion of the nuclear response itself. The general situation involves a treatment of cross sections labelled Σ_{fi} and Δ_{fi}, where "f" and "i" signify specific polarizations for the final and initial nuclear states involved. We shall usually focus on the more restricted category involving only polarized targets and so responses labelled Σ_{fi} and Δ_{fi}, where f indicates that no final-state polarization information is presumed to be known. The target polarization is referred to a polarization axis which may be oriented in an arbitrary direction specified by the angles (θ^*, ϕ^*) as shown in Fig. 1. We begin with a discussion of single-arm (inclusive) scattering.

Single – Arm Scattering

Recently,[1] the subject of single-arm (inclusive) electron scattering from polarized targets has been discussed in some depth and applied to a variety of nuclear structure examples (see also Refs. [2]-[5]). Here only the most salient features are extracted for presentation, together with a few specific (interesting) examples to illustrate the basic ideas involved.

Unpolarized Electrons

Let us begin by discussing the scattering of unpolarized electrons from polarized targets, $\vec{A}(e,e')$. Only the cross section Σ_{fi} is then accessible. Using the known properties of the electron-photon part of the problem (just pure quantum electrodynamics), we may decompose this into four basic classes of response:[1]

$$\Sigma_{fi} = \sigma_0\{v_L W^L_{fi} + v_T W^T_{fi} + \cos\phi^* v_{TL} W^{TL}_{fi} + \cos 2\phi^* v_{TT} W^{TT}_{fi}\} \ , \tag{3}$$

where σ_0 is the elementary cross section (proportional to the Mott cross section) and the v's are factors involving the electron kinematics ($L, T \leftarrow$ longitudinal and transverse projections with respect to $\vec{q}$):

$$\begin{aligned} v_L &= \lambda^2 \\ v_T &= \frac{1}{2}\lambda + \tan^2\frac{\theta_e}{2} \\ v_{LT} &= -\frac{1}{\sqrt{2}}\lambda\sqrt{\lambda + \tan^2\frac{\theta_e}{2}} \\ v_{TT} &= -\frac{1}{2}\lambda \ , \end{aligned} \tag{4}$$

where $\lambda \equiv -q_\mu q^\mu/q^2$ so that $0 \leq \lambda \leq 1$. These factors together with σ_0 contain the entire dependence on θ_e for fixed q and ω. The entire dependence on the azimuthal polarization angle ϕ^* (see Fig. 1) is contained in the factors $\cos\phi^*$ and $\cos 2\phi^*$ and so by varying θ_e and ϕ^* it is possible to extract the four nuclear response functions W^L_{fi}, W^T_{fi}, W^{TL}_{fi}, and W^{TT}_{fi} in what might be termed a "super-Rosenbluth" decomposition. Each response still depends on (q,ω) and the polar angle of polarization θ^* (see Fig. 1). This latter dependence may also be made explicit[1] yielding a decomposition into *reduced response functions* which contain the dependence on q (and ω, which we take to be fixed to study some specific excitation):

$$W^L_{fi} = F^2_L(q) + \sum_{\substack{J\geq 2 \\ \text{even}}} f_J^{(i)} P_J(\cos\theta^*) W^L_J(q)_{fi} \tag{5a}$$

$$W^T_{fi} = F^2_T(q) + \sum_{\substack{J\geq 2 \\ \text{even}}} f_J^{(i)} P_J(\cos\theta^*) W^T_J(q)_{fi} \tag{5b}$$

$$W^{TL}_{fi} = \sum_{\substack{J\geq 2 \\ \text{even}}} f_J^{(i)} P^1_J(\cos\theta^*) W^{TL}_J(q)_{fi} \tag{5c}$$

$$W^{TT}_{fi} = \sum_{\substack{J\geq 2 \\ \text{even}}} f_J^{(i)} P^2_J(\cos\theta^*) W^{TT}_J(q)_{fi} \ . \tag{5d}$$

The first terms in Eqs. (5a) and (5b) involve the familiar longitudinal and transverse form factors and are present whether or not the target is polarized:

$$F^2_L(q) = \sum_{J\geq 0} F^2_{CJ}(q) \tag{6a}$$

$$F^2_T(q) = \sum_{J\geq 1} \{F^2_{EJ}(q) + F^2_{MJ}(q)\} \ . \tag{6b}$$

These involve only incoherent sums of squares of Coulomb (C), Electric (E) and Magnetic (M) form factors. For example, suppose the ground state has $J_i^{\pi_i} = \frac{3}{2}^-$ and we consider only electro-excitation to a state having $J_f^{\pi_f} = \frac{5}{2}^+$. The allowed multipoles are $C1/E1$, $M2$, $C3/E3$ and $M4$, and we have

$$F_L^2 = F_{C1}^2 + F_{C3}^2$$
$$F_T^2 = F_{E1}^2 + F_{M2}^2 + F_{E3}^2 + F_{M4}^2 \ .$$

Clearly, we cannot isolate the individual multipoles if we only have F_L^2 and F_T^2; this is the frustration we are faced with in studying unpolarized electron scattering. However, with polarized targets, more information is present in general. In Eqs. (5) the terms involving the sums occur only when the target is polarized. The factors $f_I^{(i)}$ contain all the information on how the target M-states are populated (these are the Fano tensors, see Ref. [1]) and are presumed to be known. The entire θ^*-dependence is now displayed in the (associated) Legendre polynomials. Thus we have sets of reduced nuclear response functions as observables which may be obtained by controlling the direction of target polarization. Importantly, the sums in Eqs. (5) are finite: $2 \leq I \leq 2J_i$, with I = even only. If $J_i = 0$, clearly none of the sums occur and we have only $W_{fi}^L = W_{f\hat{i}}^L = F_L^2$, $W_{fi}^T = W_{f\hat{i}}^T = F_T^2$, $W_{fi}^{TL} = W_{fi}^{TT} = 0$, yielding for Eq. (3) just the familiar Rosenbluth formula for unpolarized electron scattering (indicated $f\hat{i}$). Note that the same is true when the target has spin-$\frac{1}{2}$; in this case we cannot form any even-rank tensors except for the $I = 0$ ones which constitute the unpolarized form factors F_L^2 and F_T^2. Thus, lacking polarized electrons (see below) there is no point in going to the trouble of polarizing spin-$\frac{1}{2}$ targets for studies of inclusive electron scattering.

The first interesting case is that of electron scattering from a polarized spin-1 target, such as $^2\vec{H}$. For instance, for elastic scattering there are three basic form factors, $C0$, $M1$ and $C2$ (see Refs. [1] and [3]). The unpolarized cross section involves the longitudinal and transverse form factors,

$$F_L^2 = F_{C0}^2 + F_{C2}^2$$
$$F_T^2 = F_{M1}^2 \ ,$$

but the $C0$ and $C2$ contributions are summed incoherently and no relative phase information is available. The additional reduced response functions which are accessible with polarized targets are[1,3,6]

$$W_2^L = -2\sqrt{3}F_{C2}\left(F_{C0} + \frac{1}{2\sqrt{2}}F_{C2}\right)$$
$$W_2^T = -\frac{1}{2}\sqrt{\frac{3}{2}}F_{M1}^2$$
$$W_2^{TL} = \frac{3}{\sqrt{2}}F_{M1}F_{C2}$$
$$W_2^{TT} = \frac{1}{4}\sqrt{\frac{3}{2}}F_{M1}^2 \ .$$

Clearly with this polarization information it is possible to separate the individual multipole form factors. Thus, the prime use of polarization in single-arm electron scattering emerges, namely as a *"Multipole Meter"*. This is more generally true, for higher spin situations and for inelastic scattering, where additional *interference information* (for example, the $F_{C2}F_{C0}$ or $F_{M1}F_{C2}$ interferences above) becomes available.

In passing, a special circumstance should be mentioned: for elastic scattering and for light nuclei it is possible to obtain the same information with polarized targets or by measurement of the final-state recoil polarization. An example is provided by the recent experiment at Bates involving a measurement of the recoil tensor polarization in elastic scattering from deuterium.[7] It should be remarked, however, that inelastic excitations are not generally accessible with the final-state polarization measurements (since the final states generally decay too fast, although the reaction $(e, e'\gamma)$ can be a powerful alternative tool here and can be related directly to the present polarization discussions[8]) and that all but the lightest targets are probably impractical (since the slow recoil is usually too hard to handle).

Polarized Electrons

Now let us extend the above ideas to include the scattering of polarized electrons from polarized targets, $\vec{A}(\vec{e}, e')$. In this case the cross section Δ_{fi} becomes accessible together with Σ_{fi}. The analog to Eq. (3) is

$$\Delta_{fi} = \sigma_0 \left\{ v_{T'} W_{fi}^{T'} + \cos\phi^* v_{TL'} W_{fi}^{TL'} \right\} \ , \qquad (7)$$

and so we have two more classes of responses, giving six in general: L, T, TL, TT, T' and TL'. The two new electron kinematical factors are[1]

$$v_{T'} = \sqrt{\lambda + \tan^2\frac{\theta_e}{2}}\tan\frac{\theta_e}{2}$$
$$v_{TL'} = -\frac{1}{\sqrt{2}}\tan\frac{\theta_e}{2} \ . \qquad (8)$$

Furthermore, analogous to Eqs. (5) we now have

$$W_{fi}^{T'} = \sum_{\substack{I\geq 1 \\ \text{odd}}} f_I^{(i)} P_I(\cos\theta^*) W_I^{T'}(q)_{fi} \qquad (9a)$$

$$W_{fi}^{TL'} = \sum_{\substack{I\geq 1 \\ \text{odd}}} f_I^{(i)} P_I^1(\cos\theta^*) W_I^{TL'}(q)_{fi} \ , \qquad (9b)$$

where the sums are restricted to odd tensors only with $1 \leq I \leq 2J_i$.

For $J_i = 0$ these electron helicity difference responses are zero. In obtaining this fact we have assumed that the scattering process is purely electromagnetic and so is parity conserving. However, at the level of the weak interaction there are interferences between the γ-exchange and Z^0-exchange (neutral current) diagrams which can occur which lead to non-zero polarization asymmetries.[9,10] An experiment at Bates involving the elastic scattering of polarized electrons from ^{12}C is in the final stages of preparation.

For $J_i = \frac{1}{2}$ we saw above that the Σ_{fi} cross section contained only the familiar unpolarized responses involving the form factors F_L^2 and F_T^2:

$$\Sigma_{fi} = \sigma_0 \left\{ v_L F_L^2 + v_T F_T^2 \right\} \ . \qquad \left[\text{spin-}\frac{1}{2}\right] \qquad (10a)$$

The helicity difference cross section is now not zero but contains interesting information since rank-1 responses can be obtained ($1 \leq I \leq 2J_i \Longrightarrow I = 1$ for $J_i = \frac{1}{2}$):

$$\Delta_{fi} = f_1^{(i)}\sigma_0\{\cos\theta^* v_{T'} W_1^{T'}(q)_{fi} + \sin\theta^*\cos\phi^* v_{TL'} W_1^{TL'}(q)_{fi}\} \ . \qquad (10b)$$

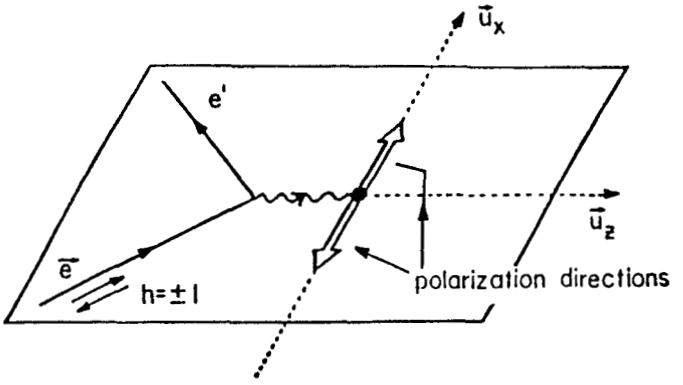

Fig. 2: Special choice of polarization directions for use with polarized spin-$\frac{1}{2}$ targets (see text).

Note that the $W_1^{TL'}$ response in the helicity difference cross section can be isolated by placing the target polarization in the special directions shown in Fig. 2. Thus for inclusive scattering of polarized electrons from polarized spin-$\frac{1}{2}$ targets there are four observables that are accessible: F_L^2, F_T^2, $W_1^{T'}$ and $W_1^{TL'}$. The general character of these responses is discussed in Ref. [5] while here we only consider two special cases.

First, consider elastic scattering in which F_{C0} and F_{M1} form factors occur (equivalently, we can use G_E and G_M for the nucleon). The unpolarized cross section involves $F_L^2 = F_{C0}^2$ and $F_T^2 = F_{M1}^2$ which can in principle be separated by making a Rosenbluth decomposition of Eq. (10a). In practice, however, one may be dominant (as occurs for some values of q for the nucleon) and it may be very difficult to extract the smaller from the larger. For example, at all but the lowest values of q the present information on G_E^n comes from unpolarized electron scattering using deuterium as perhaps the simplest target containing neutrons. But at low-to-intermediate values of q, $|G_E^n| << |G_M^n|$ and the separation is very poorly defined. Now suppose this polarized electron/polarized target information is added. We have[1,3,6]

$$W_1^{T'} = -\sqrt{2}F_{M1}^2$$
$$W_1^{TL'} = -2\sqrt{2}F_{C0}F_{M1} \ .$$

The former just involves F_T^2 again, whereas the latter is the one of interest for the present purposes: it involves the *interference* between the two form factors and, when one is small in magnitude and the other large, it provides a much more sensitive way to extract one from the other. Note that this is the contribution which is isolated by using the special polarization orientation shown in Fig. 2. The specific measurements which are of high priority here are $\vec{p}(\vec{e},e')p$ (to extract G_E^p from G_M^p; even this is interesting for some values of momentum transfer) and $^2\vec{H}(\vec{e},e')$ or $^3\vec{H}e(\vec{e},e')$ in the region where the process corresponds best to quasi-free scattering from a nucleon (to extract G_E^n from G_M^n and to check the approximations involved by extracting G_E^p and G_M^p as well).

Next consider inelastic scattering for the transition $\frac{1}{2}^{\pm} \rightarrow \frac{3}{2}^{\pm}$ in which F_{M1}, F_{C2} and F_{E2} form factors occur. The four accessible responses here are[1]

$$F_L^2 = F_{C2}^2$$
$$F_T^2 = F_{M1}^2 + F_{E2}^2$$
$$W_1^{T'} = \frac{1}{\sqrt{2}}\left(F_{M1}^2 - F_{E2}^2 - 2\sqrt{3}F_{M1}F_{E2}\right)$$
$$W_1^{TL'} = -\sqrt{2}F_{C2}\left(F_{M1} + \sqrt{3}F_{E2}\right) \ .$$

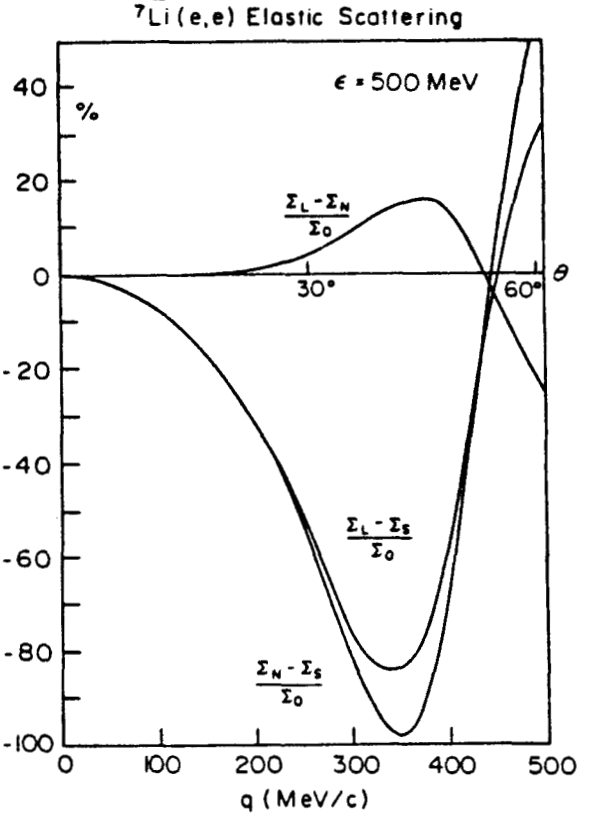

Fig. 3: Elastic electron scattering from the $\frac{3}{2}^-$ ground state of polarized ^{7}Li. The polarization asymmetries displayed correspond to taking the target to be 100% polarized along the L, N and S directions in Fig. 1 and then forming differences and dividing by the unpolarized cross section Σ_0.

A specific situation is the $N \rightarrow \Delta$ transition, say in $\vec{p}(\vec{e},e')\Delta$. To the extent that other channels than the $\frac{3}{2}^+$ final state can be neglected, we have the above responses. For the $N \rightarrow \Delta$ transition the $M1$ contribution is dominant and the $C2/E2$ pieces, which reflect the baryon deformations, are small. Again, a straightforward Rosenbluth separation of the unpolarized cross section yields F_L^2 and F_T^2 where the former is very small compared to the latter (and furthermore, where the latter contains two contributions, one very large and the other very small). The polarization responses involve interferences and especially the $W_1^{TL'}$ contribution is interesting, since it can only be non-zero when $F_{C2} \neq 0$. Moreover, the $W_1^{TL'}$ response is linearly proportional to F_{C2}, whereas F_L^2 involves the square F_{C2}^2.

Our conclusions from this simple analysis have important practical implications: to obtain new information particularly of the type involving interesting interferences using single-arm electron scattering to study spin-$\frac{1}{2}$ targets, it will be necessary to have polarized targets *and* longitudinally polarized electrons.

Finally, to set the scale of the asymmetries which are typical for studies of nuclear structure, let us extract some of the results from Ref. [1] for scattering of electrons (polarized or unpolarized) from polarized ^{7}Li. Two transitions are considered, elastic scattering from the $\frac{3}{2}^-$ ground state and inelastic scattering to the first excited state at 0.478 MeV, $\frac{3}{2}^- \rightarrow \frac{1}{2}^-$. The resulting polarization effects are displayed in Figs. 3—6.

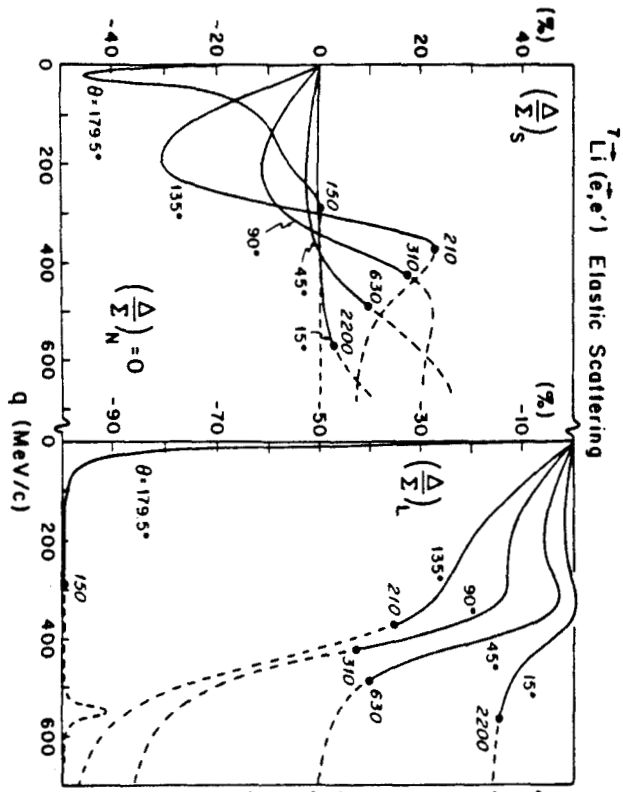

Fig. 4: Elastic polarized electron scattering from the $\frac{3}{2}^-$ ground state of polarized ^{7}Li. The polarization ratios Δ/Σ are given for the situations where the target is 100% polarized along the L, N and S directions in Fig. 1. Solid lines correspond to unpolarized cross sections above $10^{-33}\,\mathrm{cm^2\,sr^{-1}}$ and dashed lines to smaller cross sections. The incident electron energy in MeV at which $10^{-33}\,\mathrm{cm^2\,sr^{-1}}$ is reached for a given scattering angle is indicated near the dot on each line. (Figure shown sideways.)

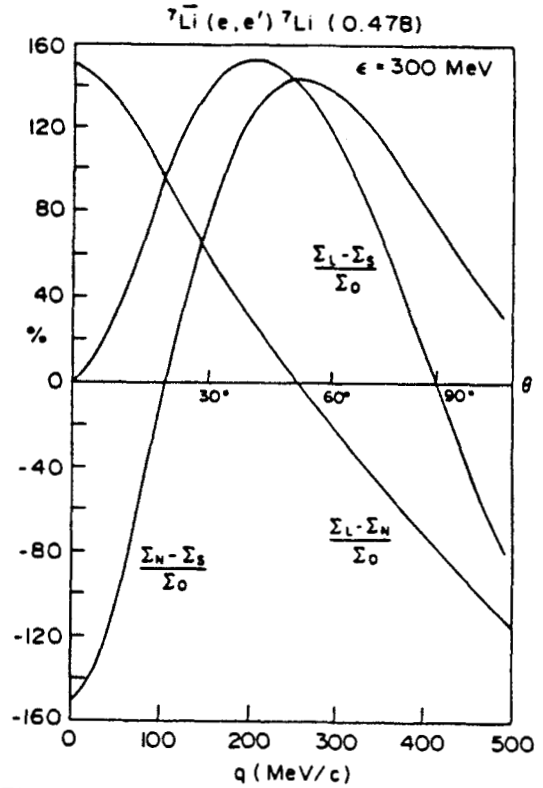

Fig. 5: Inelastic electron scattering from polarized ^{7}Li involving the transition $\frac{3}{2}^-$ (g.s.) $\rightarrow$ $\frac{1}{2}^-$ (0.478 MeV). The asymmetries are defined as in Fig. 3.

The main observations to be drawn here are (1) the cross sections are $\geq 10^{-33}\,\mathrm{cm^2\,sr^{-1}}$ over an interesting range of momentum transfers (this will have implications for the relevant range of luminosities, as discussed in the last section), and (2) the polarization asymmetries are typically large and vary significantly as q is changed or as the polarization direction is changed.

Coincidence Reactions

Let us now turn briefly to the exclusive-1, $(e,e'x)$ coincident reactions in Figs. 7 and 8. We consider two situations, the first without polarized targets but where the polarization of the particle x in the final state is measured (Fig. 7) and the second where the target is polarized but no final-state polarization is measured (Fig. 8). In both cases the electrons may or may not be longitudinally polarized. The former situation is pertinent for external beams and targets and requires the use of a polarimeter to measure the polarization of particle x (this is usually a limitation, since polarimeter efficiencies are typically quite low); the latter is pertinent for internal (polarized) target studies, just as for inclusive scattering (see above and the last section).

The decomposition made above into the six major classes of response (L, T, TL, TT with electrons unpolarized; T', TL' with polarized electrons) is quite general and applies here as well. The form of Eq. (1) is valid for the electron helicity dependence of the cross section in the ERL and, as above, two sets of responses may be separated using this dependence (see Eqs. (2)):

$$\Sigma \sim v_L R^L + v_T R^T + v_{TL} R^{TL} + v_{TT} R^{TT} \qquad (11a)$$

$$\Delta \sim v_{T'} R^{T'} + v_{TL'} R^{TL'} \ , \qquad (11b)$$

in parallel with Eqs. (3) and (7) for inclusive scattering. The six responses here depend on (q,ω), the energy and angles for the outgoing particle x (E_x, θ_x, ϕ_x: see Figs. 7 and 8) and the polarization angles. For the case of the reaction $A(\vec{e},e'\vec{x})$ in Fig. 7, these are the angles (θ_x^*, ϕ_x^*) as shown; for the case of the reaction $\vec{A}(\vec{e},e'x)$ in Fig. 8, these are the target polarization angles (θ^*, ϕ^*) where ϕ^* is now measured relative to the plane with azimuthal angle ϕ_x. The dependence on the azimuthal angle ϕ_x can be isolated:[5,11]

$$R^{TL} \equiv \cos\phi_x W^{TL} + \sin\phi_x \tilde{W}^{TL} \qquad (12a)$$

$$R^{TT} \equiv \cos 2\phi_x W^{TT} + \sin 2\phi_x \tilde{W}^{TT} \qquad (12b)$$

$$R^{TL'} \equiv \sin\phi_x W^{TL'} + \cos\phi_x \tilde{W}^{TL'} \qquad (12c)$$

$$R^L,\ R^T,\ R^{T'} :\ \text{independent of } \phi_x \ ,$$

and so at this stage there are nine basic classes to consider in general.

Let us specialize first to a discussion of inclusive-1 electron scattering with only the electron possibly being polarized, $A(e,e'x)$ and $A(\vec{e},e'x)$. Then it can be shown[5,11] that $\tilde{W}^{TL} = \tilde{W}^{TT} = R^{T'} = W^{TL'} = 0$. In the completely unpolarized situation, $A(e,e'x)$, there are the four familiar responses to consider (R^L, R^T, W^{TL} and W^{TT}), which may be separated using the θ_e- and θ_x-dependences displayed above.

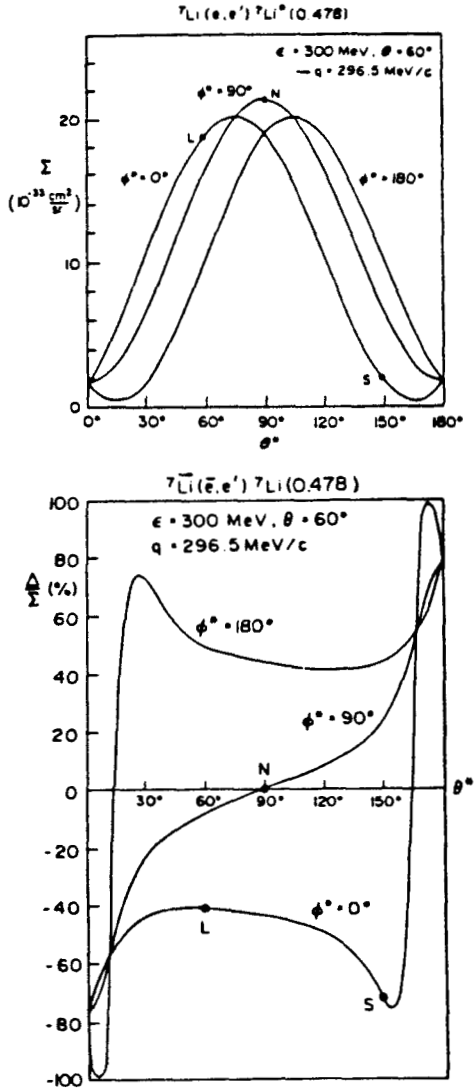

Fig. 6: Inelastic electron scattering from polarized ^{7}Li using unpolarized (upper figure) or polarized (lower figure) electrons for the same transition as that in Fig. 5. For specific electron scattering kinematics the quantities Σ and Δ/Σ are shown as functions of the target polarization angles θ^* and ϕ^* (see Fig. 1). The points corresponding to the L, N and S directions in Fig. 1 are indicated.

Having polarized electrons and studying the electron helicity-difference cross section for $A(\vec{e},e'\vec{x})$ yields another, the so-called "fifth" response function $W^{TL'}$ (note that this requires an out-of-plane measurement because of the factor $\sin\phi_x$ in Eq. (12c)). In contrast to single-arm scattering with polarized electrons but unpolarized targets, this fifth response function is non-zero in general even when parity is conserved. Thus only the helicity-difference cross section in $A(\vec{e},e')$ is likely to be practical for studies of electroweak parity violating effects: such effects would usually be overwhelmed by the non-zero parity conserving asymmetries. The TL' fifth response function and the usual TL response have similar structures:

$$W^{TL} \sim \mathrm{Re}(T^*L)$$
$$W^{TL'} \sim \mathrm{Im}(T^*L) \ ,$$

where T^*L represents the appropriate (*i.e.* determined by the dynamics of the specific problem of interest) bilinear combination of (transverse)*×(longitudinal) matrix elements. The

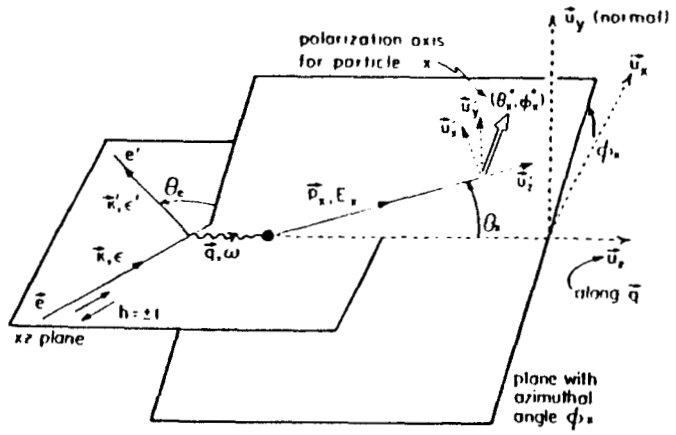

Fig. 7: Coincidence electron scattering from unpolarized targets including the possibility of having longitudinally polarized electrons and of detecting the polarization of the outgoing particle x, $A(\vec{e},e'\vec{x})$. The direction of the particle x is specified by the angles (θ_x,ϕ_x) referred to the xyz coordinate system as shown. Furthermore, the polarization of the particle x is specified by the angles (θ_x^*,ϕ_x^*), but now referred to the $x'y'z'$ coordinate system where z' is along $\vec{p}_x$, y' is orthogonal to $\vec{q}$ and $\vec{p}_x$ (along $\vec{q}\times\vec{p}_x$), and x' is orthogonal to both of these (along $\vec{u}_{y'}\times\vec{u}_{z'}$ and so is in the plane containing $\vec{q}$ and $\vec{p}_x$).

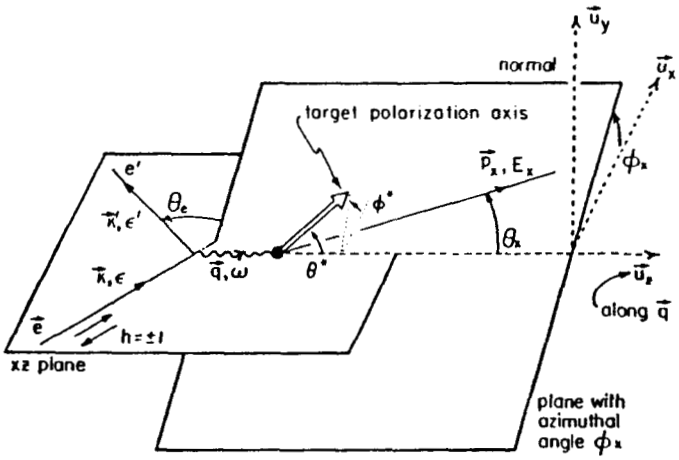

Fig. 8: Coincidence electron scattering from polarized targets including the possibility of having longitudinally polarized electrons, $\vec{A}(\vec{e},e'\vec{x})$. The direction of the particle x is specified by the angles (θ_x,ϕ_x) as in Fig. 7 and the target polarization directions is specified by (θ^*,ϕ^*) where θ^* is as in Fig. 1 and ϕ^* is measured relative to the plane with azimuthal angle ϕ_x.

same combinations occur in the two responses; the only difference is that one has the real part and the other the imaginary part. Now, if the reaction proceeds through a channel in which a single phase dominates for all projections of the current ($T \sim |T|e^{i\delta}$, $L \sim |L|e^{i\delta}$, with the same δ), the T^*L is real and, while W^{TL} is non-zero in general, $W^{TL'}$ vanishes.

Moreover, it happens that $W^{TL'}$ also vanishes in the absence of final-state interactions. Therefore, if $W^{TL'} \neq 0$, then interesting effects must be coming into play. For example, in the Δ-region coincidence electron scattering will be driven to a large degree by the 33-amplitude with a single phase, δ_{33}, and, while $W^{L,T,TL,TT}$ may all be non-zero, $W^{TL'}$ may be expected to vanish. To the extent that it does not vanish, we will be able to access information concerning interferences of the 33-amplitude with amplitudes for other channels which are usually too weak to be studied directly.

The L, T, TL and TT (unpolarized) responses on the one hand and the TL' (polarized electrons, but otherwise unpolarized) response on the other may be characterized by their time-reversal properties, even and odd, respectively. Time-reversal even responses are always real parts of bilinear products involving the currents, while time-reversal odd responses involve imaginary parts (as for TL and TL' above, respectively). The specific responses discussed so far where the electron was the only particle whose polarization was presumed to be known are members of larger sets of responses all of which may be characterized as time-reversal even or odd. These extended sets become accessible when target polarizations and/or final-state polarizations (other than the scattered electron) are presumed to be known. This polarization information may be organized into spherical tensors characterized by rank I, where I may be even or odd with $I = 0$ corresponding to the unpolarized cross sections above. When target polarizations are considered, this is the same type of tensor decomposition that we encountered earlier for single-arm scattering; when the polarization of particle x in $(e, e'\vec{x})$ and $(\vec{e}, e'\vec{x})$ is measured, then I labels the tensor polarization measured in some second scattering experiment. The general break-down into time-reversal even and odd responses is as follows:[12]

		I = even	I = odd
Σ	L	TRE	TRO
$\left\{\begin{smallmatrix}\text{electron}\\ \text{unpolarized}\end{smallmatrix}\right\}$	T	TRE	TRO
	TL	TRE	TRO
	TT	TRE	TRO
Δ	T'	TRO	TRE
$\left\{\begin{smallmatrix}\text{electron}\\ \text{polarized}\end{smallmatrix}\right\}$	TL'	TRO	TRE

where TRE (TRO) refers to time-reversal even (odd).

Let us consider a more specific situation to help clarify these ideas. Suppose the target is unpolarized and we consider reactions of the sort $(e, e'p)$, $(\vec{e}, e'p)$, $(e, e'\vec{p})$ and $(\vec{e}, e'\vec{p})$, where in fact the proton ($x = p$) could be any spin-$\frac{1}{2}$ particle as far as the characterization of the cross section is considered. Since the particle whose polarization may be detected in the final state has spin-$\frac{1}{2}$, the only allowed values of I are 0 and 1 ($I = 0$ corresponds to the unpolarized cross sections discussed above, the first two in this list; $I = 1$ corresponds to measurements of the vector polarization of the out-going proton, the last two in this list). So for the $I = 0$ pieces we have the previous results:

$$
\begin{aligned}
(e, e'p): \quad & R^L_{I=0} = R^L_{\text{unpol.}} \\
& R^T_{I=0} = R^T_{\text{unpol.}} \\
& R^{TL}_{I=0} = \cos\phi_p W^{TL}_{\text{unpol.}} \\
& R^{TT}_{I=0} = \cos 2\phi_p W^{TT}_{\text{unpol.}} \qquad (13) \\
(\vec{e}, e'p): \quad & R^{T'}_{I=0} = 0 \\
& R^{TL'}_{I=0} = \sin\phi_p W^{TL'}_{\text{unpol.}} \ ,
\end{aligned}
$$

where the first four are time-reversal even and the fifth response function is time-reversal odd. For the $I = 1$ pieces we have

$$
\begin{aligned}
R^K_{I=1} = a_p \{ & \cos\theta^*_p R^K_{\text{pol.}}(\ell') + \sin\theta^*_p \cos\phi^*_p R^K_{\text{pol.}}(s') \\
& + \sin\theta^*_p \sin\phi^*_p R^K_{\text{pol.}}(n') \} \ , \qquad (14)
\end{aligned}
$$

where a_p is the vector polarization of the proton, $-1 \leq a_p \leq 1$ and where we have decomposed the responses $R^K_{I=1}$, $K = L$, T, TL, TT, T' and TL', into components involving the ℓ', s' and n' directions, *i.e.* the z', x' and y' directions in Fig. 7 (see Refs. [12] and [13]). In this case, the following ϕ_p-dependences are found for the $I = 1$ responses (Cf. Eqs. 12)):

		ℓ'	s'	n'
$(e, e'\vec{p})$:	L	0	0	1
	T	0	0	1
	TL	$\sin\phi_p$	$\sin\phi_p$	$\cos\phi_p$
	TT	$\sin 2\phi_p$	$\sin 2\phi_p$	$\cos 2\phi_p$
$(\vec{e}, e'\vec{p})$:	T'	1	1	0
	TL'	$\cos\phi_p$	$\cos\phi_p$	$\sin\phi_p$,

(15)

where the first four classes are time-reversal odd and the last two are time-reversal even. Thus, for example, the entire L response is

$$
\begin{aligned}
R^L &= R^L_{I=0} + R^L_{I=1} && \text{(16a)} \\
&= R^L_{\text{unpol.}} + a_p \sin\theta^*_p \sin\phi^*_p R^L_{\text{pol.}}(n') && \text{(16b)}
\end{aligned}
$$

and the entire TL response is

$$
\begin{aligned}
R^{TL} &= R^{TL}_{I=0} + R^{TL}_{I=1} && \text{(17a)} \\
&= \left\{\cos\phi_p W^{TL}_{I=0} + \sin\phi_p \tilde{W}^{TL}_{I=0}\right\} \\
&\quad + \left\{\cos\phi_p W^{TL}_{I=1} + \sin\phi_p \tilde{W}^{TL}_{I=1}\right\} && \text{(17b)} \\
&= \left\{\cos\phi_p W^{TL}_{\text{unpol.}}\right\} \\
&\quad + a_p \left\{\cos\phi_p \left(\sin\theta^*_p \sin\phi^*_p W^{TL}_{\text{pol.}}(n')\right)\right. && \text{(17c)} \\
&\quad \left. + \sin\phi_p \left(\cos\theta^*_p W^{TL}_{\text{pol.}}(\ell') + \sin\theta^*_p \cos\phi^*_p W^{TL}_{\text{pol.}}(s')\right)\right\} \ ,
\end{aligned}
$$

and so on for the other cases. There are 18 responses to be separated in this way; nine are time-reversal even and nine are time-reversal odd. The former are obtained using the reactions $(e, e'p)$ and $(\vec{e}, e'\vec{p})$; the latter use $(\vec{e}, e'p)$ and $(e, e'\vec{p})$.

A specific set of measurements of this sort which may require the determination of several of these responses is the following. One way to obtain information on G^n_E is to use an unpolarized deuteron target and study the (TRE) polarization transfer reactions $^2H(\vec{e}, e'\vec{p})n$ or $^2H(\vec{e}, e'\vec{n})p$ in the quasi-free region where final-state interactions are supposed to be weak enough to permit the (small) effects which are proportional to G^n_E to be isolated. An important question will be: How important are the final-state interaction uncertainties in confusing the G^n_E determination? A possible answer may lie in measuring one of the time-reversal odd responses using $^2H(\vec{e}, e'p)n$ or $^2H(e, e'\vec{p})n$ (or $p \leftrightarrow n$) which are sensitized to these effects as discussed above.

A similar structure occurs for exclusive-1 reactions involving polarized targets, $\vec{A}(e, e'x)$ and $\vec{A}(\vec{e}, e'x)$. The general TRE/TRO decomposition involving I = even and odd tensors pertains as well. In fact, for spin-$\frac{1}{2}$ targets the same characterization given above for $(e, e'p)$ also works, now with angles (θ^*_p, ϕ^*_p) replaced by (θ^*, ϕ^*), the angles specifying the

target polarization direction. For targets with spin ≥ 1, however, the response structure is richer. For example, for the reactions ${}^2\vec{H}(e,e'p)$ and ${}^2\vec{H}(\vec{e},e'p)$ with polarized deuterium, I may be 0, 1 or 2. The first two are classified just as above, while 15 new $I = 2$ responses have the following breakdown:[12] $L(3\mathrm{TR}\,E)$, $T(3\mathrm{TR}\,E)$, $TL(3\mathrm{TR}\,E, \sim \cos\phi_p)$, $TT(3\mathrm{TR}\,E, \sim \cos 2\phi_p)$, $T'(0)$, $TL'(3\mathrm{TR}\,E, \sim \sin\phi_p)$. Using polarized targets there are then 33 responses available in this example.

The formalism for the general problem with any spins with/without electron, target or outgoing coincident particle polarizations now exists;[12] our current efforts are directed towards specific problems of interest to evaluate the relative merits of using external unpolarized targets but presuming that an outgoing particle polarization is measured and of using polarized internal targets without requiring final-state polarization determinations.

To end these discussions, let us conclude with one very explicit example to illustrate the content of the many responses a little more concretely. Let us consider the reactions $p(e,e'p)X$, $p(\vec{e},e'p)X$, $p(e,e'\vec{x})X$ and $p(\vec{e},e'\vec{p})X$ (or equivalently for the last two, $\vec{p}(e,e'p)X$ and $\vec{p}(\vec{e},e'p)X$). The general decomposition is given in Eqs. (13) and (15). Let us first specialize to co-planar geometry where $\phi_p = 0$; then we have four $\mathrm{TR}\,E$ $I = 0$ responses, no $\mathrm{TR}\,O$ $I = 0$ responses (Eqs. (13), four $\mathrm{TR}\,O$ $I = 1$ responses, all of n' character and four $\mathrm{TR}\,E$ $I = 1$ responses, two of ℓ' character and two of s' character (Eqs. (15)). Such measurements are made easier by not having to place a proton spectrometer out of the electron scattering plane (Cf. Figs. 7 and 8). Let us be even more specific and consider parallel kinematics where $\theta_p = 0$ so that the proton is detected along $\vec{q}$ (see Fig. 9). Now the TT response vanishes and we are left with the following behavior:[12]

$$R^L = R^L_{\mathrm{unpol.}} = N^2|S|^2 \tag{18a}$$

$$R^T = R^T_{\mathrm{unpol.}} = N^2|T|^2 \tag{18b}$$

$$R^{TL} = a_p \sin\theta^*_p \sin\phi^*_p W^{TL}_{\mathrm{pol.}}(n') = -a_p \sin\theta^*_p \sin\phi^*_p N^2 2\,\mathrm{Im}\,(S^*T) \tag{18c}$$

$$R^{TT} = 0 \tag{18d}$$

$$R^{T'} = a_p \cos\theta^*_p W^{T'}_{\mathrm{pol.}}(\ell') = a_p \cos\theta^*_p R^T \tag{18e}$$

$$R^{TL'} = a_p \sin\theta^*_p \cos\phi^*_p W^{TL'}_{\mathrm{pol.}}(s') = a_p \sin\theta^*_p \cos\phi^*_p N^2 2\,\mathrm{Re}\,(S^*T) \tag{18f}$$

where N^2 is an overall kinematic factor and where

$$S \equiv \frac{1}{\sqrt{2}} \sum_\ell \left\{ \ell^2 S_{\ell-} + (\ell+1)^2 S_{\ell+} \right\} \tag{19a}$$

$$T \equiv \frac{1}{2} \sum_\ell \left\{ (\ell+1)(\ell+2) E_{\ell+} - \ell(\ell-1) E_{\ell-} + \ell(\ell+1)\left[M_{\ell+} - M_{\ell-} \right] \right\} , \tag{19b}$$

using the multipole notation familiar from studies of pion electroproduction. These are for the reactions where the outgoing proton polarization is possibly measured. For the corresponding situation where the proton target is polarized, it is necessary only to change (θ^*_p, ϕ^*_p) into (θ^*, ϕ^*) and to replace a_p by $-\sqrt{2} f_1^{(i)}$.

Suppose only the $M1$ piece of the $N \rightarrow \Delta$ transition is important. Then M_{1+} is non-zero, but all other multipoles may be neglected. Then we would have

$$R^L = R^{TL} = R^{TT} = R^{TL'} = 0$$
$$R^T = N^2|M_{1+}|^2$$
$$R^{T'} = a_p \cos\theta^*_p R^T \ .$$

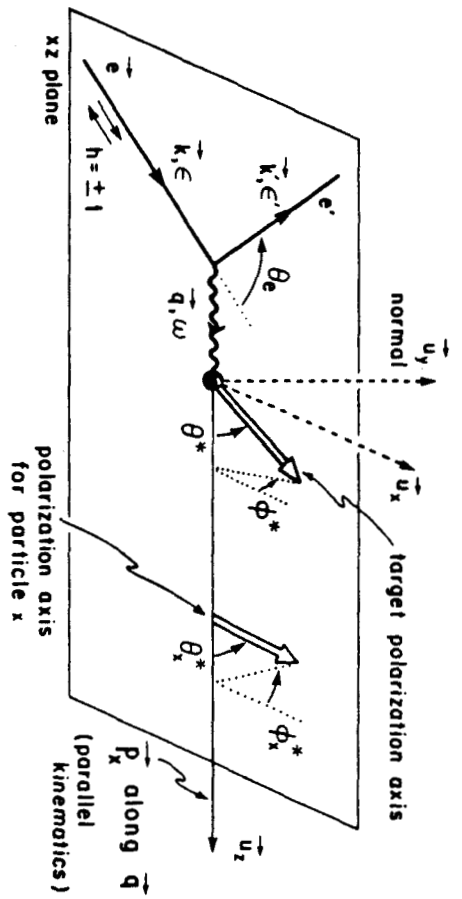

Fig. 9: Specialization of Figs. 7 and 8 to the situation where $\vec{p}_x$ is along $\vec{q}$ (parallel kinematics). (Figure shown sideways.)

If, on the other hand, the $C2/E2$ multipoles are also non-zero (Cf. discussion of inclusive scattering above), then we would have

$$R^L = N^2 8|S_{1+}|^2$$
$$R^T = N^2|M_{1+} + 3E_{1+}|^2$$
$$R^{TL} = -a_p \sin\theta^*_p \sin\phi^*_p N^2 4\sqrt{2}\,\mathrm{Im}\,\left(S^*_{1+}(M_{1+} + 3E_{1+})\right)$$
$$R^{TT} = 0$$
$$R^{T'} = a_p \cos\theta^*_p R^T$$
$$R^{TL'} = a_p \sin\theta^*_p \cos\phi^*_p N^2 4\sqrt{2}\,\mathrm{Re}\,\left(S^*_{1+}(M_{1+} + 3E_{1+})\right) \ .$$

The TL and TL' responses in particular are interesting, since they involve the imaginary and real parts of the interference $S^*_{1+}(M_{1+} + 3E_{1+})$, respectively. For fixed θ^*_p, as the angle ϕ^*_p varies the proportions of these two contributions also vary (weighted by $-\sin\phi^*_p$ and $\cos\phi^*_p$, respectively.

Of course, the analysis can be continued to include other partial waves and multipoles in the final state. Furthermore, relatively simple expressions are also obtained[12] for reactions involving deuterium instead of the proton, except that now there are differences when the outgoing proton's polarization is measured versus when the deuterium target is polarized. The former class of reaction has responses which involve an interference between amplitudes containing singlet and triplet partial waves, but only rank 0 and 1 information; no such interferences occur for the latter class, but additional rank 2 information is now present.

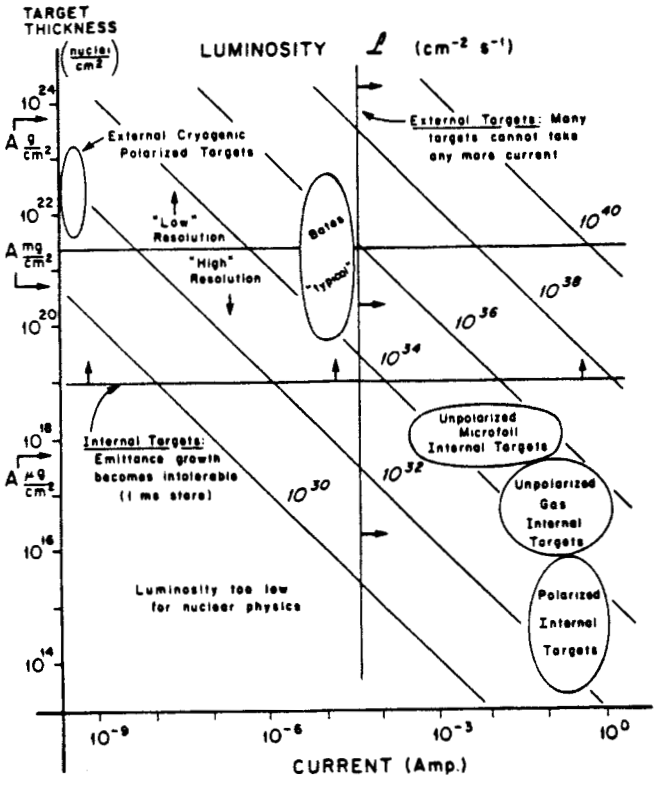

Fig. 10: Luminosity as a function of target thickness and electron current. The former is given in units of nuclei/cm^2 with the specific values of A g/cm^2, mg/cm^2 and μg/cm^2 indicated as well. The various regions are discussed in the text

Summary and Practical Implications

What has been presented here is a brief overview of some of the highlights of "spin physics" in electron scattering. Interesting interference effects become accessible when polarization degrees of freedom can be controlled. For inclusive (single-arm) scattering the general case requires that polarized targets be available, with studies involving the detection of final-state polarizations comprising a more limited range of possibilities. For exclusive (coincidence) reactions there are interesting processes to explore in both cases, with targets polarized and when a specific particle in the final state is detected together with its polarization. In many cases, it is important (or essential, such as with single-arm scattering from polarized spin-$\frac{1}{2}$ targets) to have longitudinally polarized electrons available.

The practical implications are severe. For detection of final-state polarizations, a polarimeter is required and these are usually devices with limited efficiencies. For polarized target studies the problem is to obtain significant luminosities and still have feasible experiments. This is illustrated in Fig. 10 where luminosity is given for ranges of target thicknesses and electron currents. To be practical for nuclear physics studies it must be possible in general to obtain luminosities above, say, $10^{30}\,\mathrm{cm}^{-2}\,\mathrm{s}^{-1}$ (and frequently considerably above this). To have good resolution capability in general requires that the target not be too thick. Typical external cryogenic polarized targets cannot withstand more than a few $\times$ 1 nAmp before depolarizing and so to reach the desired range of luminosity requires a very thick target. In fact, with such targets the degree of polarization is usually rather low and so the effective luminosity is actually quite a bit smaller than the nominal value. With internal targets using a circulating electron beam the current can be very high (Bates is designed for 80 m Amp internal current, for example[14]). The implications here are clear: for such studies in the region indicated in the figure, it is necessary to have internal polarized target densities lying above 10^{14} nuclei/cm^2.

References

1. T. W. Donnelly and A. S. Raskin, *Ann. Phys.* **169**, 247 (1986).
2. T. W. Donnelly, "Considerations of Polarization in Electron Scattering," at the Workshop *Perspectives in Nuclear Physics at Intermediate Energies*, Trieste (1983).
3. T. W. Donnelly and I. Sick, *Rev. Mod. Phys.* **56**, 461 (1984).
4. T. W. Donnelly, "Polarized Electron Scattering from Polarized Nuclei," at the 6$^{\mathrm{th}}$ Seminar *Electromagnetic Interactions of Nuclei at Low and Medium Energies*, Moscow (1984).
5. T. W. Donnelly, "Polarization Degrees of Freedom in Electron Scattering from Nuclei," at the Summer School *New Vistas in Electro-Nuclear Physics*, Banff, Canada (1985).
6. R. G. Arnold, C. E. Carlson and F. Gross, *Phys. Rev.* **C23**, 363 (1981).
7. M. E. Schultze *et al.*, *Phys. Rev. Lett.* **52**, 597 (1984).
8. T. W. Donnelly, A. S. Raskin and J. F. Dubach, (to be published).
9. J. D. Walecka, *Nucl. Phys.* **A285**, 349 (1977).
10. T. W. Donnelly and R. D. Peccei, *Phys. Rep.* **50**, 1 (1979).
11. T. W. Donnelly, "Electron Scattering and Neutrino Reactions in Nuclei," in the proceedings of *Nuclear and Subnuclear Degrees of Freedom and Lepton Scattering*, Erice, Sicily (1984).
12. A. S. Raskin, Ph.D. Thesis (M.I.T., 1987, unpublished).
13. A. Picklesimer, J. W. Van Orden and S. J. Wallace, *Phys. Rev. C* **32**, 1312 (1985); A. Picklesimer and J. W. Van Orden, *Phys. Rev. C* **35**, 266 (1987).
14. Proposal for a CW Upgrade of the William H. Bates Linear Accelerator Center (June, 1984).

Storage Rings, Internal Targets and PEP*

J. E. Spencer
Stanford Linear Accelerator Center
Stanford University, Stanford, CA 94305

Prologue

Most of the talks here will be on physics **from** accelerators and storage rings rather than the physics **of** such systems since the "physics" is hard enough without having to worry about the beams or how you get them. As a result, this remains transparent to the user via an equipartition of effort worthy of a business school. This is especially debatable for colliding beam storage rings and leads to the corollary that most rings will be born, live and die as dedicated systems. SPEAR is a notable exception while PEP is not – even though PEP seems to provide more unique opportunities over a broader spectrum of physics. Examples include one and two photon physics with real and virtual photons to make all J^{PC} quark combinations as well as high luminosity QCD confinement studies with internal targets as discussed at this workshop. Some related possibilities include external beams of high energy photons; single-pass, free-electron lasers and x-ray synchrotron radiation which could all be the highest energy, resolving power, intensity and brilliance anywhere. From the viewpoint of accelerator physics, such examples fall into three categories: colliding beam physics, internal and external target physics.

How unique such possibilities are, whether they are truly possible e.g. what modifications might be required and questions of compatibility are discussed. Some systematic accelerator physics studies are suggested with implications for this and other proposed projects. As a fan of Gary Larson, I begin with Fig.1 showing his perspective of the PEP tunnel relevant to this occasion. Figure 2 is about reinventing the wheel(or ring in this case) with a lot of people trying to figure out what it is and how you use it. While one can't be sure what they'll come up with it's certain to be "interesting". However, because there have been several proposals for dedicated rings with properties which seem no better than PEP, perhaps Evelyn Waugh should have the last word here: *"If politicians and scientists were lazier, how much happier we should* all *be."*

1. Introduction

The goal is to describe storage rings with internal targets using PEP as example. Although fixed-target experiments were suggested some twenty-five years ago[1] little work of this kind has been done[2]. The differences between electrons and heavier particles such as protons, antiprotons or heavy ions is significant and is also discussed because it raises possibilities of bypass insertions for more exotic experiments. Finally, I compare PEP to other rings, in various contexts, while examining and verifying the statements made in the prologue e.g. that it is an ideal ring for many fundamental and practical applications that can be carried on simultaneously.

A. Some History and Perspective

In a sense, the SLAC linac was built to provide space-like photons[3] for deep inelastic scattering experiments on few nucleon systems. Such experiments demonstrated the basic underlying parton structure of the nucleon. In direct contrast, the subsequent development of SPEAR provided highly time-like photons via the (e^+, e^-) annihilation process shown in Fig. 3(b) which led to the first observations of resonant production of charmed quark pairs$(q_c, \bar{q}_c)$ as well as the heavy, electron-like particle called the tau. Related work is still being done at SPEAR together with a considerable amount of synchrotron radiation research.

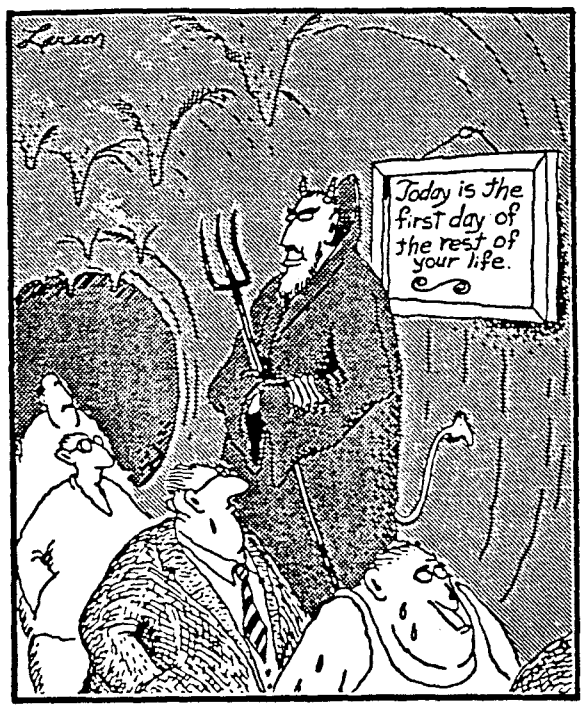

Fig. 1: Perspective of the PEP tunnel.

* Work supported by the Department of Energy, contract DE-AC03-76SF00515.

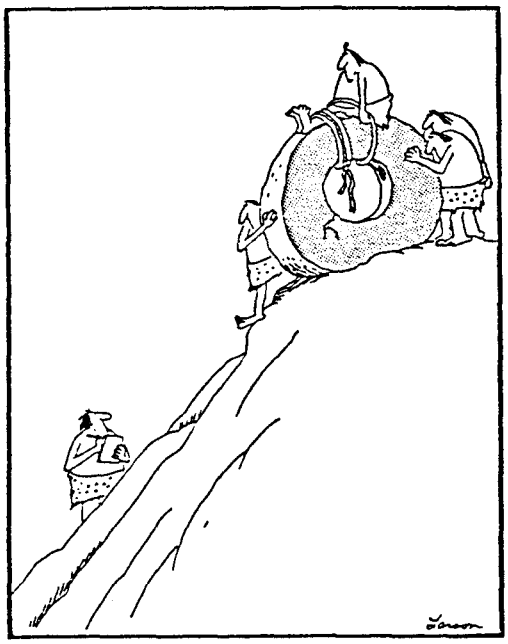

Fig. 2: Early experiments in transportation

With the higher energies available at PEP, higher-order processes become important with the space-like photon production processes of Fig. 3(c) being dominant. This two photon reaction is the main production channel for C-even particles with the physics at the internal vertices in diagrams such as Fig. 3(f) where $X \equiv f\bar{f}$. In all diagrams except Fig. 3(c), the cross sections fall with energy predominately as $1/s$ whereas 3c increases[3,4] in such a way that the crossover between it and processes such as 3b occur at beam energies above $\sqrt{s}/2 = 1\text{GeV}$ depending on the mass m_f.

Concerning internal targets, the first experimental work at SLAC will be discussed at this workshop. My own interest in this area began in 1981 with the question[5]: "Is it possible to use internal foils to reduce phase space and simultaneously serve as a scattering target for an external, high-resolution spectrometer?" With dispersion at the target and the low ring emittance, this would be a consistent and significant improvement in SLAC's capabilities. Unfortunately, the answer to both questions was no unless the foil was a scraper or stripper which was neither new nor very interesting.

More recently, the subject was again considered[4] at an high energy e^+-e^- workshop on PEP because of new developments in polarized gas targets[6]. In this context, the results were quite positive and led to simple scaling relations for internal target luminosity. Furthermore, this option was just one of several to obtain higher luminosities with alternative incident channels: 1) e-γ, 2) γ-γ, and 3) e-A and γ-A. Using high current, stored bunches to produce the primary photon beam which is Compton converted to high energy by backscattering on a high current, high energy linac beam appeared to be an excellent way to upgrade the effective energy and luminosity of existing storage rings. Reaction rates would be improved because photoproduction cross sections are larger than electroproduction and higher current densities are possible by eliminating the conventional beam-beam interaction. While the primary and secondary photon beams would be a significant new research tool, only the e-A option will be discussed further here.

B. A Short History and Description of PEP

Figure 4 shows a schematic layout of the Positron-Electron Project, PEP, as used for colliding beam physics up to 1986. The ring has sixfold symmetry and divides into 12 regions of alternating arcs and long straight sections for experiments called insertions. The odd-numbered regions are the arcs which are subdivided into 19 FODO cells containing a Focusing quad(F), bending magnets with little or no focusing(O) and a Defocusing quad(D). Insertions for injection, extraction or experiments are so labelled because they perturb the otherwise simply periodic structure of identical FODO or unit cells introducing what are called superperiods into the structure. Individual particles can be thought of as oscillators under these focusing forces with frequencies that depend on particle energy.

A good description, including initial operating results and funding history, is available elsewhere[7]. In brief, formal ground breaking took place in June 1977, the ring was completed by April 1980 and delivered $\mathcal{L} > 10^{30} cm^{-2} s^{-1}$ at 11GeV by June.

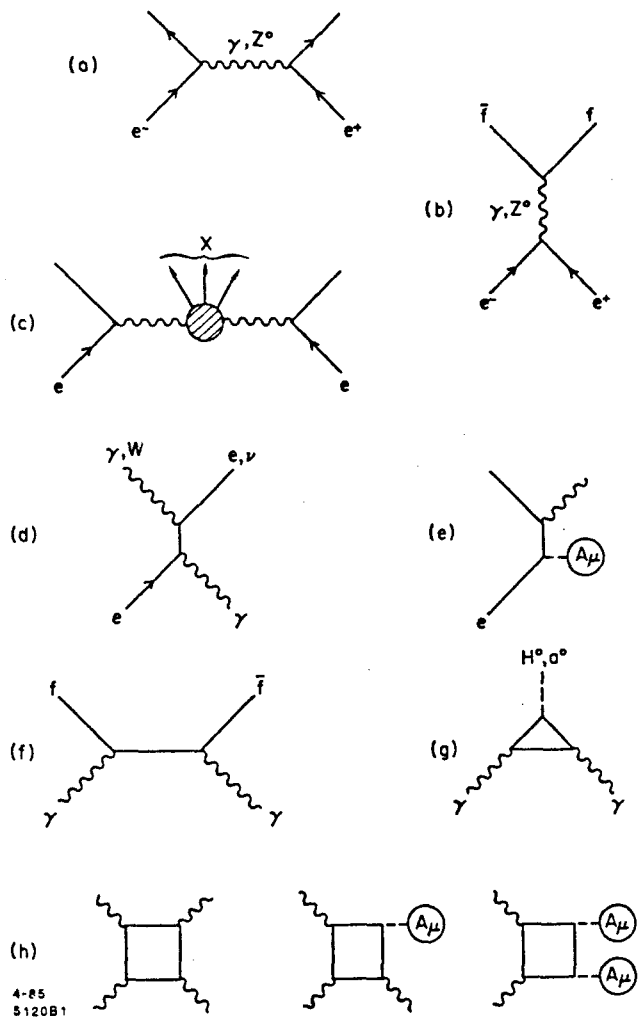

Fig. 3: Low order diagrams in the standard model for: (a,b) elastic, electroweak scattering; (b) electron-positron annihilation into elementary fermions $f = e, \mu, \tau \ldots q_u, q_d, q_s \ldots \nu_{e,\mu,\tau} \ldots$ as well as elementary bosons $(W^{\pm}, Z^o H^o, H^{\pm}?)$; (c) two-boson, electro-weak production; (d) Compton scattering or conversion $(\gamma \rightarrow W^{\pm})$; (e) potential bremsstrahlung; (f) two-photon annihilation to fermions; (g) two-photon annihilation to bosons; and (h) photon-photon scattering, inverse photon bremsstrahlung (harmonic production) and Delbrück scattering.

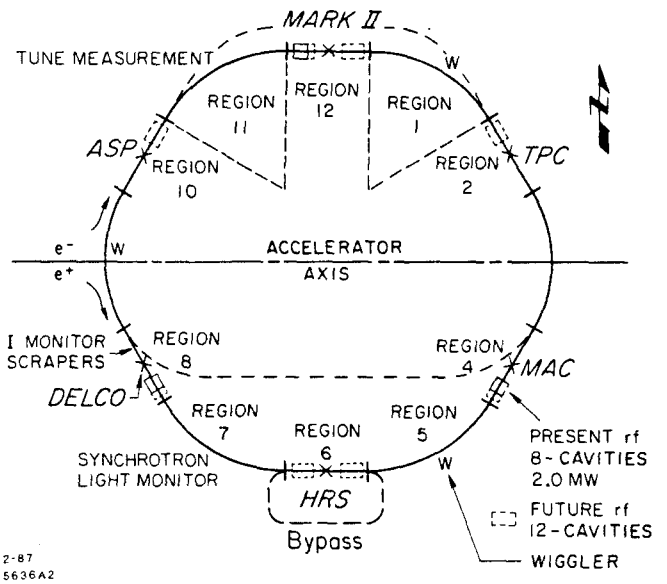

Fig. 4: Schematic layout of PEP showing some characteristics of interest here.

Typical values circa 1984 with all interaction regions active with good detector deadtimes and beam lifetimes at 14.5GeV were $\mathcal{L} \approx 3-4\times10^{31}$ giving integrated luminosities per IR of

$$\int_{Day} \mathcal{L}dt \approx 1500\ \text{nb}^{-1} \quad \text{or} \quad \bar{\mathcal{L}} \approx 1.8\times10^{31}\ cm^{-2}s^{-1}\ .$$

This implies reaction rates on the order of 1 event per picobarn of cross section per day.

The different detectors then were an upgraded MarkII from SPEAR which will be used on SLC next. At 2 o'clock was the Time Projection Chamber which can track and identify all particles such as pions, kaons, protons etc. At 4 o'clock was the MAgnetic Calorimeter for measuring total, final state hadron energy including neutrons and K^0_L followed by the High Resolution Spectrometer at 6 o'clock which had significantly better mass resolution than the other detectors. The Direct Electron Counter identified all final state electrons and the Assymetric Photon search was a supersymmetry experiment looking for new particles like the photino. MAC was also used for these experiments because PEP provided an ideal operating range for them.

Such experiments demonstrated the ability to measure cross sections on the order of tens of femtobarns(10^{-39}cm^2) with storage rings which is an impressive achievement. Notice that the basic annihilation cross ection is

$$R = \frac{4}{3}\pi\alpha^2/s = 86.8/E_{cm}(TeV)^2 \ \text{fb}$$

for processes such as Fig. 1(b) which is independent of mass m_f.

Some other elements in PEP besides those shown in Fig. 4 include beam position monitors and vacuum hardware around the ring, a tune measuring setup as well as transverse and longitudinal feedback hardware. Table I updates the more important parameters and capabilities of PEP which will be discussed in more detail after we motivate and define some terms.

2. The View From Mt. Hamilton

This section is a description of storage rings for physicists. The first problem is how to confine high intensity bunches of charged particles in stable 3-dimensional potential wells for long periods of time. In the rest frame of the bunch, a transverse electric potential results from transverse magnetic fields and the longitudinal well results from the RF field required to replace energy lost to synchrotron(and bremsstrahlung) radiation. The relativistic equation of motion of charged particles in an electromagnetic field in Hamiltonian form i.e. the total energy as a function of canonical variables q and p is:

$$H\Psi = i\dot{\Psi} = (H_{rad} + H_{part} + H_{int})\Psi$$

$$H_{rad} = \frac{1}{8\pi}(E^2+B^2)\delta v; \quad H_{part} + H_{int} = \sum_i H_i$$

$$H_i(p,q) = e_i\phi(\vec{r}_i) + [(\vec{p}_i - e_i\vec{A}(\vec{r}_i))^2 + m_i^2]^{1/2}$$

where $A = (\phi, \vec{A})$ is the external field from the magnets, atoms, or lasers as well as the fields produced by the charges themselves. H_{rad} is the field energy and H_i is the total particle energy in the field.

Table I: Some Representative Storage Ring Parameters for PEP

Characteristic	Value
Nominal Maximum Energy per Beam[a]	17 GeV
Nominal Minimum Energy per Beam[a]	2 GeV
Maximum Current per Beam at 15GeV[b]	46 mA
Number of Particles per Beam at 15GeV	2.1×10^{12}
Maximum Colliding Bunches per Beam	3
Design Luminosity per Interaction Region $\mathcal{L}_{CB}$(Below 15 GeV)	$10^{32}(E/15)^2$ cm^{-2} sec^{-1}
Number of Interaction Regions	6
$\mathcal{L}_{IT}$ (Constant τ_t and I)[c]	$10^{34}/Z(Z+1)$ cm^{-2} sec^{-1}
Average Vacuum in Ring	10^{-9} Torr
Energy Spread (σ_E/E)	$6.7\times10^{-5}E$(GeV)
Natural Emittance (ϵ_x)[d]	$5.5E(\text{GeV})^2$ Å
Length of Each Straight IR Insertion	120 m
Available Free Length for Experiments	15 m
Circumference	2200 m
Symmetry	6
RF Power Installed[e]	6.0 MW
Number of Accelerating Sections	24
Number of 0.5 MW Klystrons[e]	12
RF Frequency	353.2 MHz
Harmonic Number	2592

a This energy has not been well defined as discussed in the text.
b For single beam operation this scales up as the number of beams.
c Assumes lifetime τ_t = 2h, current I=100mA for atomic number Z.
d This can be significantly reduced as discussed in the text.
e Commercial klystrons are now available with twice this power.

Spin terms are ignored together with the whole question of beam polarization because our concern is with the classical dynamics of motion which should not be influenced by spin effects even for the "small" emittances of interest here. However, if such effects were to be emphasized, superconducting or permanent magnet storage rings would be an ideal place for them.

Retaining only first degree terms in $\vec{A}_o$, in the rest frame, gives

$$H_{oi} - m_i = (\vec{p}_{oi} - e_i\vec{A}_o(\vec{r}_{oi}))^2/(2m_i) + e_i\phi(\vec{r}_{oi}) + V \ .$$

For a pure electrostatic field ($\vec{A} = 0$) this gives the familiar nonrelativistic expression for the energy. Neither H nor H_i includes interaction between particles unless we add a term such as V with subscripts ij, ijk etc. which then gives coupled equations. If we are interested in such beam dynamics as coherent effects within a beam bunch, or various excitation modes in a laser medium, crystal lattice, atom or "elementary" particle we must include such terms.

The fields $\vec{A}$ and ϕ are generally nonlinear due to magnet errors and end fields, the sinusoidal character of the RF and the fields induced by the beam through self forces(e.g. the so-called ponderomotive potentials) or wake fields(interaction with the rest of the external world exclusive of guide fields). Such fields can couple the degrees of freedom of the single particle e.g. provide transverse-transverse (x-y) and transverse-longitudinal (x-z) coupling. Furthermore, since wake fields can be either transverse or longitudinal as well as fast or slowly decaying ($\tau \gtrsim 1/\omega_z$ or $1/\omega_{z,y}$ for fields with Fourier components $\omega \lesssim c/L$), one expects that both single and multibunch instabilities will be possible.

Even assuming only one beam and one bunch, there are a number of current dependent effects which can cause beam blowup and subsequent particle loss by leakage out of the well. A good general reference for single-particle effects is Ref's. 8& 9. Collective effects have been discussed in Ref. 10. They may be broken down into coherent and incoherent depending on whether there are phase relations between individual particles or not. Where there are, one can think of modes of motion like that of the incompressible liquid drop of Bohr and Mottelson i.e. one has dipole and quadrupole motion that can be quite dramatic. There are many ways to both induce and cure such coherent effects. Thus, as the bunch oscillates, the potential well dynamically distorts which can produce an oscillating force back on the beam that can either drive or damp it. Similarly, the external potential well can be made to act the same way – usually via negative electronic feedback that senses and then feeds back to damp an instability. One can also add harmonic cavities to statically distort the potential well for various reasons[11] such as bunch length control or power consumption.

The canonical position, q, can be understood to represent the transverse displacement x and y from the equilibrium orbit and is a function of time, the independent variable, or equivalently, the distance along the central orbit s (or z). The momentum, $p \approx \gamma m q'$ where $q' = dq/ds$ so the important Liouville invariant is

$$\int pdq = m\int \gamma q' dq \equiv m\gamma\epsilon \equiv m\epsilon_n$$

for any particle with ϵ its area in transverse phase space. A beam of particles has a distribution function in phase space which convention describes by

$$\epsilon_n \equiv \gamma\sigma\sigma' = \gamma\frac{\sigma^2}{\beta}$$

where ϵ_n defines the normalized, "invariant", transverse emittance in any direction with σ, σ' the rms size and divergence and β the focusing or betatron function of the cells in that coordinate(x,y). It is also called a Twiss parameter[8].

The phase space trajectory of a representative particle that defines the rms beam envelop can be expressed[8,9] as

$$q = \sqrt{\epsilon\beta(s)}\cos(\phi(s) - \phi_0)$$

$$q' = -\sqrt{\frac{\epsilon}{\beta}}\left[\sin(\phi(s) - \phi_0) - \alpha\cos(\phi(s) - \phi_0)\right]$$

where $\alpha = \beta'/2$ and the phase

$$\phi(s) = \int_0^s \frac{ds}{\beta(s)}$$

with $\phi(0) = 0$ and $\phi(s)$ is another twiss parameter. Integrated around the ring, it gives the tune or betatron number

$$\nu = \frac{1}{2\pi}\int_0^L \frac{ds}{\beta(s)} = \frac{1}{2\pi}\oint \frac{ds}{\beta} \ .$$

The transformation of $\{q\} = (q, q')$ from one place to another, $\{q_2\} = R\{q_1\}$, is derivable from these expressions in a number of ways[8] e.g. using two linearly independent solutions such as $\phi_0 = 0, \frac{\pi}{2}$ giving:

$$R_{11} = \sqrt{\frac{\beta_2}{\beta_1}}\left[\cos\Delta\phi + \alpha_1\sin\Delta\phi\right]$$

$$R_{12} = \sqrt{\beta_1\beta_2}\sin\Delta\phi$$

$$R_{21} = \frac{1}{\sqrt{\beta_1\beta_2}}\left[(\alpha_1 - \alpha_2)\cos\Delta\phi - (1 + \alpha_1\alpha_2)\sin\Delta\phi\right]$$

$$R_{22} = \sqrt{\frac{\beta_1}{\beta_2}}\left[\cos\Delta\phi - \alpha_2\sin\Delta\phi\right]$$

where $\Delta\phi = \phi_2 - \phi_1$. These expressions are the first order transformations for the transverse motion of the Hamiltonian system and allow tracking with nonlinear perturbations etc. More importantly we have defined most of the terms used in Table I and needed for a more detailed study of rings such as PEP.

3. Three Kinds of Luminosity

A good place to begin is to define some different kinds of luminosity and what I mean by high and low luminosity and thick and thin targets etc. Conventional colliding beam luminosity which I will call $\mathcal{L}_{CB}$ has been discussed in detail[9,4].

A. Colliding Beam Luminosity

The incoherent beam-beam interaction between colliding bunches produces strong, nonlinear forces on the bunches which limit the operation of present rings. The leading-order, linear focusing force for head-on $e^{\pm}$ collisions, expressed as a tune perturbation per crossing, is[9]

$$\Delta\nu_{x,y} = \frac{r_e N_e \beta^*_{x,y}}{2\pi\gamma\sigma^*_{x,y}(\sigma^*_x + \sigma^*_y)}$$

where σ is the rms bunch size, N_e is the number of particles per bunch and β^* is the beta function at the crossing point or IR. For protons one would use the classical proton radius, r_p. Notice that γ for 20 TeV SSC protons is the same as for 10 GeV PEP electrons. The limiting magnitude of this number for most electron rings is $\Delta\nu^*_{x,y} \lesssim 0.05$.

With internal targets, this number can serve as a benchmark to compute the allowable number of ions replacing N_e with $-sgn(\frac{q}{e})N_i$, depending on whether we use an $e^{\pm}$ beam, before a clearing field is needed. The expressions are otherwise the same i.e. higher energy beams are preferred. Constraints from the operation of the target are generally more stringent i.e. depolarization and replenishment rates that are possible but multi-bunch instabilities with electron beams also have to be considered.

Although the above expression can be identified with the *average*, small amplitude tune shift for gaussian bunches it is best thought of as the tune *spread* in the core of the bunch[9]. At some limiting value of this tune spread ($\Delta\nu^*$) or bunch current (N^*_e) the bunch cross-section ($\sigma^*_x\sigma^*_y$) increases, luminosity fails to increase and may decrease and the lifetime may well decrease. If this limit is made the same in both transverse directions by making $\beta^*_y/\beta^*_x \simeq K(\equiv \epsilon_y/\epsilon_x)$, the tune independent, x-y coupling in the machine), one expects the maximum achievable luminosity when $\sigma^*_x \gg \sigma^*_y$ to be:

$$\mathcal{L}_{max} = \frac{(N^*_e)^2}{4\pi\sigma^*_x\sigma^*_y} f n = (\Delta\nu^*)^2(\frac{\gamma}{r_e})^2\frac{\epsilon_x}{\beta^*_y} f n$$

where $\epsilon_x = \pi\sigma^2_x/\beta_x$, f is the revolution frequency and n is the number of bunches per beam. Table II for PEP and SPEAR shows they are both near their limits of $10^{31} < \mathcal{L}_{CB} < 10^{32}$.

B. External Target Luminosity

For resolutions of order 20-50 keV at energies typical of Bates or LAMPF one must use target thicknesses of $t_t \approx$10–50mg/cm^2. Typical currents with a consistent phase space and energy spread are $I_b \approx$50–100μA. Translating these numbers into an equivalent luminosity gives:

$$\mathcal{L}_{ET} = (\frac{I_b}{e})N_A(\frac{\rho x}{\mathcal{A}}) = 3.1\times10^{35}[\frac{I_b}{100\mu A}][\frac{t_t}{10mg/cm^2}][\frac{12}{A}]$$

where N_A is Avogadro's number, $\mathcal{A}$ the gram-molecular weight and A the atomic mass number in carbon units. This is a good benchmark for comparison to other facilities.

Table II: Some current operating parameters for the SPEAR and PEP storage rings for both colliding and single beams. These numbers do not involve the use of wigglers except during PEP injection at 5 GeV.

Energy(GeV)	2 SPEAR	5 PEP	10 PEP	15 PEP	
Beam Current, I_t^{Max}	100	30(?)	120(?)	92	mA
Beam Current, I_t^{Col}	25	5	20	46	mA
Coupling, $K \equiv \epsilon_y/\epsilon_x$	6.3	6.3	7.6	7.6	%
Emittance, $\epsilon_x \equiv \sigma^2_x/\beta_x$	0.195	0.0138	0.055	0.124	mm-mr
Emittance, $\epsilon_y \equiv \sigma^2_y/\beta_y$	12.2	0.866	4.19	9.43	μm-mr
Energy Spread, σ_E/E	0.048	0.033	0.067	0.10	%
Damping Time, $\tau_{x,y}$	28.3	100	27.5	8.2	msec
Revolution Time, T_o	0.78	7.34	7.34	7.34	μsec
IR Beta, β^*_x	0.9/20	3.0/15	3.0/15	3.0/15	m
IR Beta, β^*_y	0.03/35	0.12/0.6	0.12/0.6	0.12/0.6	m
IR Size, σ^*_x	0.42/1.97	0.20/0.45	0.41/0.91	0.61/1.36	mm
IR Size, σ^*_y	.019/0.65	.010/.023	.022/.050	.034/.075	mm
Divergence, $\sigma^*_{x'}$	.465/.099	.068/.030	.136/.061	.203/.091	mr
Divergence, $\sigma^*_{y'}$	.638/.019	.085/.038	.187/.084	.280/.125	mr
Energy Loss/Turn	0.110	0.333	5.33	27.0	MeV
Peak RF Voltage, V_p	0.495	0.650	8.49	39.1	MV
Bunch Length, σ_s	3.5	2.8	2.3	2.0	cm

C. Internal Target Luminosity

One can write the internal target luminosity in terms of the target thickness, n_t, as

$$\mathcal{L}_{IT} = (\frac{I_b}{e})N_A(\frac{\rho x}{\mathcal{A}}) = 6.2\times10^{32}[\frac{I_b}{100mA}][\frac{n_t}{10^{15}/cm^2}]\ cm^{-2}s^{-1}.$$

One will find that luminosities on the order of 10^{33} are possible without significant effects on the beam. Targets on the order of $n_t \sim 10^{15}/cm^2$ or tens of ng/cm^2 are very thin but the currents are greater than for $\mathcal{L}_{ET}$ because of the more than 10^5 traversals per second in the ring. Such thicknesses appear *ideal* for optically pumped, *polarized* targets because of depolarizing effects due to beam heating in solid targets. Furthermore, there appears[7] to be a large range of (A,Z) available including H^1, D^2 and He^3 i.e. the 3, 6 and 9 quark systems.

Because $\mathcal{L}$ does not depend on the beam cross-section, one can operate in a mini-maxi β configuration with small angular spreads at the target *and* small $\mathcal{L}_{CB}$. Considerably thicker targets are also possible through the use of "target scrapers" and a better understanding of dynamic aperture.

There could also be a tune perturbation as mentioned above and the same limit $\Delta\nu^*$ can be used as a guideline. Such questions are interesting and should be studied. An appropriately designed target would also allow study of wake fields, plasma lenses and their control of β^* as well as various tune modulation and feedback effects just to mention a few possibilities.

4. Luminosity Limitations

A. Colliding Beams

Increasing the frequency via superconducting magnets, or the number of bunches or the energy i.e. stiffening the beam are all expected to improve luminosity. Unfortunately, increasing the number of bunches (and duty factor) produces multibunch instabilities and other problems when the total number of bunches exceeds the number of IR's. Thus, one seldom sees a linear increase in luminosity with n unless $\Delta\nu < \Delta\nu^*$. Decreasing either β_y^* or increasing the horizontal emittance ϵ_x reduces the beam-beam force but is difficult because this increases the sensitivity to transverse instabilities. Decreasing β_y^* also implies shorter bunches which increases the sensitivity to transverse-longitudinal couplings i.e. synchrobetatron resonances. Using wigglers in existing rings to increase ϵ_x with *decreasing* energy[12] is now well established and relatively benign but the reverse is not true. In PEP, the wigglers are used to both decrease damping time and increase emittance.

Evidence from many rings has shown[13] that $\Delta\nu^* \lesssim 0.05$ and that it is difficult to keep this matched in both directions with increasing beam currents. Nevertheless, this number can presumably be increased in a variety of ways e.g. by increasing damping by going to higher bend fields (and thus also increasing f) or by incorporating more wigglers. However, because the multipole expansion of the beam-beam interaction goes to high order and these multipoles can't be reduced by simply increasing the aperture as for quadrupoles it is clear that the linear description of the beam-beam interaction is not adequate. At the same time, it is not at all clear how to deal with such nonlinearities or even to simulate them in a self-consistent way. Furthermore, very little effort has gone into this and related questions such as multibunch instabilities.

I will not go into the many attempts to compensate or cancel $\Delta\nu$ except to mention the charge-neutralization scheme of the Orsay Group[14] using 4 beams and double rings. It was hoped this approach would provide an improvement in $\mathcal{L}_{max}$ of two-orders of magnitude but so far has not been made to work. The Stanford single-pass collider (SLC) represents the opposite extreme where it seeks to maximize $\Delta\nu^*$ with high bunch current and low-emittance to enhance luminosity through a pinch effect. Another attitude we have taken is to avoid the beam-beam problem[3,4] through conversion of the charged particles into photons. The limits in this case are presumably the maximum, single bunch currents which a linac can provide and a storage ring can store with good stability and emittance. This can be limited by many external effects before internal space-charge becomes important but again there is very little systematic information available on this question. The "external" photon beam from this technique would also be a unique resource for fixed target experiments.

B. Internal Targets

The current limits discussed above apply here as well. In addition, there is the beam lifetime and emittance due to internal target density. The PEP handbook shows the expected lifetimes due to various sources of loss in PEP. While this implies the importance of three different processes over the range of energies of interest, the most important one for our purposes is atomic bremsstrahlung since we assume the Touschek effect will only be important near the IR's and that the particle density can easily be varied by the required factor of two or so. This same factor of two might also be obtainable by manipulating $(\beta^*_{min}, \beta^*_{max})$ in a mini-maxi beta scheme. This is clearly not a problem but bremsstrahlung from "residual-gas" is – because the differential probability for radiation loss is roughly constant up to the full electron energy for the electron energies of interest here.

Integrating Rossi's expression[15] for the differential radiation probability per unit radiation length gives:

$$\int_{(\frac{t_R}{\tau})_{RF}}^{1} \Psi_{rad}(x)dx = [\frac{4}{3}\ln(\frac{\gamma}{\delta\gamma})_{RF} - \frac{5}{6}]$$

where x is the fractional photon energy, ω/ϵ. The fractional particle loss is then

$$\frac{dN_b}{N_b} = -[\,]\frac{\rho}{X_o}dx \longrightarrow \frac{1}{\tau} = [\,]\frac{c\rho}{X_o}$$

assuming a simple target uniformly distributed around the ring like residual gas. Here $1/X_o \equiv N_A\sigma_{rad}/\mathcal{A}$ with σ_{rad} the total bremsstrahlung cross section per nucleus or atom and x is the lineal thickness. In terms of both ring and target components, the expression is

$$\frac{1}{\tau} = [\,][\sum_i \frac{c\rho_i^{STP}}{X_{oi}}(\frac{P_i}{760}) + \sum_j \frac{c\rho_j^{STP}}{X_{oj}}(\frac{l_t}{l_R})(\frac{P_j}{760})(\frac{273}{T_j})]$$

where l_t/l_R is the ratio of target length to ring circumference. Including both the atomic bremsstrahlung cross section for electrons and nucleus so that $\sigma^i_{rad} = 4\alpha Z_i(Z_i+1)r_e^2[\ln 183/Z_i^{1/3} + \frac{1}{18}]$ but ignoring all but one target component (i.e. considering only the partial lifetime due to the target) in an otherwise perfect vacuum gives:

$$\frac{T_o}{\tau_t} \simeq [\,]4\sigma_o Z(Z+1)\ln(183/Z^{1/3})[\frac{N_A}{\mathcal{A}}\rho^{STP}l_t(\frac{P}{760})(\frac{273}{T})].$$

The last factor in brackets is just the target thickness n_t (#/unit area), $\sigma_o \equiv \alpha r_e^2$ and T_o is the revolution time around the ring (see Table II). For hydrogen, $\rho^{STP}_{H_2} = 0.090\ kG/m^3$ so for $l_t = 10$ cm

$$n_t = \frac{2N_A}{\mathcal{A}_{H_2}}\rho^{STP}_{H_2}l_t(\frac{P_t}{760}) = 5.38\times10^{20}(\frac{P_t}{760})[atoms/cm^2].$$

For $n_t = 10^{14}/cm^2$, this implies $P_t = 1.4\times10^{-4}$ Torr or a required differential pumping rate of $\sim 10^{-5}$ Torr at room temperature which is reasonable. One wants this differential rate to roughly correspond to the l_t/l_R factor ($\simeq 4.5\times10^{-5}$ in PEP) since the two main, residual gas components observed with mass analyzers are hydrogen and carbon monoxide.

Because the RF capture bucket width can be $\delta\epsilon_e/\epsilon_e \gtrsim \pm 1\%$ in both SPEAR and PEP, the corresponding partial lifetime for a $10^{14}/\mathrm{cm}^2$, hydrogen target is:

$$\frac{\tau_t^H}{T_o} \simeq (5.31 \times 4 \times 0.58mb \times 10.42 \times 10^{14})^{-1}$$

$$= 7.8 \times 10^{10} \begin{cases} 159 \text{ hrs} & \text{(PEP)} \\ 16.9 \text{ hrs} & \text{(SPEAR)} \end{cases}$$

This indicates these experiments can be done on both SPEAR and PEP without requiring dedicated operation with $\mathcal{L} \gtrsim 10^{33}$ $\mathrm{cm}^{-2}\mathrm{s}^{-1}$ using state-of-the-art polarized gas targets! This is independent of beam energy and valid for all energies of current interest ($\epsilon \gtrsim 1.5$ GeV) as well as elements with $\alpha Z \ll 1$. PEP, with its large radius and large energy range, would seem to be an ideal system for these experiments especially when multibunch operation with higher duty factor and current is developed. These operating conditions are ideally matched to simultaneous synchrotron radiation operation.

C. Accelerator Physics Studies

Systematic machine physics studies on PEP with a single beam that are relevant to these questions include bunch cross-section measurements versus all of the following: bunch current (N_b); bunch number (n_b) and distribution; both high and low $\beta_{x,y}^*$; ν_s, σ_z, σ_ϵ and V_{RF}; and $\nu_{x,y}$. These should be done at a couple of energies e.g. a low (5 GeV), intermediate (10 GeV) and high energy (15-17 GeV). Any instabilities observed should be characterized by their threshold behavior (N_{th}) versus these parameters including possible differences between electrons and positrons.

5. PEP Capabilities

Designing storage rings for a specific process in Fig. 3 might emphasize energy spread for Fig. 3(b) and electron polarization for Fig. 3(c) but the most important parameters characterizing both accelerators and storage rings are the energy range (C-M) and the beam current or luminosity available over this range. While the primary goal is to reach higher energies, it also seems important to improve the luminosity and range of capabilities of existing facilities. The PEP storage ring, with its large, single-beam energy range ($E_b \sim 2 - 17(25)$ GeV) in conjunction with the SLAC high energy, high current, low emittance linac beam provides some unique opportunities. Here we will discuss some of the factors each application wants and try to show how PEP can supply them.

A. Synchrotron Radiation

Figure 5 compares the synchrotron light spectra available from the cell bending magnets for a number of existing and proposed facilities. While most of these have wigglers which enhance such spectra, these comparisons appear to be easily biased and also change rapidly. Nonetheless, PEP has some unique possibilities here as well e.g. it has 5m symmetry straight sections midway between interaction regions which already have 2T wigglers as shown in Fig. 4. In addition, I have shown some bypass possibilities in Fig. 4 and from Table I and Figs. 4 and 6 one sees there are already several long, straight insertions with lengths up to 120m which could be used for coherent undulators. Because there are also a number of new, low emittance configurations possible for PEP[16], some of which are shown in Table III, such options seem inevitable.

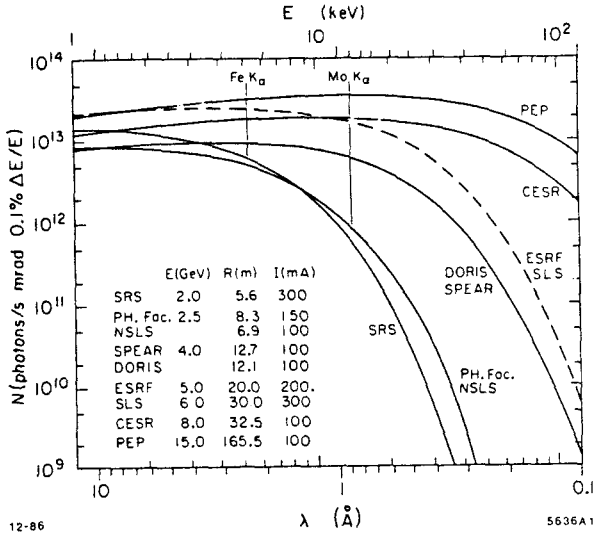

Fig. 5: Comparison of PEP's synchrotron radiation spectrum with a number of existing and proposed rings such as the European Synchrotron Radiation Facility and the Argonne Synchrotron Light Source.

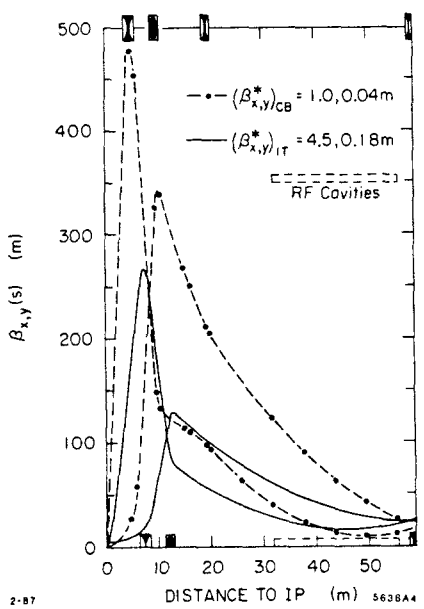

Fig. 6: Beta functions for the new colliding beam configuration of Table III around the Interaction Region(IR) and RF cavities.

For high brightness you need low emittance. Let's compare to SLS whose design emittance[17] at 6 GeV is $\epsilon = 65$Å compared to PEP's 45Å. This can also be improved[18] by at least another factor of two by using Robinson wigglers to increase the horizontal damping partition, J_x. It seems almost too good to be true but higher brightness also requires high current capability at the lower energies which is discussed in the next section.

Table III: Some New Operating Configurations for use at PEP.

	Mini-Beta 1-Fold	Low Emittance 6-Fold	Low Emittance 1-Fold	
Hor. Tune, ν_x	21.28	29.28	29.28	
Vert. Tune, ν_y	18.22	13.20	13.20	
Mom. Comp., α	0.00255	0.000986	0.000973	
$\epsilon_x/E(GeV)^2$	5.49	1.30	1.27	$\AA\cdot GeV^{-2}$
$(\sigma_E/E)/E(GeV)$	0.00666	0.00666	0.00666	$\%\cdot GeV^{-1}$
β_x^*	1.00	67.9	54.0	m
β_y^* IR	0.04	100.0	356.6	m
η^*	-0.093	-2.0	0.0	cm
$\hat{\beta}_x$	22.6	20.8	20.2	m
$\hat{\beta}_y$ Cell	36.8	43.0	44.0	m
$\hat{\eta}$	1.23	0.55	0.51	m
β_x	32.3	26.0	26.4	m
β_y S.P.	5.5	5.7	5.3	m
η	1.49	0.62	0.53	m
β_x^*	4.50		79.3	m
β_y^* 5 IR's	0.18		96.6	m
η^*	0.004		0.0	cm

B. Internal Targets

PEP, with its large radius ($2\pi\bar{R}$ = 2.20 km) and large energy range would also seem to be an ideal system for these experiments especially when multibunch operation with higher duty factor and current is developed. The beam lifetime was shown to be the product of three terms, relating to the RF capture bucket, the electron-nuclear bremstrahlung cross-section and the target thickness. The log factors can each be approximated by 5, so one has:

$$\mathcal{L}_{IT} = \left(\frac{I_b}{100mA}\right)\left(\frac{2}{\tau(h)}\right)\left(\frac{T_o(\mu s)}{7.34}\right)\left(\frac{1}{Z(Z+1)}\right) \times 10^{34}\ cm^{-2}s^{-1}.$$

Such conditions are ideally matched to simultaneous synchrotron radiation operation so long as there is no significant increase in emittance. The lifetime due to single coulomb scattering goes as $E^2A_s^2/Z^2\beta_t\beta_s n_t$ and is orders of magnitude larger than for bremstrahlung so that setting the aperture (or scrappers) at $\pm A_s$ allows an analytic approach to emittance growth and indicates no growth at PEP for bremstrahlung limited target densities. This also allows experiments when an internal target with variable n_t is available. Lower emittance (higher tune) configurations than used in Table I for colliding beam operation are clearly possible at lower energies because the goals are reversed. At some point emittance growth could become a problem but only at the lowest energies where currents are also a problem. Similarly, the harmonic number of the ring is $h = 2592$ but only three bunches per beam have been seriously studied.

A major limitation on the total and single-bunch currents is the impedance of the ring which is dominated by limiting apertures such as the RF cavities shown in Figs. 4 and 6 and, of course, any gas cell – especially one that is poorly designed. A considerable amount of work has gone into the design of the PEP vacuum and RF system[19] and this has undergone several changes[20] based on optics changes and measurements of the limiting currents observed[21]. Figure 7 shows the latest calculations for PEP based on Table I and the new colliding beam configuration[22] in Table III. Figure 6 shows $\beta_{x,y}$ in the vicinity of the cavities. This distribution is clearly not optimal and never was which explains why the previous single-bunch, fast, head-tail threshold was roughly consistent[21] with the PEP transverse cavity impedance.

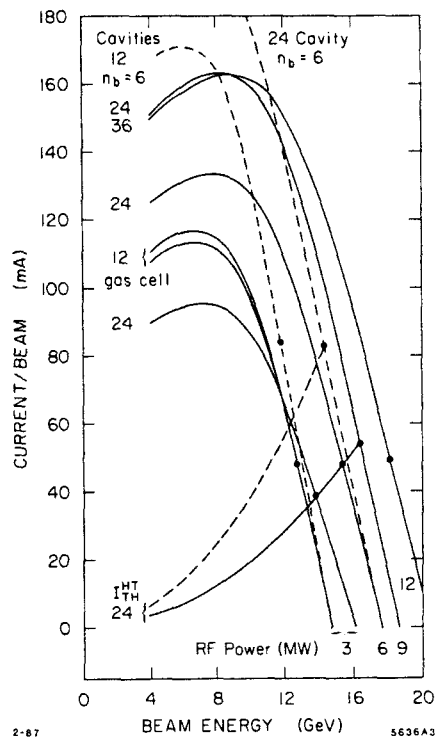

Fig. 7. Some representative RF limited current characteristics for PEP. Currently it runs with three bunches per beam with 24 cavities and 6 MW (Table I). Solid curves assume 3 bunches and dashed 6 bunches per beam. The intersection of these curves with the predicted current limits from the single-bunch, fast head-tail effect are shown as dots marking the dominance of these two regimes.

A number of different possibilities are considered in Fig. 7 such as adding and removing cavities, increasing the number of bunches and running with a single gas cell such as the one described in Ref. 23 with conditions where the effects should be most evident. A properly terminated cell of this type does not influence the beam significantly but the reverse may not be true. Although the beam will tend to drop some energy in it, this should be small in the practical domain of operation. The limit will be determined by multibunch instabilities and could cause depolarization. This is another area for study and testing.

One predicts from Fig. 7 that the current becomes RF limited below the dots on each curve i.e. at higher energies. The dots represent the threshold for dominance of the the transverse mode coupling instability or fast, head-tail effect[20,21]. To my knowledge there is no evidence for multi-bunch instabilities in PEP except for those associated with colliding beam operation. N-bunch, single beam operation can be thought of

as N coupled oscillators with N normal modes which require N-independent tuning knobs which are available from the RF cavities around the ring. The present distribution is not optimal for this but could certainly be improved. Several points can now be made. First, higher energies are best, both from the maximum single bunch limit and for multi-bunch operation i.e. we don't want to simply remove our sources of pickup and feedback and also that the bunch spacing and harmonic number are so large in PEP that it is certainly possible to use feedback to deal with such problems. Also, while one expects coupled bunch instabilities and other problems, a stable, single bunch current of $\approx$ 1 mA at 4.5 GeV has been verified so we have used very conservative numbers for the beam currents at the lower energies in the various Tables. Concerning higher energies, Fig. 8 shows a typical magnetization cycle that every cell dipole magnet was subjected to and measured along. While the current supplies will only go to about 17 GeV the magnets go much higher and the character of the curves imply reasonably simple operation from $2 < E(\text{GeV}) < 25$. Several systematic machine physics studies on PEP are clearly suggested by such questions.

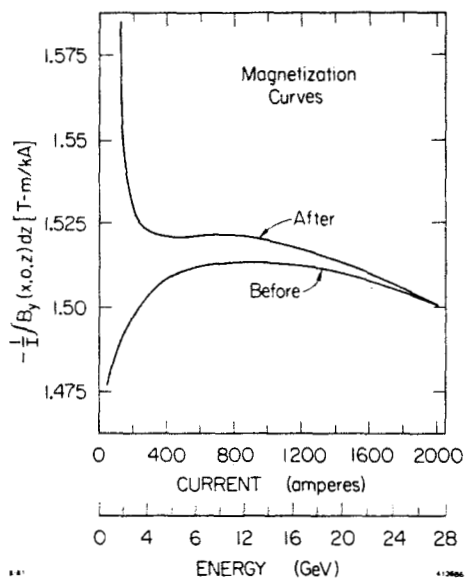

Fig. 8. Field integrals measured before and after subjecting a virgin PEP bending magnet to a magnetization cycle. Every PEP magnet was measured in this way with data taken from 1-27 GeV.

Other questions also include various polarization effects. The scattering of circularly polarized light by $e^{\pm}$ can be used to measure polarization of the $e^{\pm}$ and can also be used to induce it but with poor efficiencies at these energies. A low-energy, polarized electron beam can be used in a similar way to the photon beam to measure the polarization of a stored electron beam or to polarize photons via Compton scattering. Implementing longitudinal polarization with the new, efficient, tensor polarized gas targets could then provide an absolutely unique facility for nuclear QCD studies from 2-17(25) GeV that would allow high luminosity $\vec{e}+\vec{\gamma}$ and $\vec{e}+\vec{A}$ and $\vec{\gamma}+\vec{A}$ studies etc. A number of alternative insertions to provide longitudinal polarization in one or more interaction regions are possible in PEP but IR 6 appears best.

6. Compatibilities

Table IV is a "truth" table showing some possible operating modes and how they interrelate to one another. No doubt everyone would like an IR hall for detectors, spectrometers, bypasses or future possibilities. While SR is produced everywhere, the IR and symmetry straight sections are the most popular for them as well. Typically, the dispersion functions are minimal near the IR and maximal at the SP so the wigglers in SP 1, 5 and 9 improve luminosity below 15 GeV by increasing emittance while putting them near the IR would have the reverse effect. Their roles for luminosity would reverse above 15 GeV. The use of dispersion at the IT implies one is using dispersion matching to achieve higher energy resolution e.g. even though PEP has a very low energy spread compared to the linac, it can still be improved to do high resolution spectrometer studies at much higher energies than Bates or LAMPF. I won't discuss the various uses of wigglers implied in the Table but leave this as a topic for future discussion among interested parties.

Table IV: Operational compatibilities between Colliding Beam physics(CB), Internal Target physics(IT) and Synchrotron Radiation physics(SR). "D" stands for experiments requiring Dispersion, "SP" stands for Symmetry Point, "IR" for Interaction Region, "U" for Undulator, "W" for standard Wiggler and W_R is a Robinson wiggler located at high η e.g. at the SP.

E(GeV)	5	10	15	20
CB	W_{SP}	W_{SP}		W_{IR},W_R
IT	Any	Any	Any	Any
ITD	U	U	U	U
SRSP	U,W_R	U,W_R	U,W_R	U,W_R
SRIR	U,W	U,W	U,W	U,W

7. A Few Conclusions (and Possibilities)

There are a remarkable number of possibilities available that can be arranged into an interesting, long-range program with well defined stages. First on the list is the new mini-beta upgrade which allows a variable mini-maxi scheme as shown in Table III. This will be tested this fall. Variable density targets, in conjunction with wigglers could improve low-energy, colliding beam operation by providing independent control over longitudinal and transverse phase space. Implementing longitudinal polarization with the new, efficient, tensor polarized gas targets could then provide an absolutely unique facility for nuclear QCD studies from 2-17(25) GeV. Multi-bunch operation in a dedicated mode of operation or even CB mode could provide high duty factors whose magnitude needs to be studied. It seems clear that an energy closer to 15 than 5 is preferred on most grounds.

Implementing a high energy photon facility would augment the internal target program as well as the high energy physics studies since one wants to use such beams near their source even though good external photon beams will naturally arise. There are many interesting research and development projects here such as the study of high current, high density bunches;

development of highly segmented, fast, efficient photon detectors and the development of long, combined function undulators to name a few. An injection IR is clearly preferred for this work which would allow high luminosity $\vec{e}+\vec{\gamma}$ and $\vec{\gamma}+\vec{A}$ studies as well as $\vec{\gamma}+\vec{\gamma}$ over a large energy range.

There are many interesting accelerator physics studies e.g. we don't really understand the low energy limits of the ring such as the fundamental limits on single and multi-bunch beams as a function of energy or operating configuration. How should one use the various wigglers, bunch lengthening cavities, higher order multipoles, internal targets and various types of feedback to control or optimize current and aperture limitations? It is interesting that a long list of such projects for PEP compiled in 1982 has gone virtually untouched even though they might have justified PEP as a national test facility.

Some of the things discussed here could be started now and when PEP resumes operation and probably should because they impact longer range planning and funding. Samuel Butler viewed "progress" as a form of generic cancer when he said: *All progress is based on a universal innate desire on the part of every organism to live beyond its means.* A possible antidote to this is better long range planning for proposed uses and funding commitments. Past parochialism or specialization in both areas is neither efficient nor effective and this seems a good place to try something different.

Acknowledgements

I should thank many people for their interest and suggestions but particularly Karl Bane, Stan Brodsky, Phil Morton, Albert Hofmann, Ewan Patterson, Ron Ruth and Perry Wilson. I should also mention Elliot Bloom who is studying the CB possibilities, George Brown and Herman Winick with whom I've discussed the SR interests and especially S.G. Popov for bringing me up to date on the Russian IT work that has been done on the VEPP rings.

References

1. W.C. Barber, G.K. O'Neill, W.K.H. Panofsky and B. Richter, "Experimental Test of QED, Proposal to U.S.A.E.C.," May 1958.
2. V.F. Dmitriev, D.M. Nikolenko, S.G. Popov, I.A. Rachek, Yu.M. Shatunov, D.K. Toporkov, E.P. Tsentalovich, Yu.G. Ukraintsev, B.B. Voitsekhovskii and V.G. Zelevinsky, "First Measurement of Asymmetry in Electron Scattering by a Jet Target of Polarized Deuterium Atoms," Phys. Lett. 157B (1985) 143.
3. I assume a natural metric for four-vectors with $p \equiv (\epsilon, \vec{p})$ and $\hbar = c = 1$ so $s = (\omega_1+\omega_2)^2 - (\vec{k}_1+\vec{k}_2)^2 \equiv 4\omega_1\omega_2$ for collinear collisions between real photons. For a discussion of the various processes in Fig. 3, see J.E. Spencer and S.J. Brodsky, IEEE Trans. Nucl. Sci. NS-32 (1985) 3431 and Ref. 4 below.
4. J.E. Spencer, "Higher Luminosities via Alternative Incident Channels," SLAC-PUB-3645, April 1985.
5. J.E. Spencer, "Storage Rings, Internal Targets and Such," Argonne Workshop on High Resolution Spectrometers, PEP-PTM-366, Sept. 1981.
6. R.J. Holt, "Polarized Gas Targets in Electron Rings," CEBAF Workshop, June 1984.
7. J.M. Paterson, Proc. XI-th Int'l. Conf. on High Energy Accelerators, CERN, July 1980; J.R. Rees, IEEE Trans. Nucl. Sci. NS-28 (1981) 1989; R.H. Helm *et al.*, IEEE Trans. Nucl. Sci. NS-30 (1983) 2001.
8. E. Courant and H. Snyder, Ann. Phys. 3 (1958) 1.
9. M. Sands, "The Physics of Electron Storage Rings – An Introduction," SLAC-121, 1970.
10. C. Pellegrini, Lectures at Varenna Summer School, June 15-30, 1969.
11. R. Gram and P. Morton, "Advantages of Second Harmonic RF Cavities," SLAC-TN-30, Dec. 1967; A. Hofmann and S. Myers, "Beam Dynamics in a Double RF System," XI-th Int'l. Conf. on High Energy Accelerators, CERN, July 1980.
12. J.M. Paterson, J.R. Rees and H. Wiedemann, PEP-Note-125 (1975); W. Brunk, G. Fischer and J. Spencer, IEEE Nucl. Sci. 26 (1979) 3860.
13. See for example: H. Wiedemann, SLAC-PUB-2320, 1979.
14. J.E. Augustin *et al.*, VII-th Int'l. Conf. on High Energy Accelerators, Vol. 2 (1969) 113.
15. B. Rossi, "High Energy Particles," Prentice Hall, Inc. (1952).
16. M. Donald, L. Rivkin and A. Hofmann, "Low Emittance Configuration for PEP," PEP-PTM-257, Oct. 1985.
17. Y. Cho *et al.*, "Conceptual Design of the Argonne 6 GeV Synchrotron Light Source," IEEE Trans. Nucl. Sci. NS-32 (1985) 3383.
18. A. Hofmann, Private Communication.
19. P.B. Wilson, "Stored Current in PEP Using the Measured Ring Impedance," PEP-PTM-216, March 1980; K.L.F. Bane, "RIPPLES," PEP-PTM-125, Nov. 1975.
20. P.B. Wilson and L. Rivkin, "Threshold Current for the Transverse Single-Bunch Instability in PEP," PEP-NOTE-374, Aug. 1982; R.D. Ruth, "Single Bunch Instabilities in an SSC".
21. P.L. Morton and PEP Group, "Correlation Between Experimental and Theoretical Results for the Fast Head-Tail Instability in PEP," SLAC-PUB-3175, July 1983.
22. M. Donald and D. Helm, private communication.
23. R.G. Milner, R.D. McKeown and C.E. Woodward, "Study of Spin Relaxation by a Charged Particle Beam in a Polarized ^{3}He Gas Target," Nucl. Instrum. Methods, to be published.
24. J.E. Spencer, "Harmonic Strengths of the PEP Dipoles and Some Related Effects and Lessons," PEP-PTM-367, Sept. 1981.

Polarized Electrons for Internal Target Experiments

Blaine E. Norum
Department of Physics
University of Virginia
Charlottesville, VA 22901

Abstract

Stated briefly, the problem is to maintain polarized electrons in a storage ring such that at a particular point in the ring the direction of polarization is parallel to the beam momentum. At other points in the ring the polarization must be oriented to ensure that the magnitude of the polarization of the stored electrons is maintained at as high a level as possible. Possible solutions for the PEP storage ring and the proposed MIT-Bates storage ring will be discussed.

Introduction

Two basic processes must be considered in order to understand the behavior of electron polarization in a storage ring. First, the evolution of the electron spin vector in the presence of a magnetic field $\vec{B}$, is described by the Bargmann-Michel-Telegdi[1] (BMT) equation:

$$\dot{\hat{s}} = \hat{s} \times \left[\frac{e}{\gamma m_e} \right] \left[(1 + a\gamma) \vec{B}_t + (1 + a) \vec{B}_l \right]$$

where: e is the electron charge,

g is the electron energy divided by its rest mass,

$a = (g-2)/2 = 0.00116$ and g is the electron gyromagnetic ratio, and

$B_t(B_l)$ = is the component of $\vec{B}$ perpendicular (parallel) to the electron momentum $\vec{p}$.

The corresponding equation of motion for the electron is:

$$\dot{\hat{p}} = \hat{p} \times \left[\frac{e}{\gamma m_e} \right]$$

Thus, an axial field does not affect the momentum but does produce a precession of the spin about the momentum, $\vec{p}$. The angle of precession is given by:

$$\theta_s[\text{rad}] = \frac{0.30}{E[\text{GeV}]} B_l L[\text{T-m}]$$

where L is the length of the trajectory in the field $\vec{B}$

A transverse field affects not only the spin, but also the momentum:

$$\frac{d}{dt} \left[\hat{s} \cdot \hat{p} \right] = \left[\frac{ea}{m_e} \right] \hat{s} \cdot \hat{p} \times \vec{B}_t$$

Thus, the spin precesses about $\vec{B}_t$. The magnitude of the precession is given by:

$$\theta_s = 2.27\ E[\text{GeV}]\ \theta_B = \frac{E[\text{GeV}]}{0.44065}\ \theta_B$$

where θ_s is the angle between the spin and the momentum and θ_B is the angle through which the electron is deflected. Note that an electron with an energy of n x 0.44065 GeV will have its spin aligned in the same direction after each time it is bent through 360°. For electrons with any other energy, the spins will be pointing in some other direction after deflection through 360°.

The second phenomenon which must be considered is that of radiative polarization.[2] Asymmetry in the polarization of the synchrotron radiation emitted by an electron as it is deflected tends to make the electron spins align themselves with the deflecting field. In the case of a storage ring where the guide field is vertical this effect causes a buildup of the polarization in the vertical direction. The asymmetry in the radiation is relatively small, so this process does not lead to unit polarization. Rather, in an ideal storage ring where the circulating electrons encounter only vertical fields the maximum attainable polarization is 92.4%.

Radiative polarization has been observed in electron storage rings at Orsay, Novosibirsk (VEPP-2, VEPP-4), SLAC (SPEAR), Cornell (CESR), and DESY (PETRA).[3] An important observation to be drawn from the SPEAR results in particular is that the observed polarization properties were very accurately described using matrix methods (a la TRANSPORT) developed by A. Chao.[4] Subsequent refinements and improvements of the methods give one confidence that

these effects can be accurately computed.[5)]

The development of the polarization is generally slow, approaching its limiting value P_0 exponentially:

$$P(t) = P_0 \{ 1 - \exp(t/\tau_p) \}$$

where the time constant τ_p is given approximately by:

$$\tau_p[s] = 16 \times \frac{C[m]\ \rho[m]^2}{E[GeV]^5}$$

where C is the circumference and ρ is the magnetic radius. Clearly, these times are strongly energy-dependant. Table I contains representative polarization times for several electron storage rings being considered for use with internal targets by the nuclear physics community. The storage times that one may hope for are at most a few hours, so it is readily apparent that radiative effects may be of concern only at PEP.

TABLE I

Radiative Polarization Rates

PEP:		
$\tau_p = 1.2 \times 10^5$ s	$\simeq$ 34 h	6 GeV
$= 9.5 \times 10^3$ s	$\simeq$ 3 h	10 GeV
$= 1.8 \times 10^3$ s	$\simeq$ 30 m	14 GeV
$= 5.0 \times 10^2$ s	$\simeq$ 8 m	18 GeV
MIT-Bates:		
$\tau_p = 1.6 \times 10^7$ s	$\simeq$ 6 m	0.5 GeV
$= 5.1 \times 10^5$ s	$\simeq$ 6 d	1.0 GeV
Saskatchewan Accelerator Laboratory:		
$\tau_p = 1.8 \times 10^8$ s	$\simeq$ 5 y	0.1 GeV
$= 7.2 \times 10^5$ s	$\simeq$ 8 d	0.3 GeV

The absence of significant radiative polarization at MIT-Bates and Saskatchewan dictates that the beam injected into these storage rings must be polarized. Since there are no immediate plans to install a polarized electron source at Saskatchewan, further discussion will be limited to the proposed MIT-Bates storage ring and the PEP storage ring.

The situation at PEP is more complicated than at MIT-Bates (see Figure 1). At the lowest energies (below 6 GeV) the polarization time is long compared to anticipated storage times so radiative polarization effect can be ignored. At higher energies τ_p is sufficiently short that radiative polarization will cause a buildup of polarization parallel to the vertical guide field over times comparable to the storage times. Above about 12-14 GeV the rate is fast enough to be useful as a means of obtaining polarized electrons; below, it is not. Consequently, as at MIT-Bates the injection of polarized electrons will be required.

The existence of a dynamic mechanism forcing the polarization into the vertical direction suggests that it would be desirable to keep the polarization oriented vertically throughout most of the ring and to rotate it into the horizontal direction just before the internal target and to rotate it back into the vertical direction just after. In this way, the radiative polarization can be useful in either enhancing the polarization of the injected beam or, at least, in helping to compensate for the loss of polarization due to other mechanisms. Various techniques of rotating the spins will be discussed.

Depolarization

Any process which causes the electron spins to point in a direction other than the desired one constitutes a depolarizing effect. These effects can be divided into two groups: non-resonant and resonant.

In the non-resonant group two effects are of major importance, one which does not involve radiation and one which does. However, both arise from imperfections and misalignments of the elements of the storage ring. In a real ring the guide field encountered by each electron is not uniformly oriented vertically. Even particles near the nominal orbit experience a random sequence of (hopefully small) vertical and horizontal fields. Consequently, their spins will precess differently and, after a large number of revolutions of the machine, may point in significantly different directions. This "diffusion" of the spins sets a limit on the ability of a ring operating at energies at which radiative effects play no role to maintain polarization.

Under conditions when radiative effects do play a role, the small "kicks" due to field irregularities play an added role. When an electron undergoes a kick it radiates and tends to align its spin along the field generating the kick. Consider the case where the nominal polarization direction is vertical. Horizontal kicks are generally not a serious problem in this regard; since the ring has a closed orbit the sum of the spurious leftward deflections must equal the sum of the rightward ones. If radiation emitted during the rightward deflections tends to polarize the beam upward

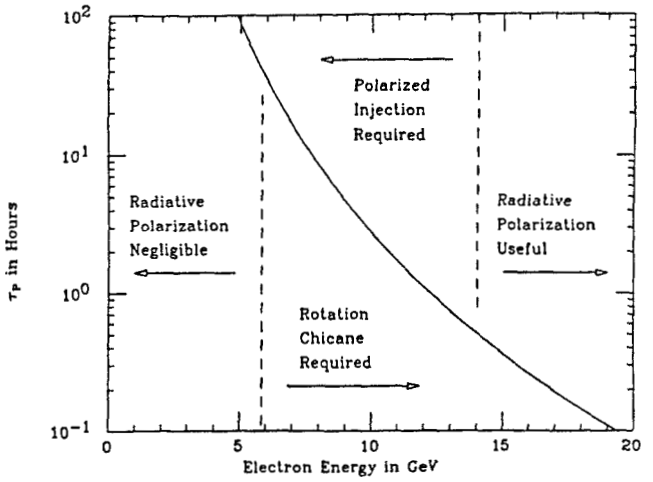

Figure 1.
Polarization Time in PEP

then that during the leftward kicks will tend to polarize it downward and the two effects will (roughly) cancel. On the other hand, vertical kicks arising from horizontal fields are particularly destructive. When an electron is deflected in the vertical plane it radiates and tends to orient its spin in the horizontal direction, to the left or the right. Either way, it generates a loss in vertical polarization.

Figure 2 (taken from Reference 6) shows the results of a calculation of the asymptotic polarization (P_0) in PEP as a function of electron energy. Note that for no energy does value of P_0 reach the ideal value of 92.4%.

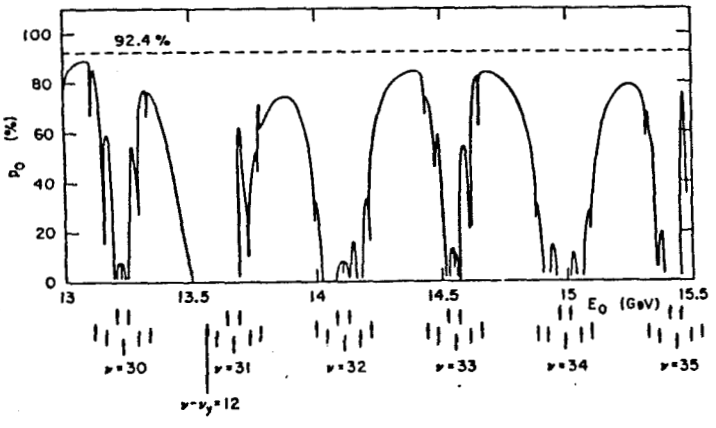

Figure 2.
Asymptotic Polarization in PEP

Resonant depolarization occurs when the rate of precession of the spins as the electron circles the ring is in resonance with the rate of other motions of the electron. The condition defining the three strongest and most damaging resonances is:

$$\left(\frac{g-2}{2}\right)\gamma = \nu + n_y\nu_y + n_s\nu_s$$

where ν, n_y, and n_s are integers and ν_y and ν_s are the vertical betatron tune and synchrotron tune respectively. The term ν corresponds to an "imperfection" resonance which depends only upon the energy of the stored beam. It occurs whenever:

$$E_r = n \times 0.44065 \text{ GeV}$$

Note in Fig. 2 the zeroes in the polarization whenever this condition is satisfied.

The term containing n_y corresponds to an "intrinsic" resonance whereby the precession of the electron spins couples to the vertical betatron oscillations. Similarly, the term containing n_s corresponds to a "synchrotron" resonance. Both of these resonances can be avoided by varying the tunes of the ring.

The depolarizing effects presented here do not preclude the storage of polarized electrons but they do provide a stringent set of constraints to be satisfied by any possible solution.

Possible Solutions

Resonant Energies

The simplest solution is to operate a planar ring at energies $E_r = n \times 0.44065$ GeV. At these energies, an electron with a properly aligned longitudinal spin on one pass will have the spin similarly aligned on subsequent passes. However, first electrons with slightly different energies will have their spins diverge from the nominal on successive passes since the required condition is not met. Moreover, these energies correspond to conditions for the imperfection resonance discussed earlier. Hence, their use is not viable.

Siberian Snake of the First Kind

First suggested by Ya. Derbenev and A.M. Kondratenko in 1976,[7] the Siberian Snake will, in principle, enable a storage ring to store longitudinally polarized electrons of any energy. In particular, a first order calculation shows it to be extremely stable with respect to deviations in the electron energy; the degree to which the polarization is maintained in the longitudinal direction (at the target) is proportional to

only fourth and higher powers of the energy deviation.

The basic concept is illustrated in Figure 3. A solenoid which precesses the spin of an electron with an energy E_0 through 180° about the electron momentum is placed opposite the target. An electron of energy E_0 which is longitudinally polarized at the target will be pointed in a direction ϕ (a function of E_0) at the solenoid. After the solenoid it will be at the same angle but on the other side of the momentum direction. The ensuing 180° bend will return it to the longitudinal direction at the target.

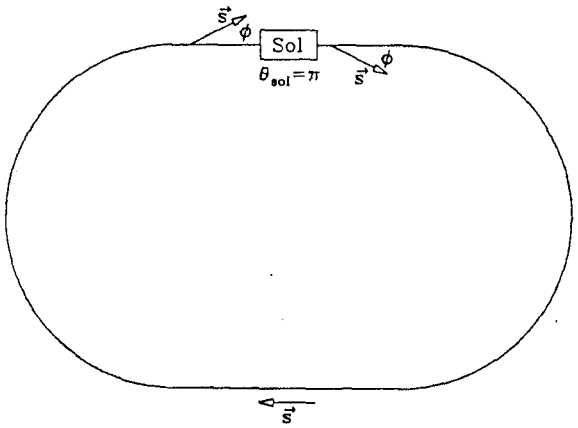

Figure 3.
Siberian Snake of the First Kind

A ring with a Siberian Snake operates, essentially, atop an imperfection resonance. However, the solenoid stabilizes it against perturbations. For example, assume that an electron receives a vertical kick such that its spin has a +y component when it reaches the solenoid. The 180° precession results in a -y component of equal magnitude. When the electron receives the vertical kick on the next revolution it cancels this -y component.

The nominal direction of the polarization in the Siberian Snake is always in the horizontal plane. As a result, it is ill-suited for use under conditions where radiative polarization plays a significant role. However, for the MIT-Bates application this would not pose a problem.

Another problem is that the scheme requires solenoids of very high fields. These introduce strong focussing and coupling between the horizontal and vertical betatron oscillations. Stringent demands are thus placed on both the tuning and dispersion control in ring.

A version of the Snake which avoids the problem of the solenoid can be constructed using an alternating sequence of horizontal and vertical bends to achieve the 180° precession. The severe problem with this scheme is that a given sequence of dipoles would provide the correct precession for only one energy. Thus, to operate the ring at different energies would involve physically reconfiguring the machine, clearly not an attractive prospect.

Siberian Snake of the Second Kind

A scheme similar to the previous one can be constructed using a 180° precession about not the momentum direction but about the horizontal direction perpendicular to the momentum (see Figure 4). However, this precession can only be achieved using a sequence of horizontal and vertical bends so the scheme suffers from the same flaw discussed above.

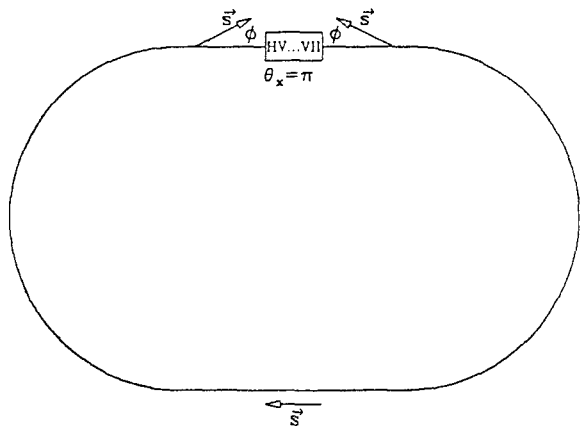

Figure 4.
Siberian Snake of the Second Kind

Figure 8

This novel solution to the problem can be considered a rather gross distortion of the Siberian Snake. Instead of precessing the spin on the side opposite the target so that the effect of the second 180° bend cancels the effect of the first, the direction of the second bend is reversed to achieve the same result (see Figure 5). The scheme has the dual advantages of working for all energies and of not requiring strong solenoids.

Unfortunately, it also has severe problems. First, its shape makes it useless as a scheme for retrofitting PEP; similarly, its shape makes it inappropriate for use

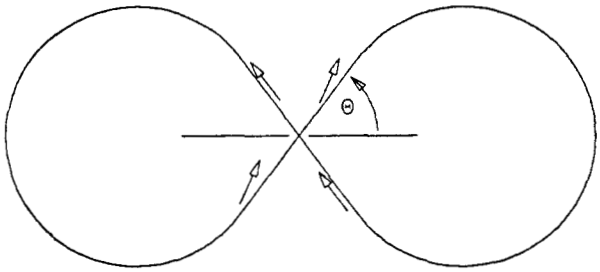

Figure 5.
Figure 8 Scheme

as a pulse stretcher which is to be the primary function of the proposed MIT-Bates ring. Moreover, like the original Siberian Snake it essentially operates atop an imperfection resonance but unlike the Siberian Snake it is a purely planar scheme. Consequently, it has no "restoring force" to control vertical excursions of the spin. The beam would therefore depolarize rapidly due to vertical kicks caused by extraneous horizontal magnetic fields.

Resonant Snake

Since the Siberian Snake already operates by construction atop an imperfection resonance, little harm is done by operating at a resonance energy (E_r = n x 0.44065 GeV). In these cases it has been shown[8] that a much weaker solenoid will suffice to maintain the polarization. For the first resonant energy, 0.44065 GeV, a solenoid capable of precessing the spin through only 5° is sufficient to maintain the polarization at the target within 1% of the stored beam polarization (for a beam with an energy spread of 10^{-3}). For the second resonant energy it still requires only a precession angle of 10° (see Figure 6).

For higher energies the required precession angle grows rapidly (45° for E_r = 3.965 GeV) until the scheme has no significant advantages over the regular Siberian Snake. It also retains the weakness of the Siberian Snake with regards radiative polarization. As a result, it is a useful possibility for the MIT-Bates storage ring but not for PEP.

When considering schemes which are useful when radiative polarization plays a role one is inexorably drawn toward the schemes wherein the spin is maintained parallel to the (vertical) guide field as much as possible. By so doing, the radiative effects in a large

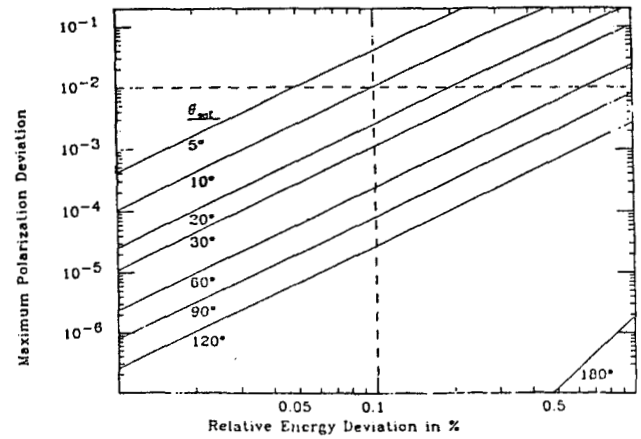

Figure 6.
Resonant Snake

part of the ring help to increase the polarization rather than decrease it. Only near the region of the target are the spins precessed into the longitudinal direction and then back into the vertical. The schemes to be considered now differ only in the technique used to perform these rotations.

Richter-Schwitters (R-S) Scheme

The scheme originally proposed in conceptual form by R. Schwitters and B. Richter[9] has two striking advantages. First, it has the spins aligned vertically throughout most of the ring. Second, it involves only bends in a single plane. Conceptually, it consists of a series of vertical bends inserted into a straight section of an otherwise planar ring (see Figure 7). The electrons are deflected first up then down so they approach the target at an angle θ to the horizontal. A mirror image sequence returns the electrons to the ring midplane and their spins to the vertical direction.

The shortcoming of this method is that it works exactly for only one energy or, more precisely, one energy modulo 0.44065 GeV x $2\pi/\theta$. For any reasonable value of θ, this means a single energy. This is however not such a serious problem as the system is stable for a broad range of energies. The only loss in operating at an energy different from the nominal design energy is that the degree of longitudal polarization at the target is reduced relative to polarization of the stored beam by a factor T given by:

$$T = \sin\left(\frac{E}{E0} \times \frac{\pi}{2}\right)$$

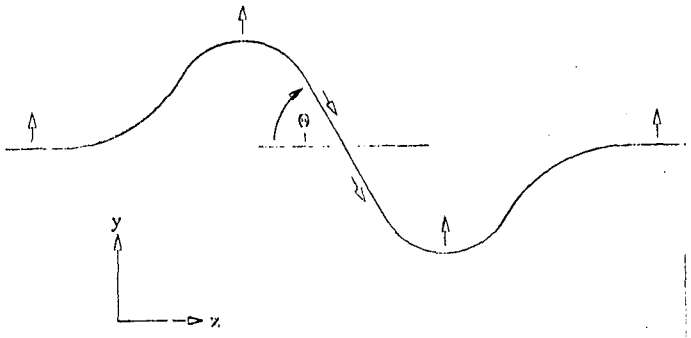

Figure 7.
Richter-Schwitters Scheme

where E0 is the nominal design energy. In the case of PEP a scheme with a nominal design energy of 10 GeV would have $\theta \simeq 4^{\circ}$ and T would exceed 0.8 for all energies between 6 GeV and 14 GeV.

A remaining shortcoming of this design is the large number of magnets that are required in the area of the target. These would severely limit the space available for detectors. A simplified version of the scheme that would involve fewer magnets would have the shape of an inverted V. The beam would simply be bent upwards through an angle $+\theta$ as before and the target would be placed in the sloped straight section. After the target an angle of -2θ would direct the beam back down to the ring midplane where a second bend of $+\theta$ would return it to the horizontal direction.

Solenoid Spin Rotator

Another way[10] of precessing a vertical spin into the longitudinal direction is first to precess it into the horizontal direction perpendicular to the beam and then precess it into the longitudinal direction by passing it through a horizontally bending dipole (see Figure 8, taken from Ref. 10). A mirror image system located after the target returns the spin to the vertical direction.

The system has the same shortcomings as the R-S scheme in that it works ideally only at one energy. Moreover, it requires two very strong solenoids, the combined strength of which equals that required by a Siberian Snake at the same energy. On the positive side, the energy limitation of the R-S scheme was seen to be minimal. Furthermore, the angle through which the electrons are bent while their spins are not parallel to the guide field is half that of the R-S scheme (for the same nominal energy E0) so the resultant depolarizing effects are reduced by a factor of two.

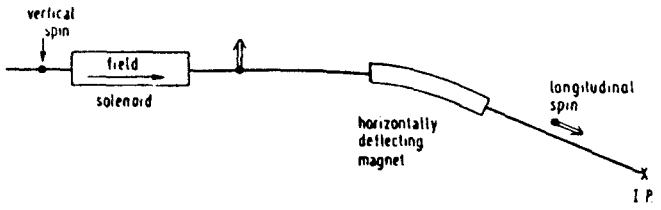

Figure 8.
Solenoid Spin Rotator

Applying this scheme to PEP would require modifications to the main lattice, not just the (straight) insertion where the target would be located. A straight section long enough to accomodate the requisite solenoid and associated quadrupoles would be needed prior to the last two dipoles before the insertion. The beam line in the insertion would therefore be parallel to the present beam line, but would be displaced outwards.

It is an idea which merits serious study.

Mini-Rotator

In 1983 K. Steffen proposed[11] a scheme for the HERA storage ring which would precess the electron spins from the vertical to the longitudinal (and back) by means of a series of small horizontal and vertical bends. The scheme has several promising features, among them the fact that no strong solenoids are required. However, it suffers from a narrow energy acceptance which can be improved only by repositioning magnets. Furthermore, compared to the R-S or Solenoid Rotator schemes electrons in this scheme pass through significantly more magnetic field wherein their spins are not aligned parallel to that field. This increases the rate of radiative depolarization. Similarly, for energies other htan the nominal energy the equilibrium direction for the spins in the main ring magnets is not quite vertical; this also increases the rate of depolarization. It was for these latter reasons that work on the Solenoid Rotators was initially pursued.

Conclusions

The problem of obtaining longitudinally polarized electrons in the proposed MIT-Bates ring and in PEP appears solvable; not easy, but solvable. In the case of the MIT-Bates ring a Siberian Snake or a derivative such as the Resonant Snake appear to be viable

alternatives. In the case of PEP, the R-S Scheme, the Solenoid Rotator, and the Mini Rotator all appear possible. Each has its stengths and should be pursued to determine the costs and limitations.

Finally, I would like to point out that with the possible exception of the highest energies possible at PEP, the degree of polarization that will be possible is limited to that of the injected beam. Consequently, it is of equal importance that attempts be made to increase the polarization obtainable from the sources used in the linac injectors.

References

1) V. Bargmann, L. Michel, and V.L. Telegdi, Phys. Rev. Lett. 2 (1959) 435.
2) A.A. Sokolov and I.M. Ternov, Sov. Phys. Dokl. 8 (1964) 1203.
3) R. Schwitters, Proc. of Workshop on Polarized Electron Acceleration and Storage, Hamburg, West Germany (1982).
4) A. Chao, Nucl. Instrum. Meth. 180 (1981) 29.
5) J. Kewisch, DESY Report 83-32 (1983).
6) A.W. Chao, PEP Report 263 (1978).
7) Ya.S. Derbenev and A.M. Kondratenko, Novosibirsk Preprint 76-84 (1976).
8) B.E. Norum, Longitudinally Polarized Electrons for Internal Target Experiments, CEBAF Report (1984).
9) R. Schwitters and B. Richter, PEP Note 87 (1974).
10) D.P. Barber et al., DESY Report 84-102 (1984).
11) K. Steffen, DESY Report PET 78/11 (1978).

USE OF INTERNAL TARGETS AT THE PROPOSED MIT/BATES RING

J. B. Flanz and the Bates Staff
MIT-Bates Linear Accelerator Center
Middleton, Massachusetts 01949

Introduction

The construction of a ring at the MIT/Bates Accelerator Center has been proposed since 1984. It would operate as a Pulse Stretcher Ring (PSR), providing near CW electron beams of up to 1 GeV to the existing experimental apparatus at Bates. The proposal also includes a unique facility for conducting experiments using internal targets (IT). The present layout of Bates is shown in Fig. 1. The machine, as shown, produces a beam whose quality is summarized by the parameters in Table I. The laboratory currently supports three experimental halls with five main beam lines. On the "B" line exists three spectrometers with characteristics that make them well suited for coincidence measurements [1]. However, at present as listed in Table I, the duty factor available is limited to one percent. the proposed additions to the laboratory are shown in Fig. 2. The pulsed beam from the accelerator would be injected into the ring in a short straight section on the right side. The CW beam would be extracted from the upper long straight section. Also included is an energy compressor system to reduce the effective energy spread of the beam. The resulting beam parameters after the proposed additions are also summarized in Table I.

An experimental hall is provided for internal target experiments on the lower long straight section. The internal target hall is currently envisioned as being 12.2 m x 15.25 m (40' x 50'). There appears to be sufficient room in the ring for optical inserts that may be useful for internal target experiments. It is workshops such as this one that are important for defining the detailed requirements of such a facility. In fact, we hope to obtain from this meeting a better feeling for the needs of an IT hall and the possible optical inserts that may be useful.

TABLE I

BATES BEAM PARAMETERS
FOR PROPOSED UPGRADE

		Single Pass	Simultaneous Recirculation	Head-Tail Recirculation
Energy	(MeV)	50-540	400-1060	400-1060
Peak I	(mA)	< 40	< 5	< 40
Average I	(μA)	< 100	< 100	< 100
Pulse Width	(μS)	< 20	< 20	2.6
PPS	(Hz)	< 1000	< 1000	< 1000
Duty	(%)	< 1	< 1	< 0.26/85
ΔE/E	(%)	< 0.3/.04	< 0.3/.04	< 0.6/.04
Δφ	(Deg)	3°/45°	3°/45°	/45°
ε/π	(mm mr)	10/γ	10/γ	30/γ

Beam Properties

The beam quality available from the Bates Linac is important in the consideration of the possible experiments that might be undertaken. Both the transverse and longitudinal phase space are very small, especially for a pulse machine. In normal operation, the longitudinal phase space is characterized by a 3° bunch width and is contained within 0.3% in energy spread. The transverse phase space is, for example, .01π mm-mr at 500 MeV. This allows sub millimeter beam size with reasonable strength quads at reasonable distances from a target. In this way, the monochromatic spot size at the target of the energy loss spectrometer has enabled the spectrometer to resolve better than 5×10^{-5} in energy.

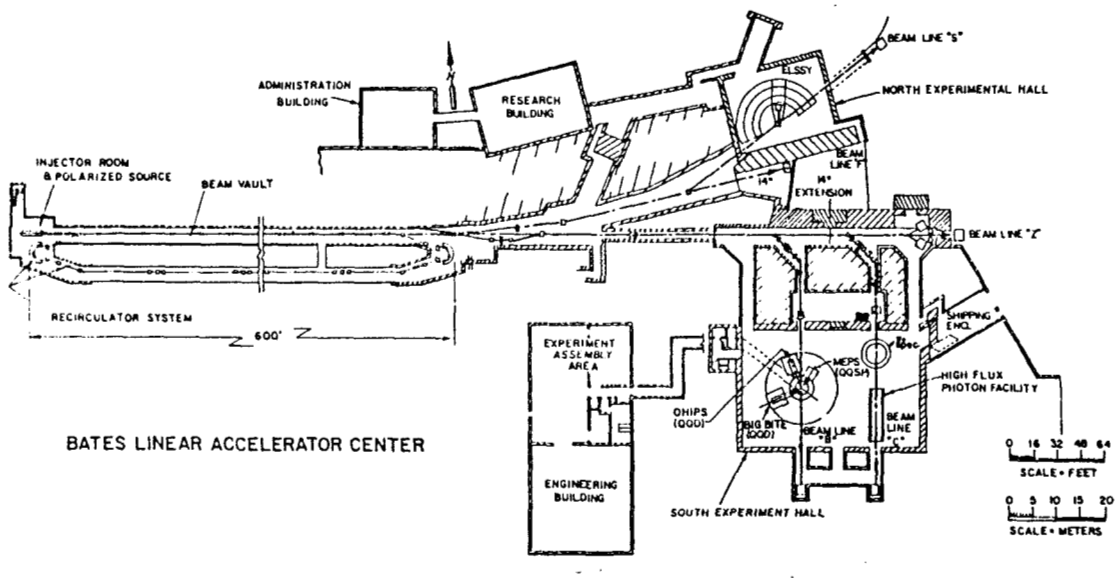

BATES LINEAR ACCELERATOR CENTER

Figure 1

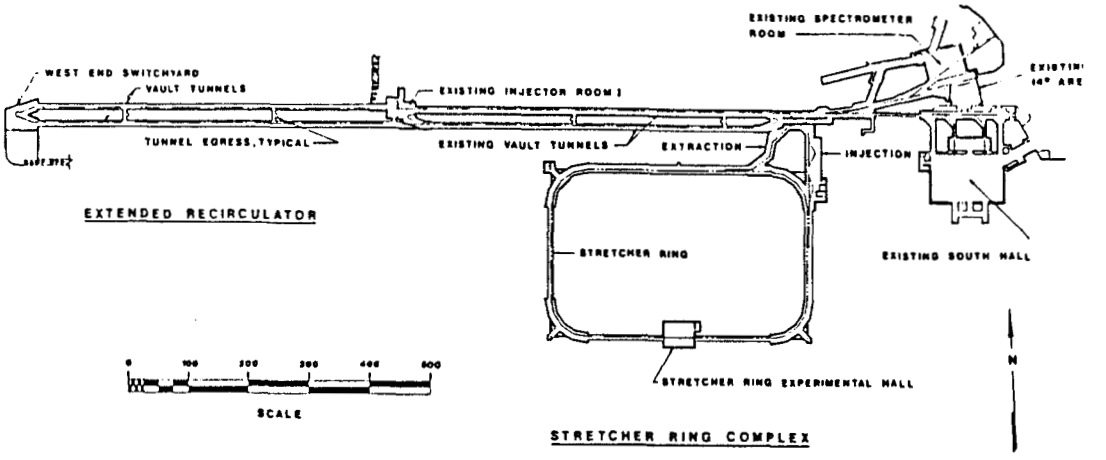

PLAN AT BEAM ELEVATION

Figure 2 Bates Linear Accelerator Center CW upgrade facilities plan.

The spacial stability of the beam is another contribution to the effective transverse emittance. Measurements have shown the beam jitter to be less than 0.2 mm rms (locked to 60 Hz) at a position where the beam size is near 1 mm (equivalent to a beta of approximately 30 m).

The Linac energy has been increased over the past few years by a variety of methods, and is continuing to be upgraded. First, a recirculation system was installed to nearly double the single pass energy by sending the beam through the accelerator twice. This system can be seen in Fig. 1. The design constraints included maintaining the 1% duty capability of the accelerator and, therefore, required long pulse simultaneous recirculation. For optical reasons, this limits the peak current (while recirculating) to less than 5 mA. In order to quickly fill a ring with electrons, it is helpful to maximize the peak current and minimize the pulse length. Therefore, 40 mA will be accelerated. Recirculation will be done in the head-to-tail scheme with an extended recirculator so that the pulse length will be 2.6 μsec. The turns of injection into the 1.3 μsec ring will provide 80 mA of circulating current, and 100 μA of extracted current at a 1 KHz cycling rate. Preliminary tests of the head-to-tail recirculation method with 40 mA of peak current were successfully conducted. An increase in both the longitudinal and transverse phase space was observed. There was no attempt to adjust the source parameters at this increase current operation. Therefore, for the purposes of the proposed ring, we assume a beam with 0.6% energy spread injected into the energy compressor and approximately double the usual transverse emittance.

The second method used to increase the energy has been the addition of a sixth modulator system, thus bringing the RF equipment complement up to that requested in the original proposal for the construction of Bates. Finally, the klystron power will be increased in the near future from 4 MW peak to over 5 MW peak to allow a recirculated beam energy up to 1 GeV.

The proposed facility includes an energy compression system (ECS). This will trade the longitudinal phase extent for energy spread. Given the small phase width, a factor of 15 can be expected in the energy spread reduction or a final energy spread of .04%. The University of Saskatoon accelerator has already demonstrated an improvement in beam energy spread of over factor of 10 with their new ECS. Other laboratories have enjoyed similar benefits when with such systems.

The "numbers" discussed above are very useful for estimating experiment parameters. However, we are currently investigating the limitations of these "numbers". For example, in principle, the energy spread on the microbunch level, considering only the phase width, should be an order of magnitude smaller than the average energy spread that is measured. The discrepancy could be due to RF fluctuations or ramps whose time constant might be on the order of the beam pulse width. If that is the case, the beam centroid energy can be tagged during an experiment and effectively reduce the beam energy spread and effective spectrometer resolution in the non-dispersion matched spectrometers.

With regard to emittance, measurements of the beam halo are in progress, in collaboration with J. Calarco (UNH) for preparation of a coincidence experiment in the giant resonance region[2]. This experiment requires the use of solid state detectors in the scattering chamber and is very sensitive to background caused by beam halo. Measurements made with the medium energy pion spectrometer (MEPS) of the counting rates for a variety of targets with different hole sizes, as well as empty target frames of different sizes, have been taken.

Although the beam emittance is small, the final focus is not strong (3 mm beam equivalent to a beta of approximately 100 m), and there are small tails which are not measurable during normal emittance measurements which consider only 68% to 90% of the beam. These tails may effect the outcome of the experiment and provide a limit on the beam size, including over 99.9% of the beam, especially if target frames of limiting apertures are used. As seen in Fig. 3, with some tuning one can achieve a situation with 0.8% of the beam outside of a 1 cm hole and less than $.5 \times 10^{-5}$ outside a 4 cm diameter. On the same figure, the fraction of a guassian beam outside a particular radius is also plotted. The difference between the two curves can be considered the beam halo. Better

conditions have also been achieved with more considerable tuning. The above situation is sufficient to allow detection of giant resonance protons and alphas in coincidence with scattered electrons. The detectors were located 20 cm from the beam, and the target frame was 2000 times thicker than the target.

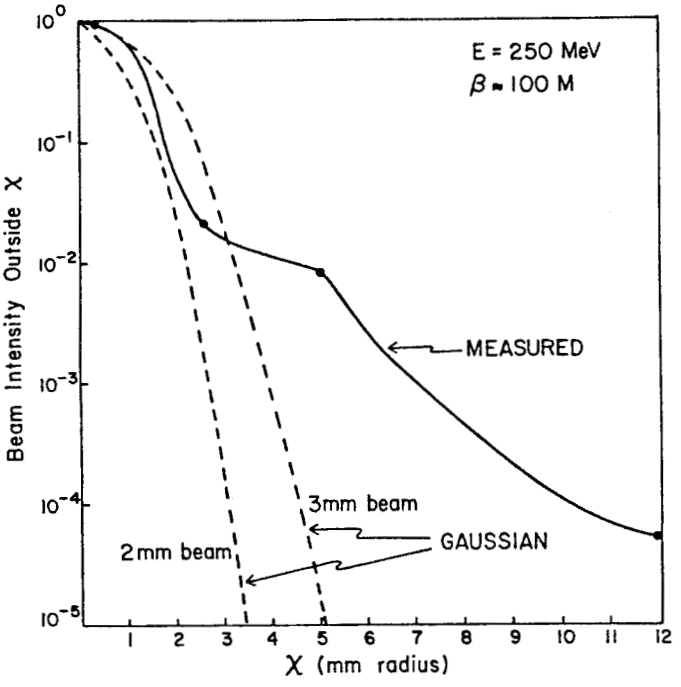

Figure 3. Beam "Halo" Measurements

Ring Description

The layout of the proposed ring lattice is shown in Fig. 4. The basic rectangular shape is made up of four 90° bend regions which are connected by four straight sections. The short sections are 42.3 m long and the two long sections are 92.6 m long. The ring circumference is 390.5 m.

The ring is composed of six basic cell types. These include bend cells (12); FODO cells (7, (5)) on the long straight sections; FODO cells on the short straight sections; matching cells (4) to match the higher beta function of the long straight section to the bend section; an extraction cell (1), to provide a higher than average beta for extraction; and an internal target cell (0, (1)) to provide a lower than average beta for internal target work. The machine functions are shown in Fig. 5 with the dashed line that of an internal target optics cell.

The basic criteria and considerations which affect the design of the PSR are summarized briefly:

- The operating energy range is 300-1060 MeV;
- Two-turn injection is planned which will fill the ring with 80 mA of circulating current;
- The bend cells, in combination with the short straight sections, are designed to be second order achromats with symmetry corrected second order centroid shift aberrations. This ensures that the geometric aberrations can be controlled and the chromaticity of the ring can be adjusted without affecting the desired geometric aberrations.

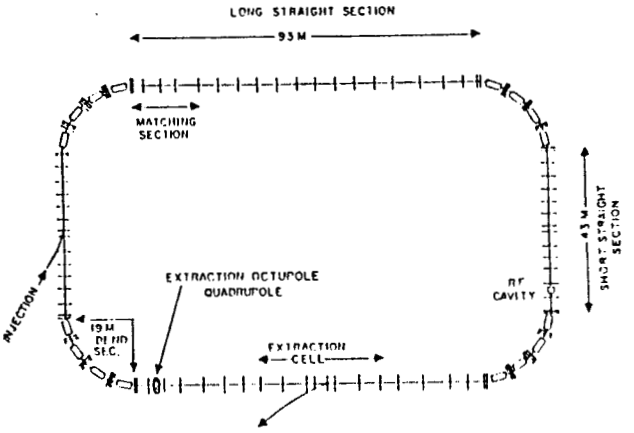

Figure 4. Layout of Pulse Stretcher Ring

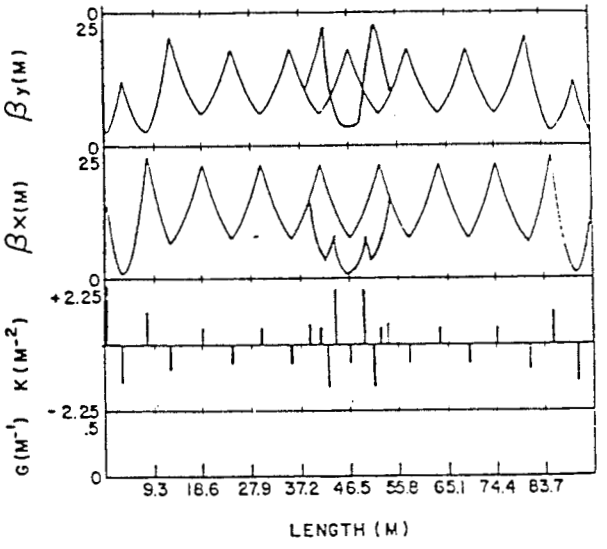

Figure 5. Long Straight Section with Internal Target

- There will be a high beta region (beta = 30 m) for extraction to minimize septum heating and decouple the extraction from the rest of the ring. It also provides a convenient place for providing collimation to clean up the emittance growth when an internal target is placed in the ring.
- An injection beta = 9 m minimizes the injector kicker strength and prevents extracted beam from hitting the injection septum.
- A lower than average beta = 1 m for internal targets will allow for slower emittance growth.
- The bending radius must be large enough to allow linear operation over the dynamic range and synchrotron losses are minimized, along with a minimized synchrotron oscillation period needed for extraction. This minimizes the RF requirements, however, it does increase the damping times.

Table II summarizes some of the interesting ring operating parameters. Given 80 mA of circulating current, the possible luminosity attainable in the proposed ring can be found in Fig. 6 for a range of internal targets.

TABLE II

RING PARAMETERS

Circumference	340.5 m
Length	131.0 m
Width	80.9 m
Bending Radius	9.1 m
Momentum Compaction	0.014
RF (Max)	2R keV @ 2856 MHz (350 sec. between bend)

Energy	250	440	880	1000
Damping Time (Sec)	9.6	1.6	0.196	0.13
Damped Emittance (mm mr)/π	0.0045	0.0147	0.0586	0.0757
Damped Energy Spread (%)	0.007	0.013	0.025	0.029

	Horizontal	Vertical
Tune	Extraction 10.46 Internal ~ 10.2	10.60 10.6
Chromaticity		
Uncorrected	- 16	- 13
Correctable to	0	0

Beta Functions		Min.	Max.	Min.	Max.
Bend	ℓ	3.6	13.9	2.6	6.1
	η	0	3.8		
Extraction Long Straight		1.0	32.0	2.6	20.3
Mini Beta Straight		1.0	13.7	3.6	24.5

Instabilities - Transverse Multi-Bunch ~ 50 msec (.1 mm rms for extraction)
for IT @ ε = 1 - ~ 10^2 - 10^3 msec

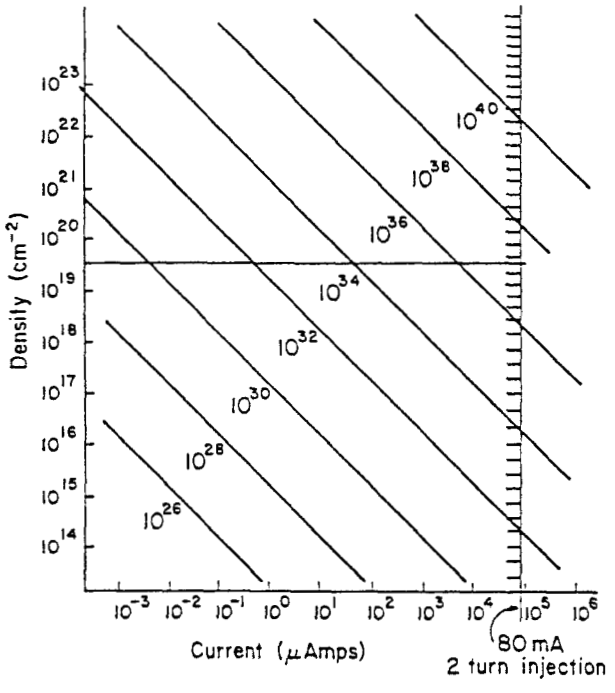

Figure 6. Luminosity in ring as a function of beam current and target density.

Ring Parameters Relevant to Internal Target Use

Vacuum Considerations

There are a few types of targets that have been discussed. They include jet-type targets and bottle targets. The vacuum requirements of the ring include long term storage, as well as an ion density low enough to produce small tune changes over the range of current of ring operation. This vacuum level is on the order of 10^{-9} torr. Consider an internal target in the ring with a density of from 10^{14} to 10^{19} atoms/cm^2. This converts to a local pressure of from 10^{-4} to 10 torr. Table III shows the nearby vacuum assuming differential pumping speeds of 60,000 l/s per chamber and conductance limiters of 1 cm and 5 mm. Note that at least two conductance limiters are needed with these available pumps for the highest target density.

For the case of cluster jet target, pollution of the ring vacuum can come from collisions within the gas, evaporation of the clusters, and evaporation induced by ionization. The approximate total loss can be 10^{-3} of the gas. Assuming thermal velocity and a 1 cm jet thickness, this corresponds to a leakup rate of .1 torr l/sec. This leakup rate also requires a conductance limiter device (at least one, probably two). It may be possible to reduce the vacuum constraints if the storage time is not important. This may be an important tradeoff since it is advantageous to reduce the mass in the region of the internal target.

In Fig. 7, some internal target sources which have been used in rings are compared with the ring vacuum resulting from having introduced these targets.[3] Included on the graph is the region that proposed

TABLE III

IT VACUUM CONSIDERATIONS

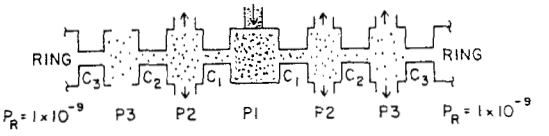

Target cm⁻²	P1 Torr	C1 ℓ/s	P2 Torr	C2 ℓ/s	P3 Torr	C3 ℓ/s	P4 Torr
10^{14}	10^{-4}	4	7(-9)				
10^{19}	10^{1}	4	7(-4)	4	4(-8)	4	< 10^{-9}
10^{14}	10^{-4}	.5	8(-10)				
10^{19}	10^{1}	.5	8(-5)	.5	7(-9)		

Assumptions - 60,000 ℓ/sec pumping capacity each cell
4 ℓ/sec conductance - 1 cm diameter pipe
0.5 ℓ/sec conductance - 0.5 cm diameter pipe

Conclusion - At least one if not two conductance limiters on each side.

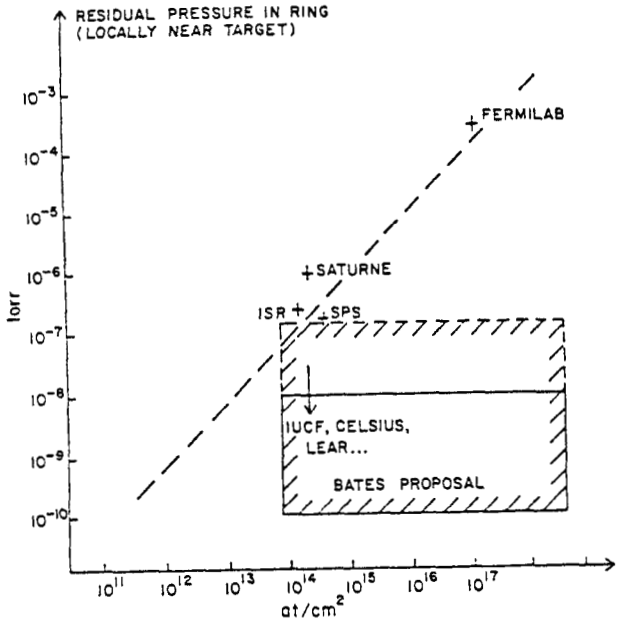

Figure 7. Pressure near IT in ring.

Bates facility hopes to operate. It should be noted that the operational vacuum measurement is near the target and not an average measurement of the entire ring. However, it is also interesting to note that in the estimated leakup, rates are generally an order of magnitude below the actual rates. We will, therefore, assume that there will be at least one 1 cm aperture on each side of the target.

Apertures

The locations in the ring that restrict the nominal aperture include:

1. RF cavity (4 cm diameter)
2. Injection septum (12 mm from closed orbit)
3. Extraction septum (8 mm from closed orbit)
(4. Internal target region target conductance limitation (1 cm diameter))
(5. Other energy and emittance limiting apertures)

The RF cavity aperture is fixed and unchangeable. The septa could be retracted for internal target usage, although it would be nice, once they are adjusted, to allow them to remain untouched. The horizontal phase space contains most of the limiting apertures and optics.

The horizontal phase space coordinates at the internal target location, with the small beta region, are plotted in Fig. 8. Also on Fig. 8 are the projected admittance limitations for the items discussed above. In an expanded view of the phase space, (Fig. 9), various possible circulating beam phase spaces are shown for comparison purposes. The smallest represents one turn of on-axis injection. The largest represents the normal phase space filled for extraction. The intersecting parabolas depict the boundary between stable and unstable oscillation of a particle in the ring. This is used for extracting in the pulse stretching mode. The intermediate case represents two turn injection with a minimum of phase space filled. This is defined by allowing the minimum of room required for the injected beam to cleanly pass by the injection septum.

To safely contain the beam within the ring and enable an internal target experiment, the beam emittance must be contained within some quantity, for example, the admittance. The emittance will grow in most cases, and one must provide a means to catch the

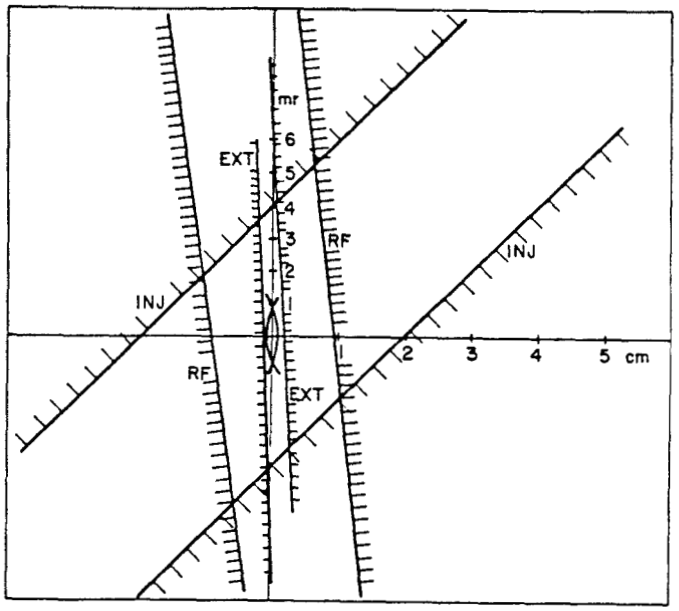

Figure 8. Ring Admittance with restricting apertures

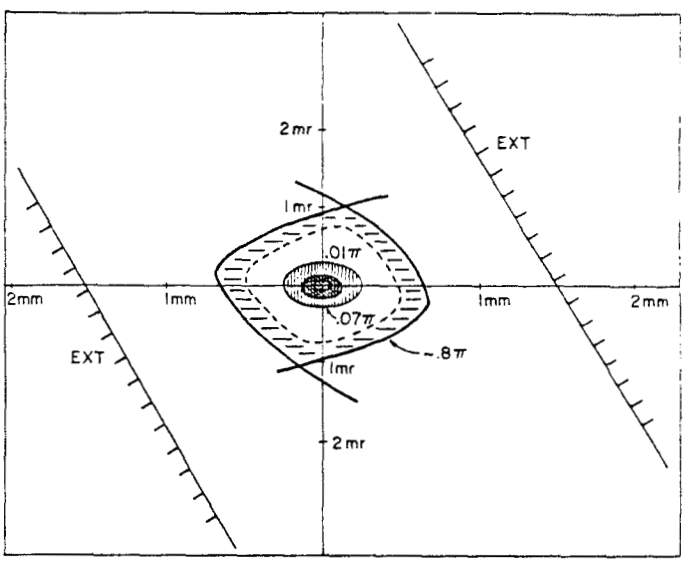

Figure 9. Expanded view of Beam Phase Space and Ring Admittance.

beam that is outside of the acceptible boundaries safely. the most logical place in this ring is at the extraction cell where the beta is 30 m. Therefore, if one wants to restrict the admittance to that defined by the septum, then a collimator of 16 mm diameter is necessary. If the septum is retracted, then the next aperture is the RF, in which case, a collimator of 6 cm diameter would be necessary at the extraction location. Note that collimators in this location maximize the necessary aperture for restricting the admittance. It (they) are also located on the opposite side of the ring from the target.

Operating Conditions

In the most straightforward injection schemes, a pulse of 2.6 (1.3) μsec of 40 mA fills the ring in two (one) turns with 80 (40) mA. this can be repeated as often as every 1 msec. Given this current capability, one can infer from Fig. 6 the luminosity that the ring is capable of providing for internal targets. This beam can be extracted if the phase space at the extraction location is filled as in Fig. 9.

At this time the ring RF will support 80 mA of stored current. If necessary, if would be possible to store more current as in other storage rings, however, that would involve more RF power for this mode. The damping time, important for storing more current, ranges from 130 msec at 1 GeV, to over a second. Thus, filling times will be seconds. The beam would have to be stored long, relative to this, for useful efficiency or the tradeoffs more carefully examined. Even without question of more current than 80 mA, the storage time question is still useful to discuss.

The ring can be filled every msec. To fill less often would save linac power. However, if one is anticipating using the linac pulsed beam elsewhere during that time, beam sharing techniques which allow recovery of machine parameters quickly, when it was time to refill would be necessary. Finally, there is the possibility of parasitic experiments that can run while the beam is being extracted, without damaging the extraction beam.

It is useful to consider some of the mechanisms which affect the beam quality and ultimately determine the experiments which are feasible. This will also yield information on the possible modes of operation of the ring. The mechanisms include the effects of the target on the beam, the effect of the ring on the beam, and the effects of the beam on the target. Some of these are summarized below.

Effects of Target on the Beam

Emittance Growth Mechanisms
- Multiple, single, and plural scattering
- Wakefield effects from target and collimators

Energy Loss Mechanisms
- Bremsstrahlung
- Wakefield effects from target and collimators

Effects of Ring on the Beam

Emittance Affecting Mechanisms
- Damping (antidamping)
- Quantum fluctuations
- Instabilities

Effects of Beam on the Target

- Dissociation
- Depolarization

Consideration of the above mechanisms can be used to establish the operational limits of the various operational modes mentioned above. In particular, the conditions for use of the different modes of operation are summarized below.

Modes and Conditions

Any mode:

a. background manageable
b. sufficient luminosity
c. beam emittance acceptable
d. target density/polarization acceptable

Storage mode (any current):

a. Emittance does not grow beyond detector limitations for i) resolution or ii) track reconstruction. For i), $e < 4\pi$ mm mrad.

b. Emittance does not grow so as to have halo hit target aperture, producing backgrounds. Since the aperture may be 100,000 times thicker than the target, that means that the emittance in this case implies that part of the beam containing more than $1.^{-5}$ of the beam. At $B = 1m$, $e < 0.5\pi$ mm mrad.

c. Emittance does not grow beyond admittance. With extraction septum $e < 4\pi$. Without extraction septum, $e < 40\pi$ mm mrad.

Parasite Mode

a. Emittance does not grow more than 10%

b. Experiment can stand extracted beam tail which contains up to .1% of beam up to a radius of 1 mm.

Beam Loss Mechanisms

Scattering

Of the emittance growth mechanisms discussed above, the most talked about and the most serious is that due to scattering. Maloney, Craft and Williamson, Crannell, and Norum, have all shown that this effect is tolerable over an acceptable range of parameters. There have been three approaches to this subject. Craft and Williamson showed the relationship between passing through an internal target once and many times within a ring, thus allowing analytical calculations based on multiple scattering[4] through a thicker target. This was compared with simulations of a particle traced through a ring undergoing single scattering with each target passage, and the agreement was found to be very good. Crannell used the approximate form for multiple scattering, while Norum used the single scattering form and included damping effects in the ring. To calculate the emittance growth for present Bates design, the approximate form was used, including a factor of .75 which yielded better results for the rms scattering angle agreement with the results of Nigam et al. The calculation also includes the effect of damping in the proposed ring.

Wakefields

Another potentially important effect is the transverse charge dependent kick that is possible when a beam crosses a transition in pipe diameter. In this case, the magnetic field lags behind the electric field caused by the beam image charges. This mismatch causes a transverse force on the beam, proportional to

the charge. This is, therefore, a spread in the angles and an increase in emittance, following Bane and Morton.[5]

The magnitude, and therefore the spread of the force, can be reduced by tapering the edges of the transitions. For the collimators considered, the effect is very small in comparison to the scattering effect, even considering the fact that actual wake forces in rings generally tend to be over an order of magnitude more than expected from calculations.

Figures 10 and 11 show the results for 440 and 880 MeV. With a beta equal to one meter at the internal target region, all reasonable operating conditions listed above are limited to an emittance growth under $1.^{-6}$. It is interesting that for long storage times (seconds), the effect of damping is important. Figures 12 and 13 compare the effects of long storage times with and without damping.

The horizontal lines on Figs. 10-13 represent the limits imposed by the constraints discussed above for the different modes of operation. By noting the time it takes to reach those lines, the plot of storage times in Fig. 14 can be formed. Each line in Fig. 14 represents a different condition as described earlier.

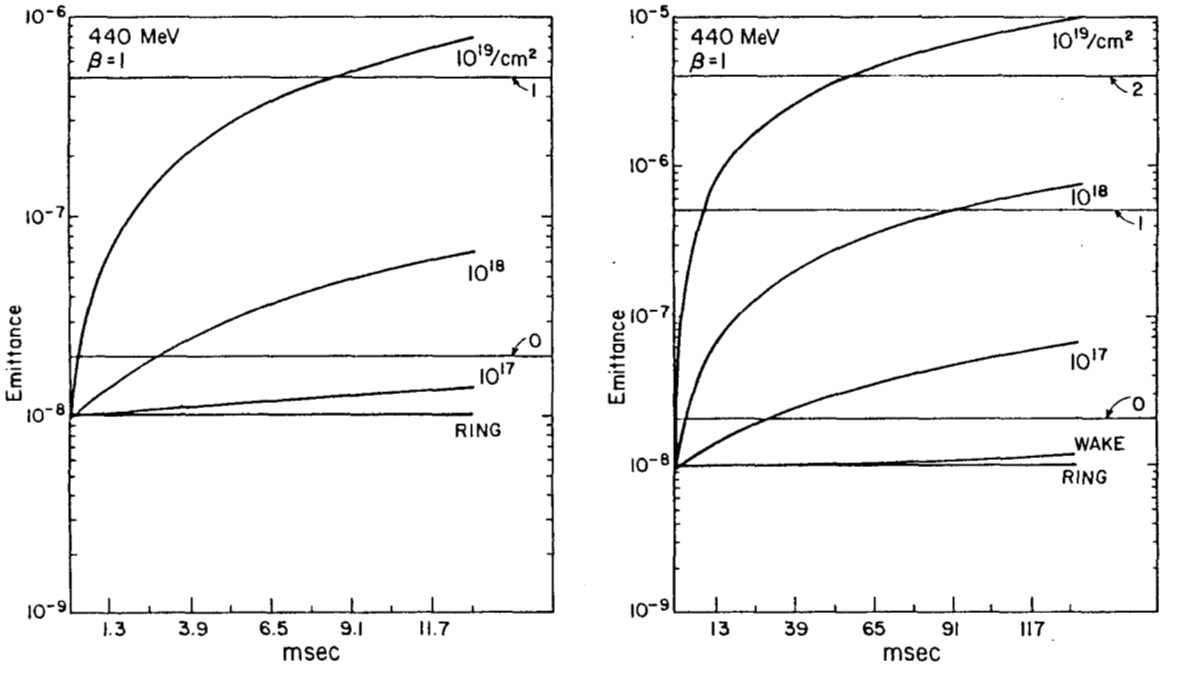

Figure 10. Emittance growth with different target thicknesses of a 440 MeV beam during the above two time scales.

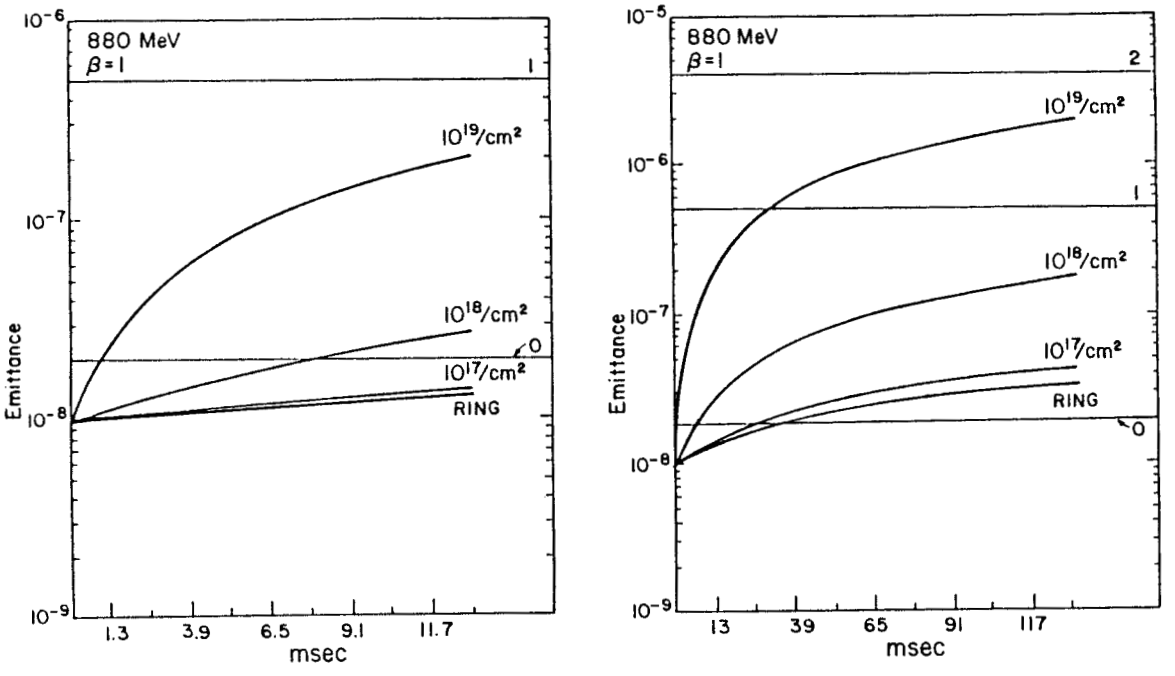

Figure 11. Emittance growth with different target thicknesses of a 880 MeV beam during the above two time scales.

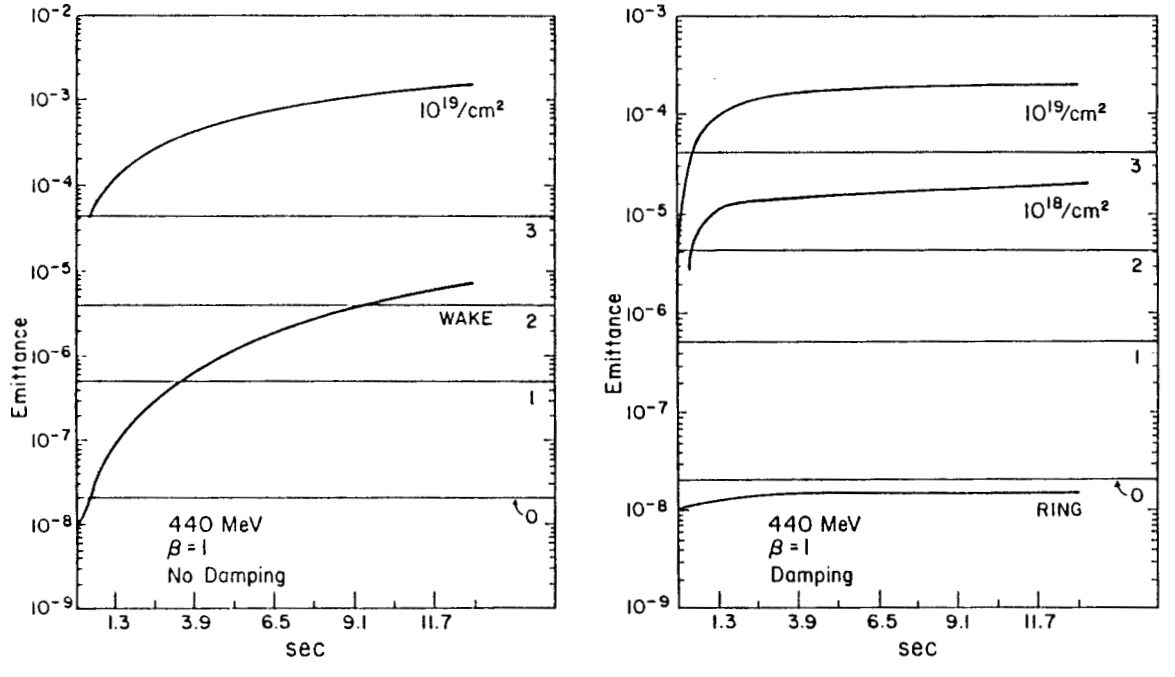

Figure 12. Emittance growth over a long time scale comparing the effects of damping with that when no damping is included for a 440 MeV beam.

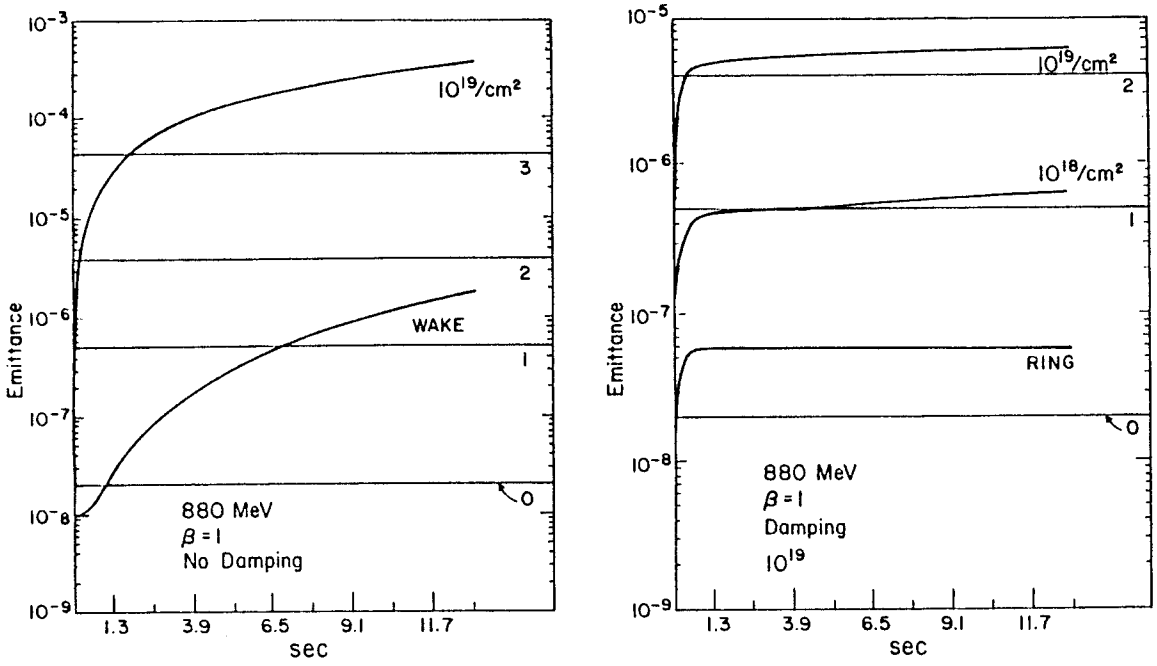

Figure 13. Emittance growth over a long time scale comparing the effects of damping with that when no damping is included for a 880 MeV beam.

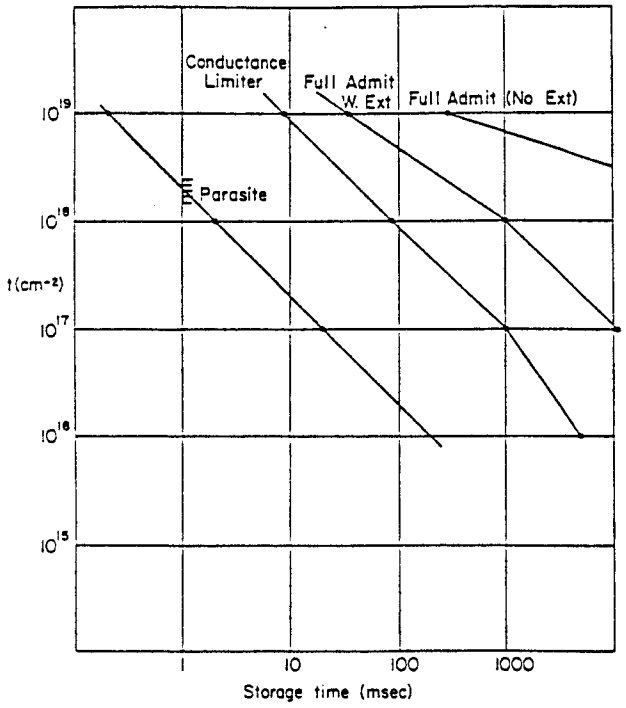

Figure 14. Storage times for different internal target densities and different conditions.

Longitudinal Phase Space

The admittance in longitudinal phase space is restricted by the RF power available. There is room in the RF bucket for 0.08% in energy. This is compared to the expected .04% to be injected. The physical limitation comes about at the point of largest dispersion which is 3.8 cm/%. Given a beam pipe size of 7.6 cm this converts to a ring acceptance of 2% in energy without any reduced apertures. Synchrotron and parasitic losses are made up with the RF. The energy lost by most of the beam going through the internal target is negligible.

Wakefields

Another source of loss is that from those collimators which were used as conductance limiters and emittance protectors. The wakefields from these discontinuities in the vacuum pipe effect the energy of the beam as a function of beam position and charge. The curve in Fig. 15 shows a beam bunch traversing a target cell. The wakefields are seen not to be perpendicular, the longitudinal component causes energy change. Figure 16 shows the wake function for that case per picoCoulomb. Given a bunch with 28 picoCoulombs the maximum energy spread incurred by this transition is 200 volts. The wake shape is reminiscent of an RF source shifted in phase by approximately the radius of the small aperture. Its voltage is too small to cause the beam to shift out acceptance of the main source of RF. Note, however, in the figure the dependence of the wakefield amplitude on taper of the collimator edge. With four collimators in the ring, this is doubled. Compared to other sources, however, this is still small. Judicious design of collimators is still prudent, considering the general discrepancies between calculated and measured ring impedances.

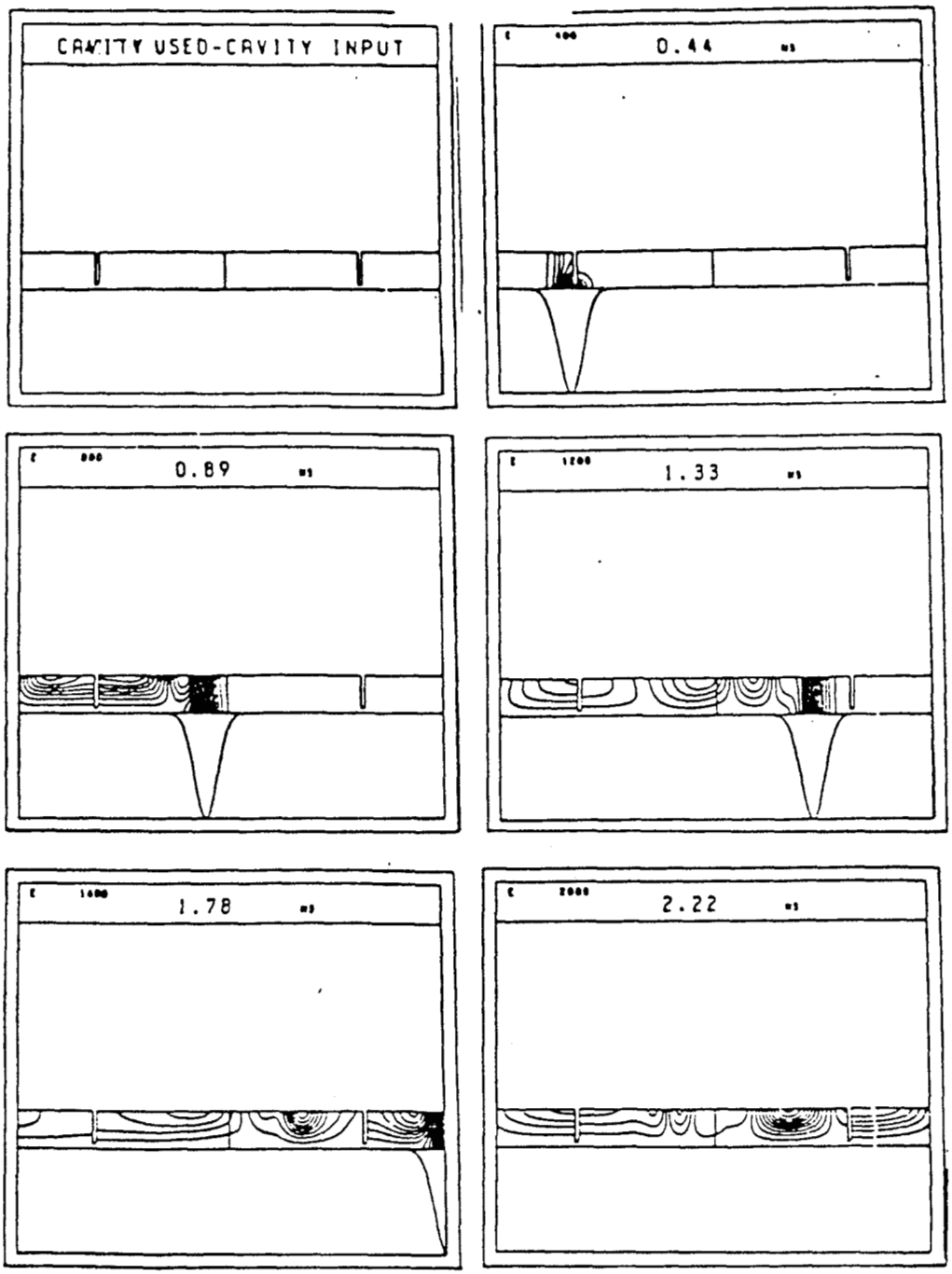

Figure 15. Electric field lines induced by gaussian beam bunch traveling through internal target at time indicated in figure (ns).

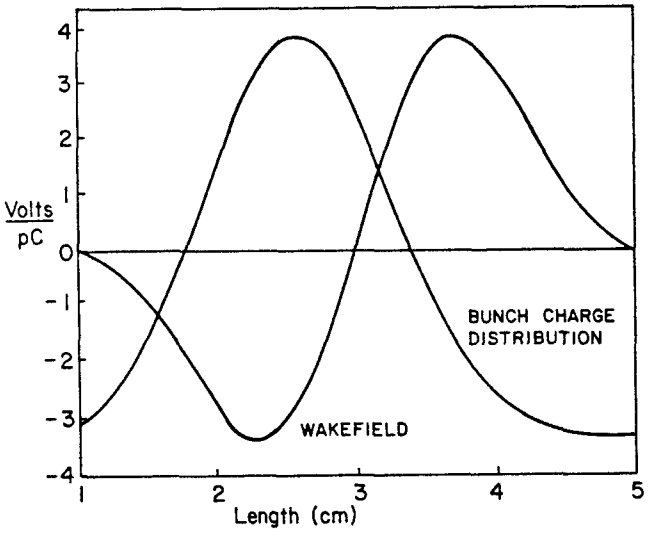

Figure 16. Wakefields of a collimator for given band bunch distribution.

Bremsstrahlung

There is some fraction of the beam that loses energy via bremsstrahlung. Some of this is lost near the target and will be treated later. Some of it, continues through the ring and would pass through the target. If one tried to limit the energy aperture to the injected energy spread of .04%, an aperture of the highest dispersion location of 1.5 mm would be necessary. This is not possible. However, it would seem that the fraction of loss is small enough so as not to affect an experiment.

Backgrounds

The above described emittance growth mechanisms become loss mechanisms. Two issues are important for ring operation. First, the collimators designed for cleaning purposes must be able to handle the power of the lost beam. Second, the losses nearest the internal target need to be investigated for background production. Sources of the latter include:

- Emittance growth halo hitting target aperture;
- Multiple and single scatterings hitting nearby beam pipe and ring elements;
- Bremsstrahlung losses coupling the energy dependence of quadrupole focussing ($\theta/x\delta$) causing overfocussing after the first quad near the internal target.

Assuming the first effect is controlled by limiting the lifetime in the ring, the other effects are independent of the lifetime and still must be considered.

Three sources of background are treated as shown in Fig. 17. Since the first quad is 2.5 m from the target, any beam scattered between 15.2 mr to 50 mr will hit the pipe and the surface of the quad. Due to the strength of the nearby quad, any beam having lost more than 25% of its energy will strike the pipe between the first and second quad. Table IV summarizes the fraction of beam lost in these areas. Also in the table is the corresponding beam lost in electrons assuming 80 mA circulating current in the ring.

TABLE IV

BACKGROUNDS

- Scattering Hitting Ring Chamber and Elements
- Energy Loss Coupled to Energy Dependent Focussing of Quads

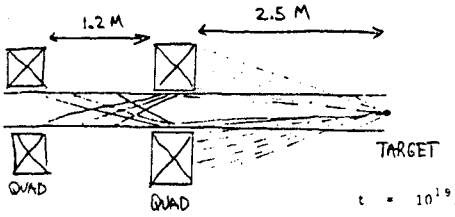

Figure 17

t = 10^{19}/cm^2

(After 1,000 turns) E = 440 MeV E = 880 MeV

Fraction Hitting Pipe	1.8(-6)	4.4(-7)
Fraction Hitting Quad + Pipe	6.3(-5)	1.6(-5)
Fraction Hitting AFter Quad	4.9(-4)	4.9(-4)

Note: 80 mA = 6.5 x 10^{14} electrons

1 x 10^{-5} x 6.5 x 10^{14} electrons ~ + 18 x 10^{12} neutrons/sec

per 1,000 turns

Figure 18 is a sketch of the beam line within the proposed internal target experimental hall. It is provided for your imagination. No cutout pieces provided.

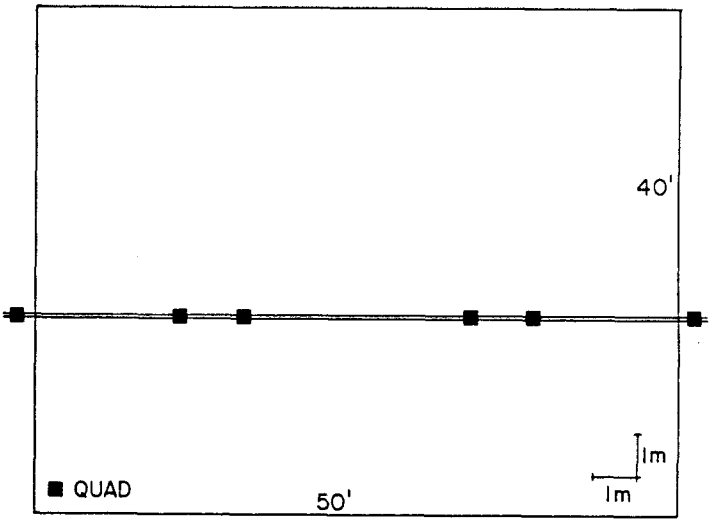

Figure 18. Beam line inside IT hall.

Conclusions

The calculations described indicated that a wide range of operational modes are possible in the proposed ring. Given the fast refill time possible, targets as thick as 10^{19} cm^{-2} are feasible, and targets as thick as 10^{18} are possible in a parasitic mode. It is also possible to store beam for many seconds and possibly longer (depending upon ring behavior) with thinner targets.

Consideration of vacuum requirements leads to the conclusion that conductance limiters near the internal target will be important for the thicker targets, as well as cleanup apertures located at the high beta region in the ring. Design of these apertures should take into account the wakefield production and have tapers near 30° for reduced wakefield effects.

The ring being proposed for Bates has several advantages for internal target work. They include:

1. Large admittance
2. Flexibility high beta and low beta
3. High space/element ratio
4. Excellent beam quality

The budget for this facility includes the cost of solenoidal magnets to contain longitudinal polarization of the electron beam in the ring as described by B. Norum (U.Va.) in this workshop.

At present, no facility for photon tagging is planned. The Bates staff is currently evaluating the experimental needs for the planned internal target hall. Figure 18 shows the internal target hall and beam line as presently planned. Input from potential users would be helpful at this stage.

I would like to thank several people who helped in the preparation of this talk. Particularly Claude Williamson and Michel Garcon for contributing details of their related work. I also would like to thank Ken Jacobs for his calculations of the longitudinal wakefields. Finally, thanks to Jim Spenser, Phil Morton, and Karl Bane for conversations relevant to this workshop.

This work was supported in part by DOE and MIT.

References

1. G. Nixon, Editor, Bates Annual Report, 1984.

2. J. Calarco, private communication.

3. M. Garcon, private communication.

4. P. Maloney, "Internal Targets in Electron Storage Rings", Master's Thesis, U.Va., 1983.

   B. Craft and C. Williamson, "A Study of Effects of Internal Targets in a 1.0 GeV Electron Storage Ring", Bates Internal Report #83-03, (1983).

   H. Crannell, CEBAF 1985 Summer Study, #12-95, (1985).

   B. Norum, CEBAF 1985 Summer Study, #12-70, (1985).

   B. P. Nigam et al., Phys Rev. 115, 491 (1959).

5. K. Bane and P. Morton, SLAC Pub-3983, May 1986.

INTERNAL TARGET PHYSICS AT 1 GeV

S. Kowalski

Bates Linear Accelerator Center
Laboratory for Nuclear Science and Department of Physics
Massachusetts Institute of Technology
Cambridge, MA 02139

Abstract

The use of internal targets operating at high luminosity in an electron storage ring in the energy range 0.3-1.0 GeV is discussed. Examples are presented of fundamental physics problems which would be ideally suited to such a unique new capability. Special emphasis is placed on the use of polarized targets to measure spin observables and thus provide a *"Multipole Meter"* for separating individual form factor multipoles. The combination of laser technology with optical pumping now makes possible the polarization of a broad class of nuclear species to useful densities. The importance of longitudinally polarized electrons for studying nuclear structure is also discussed.

I. Introduction

The electromagnetic probe is an important tool as a precise microscope in unraveling the structure of nucleons and nuclei. It involves a fundamental well understood weak interaction (QED) with unmatched specificity. Modern facilities have exploited high resolution electron scattering to probe distances of much less than 1 fm with great precision. A new generation of medium energy CW accelerator facilities, 0.3 - 4 GeV, are being developed to expand our present capabilities; particularly those for coincidence experiments and those emphasizing the measurement of spin observables.

The proposed Bates upgrade involves the use of a storage ring which would make possible experiments with very thin internal targets at high luminosity. The description of this pulse stretcher ring is summarized in a contribution to this conference by Flanz. Key parameters for internal target operation are:

Energy	0.3 - 1.0 GeV
$\Delta E/E$	~0.04%
Current	40 mA/turn
Duty Factor	100%
Emittance (1-turn)	$.01\pi$ mm•mr
Beam Polarization	~40%
Vacuum	10^{-8} torr
Internal Targets	$< 10^{19}$/A nuc/cm^2

There has developed a strong interest over the past few years for such an internal target facility that could provide a unique capability for addressing fundamental problems in nuclear physics. The combination of ultra-thin targets ~10^{17}/cm^2 and large circulating currents ~80mA results in high effective luminosities ~5×10^{34}cm^{-2}s^{-1}. This is competitive with luminosities generally used with external beams. In addition the low target density opens up entirely new fields of study.

One important area involves experiments detecting relatively low energy, highly ionizing reaction products. Such studies would include electrofission, giant resonances and threshold pion production. In all cases there will be an emphasis on exploiting our ability to map out the (q,ω) plane for the reaction process as well as to isolate contributing multipoles.

Polarized electrons and/or polarized targets have up to now played only a minor role in nuclear physics. At high energies the SLAC parity violation experiment[1] involving the scattering of longitudinally polarized electrons from quarks provided a crucial test of our understanding of electro-weak processes. Other experiments[2] using polarized electrons and polarized H studied the spin structure function of the proton. Parity violating electro-weak experiments in the nuclear physics regime are underway at both MAINZ and MIT.

It is now clear that spin measurements can play a much broader role in nuclear physics than simply searching for parity violation. Recent theoretical studies[3] have shown that the capabilities of polarized electrons and polarized targets will provide a unique opportunity for addressing some long standing physics problems. They would allow in principle a complete experimental determination of the form factor multipole structure. Such a decomposition represents the most complete characterization possible of the electromagnetic structure of nucleons and nuclei. Electron scattering can achieve this in a model independent way.

The full power of the electromagnetic probe is realizable only with the measurement of spin observables: polarized targets, polarized beam and recoil polarizations. In such measurements one can exploit the interference nature of an asymmetry to measure small but important amplitudes. Fundamental physics problems include the deuteron t_{20}, neutron charge form factor and the deformation of the delta. More speculative weak interaction studies may also be possible.

Developing laser technology has made possible the polarization of a broad class of nuclear species to interesting densities (10^{14-18}nuc/cm^2). Combining a storage cell geometry with the high circulating current of a storage ring would make spin measurements in electromagnetic physics for the first time practical.

In this review we will present examples of the kinds of physics problems that could be studied in the near future with the development of internal target facilities. These include experiments in nuclear spectroscopy, those involving ionizing recoils, some fundamental measurements on nucleons and few-body systems and weak interaction studies.

II. Internal Targets

An important practical consideration for carrying out an effective internal target program is the question of luminosity. Comparing typical

luminosities for both external and internal beams we have:

External Beam:

$I \sim 25\mu A$

$t \sim (1\text{-}100)\,mg/cm^2$

$L_{ext} = 10/A \times 10^{34\text{-}36}\,cm^{-2}s^{-1}$

Internal Beam:

$I \sim 80mA$

$t \sim 10^{14\text{-}16}\,nuc/cm^2$ (polarized targets)
$> 10^{17}$ nuc/cm^2 (unpolarized jets or microfoils)

$L_{int} = 5 \times 10^{31\text{-}34}\,cm^{-2}s^{-1}$

Although the internal target luminosities are in general smaller, such luminosities are more than sufficient to carry out a broad program of electronuclear studies. Experiments detecting low energy highly ionizing reaction products, such as those resulting from electro-fission or threshold pion production, require the use of very thin targets.

A very important class of experiments for an internal target program involves the use of polarized targets. The standard techniques used to produce dense polarized targets in nuclei such as H and D involve low temperatures and very high magnetic fields. Such targets have limited usefulness. For example, polarized deuterium targets which are used in external beams are limited to a few nA of current due to beam heating and radiation damage. The effective luminosity is substantially reduced.

The use of laser driven optical pumping and spin exchange techniques opens the possibility of polarizing a broad class of nuclear species. When combined with internal beams, such targets with densities of $10^{14\text{-}16}$ nucl/cm^2 give high luminosities. They have, in addition, much higher polarization resulting in a better overall figure-of-merit. Since the internal targets can operate at low magnetic fields the spin orientation is easily controlled and rapid spin reversal for control of systematic errors is a relatively straight forward operation.

There is presently extensive activity in constructing polarized gas targets of useful densities for nuclear physics studies. A tensor polarized deuterium target and a polarized ^{3}He target are under development at ANL[4] and Cal Tech,[5] respectively. Further, as techniques are advanced, for both polarized and unpolarized targets one sees potential experimental advantages involving high accuracy and low background operation.

Various target geometries have been considered for use in storage rings. An important requirement is to provide adequate clearance for the circulating beam and to maintain low vacuums outside of the target region. The most promising target configurations are gas jets and storage cells. These are illustrated in Figure 1.

GAS JET TARGET

- TARGET MATERIAL UNDER HIGH PRESSURE
- SPECIALLY DESIGNED MOZZLES
- GAS COLLECTION/PUMPING

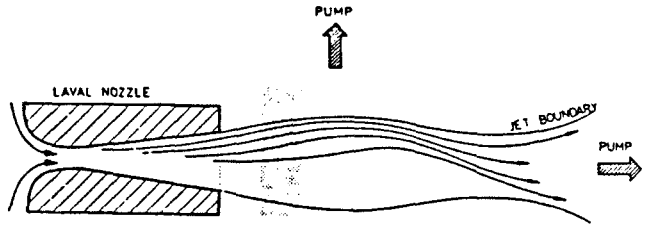

STORAGE CELL TARGET

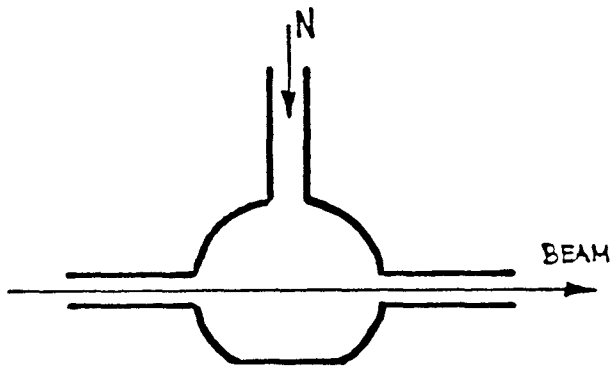

Fig. 1: Schematic gas jet and storage cell internal target geometries.

Another important consideration in the use of internal targets involves the beam-target interaction. Important issues include:

- energy loss
- emittance growth
- pumping apertures
- target depolarization.

A complete discussion of these and other targeting problems in the proposed Bates 1-GeV ring is reviewed in the contribution to this conference by Flanz.

III. Nuclear Spectroscopy

High resolution single-arm electron scattering is the source of much of our precise and detailed information on the electromagnetic structure of complex nuclei. An example which emphasizes both the specificity and shortcomings of this simple process is ^{17}O. The data[6] for the transverse form factor of the ^{17}O ground state in the effective momentum transfer range $0.5 < q_{eff} < 2.8$ fm^{-1} are shown in Figure 2.

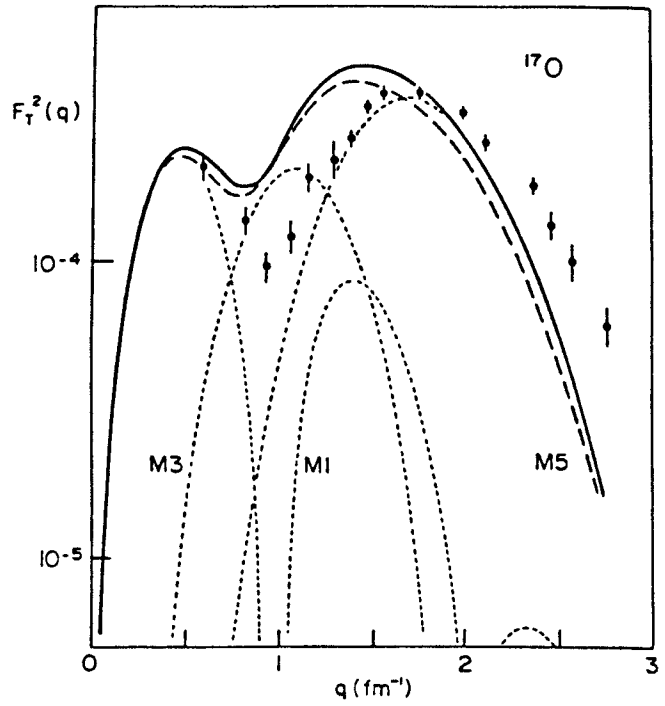

Fig. 2: The ^{17}O data of Hynes et al., are compared to the prediction of the extreme single-particle model calculation using a harmonic oscillator wave function (solid curve and dotted curves for individual multipoles). The dashed curve is calculated using a Woods-Saxon radial wave function.

In the simplest picture of ^{17}O a $d_{5/2}$ neutron is bound to a possibly deformed ^{16}O core. Both the longitudinal and transverse form factors have contributions from several multipoles.

$$F_L^2 = F_{C0}^2 + F_{C2}^2 + F_{C4}^2$$
$$F_T^2 = F_{M1}^2 + F_{M3}^2 + F_{M5}^2$$

These incoherent combinations of multipoles cannot be separated in a model independent way without polarization information. Single particle calculations using HO wave functions indicate that there is a sizeable suppression of the M3 component. Neither core-polarization nor meson exchange effects can account for the observations.

The detailed discussion of the nuclear structure information made accessible through the use of polarized targets and longitudinally polarized electrons is summarized in a recent review by Donnelly and Raskin.[3] The *"Multipole Meter"* aspect of spin observables is demonstrated by examples involving elastic and inelastic scattering in complex nuclei. All show the detailed sensitivity that these new techniques provide for separating the nuclear structure information into the maximal fundamental information that is allowed by a measurement of the individual electromagnetic form factors.

As a specific example we will consider elastic electron scattering from $^{39}K(I=3/2)$. This nucleus can be described in the extreme single-particle model as a $1d_{3/2}$ proton hole relative to ^{40}Ca using simple harmonic oscillator wavefunctions. The effects of core polarization and meson exchange currents are included in the characterization of the measured[7] transverse form factors (Figure 3).

In Figure 4 are shown the predicted results for the asymmetries. The plotted asymmetries are:

$$A_{NS} = (\Sigma_N - \Sigma_S)/\Sigma_0$$
$$A_{LN} = (\Sigma_L - \Sigma_N)/\Sigma_0$$
and
$$A_{LS} = (\Sigma_L - \Sigma_S)/\Sigma_0$$

where the Σ_i are the respective polarization cross sections and Σ_0 is the unpolarized cross section and i = L, N and S refer to the usual[3] target polarization directions with respect to the incident electron direction. The polarization ratio $(\Delta/\Sigma)_i$, calculated for specific orientations of the target polarization, is shown in Figure 5.

The results show significant variations for both the asymmetries and polarization ratios as a function of momentum transfer. These variations result from a complicated interference between the contributing form factors and are particularly emphasized when any of

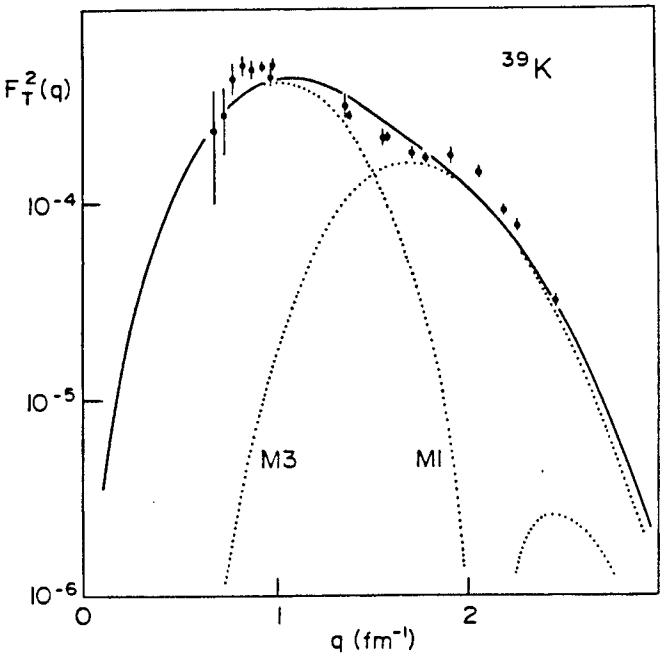

Fig. 3: The ^{39}K data of DeJager et al., are compared to a phenomenological fit made using $d_{3/2}^2$ and $f_{7/2}^2$ matrix elements and a harmonic oscillator radial wave function.

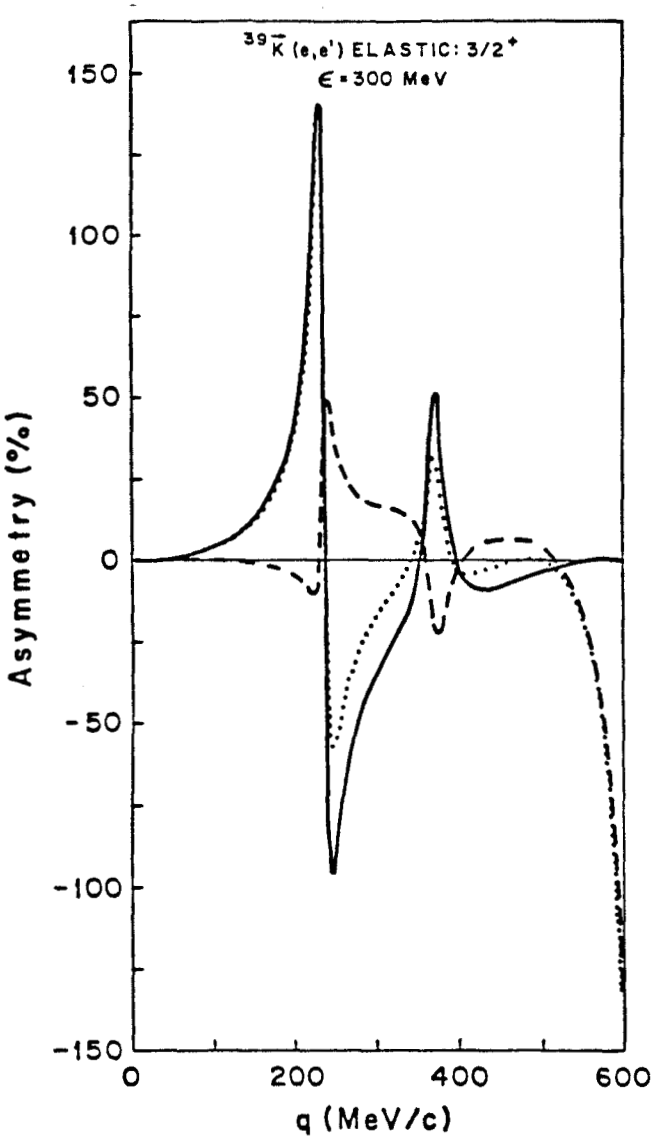

Fig. 4: Elastic electron scattering from polarized ^{39}K. The polarization asymmetries correspond to taking the target to be 100% polarized along the L, N, and S directions and forming the differences and dividing by the unpolarized cross section Σ_o.

the individual form factors goes through zero. Precise measurements of cross sections and asymmetries when combined with the usual longitudinal-transverse separation using unpolarized targets will allow a complete separation of the four form factors which contribute in this case.

IV. Ionizing Recoils

Internal targets will also offer a unique capability for studies of the nuclear continuum. Experiments requiring the detection of highly ionizing reaction products are in many cases severely limited by targeting requirements in external beams. Gas jet

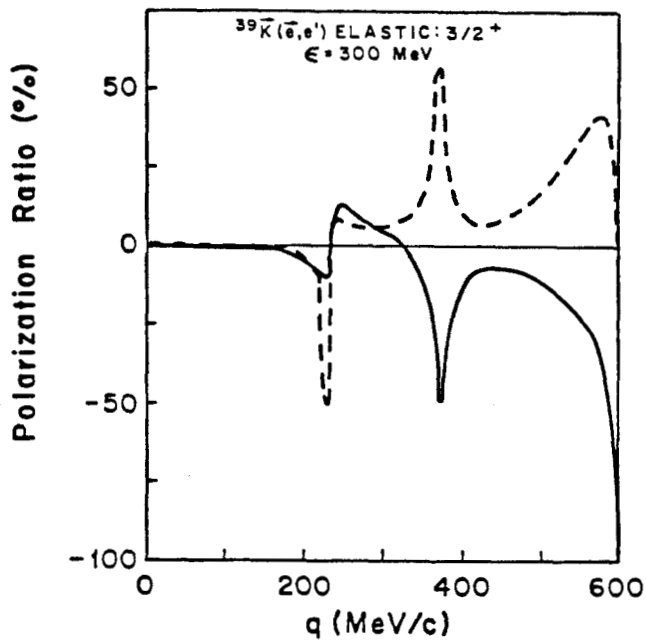

Fig. 5: Elastic longitudinally polarized electron scattering from polarized ^{39}K. The polarization ratios $(\Delta/\Sigma)_L$ (solid line), and $(\Delta/\Sigma)_S$ (dashed line) are calculated for a 100% polarized target.

while at the same time allowing for in-vacuum coupling between the detector and target.

Examples of areas of research which could benefit from the use of internal targets include:

- Electrofission
- Giant Resonance
- Pion Electroproduction

1. Electrofission

Reactions such as $^{24}Mg(e,^{12}C\ ^{12}C)e'$ have been studied using CW accelerators. Several sharp structure resonances were discovered[8] in the GR region of ^{24}Mg and ^{28}Si. They exhausted a significant fraction of the E2 and E0 sum rules and decayed primarily into "exotic" channels such as binary or near binary fission. The nuclear structure of these resonances still remains a puzzle. It would be very interesting to do a complete (q,ω) map of the process by detecting the scattered electron in coincidence. Such experiments appear to be practical only with internal targets.

In the HEPL experiments using 400μA average currents on targets of 3$\mu g/cm^2$ the luminosity was $3x10^{32} cm^{-2} sec^{-1}$ for ^{24}Mg. An internal target could in principle be four times thicker and with the large circulating current the resulting luminosity would be higher by more than two orders of magnitude. It would be sufficient to carry out a full coincidence program.

2. Giant Resonance

The objective of much of the current work in giant resonance studies is to separate modes of different multipolarity and to carry out a spatial mapping of the coupling to various decay channels. Luminosities for both external and internal target experiments are similar. There are, however, other advantages offered by the use of thin internal targets.

One can achieve better energy resolution in (e,e'x) experiments where target thickness is a serious limiting factor. The use of thin targets, either gas jets or very thin foils, allows the study of rare (and/or expensive) nuclear species.

One final important consideration is that internal targets allow the detection of very heavy and highly ionizing recoil particles. For example, experiments such as (e,e'n), which are difficult to do otherwise, could be carried out by detecting the recoiling residual nucleus if it is sufficiently stable. The study of $^{13}C(e,e'n)$ by detecting ^{12}C and measuring its energy is one possibility. Other interesting examples of light nuclei include ^{4}He, ^{7}Li, ^{11}B, ^{13}C, ^{15}N, etc... Recoil species such as ^{11}C, ^{15}O, ^{19}Ne are sufficiently long lived as well. A real advantage would be the study of (e,e'p) and (e,e'n) in the same apparatus.

Figure 6 shows a typical apparatus of a coincidence GR experiment[9] in the Novosibirsk ring and some results for the $^{16}O(e,e'\alpha_0)$ decay channel. This was a relatively low energy (130 MeV) experiment using a gas jet target.

3. Threshold Electroproduction of Pions

A special type of experiment which requires thin targets and high luminosity is the study of pion electroproduction from nuclei near threshold. The standard technique involves pion detection in reactions of the type $_{Z}^{A}(e,e'\pi^{\pm})_{Z\mp1}^{A}$.

One could alternatively measure the recoiling daughter nuclei in the reactions $_{Z}^{A}(e,e'_{Z\mp1}{}^{A})\pi^{\pm}$. The very thin targets required to detect heavy recoils combined with the high circulating current provide the necessary luminosities. Predicted cross sections are very small.

Coincidence experiments such as these would involve a complete mapping of the (q,ω)-plane for which the relative energy of the pion daughter-nucleus system is near threshold. The (γ,π) reaction only studies the process where $q=\omega$. Reaction kinematics shows a one-to-one relationship between pion angle in the CM frame and residual nucleus kinetic energy in the laboratory frame. The nucleus energy distribution yields a measurement of the pion angular distribution. An accurate spectrum measurement would allow a separation of s- and p-wave components for the process.

Motivations for such studies include:

- Measure for virtual photons to compliment real photon results.
- Measure the spatial distribution of the pion wavefunction and use it to decide on the correct form of the π-nucleus optical potential at low energies.
- Study π^{+} and π^{-} production between analog states. Coulomb interaction modifies the strong interaction and could provide a measure of where the strong interaction distortion is turned on and off.
- Study the production amplitude as final state CM energy is increased from threshold. At higher energies the leading Kroll-Ruderman $\vec{\sigma} \cdot \vec{\epsilon}$ term is modified by the addition of momentum dependent terms.

V. Fundamental Measurements

The high luminosity of a stretcher ring will make practical the precise measurement of spin observables in nucleon and few nucleon systems using polarized electrons and/or polarized targets. Some of the most fundamental of such studies which now appear feasible include the separation of the deuteron charge monopole and quadrupole form factors, the neutron charge form factor and the deformation of the delta.

1. Deuteron Form Factors

The deuteron is our simplest bound nuclear system. All of its static properties have been

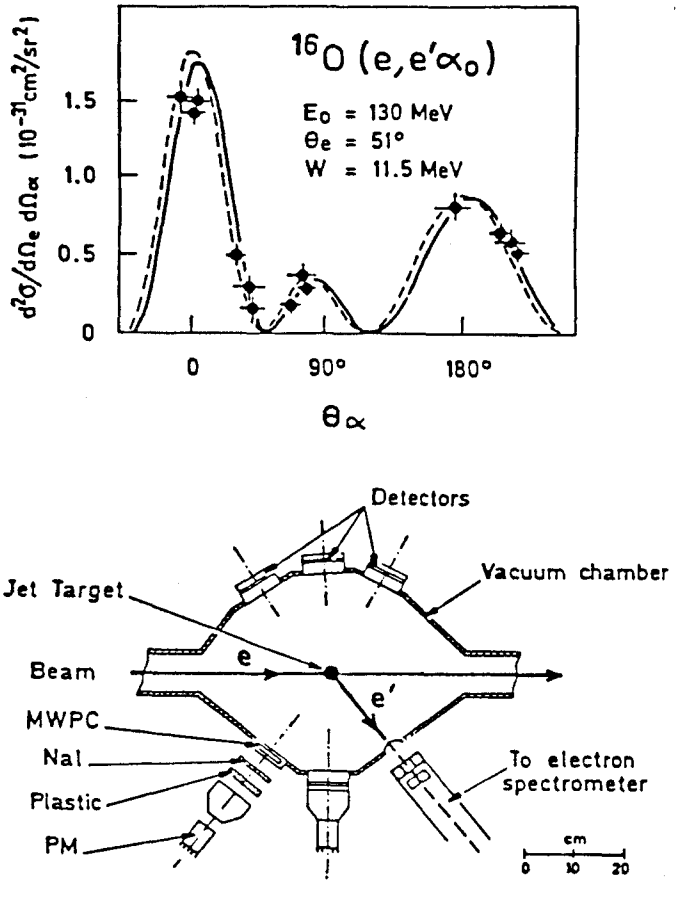

Fig. 6: Data and schematic experimental layout for an $^{16}O(e,e'\alpha_0)$ measurement using internal targets in the VEPP-2 ring at Novosibirsk.

precisely measured. Electron-deuteron scattering provides important information on the short range behavior of the deuteron wavefunctions as well as a measure of non-nucleonic degrees of freedom such as isobar and meson exchange currents. Quark degrees of freedom are expected to contribute at large q^2.

A complete description of the electromagnetic properties of the deuteron (J=1) requires a measurement of three form factors: charge monopole (F_C), charge quadrupole (F_Q) and magnetic dipole (F_M) as a function of an extensive range in momentum transfer.

The unpolarized e-d elastic cross section is usually written as:

$$\frac{d\sigma}{d\Omega} = \sigma_M \left\{A(q^2) + B(q^2)\tan^2\theta/2\right\}$$

where

$$A(q^2) = F_C{}^2(q^2) + \frac{8}{9}\eta^2 F_Q(q^2) + \frac{2}{3}\eta F_M(q^2)$$

$$B(q^2) = \frac{4}{3}\eta(\eta+1)F_M{}^2(q^2)$$

$$\eta = \frac{q^2}{4M_D{}^2}$$

The two structure functions $A(q^2)$ and $B(q^2)$ have been measured to high q^2 and are separated using the usual Rosenbluth method. Such an angular distribution provides a measure of F_M but F_C and F_Q cannot be separated in a model independent manner. The location of a zero in the charge monopole contribution is important to our understanding of the validity of different potential models as well as providing a measure of two body currents.

The measurement of a spin observable in principle allows the complete separation of the individual multipole contributions. Electron scattering from a tensor-polarized deuterium target is sensitive to additional interfering bilinear combinations of deuteron form factors. The t_{20} component of the tensor polarization,

$$t_{20} = -\sqrt{2}\sigma_M\left[\frac{4}{9}\eta^2 F_Q{}^2 + \frac{4}{3}\eta F_C F_Q + \frac{1}{3}\eta F_M{}^2\left(\frac{1}{2}+(1+\eta)\tan^2\frac{\theta}{2}\right)\right]/\frac{d\sigma}{d\Omega}\ .$$

The most important contribution to t_{20} in the momentum transfer range $q^2 < 1.2(GeV/c)^2$ comes from the interference term $F_C F_Q$. This provides the additional handle which allows a separation of the multipole contributions.

In a recent Bates experiment,[10] the tensor polarization was determined by measuring the polarization of the recoil deuterons (electron beam and target unpolarized) in coincidence with the scattered electrons. Such an experiment involves a second analyzing scattering of known sensitivity to tensor polarized deuterons. In this case the reaction $\vec{d}(^3He,p)$ was used. The extracted values of t_{20} are compared with theoretical predictions of several realistic potential model calculations in Figure 7.

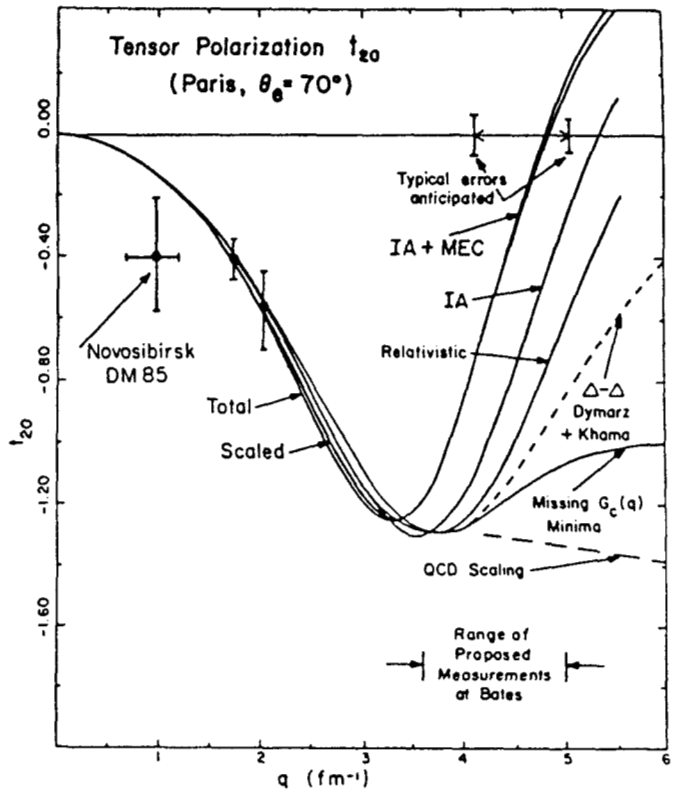

Fig. 7: Comparison between different theoretical predictions for deuteron t_{20} including QCD scaling, Δ-Δ admixtures and the effect implied by the filling in of the minima in $G_C(q)$. The Novosibirsk and Bates experimental data are shown as well as the q-range and anticipated sensitivity of the proposed new measurements.

Extensions of these measurements to regions of momentum transfer Q~1GeV/c are under way[11] and involve some very interesting physics. The potential model dependences are sizeable and perturbative QCD predictions are completely at variance with the potential model results. These new measurements do not involve the use of polarized targets but rely on the use of a polarimeter whose properties and performance must be accurately known.

An alternative approach involves measuring the asymmetry in elastic electron-deuteron scattering from a tensor polarized target. Such measurements are currently underway at the Bonn synchroton where 1nA beams of electrons are incident on a tensor polarized liquid ND_3 target. A Q^2 up to 0.7 GeV^2/c will be probed and in the future extended to $Q^2 > 1$ GeV^2/c on the ELSA ring.

Holt[4] at ANL is developing a tensor polarized deuterium target for use as a gas jet internal to the Aladdin 1 GeV storage ring. A target density of $\sim 10^{14}$ atoms/cm^2 in a circulating current of 100 mA results in luminosities of the order of $10^{32} cm^{-2} s^{-1}$. Such a

high density of polarized deuterium nuclei is obtained by using optically-pumped polarized alkali atoms which transfer polarization to deuterium atoms by atomic spin exchange. Densities in excess of 10^{15} atoms/cm^2 appear feasible with present-day techniques.

2. Neutron Electric Form Factor

The elastic scattering of unpolarized electrons from unpolarized nucleons (J_i=1/2) involves a measurement of the cross section

$$\frac{d\sigma}{d\Omega} = \sigma_M f_{rec}^{-1}\left[G_{EN}^2(Q^2)+\tau G_{MN}^2(Q^2)\left\{1+2(1+\tau)\tan^2\frac{\theta}{2}\right\}\right]$$

where

$$\tau = -Q^2/4M_N^2$$

The electric and magnetic form factors, $G_{EN}(Q^2)$ and $G_{MN}(Q^2)$, respectively, are related to the $F_L(Q)$ and $F_T(Q)$ by

$$\sqrt{4\pi}F_L = (1+\tau)G_{EN} \text{ and } \sqrt{4\pi}F_T = -\sqrt{2\tau(1+\tau)}G_{MN}.$$

A Rosenbluth separation of the form factors allows for reasonable accuracy only when the two amplitudes are comparable. In the nucleon case the magnetic form factor dominates over the electric one at high momentum transfer. As a result only the magnetic form factor is relatively well known over an extended range in momentum transfer.

The electric form factor is directly related to the charge distribution of the nucleon and is a fundamental quantity whose knowledge is important for the detailed understanding of both nucleon and nuclear structure. For the proton, reasonable knowledge of G_{Ep} exists only up to $4(GeV/c)^2$. In the case of the neutron, which is charge neutral, G_{En} is very small and as a result is very poorly known for all q, except for q=0.

The usual method of measuring G_{En} involves the Rosenbluth decomposition of electron-deuteron elastic and quasi-elastic scattering. Interpretation of the results is plagued with both model dependence and large systematic errors. The available body of data for G_{En} up to q^2~1.5$(GeV/c)^2$ are shown in Figure 8.

For the nucleon case (J_i=1/2) polarized targets without polarized electrons yields no new information. The polarization cross section for scattering from polarized nucleons is

$$\Delta_{fi} = -\Sigma_o\left\{\sqrt{2}F_T^2(q)v_{T'}\cos\theta^*+2\sqrt{2}F_L(q)F_T(q)v_{TL'}\cdot\sin\theta^*\cos\phi^*\right\}/\sqrt{2}F^2$$

where

$$F^2(q) = v_L F_L^2(q) + v_T F_T^2(q).$$

A measurement of the polarization ratio Δ_{fi}/Σ_o (asymmetry) or equivalently that of the recoil nucleon polarization by means of a second scattering involves

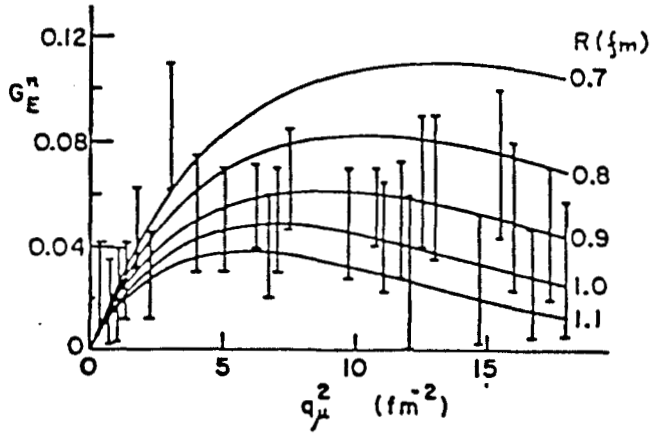

Fig. 8: Neutron electric form factor for different bag radii and existing experimental data.

the interference term $F_L(q)\,F_T(q)$ which is directly sensitive to the small form factor and to their relative sign. The simple Rosenbluth separation is insensitive to the small amplitudes.

Possible experiments which can be exploited to measure the neutron electric form factor G_{En}, include:

$^2\vec{H}(\vec{e},e'n)p$ exclusive

$^2\vec{H}(\vec{e},e')x$ inclusive

$^2H(\vec{e},e'\vec{n})p$

$^3\vec{He}(e,e')x$ inclusive.

The sensitivity of the polarized-electron polarized-deuteron experiment to G_{En} has recently been calculated by Cheung and Woloshyn.[12] The results for the cross section and polarization asymmetry at an electron energy of 1 GeV are shown in Figure 9. The deuteron is polarized in the scattering plane at 45° to the incident electron direction. The neutron electric form factor has been parametized by:

$$G_{En}(Q)^2 = \frac{-\mu_n\tau}{(1+\eta\tau)\left[1+\frac{Q^2(GeV)^2}{0.71}\right]^2}$$

with $0 < \eta < \infty$. The asymmetry shows large sensitivity to G_{En} and appears to be measurable.

The sensitivity to G_{En} has also been calculated[13] for scattering from polarized ^{3}He. In the simplest picture of ^{3}He the protons have opposite spins, and their contributions to spin-effects should essentially cancel. The spin-dependent effects are then primarily due to the neutron and the results for inclusive scattering are shown in Figure 10. The same parameterization was used for the neutron electric form factor and β is the angle in the scattering plane between the polarization axis of ^{3}He and the incident electron direction.

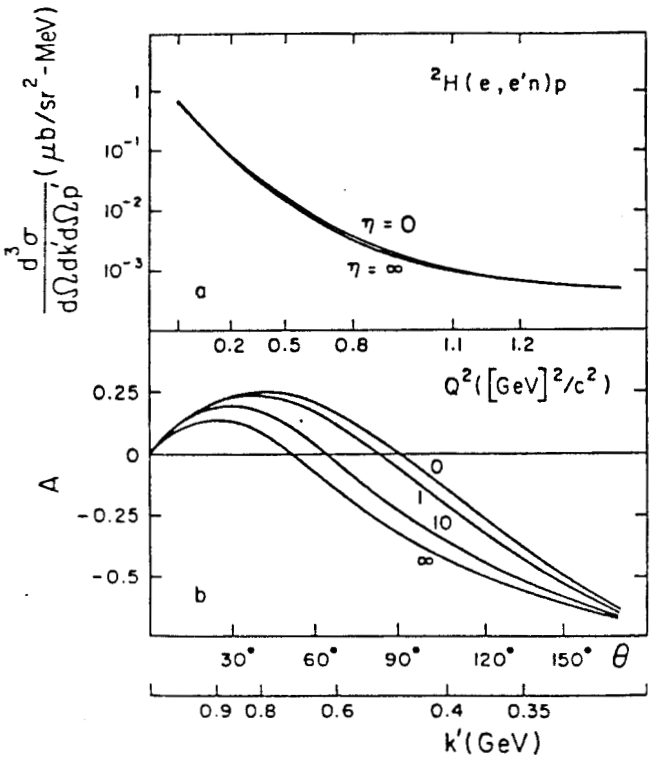

Fig. 9: Exclusive cross section for $^2\vec{H}(\vec{e},e'n)p$ at quasi-free kinematics for different neutron electric form factors using 1 GeV incident electrons. Asymmetry with respect to change in the electron longitudinal polarization for different neutron electric form factors. The deuteron is polarized at 45° to the incident electron direction.

An experiment to measure G_{En} using polarized electrons and a recoil neutron polarization measurement is being planned at MIT-Bates.[14] Future experiments involving polarized targets will require internal target capabilities at the new electron stretcher ring facilities now under development. The present technology for polarized targets needs the high luminosity of an internal target to make such experiments realistic. Such facilities are likely to provide our most precise measurements of G_{En} over an extended range in q.

3. N → Δ Transition

The N→Δ transition involves the lowest spin-isospin excitation of the nucleon. Angular momentum and parity considerations allow three form factors F_{M1}, F_{E2} and F_{C2}. In a naive spherically symmetric quark model the nucleon and delta are each made up of three 1s-quarks. The transition then corresponds to a pure M1 spin-isospin flip of a 1s quark with no quadrupole contribution. Non-spherical admixtures to the Δ arising from a tensor quark-quark interaction would allow for L=2 contributions as well.

Quark models have been used to estimate the quadrupole C2 contribution. In such models a nucleon s-quark makes a transition to a d-quark in the delta.

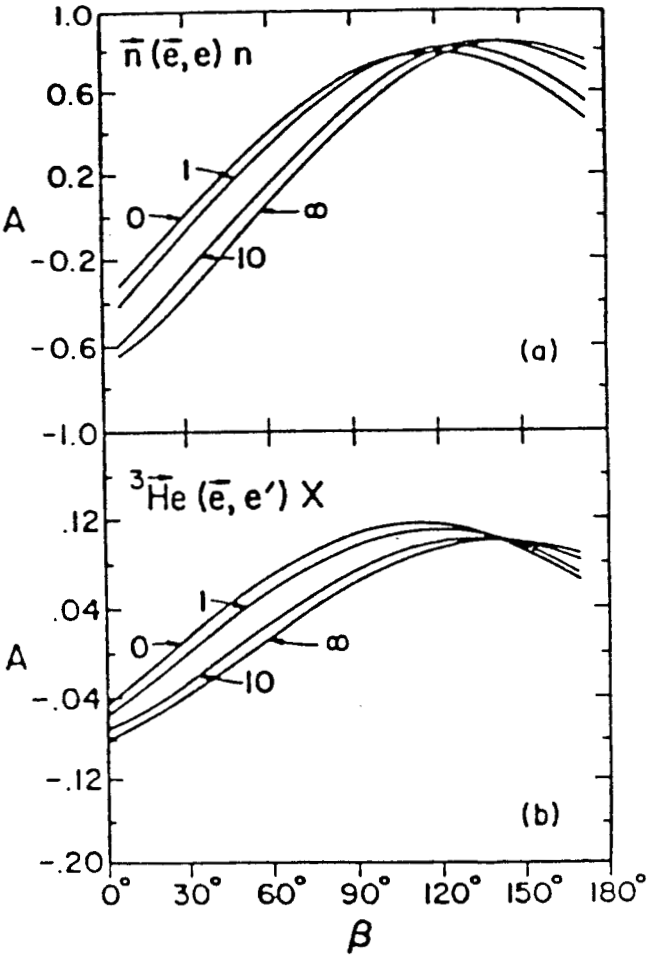

Fig. 10: Asymmetries as a function of target polarization angle β for a) polarized electron-polarized neutron scattering, b) inclusive polarized electron scattering from polarized ^{3}He at the quasi-free peak. Incident 1.5 GeV electrons are scattered at 60° for different choices of the neutron electric form factor.

A precise measurement of the C2 amplitude could shed some light on a possibly deformed delta.

The polarization cross section for a 1/2 → 3/2 transition on polarized nucleons is given by

$$\Delta = 4\pi\sigma_M f_{rec}^{-1}\left\{v_T,\cos\theta^*\left[F_{M1}^2 - F_{E2}^2 - 2\sqrt{3}F_{M1}F_{E2}\right]/\sqrt{2}\right.$$
$$\left. - \sqrt{2}\, v_{TL},\sin\theta^*\cos\phi^*\left[F_{C2}(F_{M1} + \sqrt{3}F_{E2})\right]\right\}$$

and the spin-averaged cross section

$$\Sigma = 4\pi\sigma_M f_{rec}^{-1}\left\{v_L F_{C2}^2 + v_T\left[F_{M1}^2 + F_{E2}^2\right]\right\}$$

Previous experiments have tried to make the usual Rosenbluth separation to determine F_{C2}. The results[15] are shown in Figure 11. The small longitudinal contribution is poorly known and is consistent with zero.

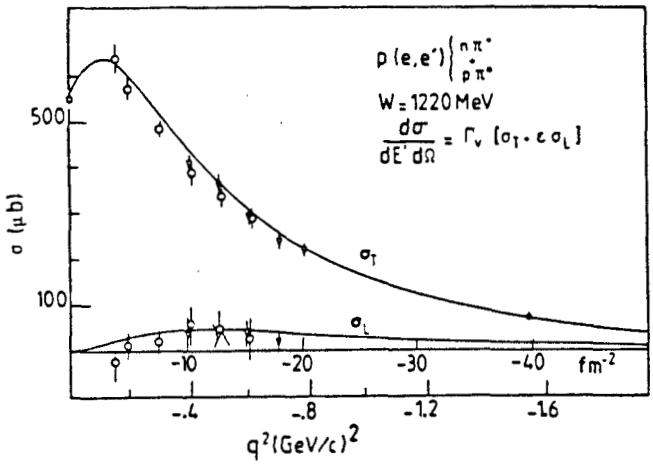

Fig. 11: Longitudinal and transverse response for p(e,e')Δ through the resonance region.

Experiments involving polarized electrons on polarized nucleon targets would be directly sensitive to the interesting $F_{C2}F_{M1}$ interference term and provide a measure of F_{C2}. Possible experiments include:

$$^1\vec{H}(\vec{e},e')\Delta \quad \text{and} \quad ^3\vec{He}(\vec{e},e')\Delta$$

The combination of both experiments would allow for a separation of neutron and proton contributions to the transition.

VI. Weak Interaction Physics

A more speculative (*"Science-Fiction"*) experiment involving the use of internal targets would be a measurement of the charge changing weak interaction process such as

$$^3He(e^-,{}^3H)\nu_e.$$

This reaction, although not as fundamental as the single-nucleon process $p(e^-,n)\nu_e$, involves a charged final state making it more amenable to experiment. The basic process is illustrated in Figure 12 for which cross section predictions have been made by Donnelly.[16]

The cross sections ($\sim 10^{-40}$ cm^{2}sr^{-1}) are very small and include contributions from vector and axial-vector terms which could in principle be separated. Combined with elastic electron scattering results this would provide a test of CVC. Based on the standard model with massless left-handed neutrinos, the cross section should be zero for right-handed electrons. A non-zero measure would indicate the presence of non-standard contributions.

The counting rates are low and would require a large acceptance detector system. Reaction kinematics show a strong correlation between recoil

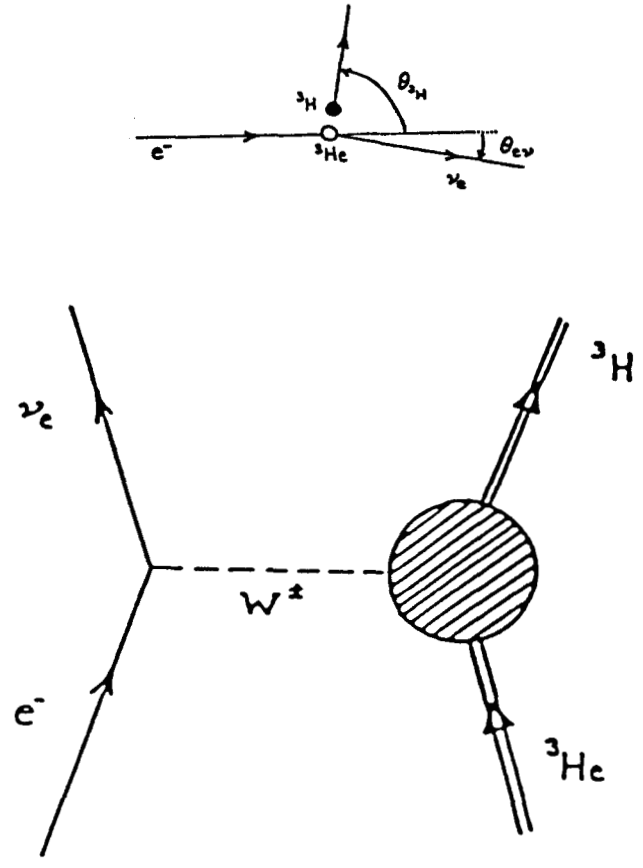

Fig. 12: $^3He(e^-,{}^3H)\nu_e$ charge-changing weak interaction physics.

angle and triton energy. This would need to be exploited to reject background events. With a circulating current of 100mA, a solid angle of 0.5sr and a target of 10^{19}atoms/cm^2 the event rate is approximately 2/hr.

The experiment, however, involves serious background problems. First, the kinematics are identical to elastic scattering. Since this is 12-14 orders of magnitude greater, the ^3He target must be ultrapure; the ^3H component must be less than 10^{-14}. Target walls must be far removed to reduce recoiling ^3He charge exchange reactions which would mask the tritons. Charge-sensitive detectors could help to overcome this problem.

This type of experiment is highly demanding but offers an exciting opportunity to measure a weak interaction form factor. It may be impractical. It should, however, be looked at as an interesting example of the kinds of *"exotic"* but very exciting experiments which may be possible using internal targets.

VII. Summary

We have tried to show in this brief review, using a few select examples, a glimpse of the new physics that would be made possible using internal targets at

a 1-GeV storage ring. The ability to measure accurately small amplitudes and interfering processes over an extended region in (q,ω) space would be an important new tool for electromagnetic nuclear physics. A basic program using spin observables to address a broad range of fundamental problems would be possible for the first time.

To make the proposed experiments a reality will require a nominal investment in the upgrade of existing accelerator facilities. The accelerator technology is well understood and only a modest investment in research equipment would be needed for carrying out many of the first interesting experiments.

There is currently much activity in the development of optically pumped polarized targets. The results look very promising.

Worldwide, the storage ring at Novosibirsk has been used for internal target nuclear physics studies. Plans are underway for possible experiments at the new Saskatoon Pulse Stretcher Ring just beginning operation. It has a maximum energy capability of up to 300 MeV. In the US, the ANL group has designed a deuteron t_{20} experiment for the Aladdin storage ring. The proposed Bates CW upgrade would provide a unique facility for such studies over an extended energy range of 0.3 - 1.0 GeV. With timely funding such a facility could be operational in a few years.

References

1. C.Y. Prescott et al., Phys. Lett. B77, 347 (1978).
2. M.J. Alguard et al., Phys. Rev. Lett 41, 70 (1978).
3. T.W. Donnelly and A.S. Raskin, Annals of Physics, 169, 247 (1986).
4. Holt, R., Proceedings of the Conference on Intersections Between Particle and Nuclear Physics, Steamboat Springs, edited by R.E. Mischke, AIP 123, 499 (1984).
5. R. McKeown and R.G. Milner, proceedings to this conference.
6. M.V. Hynes et al., Phys. Rev. Lett. 42, 1444 (1979).
7. K. DeJager et al., quoted by L. Lapikas, Proc. Conf. Nucl. Phys. Electrom. Int., Mainz, Lecture Notes in Physics 108, 41 (1979).
8. A.M. Sandorfi et al., Phys. Rev. Lett. 45, 1615 (1980).
9. S.G. Popov, Proc. of Workshop on the Use of Electron Rings for Nuclear Physics Research, Lund 1982, p150. D.M. Nikolenko et al., Europhysics Conference Abstracts 90, 242 (1985).
10. M.E. Schulze et al., Phys. Rev. Lett. 52, 597 (1984).
11. J. Cameron et al., Bates Proposal (1984).
12. C.Y. Cheung and R.M. Woloshyn, Phys. Lett. 127B, 149 (1983).
13. B. Blankleider and R.M. Woloshyn, Phys. Rev. C29, 538 (1984).
14. R. Madey and S. Kowalski, Bates Proposal (1985).
15. W. Bartel et al., Phys. Lett. 35B, 181 (1971).
16. T.W. Donnelly et al., Research Program at CEBAF, Report of the 1985 CEBAF Summer Study Group.

VECTOR DOMINANCE REVISITED BY A QUARK THEORIST

C.E.Carlson
Physics Department
College of William and Mary
Williamsburg, VA 23185, USA

Abstract: We examine from the viewpoint of QCD some topics that are often treated at lower energies by other means, particularly vector meson dominance, VMD. We would like to see why the older methods worked well enough to be pursued and what limits QCD says they should tend toward at higher energies.

I. Introduction

We will examine a trio of "old" topics, which have often been analyzed using vector meson dominance[1], from the viewpoint of a modern theorist who likes to analyze in terms of quarks and quantum chromodynamics. The three topics selected are the electromagnetic N-Δ transition form factors (where we don't mention VMD), the nucleon form factors, and Compton scattering from a proton target.

We will try to see either why VMD gave decent results in some situations or what contraints QCD will set upon putative models that one uses when a simple (i.e., coupled with perturbation theory) QCD won't work because the energy is too low. The latter of course is the problem. When an adequate calculation beginning from QCD is intractable, we use models like VMD that use some experimental data to say for example that there exist bound states with certain masses, that have the same coupling constants in a variety of situations, etc. In addition to seeing why VMD worked we would like to establish its domain of validity and see if it agrees with QCD in kinematic regions where perturbative QCD is applicable. We will in turn examine our three subjects and then make some closing remarks.

II. N-Δ transitions

The goal here is to compare expectations at high Q^2 and low Q^2, particularly regarding spin observables such as the E2/M1 ratio, and to see how the underlying theory gives high Q^2 trends and helps interpret the data.

E2/M1 ratio. At low Q^2 it is natural to analyze reactions in terms of multipole amplitudes, which we could well call multipole form factors. For N-Δ electromagnetic transitions with the photon off shell, there are two electric quadrupole amplitudes called E2 and C2 and a magnetic dipole amplitude M1. If the N and Δ both have spherically symmetric spatial wave functions and recoil is neglected, then the E2 and C2 amplitudes are both zero and the M1 dominates[2].

At high Q^2, because the quarks are loathe to flip their helicity, it is more natural to analyze in terms of helicity amplitudes[3]. The three helicity amplitudes are illustrated in Fig. 1, where we always give the incoming nucleon helicity +½ and label the amplitude by the helicity of the incoming photon.

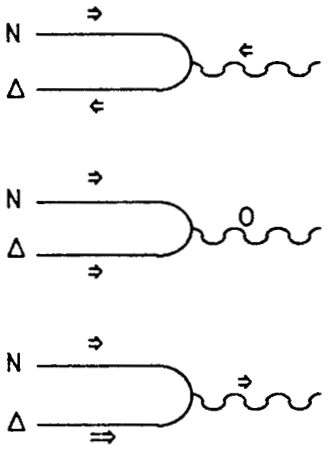

Fig. (1)

Notice that amplitude G_+ requires no quarks to flip helicity, G_0 requires at least one quark helicity flip, and G_- requires at least two quarks to flip helicity. Since each quark helicity flip costs a factor of $O(m/Q)$, where m is some relevant mass scale, we learn that G_- is smaller than G_+ at high Q^2 by a factor of $O(m^2/Q^2)$. Translating into helicity amplitudes,

$$G_- = \sqrt{\pi}\,(-\sqrt{3}\,F_{M1} + F_{E2}),$$
$$G_+ = \sqrt{\pi}\,(F_{M1} + \sqrt{3}\,F_{E2}), \qquad (1)$$

where we have followed Donnelly et al's notation[4]. The cancellation necessary for the asymptotic G_-/G_+ result leads to[5]

$$\begin{cases} F_{E2}/F_{M1} = \sqrt{3} & \text{Donnelly et al}^4, \\ E_{1+}/M_{1+} = 1 & \text{Many authors}^6, \\ E2/M1 = -\sqrt{5} & \text{Durand, DeCelles, and Marr}^7, \end{cases} \qquad (2)$$

where we have quoted the same result in several different conventions. The result is in great constrast

to the low Q^2 expectation. The data at 3 GeV^2 is still consistent with zero[8] and it will be interesting to see what happens just a few GeV^2 higher.

Q^2 falloff of leading form factor. The data on the high Q^2 falloff of the leading N-Δ form factor is usually quoted in terms of a form factor G_M^* which is defined operationally[9] from the cross section for $eN \to e\pi N$ and plotted compared to the dipole form. We show this in Fig. (2a) where

$$\frac{G_M^*(Q^2)}{G_D(Q^2)} = \frac{G_M^*(Q^2)}{G_M^*(0)\left(1 + Q^2/0.71\text{GeV}^2\right)^{-2}} \qquad (3)$$

is squared and shown plotted vs. Q^2. $G_M^*(Q^2)$ clearly falls faster with Q^2 than the dipole form.

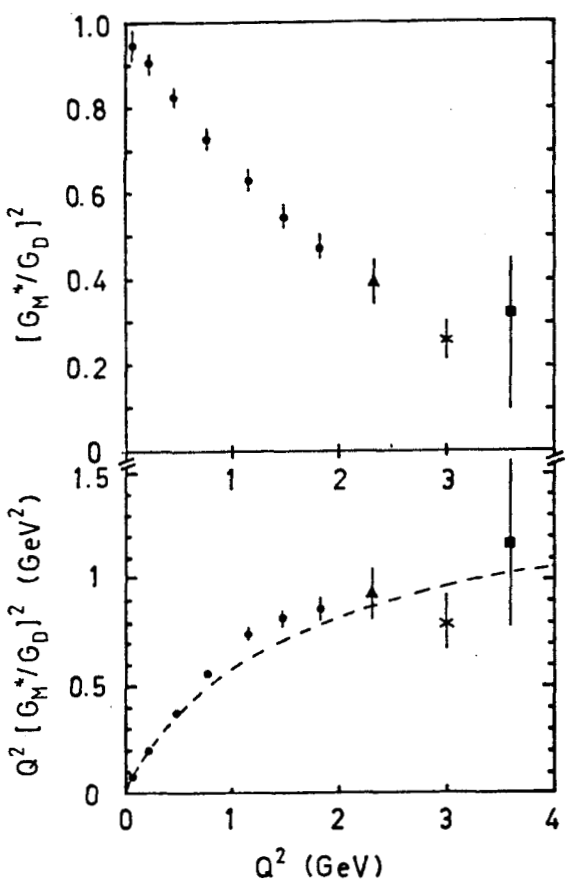

Fig. (2)

However, we must also consider what QCD would teach us to expect. By direct calculation or dimensional analysis of the lowest order perturbation theory diagram for G_+, Fig. (3), one can show at high Q^2 that

$$G_+ \propto 1/Q^3. \qquad (4)$$

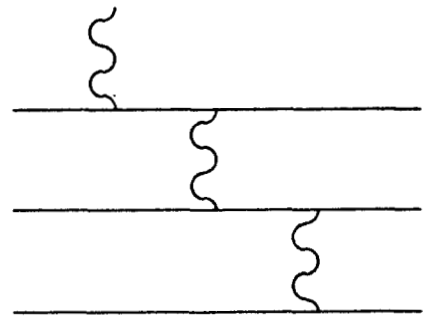

Fig. (3)

Chasing down the kinematic factors one discovers that[5]

$$G_M^* = (m_N^2\sqrt{8}/Q^2)\,G_+ \sim 1/Q^5 \qquad (5)$$

at high Q^2. Hence one expects that G_M^* will fall faster with Q^2 that the nucleon elastic form factors. One should really plot $Q^2\cdot[G_M^*/G_D]^2$ vs. Q^2 as in Fig. (2b) before interpreting any difference of behavior with Q^2 between the N-Δ transition form factor and the elastic nucleon form factor.

III. VMD and nucleon form factors

VMD can be implemented in several ways. How does it get the right Q^2 falloff and why can it fit the data so well? We will see how Iachello, Jackson, and Lande[10] (IJL) did it in 1973 and how Gari and Krümpelmann[11] (GK) did it in 1985. Those two treatments are similar enough to be discussed together but are by no means unique, as one can learn by examining Höhler et al[12] or Körner and Kuroda[13], for examples.

Basic implementation of VMD. To begin, one doesn't do the most naive thing, illustrated on the next page in Fig. (4a). Here there is just a vector meson connecting the photon to the nucleon so

$$F(Q^2) \propto \frac{1}{Q^2 + m_V^2}\, F_{VNN}(Q^2) \qquad (6)$$

Data (even before QCD!) show a $1/Q^4$ falloff so that giving F_{VNN} a monopole falloff implied the correct high Q^2 form. (This is one of the arguments for using monopole forms for the meson-nucleon-nucleon form factors as is often done in nuclear force calculations.) But even with the correct high Q^2 form, the fit to the

data is not good enough at all Q^2.

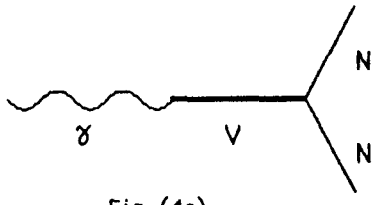

Fig. (4a)

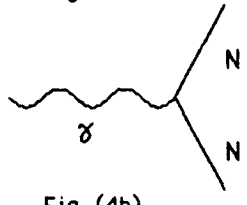

Fig. (4b)

Instead, IJL and GK add a "direct term," Fig. (4b), as well as the VDM term, Fig. (4a). For the isovector and isoscalar dirac form factors including just the ρ and ω vector mesons, they have

$$F_{1V}(Q^2) = (\tfrac{1}{2})g(Q^2)\,[\,1 - \beta_\rho + \beta_\rho m_\rho^2/(m_\rho^2 + Q^2)\,]$$

$$F_{1S}(Q^2) = (\tfrac{1}{2})g(Q^2)\,[\,1 - \beta_\omega + \beta_\omega m_\omega^2/(m_\omega^2 + Q^2)\,] \qquad (7)$$

The "intrinsic form factor" is given by

$$g(Q^2) = (1 + \lambda Q^2)^{-2} \quad . \qquad (8)$$

(Actually IJL give several choices for the intrinsic form factor, but with hindsight we should only consider the one that gives the asymptotic falloff predicted by QCD.) Note that

(i) We have the right falloff at high Q^2 but it comes form the extra intrinsic form factor and the direct coupling.

(ii) The VMD term is not significant at high Q^2. (Also, the argument given parenthetically above that F_{VNN} has a monopole form is no longer valid.)

(iii) From fitting data

$$\beta_\rho = \begin{cases} 0.4 & \text{GK} \\ 0.7 & \text{IJL } (\Gamma_\rho \neq 0 \text{ choice, below}) \end{cases} \qquad (9)$$

so that the VMD terms are not in fact dominant for any $Q^2 > 0$.

Asymptotic VMD contribution. What does QCD say about the high Q^2 behavior of γ-nucleon couplings via vector mesons. The relevant diagram is drawn in Fig. (5).

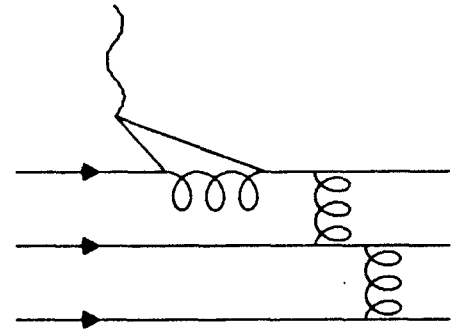

Fig. (5)

There are three extra propagators as compared to the intrinsic form factor diagram, which is identical to Fig. (3). The two extra quark propagators are absorbed into the vector meson wave function, and the loop integral is over the momentum fractions and relative transverse momenta carried by the quarks of the vector meson. The only extra Q^2 dependence is a $1/Q^2$ from the extra gluon propagator. Hence the entirety of Fig. (5) gives a $1/Q^6$ contribution to the form factor[14] which is exactly what is used.

Thus, by coincidence or otherwise, the asymtotic Q^2 dependence of both the direct and vector dominance terms are correct in these fits to the nucleon form factors, and clearly the vector dominance term has a pole in the right location, so one can understand why the fits to the form factors can be good.

Asymptotic neutron/proton ratio. IJL and GK give rather different values for the ratio F_{1n}/F_{1p} at high Q^2 and we would like to understand why this is so. The answer has to do with differing ways of accounting for the width of the ρ meson.

In a preliminary way, let us quote that at high Q^2 the form factor F_1 falls like $1/Q^4$ and will dominate the cross section unless it is unusually small and the form factor F_2 fall like $1/Q^6$. This means that at sufficiently high Q^2, F_1 and G_M are identical. We can also give a brief catalog of what is firmly known about the neutron form factors:

(a) $F_{1n}(0) = 0$ and $F_{2n}(0) = \kappa_n = -1.913$.

(b) From scattering of thermal neutrons off atomic electrons[15],

$$\frac{dG_{En}}{dQ^2}(0) = \frac{dF_{1n}}{dQ^2}(0) - \frac{\kappa_n}{4m_n^2} = 0.510 \pm 0.007 \text{ GeV}^{-2}$$

$$\frac{dF_{1n}}{dQ^2}(0) = -.0031 \pm 0.007 \text{ GeV}^{-2} \qquad (10)$$

Thus the slope of F_{1n} is small.

(c) The ratio of differential cross sections σ_n/σ_p is measured[16] at Q^2 = 2.5, 4, 6, 8, and 10 Gev^2 at one scattering angle. The ratio is about 1/4 at 10 GeV^2 which allows us to state

$$|G_{Mn}/G_{Mp}| \leq 1/2 \qquad (11)$$

at 10 GeV^2 and the upper limit is falling betweeen 5 and 10 GeV^2.

So if

$$F_{1n} = \frac{1}{2} g(Q^2) \left[\beta_\omega - \beta_\rho - \frac{\beta_\omega m_\omega^2}{m_\omega^2 + Q^2} + \frac{\beta_\rho m_\rho^2}{m_\rho^2 + Q^2}\right] \qquad (12)$$

and $m_\rho \approx m_\omega$ then forcing $F_{1n}' \approx 0$ at low Q^2 makes $F_{1n} \approx 0$ at all Q^2. But the ρ has a large width and we should account for it, for example following, as IJL do, Frazier and Fulco[17]. Using labels $f_{1,2}$ for convenience below we make a replacement for the ρ propagator in the preceding formula,

$$f_1 = \frac{m_\rho^2}{m_\rho^2 + Q^2} \Rightarrow$$

$$f_2 = \frac{m_\rho^2 + 8\Gamma_\rho m_\pi/\pi}{(m_\rho^2+Q^2) + (4m_\pi^2+Q^2)\Gamma_\rho A(Q^2)} \qquad (13)$$

with

$$A(Q^2) = \frac{2}{\pi}\sqrt{\frac{Q^2+4m_\pi^2}{Q^2}}\ \ln\left[\frac{\sqrt{Q^2+4m_\pi^2}+Q}{2m_\pi}\right] \qquad (14)$$

After this replacement, we still have $F_{1n}(0) = 0$, but

$$\frac{df_1}{dQ^2}(0) = -\frac{1}{m_\rho^2} \qquad (15)$$

whereas

$$\frac{df_2}{dQ^2}(0) = -\frac{1 + 8\Gamma_\rho/3\pi m_\pi}{m_\rho^2 + 8\Gamma_\rho m_\pi/\pi} \approx -\frac{2}{m_\rho^2} \qquad (16)$$

thus upsetting the balance between β_ρ and β_ω when the slope of F_{1n} is fit. One then gets the asymptotic result

$$\lim_{Q^2\to 0} \frac{F_{1n}}{F_{1p}} = \begin{cases} -4.40 & \text{IJL } (\Gamma_\rho \neq 0) \\ -0.028 & \text{GK } (\Gamma_\rho = 0) \end{cases} \qquad (17)$$

(More accurately, GK do say they account for the width of the ρ but in a way that doesn't have any affect on their fitting of the β's.)

The result seems unfair. The width of the ρ is large and should be taken into account, but the result IJL got by doing so is incompatible with the high Q^2 neutron data subsequently obtained. The result of GK fits the cross sections well.

IV. Proton Compton scattering

The elastic reaction $\gamma p \to \gamma p$ rpovides another check of vector meson dominance. We separate discussion of the high momentum transfer and low momentum transfer regions. At fixed large scattering angle in the center of mass, using QCD and direct coupling of the photons to the quarks in the proton illustrated in Fig. (6a) we have

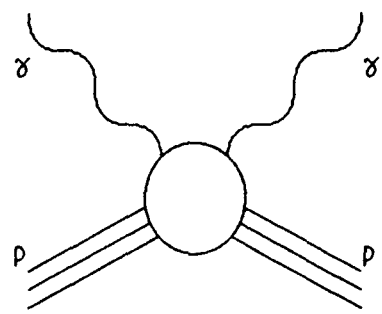

Fig. (6a)

a rule which follows from dimensional counting[18] which we quote and then use, (18)

$$\frac{d\sigma_{\gamma p\to\gamma p}}{dt} \propto s^{2-n_A-n_B-n_C-n_D} = s^{-6}$$

Here s is the c.m. energy squared, t is the momentum transfer squared, and n_A is the number of elementary fields in particle A.

If we mix QCD with vector meson dominance, then Fig. (6b) pertains and VMD tells us that

$$\frac{d\sigma_{\gamma p\to\gamma p}}{dt} = \sum_V \frac{e^2}{f_V^2} \frac{d\sigma_{Vp\to Vp}}{dt} \qquad (19).$$

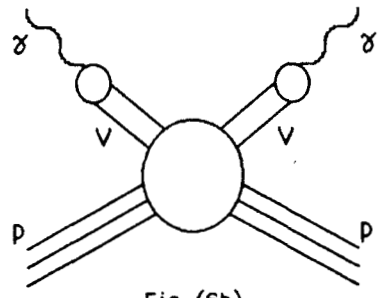

Fig. (6b)

Since there are now two extra elementary fields involved in the actual scattering,

$$\frac{d\sigma}{dt}_{\gamma p\to\gamma p} \propto s^{-8} \qquad (20).$$

Data from Shupe et al[19] is shown in Fig. (7), and it is clear that the s^{-6} behavior is more compatible with the data than s^{-8}. The direct coupling dominates.

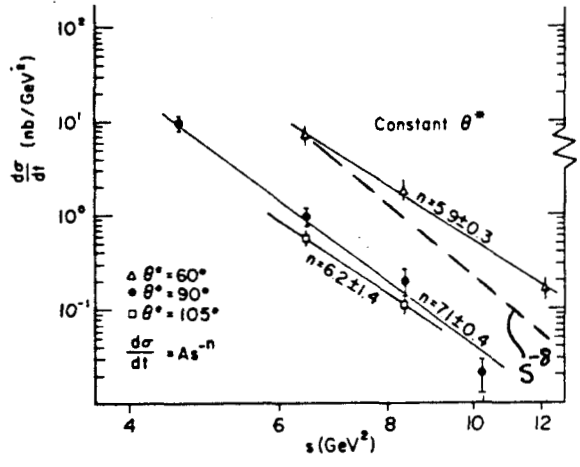

Fig. (7)

Compton scattering cross sections at constant c.m. scattering angle θ*. The straight lines are fits to the data.

On the other hand for total cross sections, the VMD relation[1]

$$\sigma_{\gamma p\to\gamma p} = \sum_V \frac{e^2}{f_V^2}\,\sigma_{Vp\to Vp} \qquad (21)$$

works to at least the 80% level with just V=ρ, ω, and φ. The total cross section of course is dominated by low momentum transfer processes, so the result seems to say that VMD gives a good result for low momentum transfer processes but not for high momentum transfer processes.

V. Concluding Remarks

Vector meson dominance is an approximation technique to be used when QCD calculations are intractable.

There are places where it works well. One example is the total Compton cross section, another is the fit to nucleon electromaagnetic form factor data inspired if not dictated by vector meson dominance. Still another not mentioned earlier is the agreement among vector meson coupling constants obtained from different reactions such as $\rho\to e^+e^-$, $\rho\to\pi^+\pi^-$, $\gamma p\to\rho p$, etc. (J.J. Sakurai published in 1966 a Physical Review Letter[20] with the fine title, "Eight ways of determining the ρ-meson coupling constant.") Let me also recommend examining Dr. Sloan's lecture in these proceedings.

However, as we have seen from some examples, VMD with a finite number of vector mesons does not give the high momentum transfer trends correctly. It might be commented that with an umlimited number of ever more massive vector mesons, it seems that high momentum transfer trends can be accomodated[21], but a detailed look at the demonstrations of this shoes that the arguments amount in the end to dimensional analysis. In any case, as a practical matter VMD is not useful if one has to use a large number of vector mesons, so its utility domain is an intermediate one where the energy is high enough so that time dilations allow any vector meson that the photon fluctuates into to live longer than a transit time across a nucleon or nucleus[1], but not so high a momentum transfer that direct couplings of the photon to quarks dominate the VMD contributions.

Acknowledgement

I thank the organizers for this fine conference and the NSF for financial support.

References and Footnotes

1. I learned much from the review article of T.H. Bauer, R.D. Spital, D.R. Yennie, and F.M. Pipkin, Rev. Mod. Phys. 50, 261 (1978). Historically, vector meson dominance has beginnings in both nuclear physics and particle physics. In the latter field, vector mesons were suggested to explain the nucleon electromagnetic form factors, for example by Y. Nambu, Phys. Rev. 106, 1366 (1957) [then using the name ρ^0 for what is today called the ω^0] and J.J. Sakurai, Ann. Phys. (N.Y.) 11, 1 (1960). In the former field, vector mesons were involved in the $\vec{L}\cdot\vec{S}$ terms in the nuclear force and one can examine G. Breit, Phys. Rev. 120, 287 (1960) [this article, incidentally, is

partly based on the thesis calculations of K. Lassila].
2. See for example H.J. Weber and M. Weyrauch, Phys. Lett. 17B, 13 (1986).
3. S.J. Brodsky and G.P. Lepage, Phys. Rev. D 24, 2848(1981).
4. T.W. Donnelly and A. Raskin, Ann. Phys. (N.Y.) 169, 247 (1986).
5. C.E. Carlson, Phys. Rev. D 34, 2704 (1986).
6. E.g., F. Foster and G. Hughes, Rep. Prog. Phys. 46, 1445 (1983).
7. L. Durand, P.C. DeCelles, and R.B. Marr, Phys. Rev. 126, 1882 (1962).
8. Foster and Hughes, Ref. 6, and V. Burkert in "Research Program at CEBAF (II): Report of the 1986 Summer Study Group" (Continuous Electron Beam Accelerator Facility, Newport News, V. Burkert et al, editors, 1987).
9. W.W. Ash etal, Phys. Lett. 28B, 148 (1967) and S. Stein etal, Phys. Rev. D 12, 1884 (1975).
10. F. Iachello, A.D. Jackson, and A. Lande, Phys. Lett. 43B, 191 (1973).
11. M. Gari and W. Krümpelmann, Z. Phys. A 322, 689 (1985) and Phys. Lett. B173, 10 (1986).
12. Höhler etal.
13. J.G. Körner and M. Kuroda, Phys. Rev. D 16, 2165 (1977).
14. I thank S.J. Brodsky for a comment on this point.
15. L. Koester, W. Nistler, and W. Waschkowski, Phys. Rev. Lett. 36, 1021 (1976); V.E. Krohn and G.R. Ringo, Phys. Rev. 148, 1303 (1966).
16. S. Rock et al, Phys. Rev. Lett. 49, 1139(1982).
17. W.R. Frazier and J.R. Fulco, Phys. Rev. 117, 1609 (1960).
18. G.P. Lepage and S.J. Brodsky, Phys. Rev. D 22, 2157(1980); S.J. Brodsky and G.R. Farrar, Phys. Rev. Lett. 31 1153 (1973) and Phys. Rev. D 11, 1309 (1975); V.A. Matveev, R.M. Muradyan, and A.V. Tavkheldize, Lett. Nuovo Cimento 7, 719 (1973).
19. M.A. Shupe etal, Phys. Rev. D 19, 1921 (1979).
20. J.J. Sakurai, Phys. Rev. Lett. 17, 1021 (1966).
21. S.J. Brodsky and J. Pumplin, Phys. Rev. 182, 1794 (1969).

SEMI-INCLUSIVE INELASTIC ELECTRON SCATTERING FROM NUCLEI

Edmond L. Berger
High Energy Physics Division
Argonne National Laboratory
Argonne, IL 60439

Abstract

A survey is presented of the physics of the electroproduction of hadrons from nuclear targets, $eA \to e'hX$. Variables and structure functions are specified. The parton model description of electroproduction is summarized; fragmentation functions are defined and their properties are listed. Specific measurements are suggested. Predictions of the pion exchange model are presented for the nuclear dependence of $eA \to e'hX$, including a discussion of the special subprocess $e\pi \to e'\pi$ in which scattering occurs from the pion constituents of nuclei.

1. Introduction

This workshop was organized to identify aspects of the structure of nucleons and nuclei which might be studied profitably with internal targets principally at the PEP electron positron storage ring at the Stanford Linear Accelerator Center. The energy of the incident electron (positron) beam would be limited initially to the "intermediate energy" range, $E \lesssim 15$ GeV.

A considerable literature has developed on nuclear dependence[1] of deep inelastic *inclusive* (or *single-arm*) lepton scattering, $eN \to e'X$, prompted by the observation[2,3,4] of intriguing differences between the inclusive structure functions of nucleons and nuclei (the "EMC" effect). In $eN \to e'X$, e and e' denote the initial and final electron, and N may be a free nucleon or a nucleus. Symbol X represents an inclusive sum over all final states. The data show directly that the quark momentum distribution of a nucleus differs significantly from that of a free nucleon. It is natural to inquire whether more differential measurements would shed further light on the dynamics underlying nuclear dependence. In this paper, I will focus on the theory and phenomenology of *semi-inclusive* (or *two-arm coincidence*) measurements: $eN \to e'hX$; h labels a specific final state hadron (e.g. π, K, p,...) whose momentum is measured.

My intent is *not* to present a comprehensive review of the electroproduction of hadrons. Rather, I will define variables and cross sections, raise some issues pertinent to nuclear dependence, provide references, and try to communicate a particle physicist's perspective on semi-inclusive processes to an audience composed primarily of nuclear physicists. One indication of the gulf that has developed between our disciplines is that we have developed different dialects and symbols: coincidence measurements and $(e, e'\pi)$ are the translations of semi-inclusive measurements and $eN \to e'\pi X$. Summaries of many general properties of the distribution of final state hadrons from leptoproduction experiments may be found in the review by Schmitz[5] and in numerous papers from the European Muon Collaboration.[6]

In Section 2, I define the five independent kinematic variables and four independent structure functions, $H_i^{N,h}$, necessary to specify the process $eN \to e'hX$. Next, in Section 3, the parton model description of inclusive and semi-inclusive inelastic electon scattering is reviewed.[7,8,9] Fragmentation functions are defined, some of their properties are listed, and measurements are suggested for determining specific fragmentation functions and their A dependence. In Section 4, I discuss a particular high twist contribution[10,11] to the quark fragmentation function.[10] Section 5 includes statements concerning the nuclear (A) dependence of $eA \to e'hX$ based on the pion exchange model[12] used to explain the nuclear dependence of the inclusive process $eA \to e'X$. In Section 6, I present predictions for the contribution of the elastic scattering process $e\pi \to e'\pi$ to $eA \to e'\pi X$, where the initial π in $e\pi \to e'\pi$ is a pion bound in nucleus A. A summary is found in Section 7.

2. Kinematics, Definitions, Cross Sections, and Structure Functions

I begin with the fully inclusive scattering of an electron or muon from either a nucleon N or a nuclear target A, sketched in Fig. 1(a). This process is usually denoted $\ell A \to \ell' X$, where symbol X represents an inclusive sum over all final states. The initial four-momenta of the lepton and the target are denoted by k and p. The four-vector q is the momentum transfer from the initial lepton to the target; that is, it is the difference between the four-momenta of the initial and final leptons. The laboratory energies of the initial and final leptons are E and E'; ν is the energy transfer, $E - E'$, in the laboratory frame. It is conventional to define $Q^2 = \mathbf{q}^2 - \nu^2 = -q^2 > 0$, and two dimensionless variables x and y, $x = Q^2/2M_N\nu$, $y = \nu/E$, where M_N is the mass of the nucleon. (Boldface symbols represent Euclidean three-vectors.)

The deep-inelastic domain is that in which the energy transfer is large compared to the four-momentum transfer,

$$\nu^2/Q^2 \equiv Q^2/(2M_N x)^2 \gg 1. \tag{1}$$

Light-front components $p^\pm$ of any four-vector p are defined by

$$p^\pm \equiv p^0 \pm \mathbf{n}\cdot\mathbf{p}, \tag{2}$$

where $\mathbf{n}$ is a unit vector chosen in the direction of the momentum transfer, $\mathbf{n} = -\mathbf{q}/|\mathbf{q}|$. For deep-inelastic scattering, $q^- \approx 2\nu$, $q^+ \approx 0$, $p\cdot q \approx \frac{1}{2}p^+q^- \approx p^+\nu$. Light-front momentum *fractions* are defined as ratios of plus-components (or of minus-components) of momenta and are thus invariant under longitudinal boosts.

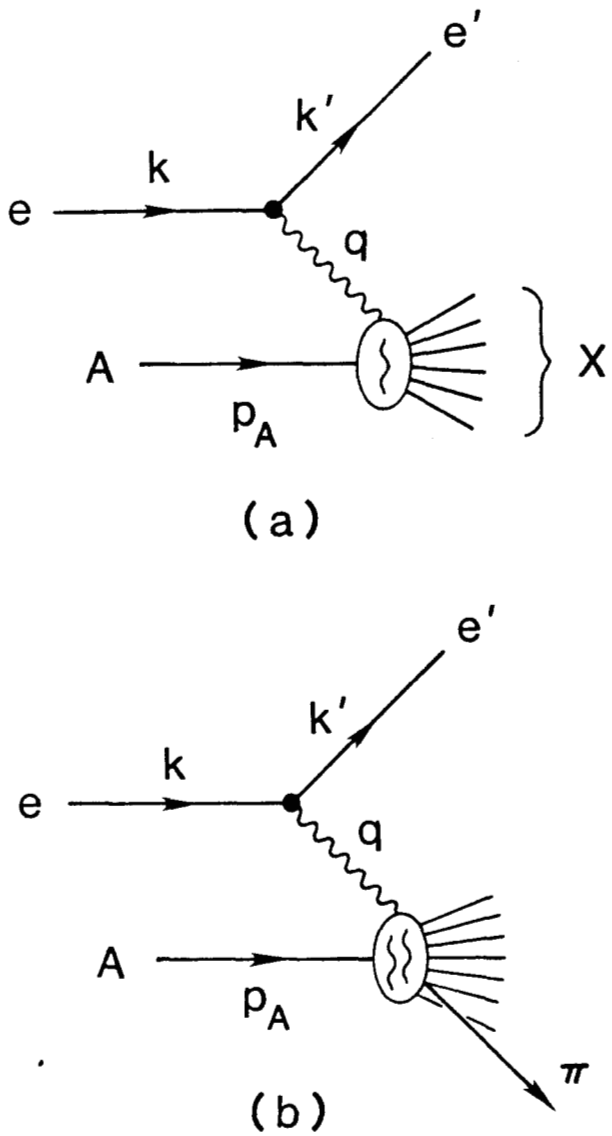

Figure 1: Sketches of a) inclusive reaction $eA \rightarrow e'X$ and b) semi-inclusive reaction $eA \rightarrow e'\pi X$.

In the one photon exchange approximation, the differential cross section for inclusive inelastic scattering of a *charged lepton* ($eA \rightarrow e'X$ or $\mu A \rightarrow \mu' X$) by any target is proportional to tensors $f_{\lambda\rho}(q,k)$ and $F^{\lambda\rho}(q,p)$ that depend respectively on the properties of the lepton and the target only:

$$\frac{d^2\sigma}{dx\,dy} = \frac{4\pi\,\alpha^2\,2M_N\,y}{Q^4} F^{\lambda\rho} f_{\lambda\rho}. \tag{3}$$

The tensor $F^{\lambda\rho}$ is a linear combination of "structure functions", invariant functions of Q^2 and $p\cdot q$, multiplied by universal covariant functions of p and q. In the case of the scattering of unpolarized particles, there are two structure functions for the conserved electromagnetic current: $F_i(x',Q^2)$, $x' \equiv Q^2/(2p\cdot q) = x(M_N\nu/p\cdot q)$.

In the deep-inelastic approximation,

$$F_N^{\lambda\rho} f_{\lambda\rho} = E\left\{(1-y)F_2^N(x',Q^2) + 2x'F_1^N(x',Q^2)(y^2/2)\right\}/y, \tag{4}$$

for scattering by a nucleon, and

$$F_A^{\lambda\rho} f_{\lambda\rho}/A = E\left\{(1-y)F_2^A(x'_A,Q^2) + 2x'_A F_1^A(x'_A,Q^2)(y^2/2)\right\}/y, \tag{5}$$

for a nucleus. Note that the nucleon number A is used as a label to identify the nucleus. In Eq. (5) for the nucleus, variable x'_A, which is a multiple of x', is defined by $x'_A \equiv Q^2A/(2p_A\cdot q)$. If the nucleus is at rest, x'_A is approximately equal to x: $x'_A = xAM_N/M_A \approx x$. The ranges allowed kinematically for x' of the nucleon and for x'_A are (0,1) and (0,A) respectively. The structure functions F_1^A and F_2^A are structure functions *per nucleon.*

In Eqs. (3)-(5) the momentum of the target enters only through the variable x'. This means that for a collection of incoherent free nucleons the *momentum averaged cross section* is related to *momentum averaged structure functions* in the same manner as the cross section per nucleon of the nucleus is related to the structure functions of the nucleus per nucleon. The momentum average is called *Fermi smearing.*

To separate the contributions of F_1^A and F_2^A at fixed x and Q^2 it is necessary to study the cross section as a function of $y = \nu/E = Q^2/(2M_NE)$, i.e., as a function of energy E. If the Callan-Gross relation is imposed, i.e. $[(F_2 - 2xF_1)/2xF_1] = \sigma_L/\sigma_T \simeq 0$, then the cross section per nucleon may be expressed in terms of $F_2^A(x,Q^2)$ alone:

$$\frac{d^2\sigma}{dx\,dy} = \frac{4\pi\alpha^2 M_N E}{Q^4}\left[1+(1-y)^2\right]F_2^A(x'_A,Q^2). \tag{6}$$

In the *semi-inclusive* or two-arm coincidence process, $eA \rightarrow e'hX$, sketched in Fig. 1(b), four momenta k, k', and p_h of the initial and final lepton and of hadron h are measured, but an inclusive sum is otherwise made over all possible final states X allowed kinematically. For a fixed total energy, five independent kinematic variables are necessary to specify the final state. Two of these variables, x and Q^2 are determined by the incident and outgoing lepton. They are identical to those of the fully inclusive case. The remaining three variables specify the final hadron h. I'll work with a set which has become standard in particle physics: z, $|\vec{p}_T|$, ϕ. Here, z is a ratio of dot products of four vectors:

$$z = \frac{p_h\cdot p_A}{q\cdot p_A}; \tag{7}$$

$\vec{p}_T$ is the component of the final hadron's three-momentum transverse to the direction specified by $\mathbf{q}$; and ϕ is an azimuthal angle:

$$\cos\phi = (-\mathbf{q}\times\mathbf{k})\cdot(-\mathbf{q}\times\mathbf{p}_h)/|\mathbf{q}\times\mathbf{k}||\mathbf{q}\times\mathbf{p}_h|. \tag{8}$$

I note that in the deep-inelastic approximation, z is the ratio of the minus-component of the momentum p_h to that of q:

$$z \cong p_h^-/q^-. \tag{9}$$

In the one photon exchange approximation, the spin-averaged cross section per nucleon for $eA \to e'hX$ may be expressed in terms of *four* independent structure functions which I denote $H_i^{A,h}(x, Q^2, z, p_T^2)$. In the deep inelastic limit, the cross section becomes

$$\frac{d\sigma^{A,h}}{dx\,dy\,dz\,dp_T^2\,d\phi} = \frac{4\pi\alpha^2 2M_N E}{Q^4}\left[xy^2 H_1^{A,h} + (1-y)H_2^{A,h} + \left(\frac{2p_T}{Q}\right)(2-y)(1-y)^{1/2}\cos\phi H_3^{A,h} + \frac{p_T^2}{Q^2}(1-y)\cos 2\phi H_4^{A,h}\right]. \quad (10)$$

Note that it is necessary to study ϕ dependence in order to isolate $H_3^{A,h}$ and $H_4^{A,h}$. Furthermore, y dependence (i.e. E dependence at fixed x, Q^2) must be measured in order to separate the four structure functions.

After integrating the cross section over ϕ, which eliminates dependence on H_3 and H_4, and over p_T^2, one obtains an expression in terms of only two independent dimensionless functions, denoted $\bar{H}_i(x, Q^2, z)$:

$$\frac{d\sigma^{A,h}}{dx\,dy\,dz} = \frac{4\pi\alpha^2 2M_N E}{Q^4}\left[xy^2\bar{H}_1^{A,h}(x,Q^2,z) + (1-y)\bar{H}_2^{A,h}(x,Q^2,z)\right]. \quad (11)$$

In terms of its dependence on y, this expression has the same structure as Eq. (4) or (5). If $R \equiv \sigma_L/\sigma_T \simeq 0$ in the semi-inclusive case, either because it is measured to be such or because the simple parton model is invoked, then $\bar{H}_2 \simeq 2x\bar{H}_1$, and Eq. (11) collapses to

$$\frac{d\sigma^{A,h}}{dx\,dy\,dz} = \frac{4\pi\alpha^2 M_N E}{Q^4}\left[1+(1-y)^2\right]\bar{H}_2^{A,h}(x,Q^2,z). \quad (12)$$

For any inclusive process, conservation of four-momentum specifies that

$$\sum_h \int d^3\mathbf{p}\, p^\mu \frac{d\sigma^h}{d^3\mathbf{p}} = P^\mu \sigma_{\rm tot}. \quad (13)$$

Here P^μ is the total four-momentum, and p^μ is the four-momentum of a hadron of species h. When this equation is applied to the *difference* $(E_h - p_{L,h})$, where E_h is the energy, and $p_{L,h}$ is the longitudinal component of $\mathbf{p}_h$ along the current-target axis, a relationship is obtained between the semi-inclusive functions, $\bar{H}_i^{A,h}(x, Q^2, z)$, and the fully inclusive structure functions, $F_i^A(x, Q^2)$. For each value of i,

$$\sum_h \int_0^1 dz\, z\bar{H}_i^{A,h}\left(x,Q^2,z\right) = F_i^A\left(x,Q^2\right). \quad (14)$$

In the next section I discuss expectations for the x, Q^2, and z dependences of $\bar{H}_i^A(x, Q^2, z)$ based on the parton model.

3. Parton Model Description

Probabilities $q_f^A(\xi, Q^2)$, $\bar{q}_f^A(\xi, Q^2)$, and $G^A(\xi, Q^2)$ are defined which represent the quark, antiquark, and gluon number densities in a *nucleus*, A. These are densities *per nucleon*, just as are $F_{1,2}^A(x, Q^2)$, meaning that a factor of A has been removed. (These densities "per nucleon" should *not* be assumed to be the parton densities of "nucleons within nuclei".) Subscript f on q_f and $\bar{q}_f$ labels the flavor of the quark or antiquark: u, d, s, c, b, t. Variable ξ is the light front fraction of the momentum of the target A carried by a parton of a given type.

In the parton model,[7,8] ξ, $q_f^A(\xi, Q^2)$, $\bar{q}_f^A(\xi, Q^2)$, and $G^A(\xi, Q^2)$ are measurable quantities. Indeed, $\xi \equiv x$, with x determined from the lepton kinematics, as defined above. Furthermore, the observable F_2^{eA} measures the fraction of the momentum of the target A, per nucleon, carried by quarks and antiquarks, weighted by the squares of the fractional quark charges e_f:

$$F_2^{eA}(x,Q^2) = \sum_f e_f^2 x\left[q_f^A(x,Q^2) + \bar{q}_f^A(x,Q^2)\right]. \quad (15)$$

3.1 Quark Fragmentation Region

Turning now to the semi-inclusive process $eA \to e'hX$, let's ask what $\bar{H}_2^A(x, Q^2, z)$ measures. Recall, $z = p_h{\cdot}p_A/q{\cdot}p_A$, Eq. (7). The answer to this question involves a discussion of what happens[7,8] to the struck quark after it absorbs the energy and momentum of the virtual photon. If quarks or gluons could be liberated, then, for sufficiently large Q^2, a free quark or free gluon would emerge from the target along the direction of the momentum of the exchanged photon. However, quarks and gluons are confined; they are not observed as asymptotic states. Thus, a spray of hadrons is observed in the final state, hadrons said to be "fragments of the struck quark". For sufficiently large ν and Q^2 this spray is a collimated "jet", well separated from the debris of the spectator partons in the target. This fragmentation process is described by a *fragmentation function*, $D_{h/f}(z, Q^2)$. (At sufficiently large Q^2, there will be a discernable gluon jet or jets in the final state in addition to the quark jet. Gluon fragmentation is also described by a fragmentation function, $D_{h/G}(z, Q^2)$. In this paper I will restrict my remarks to quark fragmentation.)

I define two regions of physical interest, distinguished by the magnitude of p_h. In the first region, the dot product $p_h{\cdot}p_A$ is finite, whereas $q{\cdot}p_A$ grows in proportion to Q^2. The final hadron h moves with small momentum in the rest frame of the target. Hadron h is said to be in the "target fragmentation region", where typical long-distance hadron physics governs the dynamics. Correspondingly, no specific parton model statements can be made about the z dependence of $\bar{H}_2^A(x, Q^2, z)$, and the concept of a fragmentation function does not apply in this region. However, one does expect scaling, i.e. approximate Q^2 independence, at fixed x.

In the second region, $p_h{\cdot}p_A$ grows in proportion to Q^2, $0 < z < 1$. It is in this region that hadron h is said to be a "frag-

ment of the quark" or antiquark struck by the virtual photon in the deep inelastic collision. If the separation in momentum of the struck quark from the target spectators is large enough, it is natural to assume that *fragmentation* of the quark into hadrons is independent of *production* of the quark. Fragmentation should therefore be described by a function of z, be independent of x, and be *independent of the process in which the quark was produced* (i.e. whether deep inelastic lepton scattering, electron-positron annihilation, hadron-hadron scattering, etc.).

After absorbing the virtual photon, the struck quark carries the same minus-component of momentum as the incident virtual photon, $q^- \simeq 2\nu$. Therefore, Eq. (9) allows us to interpret z as the fraction of the (light-front) momentum of the struck quark carried by h.

A word of caution is in order concerning the applicability of the concept of distinct regions of *target fragmentation* and *quark fragmentation*. Observably distinct regions require large enough separation in momentum of quark and target fragments. Rapidity is a useful variable for examining this issue.

The rapidity y_h of final state hadron h in $eA \to e'hX$ is defined as

$$y_h = \frac{1}{2} \ln \left[\frac{E_h + p_{h,L}}{E_h - p_{h,L}} \right], \tag{16}$$

where $E_h, p_{h,L}$ are the energy and longitudinal component of momentum of hadron h. (Longitudinal is defined by the direction of the momentum q.) The full range of y_h allowed kinematically is $Y = \ln W_X^2 = \ln(Q^2(1-x)/x)$; W_X is the invariant mass of the system X in the fully inclusive $eA \to e'X$.

It has been established[13] experimentally that the typical hadronic correlation length in rapidity is $\Delta y_h \simeq 2$. Therefore, if the dynamics of quark fragmentation is to be studied independently of "contamination" from target fragmentation, it is necessary that $Y \gtrsim 4$, or, equivalently, that

$$W_X = \left[\frac{Q^2(1-x)}{x} \right]^{1/2} \gtrsim 7.4\text{GeV}. \tag{17}$$

Studies of hadrons produced by neutrino interactions on protons[5] confirm that the separation of quark and target fragmentation products is apparent for $W_X > 8$ GeV but not for $2 < W_X < 4$ GeV. The values of W_X accessible in the CERN EMC[6] and Fermilab E-665 experiments extend high enough to satisfy Eq. (17). However, it appears doubtful that large enough values can be obtained at SLAC with $E \lesssim 15$ GeV.

If the inequality Eq. (17) is satisfied, it should be possible to measure fragmentation functions $D(z, Q^2)$ over essentially the full range of z, $0 < z < 1$. Somewhat smaller values of W_X may be adequate if attention is restricted to the large z region. As Y is increased above 2, or

$$W_X \gtrsim 3 \text{ GeV}, \tag{18}$$

the quark and target fragmentation regions begin to separate. As long as $Y \gtrsim 2$, the hadrons with the largest values of z are most likely quark fragments. Data[14] from $e^+e^- \to hX$ show that a distinct function $D(z)$ may have developed for $z \gtrsim 0.5$ at $W = 3$ GeV. The region extends to $z \simeq 0.2$ for $W = 4.8$ GeV, and to $z \simeq 0.1$ for $W = 7.4$ GeV. For $z > 0.3$, fragmentation functions have been obtained from data[15] on $ep \to e'\pi^\pm X$ at $E = 11.5$ GeV, with $3 < W_X < 4$ GeV.

At low values of Q^2, where the target and quark fragmentation regions overlap in momentum space, the concept of distinct production and fragmentation processes may not be relevant for the description of hadron formation in $eA \to e'hX$. This means, in particular, that nuclear A dependence observed in $H_2^A(x, Q^2, z)$ at modest values of Q^2 could not be attributed cleanly to nuclear dependence of the fragmentation process.

3.2 Quark Fragmentation Functions

In the region $0 < z < 1$ a function $D_{h/f}(z, Q^2)$ is defined which is the probability for a quark of flavor f to fragment into hadron h in an interval dz about z. In other words, $D_{h/f}(z, Q^2)$ is the *number density* in the quark of flavor f of hadrons of type h which carry a fraction z of the (light-front) momentum of the quark.

In the simple parton model $D(z, Q^2)$ is independent of Q^2, just as is $q_f(x, Q^2)$. Gluonic radiation in QCD generates logarithmic dependence[9] on Q^2 in both $D(z, Q^2)$ and $q_f(x, Q^2)$. Neither the full x dependence of $q(x, Q^2)$ nor the full z dependence of $D(x, Q^2)$ can be calculated as yet from first principles in quantum chromodynamics. At small values of z one expects[7] $D(z, Q^2)$ to be proportional to $1/z$, whereas at large z constituent counting rules and spin considerations may be used to specify[16,17,10] the power p in an expansion of the form $zD(z, Q^2) \propto (1-z)^p$.

In addition to Q^2 dependence of $q_f(x, Q^2)$ and $D(z, Q^2)$, gluonic radiative contributions in QCD generate a finite longitudinal structure function $\bar{H}_L(x, Q^2, z) = \bar{H}_2(x, Q^2, z) - 2x\bar{H}_1(x, Q^2, z)$ as well as finite contributions[18] proportional to H_3 and H_4 in Eq (10). In $eA \to e'hX$, intrinsic transverse momenta[19] of the partons in the initial hadron A and final hadron h are also a source of finite H_3 and H_4 contributions, as are higher twist effects.[10]

The statement of factorization plus the definition of fragmentation functions, $D(z, Q^2)$ for quarks and $\bar{D}(z, Q^2)$ for antiquarks, result in the following expression for the semi-inclusive structure function $\bar{H}_2(x, Q^2, z)$, valid in the quark fragmentation region, $z > 0$:

$$\bar{H}_2^{A,h}(x, Q^2, z) = \sum_f e_f^2 x \Big[q_f^A(x, Q^2) D_{h/f}(z, Q^2) + \bar{q}_f^A(x, Q^2) \bar{D}_{h/f}(z, Q^2) \Big], \tag{19}$$

with

$$\sum_h \int_0^1 dz\, z D_{h/f}(z, Q^2) = \sum_h \int_0^1 dz\, z\, \bar{D}_{h/f}(z, Q^2) = 1. \tag{20}$$

Combining Eqs. (6), (12), (15), and (19), we may observe that when $\sigma_L/\sigma_T \simeq 0$,

$$\frac{1}{\sigma_{\rm tot}}\frac{d\sigma(eA \to e'h\,X)}{dz} \equiv \frac{\dfrac{d\sigma(eA \to e'h\,X)}{dx\,dy\,dz}}{\dfrac{d\sigma(eA \to e'\,X)}{dx\,dy}}$$
$$= \frac{\sum_f e_f^2\left[q_f^A(x,Q^2)D_{h/f}(z,Q^2) + \bar{q}_f^A(x,Q^2)\bar{D}_{h/f}(z,Q^2)\right]}{\sum_f e_f^2\left(q_f^A(x,Q^2) + \bar{q}_f^A(x,Q^2)\right)}. \tag{21}$$

This equation simplifies considerably the case of a nucleus with an equal number of protons and neutrons *and* $x \gtrsim 0.3$. (For $x \gtrsim 0.3$, antiquark densities as well as the strange quark density may be ignored.) Thus,

$$\left.\frac{1}{\sigma_{\rm tot}}\frac{d\sigma(eA \to e'h\,X)}{dz}\right|_{\substack{x \gtrsim 0.3 \\ \text{Isoscalar} \\ \text{Target}}} = \frac{1}{5}\left[4D_{h/u}(z,Q^2) + D_{h/d}(z,Q^2)\right]. \tag{22}$$

The number of independent fragmentation functions is limited by isospin and charge conjugation invariance. For example, for pion production,

$$D_{\pi^+/u} = D_{\pi^-/d} = \bar{D}_{\pi^+/d} = \bar{D}_{\pi^-/u}. \tag{23}$$
$$D_{\pi^+/d} = D_{\pi^-/u} = \bar{D}_{\pi^+/u} = \bar{D}_{\pi^-/d}. \tag{24}$$
$$D_{\pi^+/s} = D_{\pi^-/s} = \bar{D}_{\pi^+/s} = \bar{D}_{\pi^-/s}. \tag{25}$$
$$D_{\pi^+/f} + D_{\pi^-/f} = 2D_{\pi^0/f}. \tag{26}$$

Data on *differences* of π^+ and π^- spectra obtained in studies with *isoscalar* targets may be used to isolate specific fragmentation functions. Using Eq. (22), together with Eqs. (23) and (24), I obtain

$$D_{\pi^+/u}(z,Q^2) = \frac{4}{3}\frac{1}{\sigma_{\rm tot}}\frac{d\sigma(eA \to e'\pi^+\,X)}{dz} - \frac{1}{3}\frac{1}{\sigma_{\rm tot}}\frac{d\sigma(eA \to e'\pi^-\,X)}{dz} \tag{27}$$

and

$$D_{\pi^-/u}(z,Q^2) = \frac{4}{3}\frac{1}{\sigma_{\rm tot}}\frac{d\sigma(eA \to e'\pi^-\,X)}{dz} - \frac{1}{3}\frac{1}{\sigma_{\rm tot}}\frac{d\sigma(eA \to e'\pi^+\,X)}{dz}. \tag{28}$$

Relationships (23) and (24) may be used to obtain a very simple expression for the *sum* of the π^+ and π^- yields from a nucleus with an *arbitrary neutron/proton ratio*. Ignoring the contributions from strange, charm, and heavier quarks and antiquarks (but retaining the contributions from the up and down antiquarks), we may show that

$$\frac{1}{\sigma_{\rm tot}}\left[\frac{d\sigma(eA \to e'\pi^+\,X)}{dz} + \frac{d\sigma(eA \to e'\pi^-\,X)}{dz}\right] = D_{\pi^+/u}(z,Q^2) + D_{\pi^-/u}(z,Q^2) = D_{\pi^+/d}(z,Q^2) + D_{\pi^-/d}(z,Q^2). \tag{29}$$

Equation (29) should be valid as long as it is safe to ignore the strange quark and antiquark densities, i.e. for $x \gtrsim 0.1$.

Note that the fully inclusive and semi-inclusive measurements provide *different* information. Inclusive scattering cross sections determine the quark and antiquark densities of the target, Eq. (15). Semi-inclusive cross sections determine fragmentation functions, Eqs. (22), (27)-(29). In rough terms, inclusive measurements provide data on constituent behavior in the initial state, *before* scattering occurs, whereas semi-inclusive measurements yield insight into the final state evolution of the scattered constituents into hadrons.

It has been suggested[20] that semi-inclusive data may be a source of information on the x dependence of quark and antiquark densities of nuclei. Equation (21) shows that extracting information on $q_f^A(x,Q^2)$ and $\bar{q}_f^A(x,Q^2)$ from semi-inclusive measurements is possible only if the fragmentation functions are known fairly precisely.

To appreciate the property of process independence of fragmentation functions, it is useful to examine briefly the description of hadron production in electron-positron annihilation at large Q^2, $e^+e^- \to h\,X$. In the one-photon approximation (ignored are effects associated with the Z^0), the cross section differential in z and angle θ is

$$\frac{d\sigma^h}{dz\,d\cos\theta} = \frac{3}{8}(1+\cos^2\theta)\frac{d\sigma_T^h(z,Q^2)}{dz} + \frac{3}{4}(1-\cos^2\theta)\frac{d\sigma_L^h(z,Q^2)}{dz}. \tag{30}$$

In this case $z = 2p_h \cdot q/Q^2$ and, in the e^+e^- center of mass frame, θ is the polar angle of hadron h with respect to the e^+e^- collision axis. The variable $\cos\theta$ replaces the variable y defined for $eA \to e'\pi\,X$. In the parton model, as extended by QCD,

$$\frac{d\sigma_T^h(z,Q^2)}{dz} = 3\sigma_0\sum_f e_f^2\left[D_{h/q}(z,Q^2) + \bar{D}_{h/q}(z,Q^2)\right], \tag{31}$$

where $\sigma_0 = 4\pi\alpha^2/3Q^2$. Through $O(\alpha_s)$, the total cross section for $e^+e^- \to X$ is

$$\sigma_{\rm tot}(Q^2) = 3\sigma_0\sum_f e_f^2\left(1 + \frac{\alpha_s(Q^2)}{\pi}\right), \tag{32}$$

where the term proportional to the strong coupling strength $\alpha_s(Q^2)$ is due to $\sigma_L^h(z,Q^2)$ in Eq. (30). Note the relative simplicity of Eq. (31) when compared with Eq. (19). Because quark and antiquark structure functions are absent from Eq. (31), the e^+e^- data permit a more direct measurement of the fragmentation function, albeit averaged over contributions from all flavors of quarks and antiquarks.

Data on the properties of fragmentation functions from e^+e^- annihilation experiments may be found in Refs. 14 and 21 and from leptoproduction experiments in Refs. 15, 22, and 23. An example is shown in Fig. 2.

3.3 Nuclear Dependence of Fragmentation Functions?

It may be noted that I have used the notation $D_{h/f}(z,Q^2)$, implicitly suggesting that this function does not depend on the target A. Should the fragmentation functions $D_{h/f}(z,Q^2)$ and $\bar{D}_{h/f}(z,Q^2)$ in Eq. (19) depend on A?

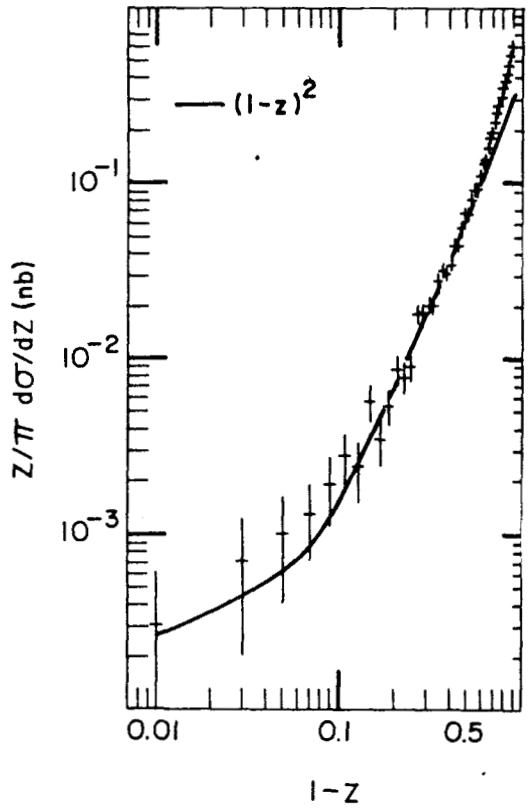

Figure 2: Fragmentation function $D(z,Q^2)$ from $e^+e^- \to \pi X$ at $Q^2 = (29\ \text{GeV})^2$, Ref. 21.

If the statement of factorization is correct, then $D_{h/f}(z,Q^2)$ must be independent of A because factorization is the assertion that this function is a process independent property of hadron h. In QCD, there can be gluon exchanges between the active quark and the spectator partons in either A or h. To demonstrate the validity of factorization one must show that these gluon interactions cancel. A proof exists[24] for the Drell-Yan process $hA \to \gamma^* X$, but no proof of factorization in QCD has yet been attempted for the crossed process of interest here, $\gamma^* A \to hX$. Presumably a "target-length condition" would emerge from such a proof, analogous to the relationship between Q^2 and A necessary for factorization in the Drell-Yan case: $Q^2 \gtrsim cA^{1/3}$.

Intuitively one would expect factorization to hold only if the separation in momentum of the struck quark from the target spectators is large enough. In a heavy nucleus, even in the quark fragmentation region, it is plausible that hadron production may be modified with respect to that observed in deuterium due to reinteraction effects of either the fragmenting quarks or the hadrons as they propagate through the nuclear medium. It is often assumed that fragmentation takes place within a limited interval in space-time.[8,25] Because of Lorentz dilation, the process will occur over a distance which increases as ν, the energy of the struck quark, increases. *For large enough ν, fragmentation would then occur outside the nucleus.* In this case the main effect on fragmentation would be the size of the quark cross section in nuclear matter. At large Q^2 this virtual quark is expected to have a small interaction probability.[26]

To explore these issues, it is of obvious interest to study possible nuclear A dependence of fragmentation as a function of ν, z, and Q^2. The dependence on all these variables is important. Equations (22), (27), (28), and (29) show that fragmentation functions, or combinations thereof, could be extracted from experiments done on different nuclei. The ratios of these results, $D^A(z,Q^2)/D^{D_2}(z,Q^2)$, should be independent of A if there is no nuclear dependence. If the ratios approach unity at large ν, the expectation of a small cross section for quark interaction in nuclear matter would be confirmed.

Available data on nuclear dependence of fragmentation are of limited statistics.[27-31] Effects of quark and/or hadron reinteraction are seen at low ν, but there is no evidence for such effects for $\nu > 70$ GeV. I will not discuss further here physical processes which may be important at low ν where the characteristic quark fragmentation length is comparable to or less than the radius of the nucleus. Treatments may be found in Refs. 8, 25, and 26.

4. High-Twist Contribution

High twist terms[10,11] in the structure functions, $q_f(x,Q^2)$, and fragmentation functions, $D(z,Q^2)$, are contributions which decrease in proportion to an inverse power of Q^2 relative to the leading scaling term. They arise from subprocesses in which more than one constituent in a given hadron is active in the hard scattering process. Sharing of the large momentum among several active constitutents requires that more than the minimum number of constituents be off-shell by $\sim Q^{-2}$. The presence of additional gluon or quark propagators supplies the additional inverse powers of Q^2 in the hard scattering amplitude.

In this section I call attention to a particular high-twist contribution to the fragmentation function[10] $D_{\pi/q}(z,Q^2)$. It is of interest in its own right and quantitatively important for the range of values of Q^2 accessible in $eA \to e'hX$ experiments at SLAC. Moreover, it is an important "background" to the coherent $e\pi \to e'\pi$ signal, discussed in Section 6, where the initial π is bound in the nucleus.

Consider the diagram for $\gamma^* q \to \pi q$ sketched in Fig. 3. The initial quark is a constituent of a target nucleon or nucleus. The final pion is represented by its minimum Fock space component $|q\bar{q}\rangle$. For "favored" fragmentation processes such as $u \to \pi^+ X$ or $d \to \pi^- X$, this diagram permits one to calculate both the expected large z form of the scaling term in $D(z,Q^2)$ and a Q^{-2} contribution appropriate at large z. Higher components, including gluons or additional $q\bar{q}$ pairs, are present and would supply terms suppressed by added powers of Q^2.

Extracting a fragmentation function from Fig. 3, one obtains[10,32]

$$D_{\pi/q}(z,Q^2) = A\left[(1-z)^2 + \frac{1}{3}F_\pi(Q^2)\right], \qquad (33)$$

where A is a normalization constant discussed below, and $F_\pi(Q^2)$

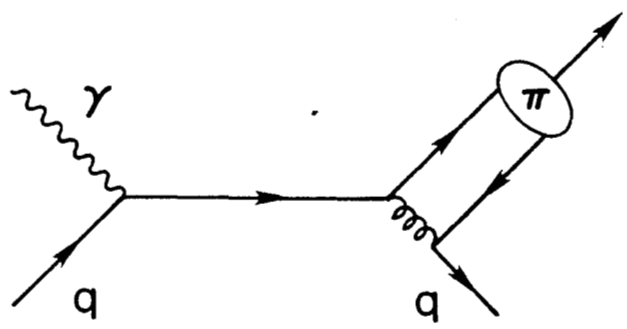

Figure 3: Diagram illustrating a higher-twist subprocess which contributes to $\gamma^* q \to \pi X$.

is the electromagnetic form factor of the pion. In the scaling limit, $Q^2 \to \infty$, Eq. (33) shows that $D_{\pi/q}(z)$ should fall off as $(1-z)^2$ as $z \to 1$. However, for finite Q^2, the function $D_{\pi/q}(z)$ is predicted to approach a finite value as $z \to 1$ whose magnitude decreases as Q^{-2}.

Information on the z dependence of $D(z, Q^2)$ at large z comes from $e^+e^- \to \pi X$. An example is shown in Fig. 2. A fit to $(1-z)^n$ for $z > 0.5$ yields[21] $n = 2.08 \pm 0.21$ compatible with the expectation of $n = 2$. The value of Q^2 for these data, $Q^2 = (29\ \mathrm{GeV})^2$, is so large that the high twist term is essentially absent.

Within the context of the approximations made in Ref. 10, the relative normalization between the two terms in Eq. (33) is specified. The overall normalization of the scaling term, $(1-z)^2$, is not fixed, but data[21] at large z can be used to determine a value of A in Eq. (33). Doing so, I find values in the range $1 \lesssim A \lesssim 2$.

For large z, the cross section corresponding to Fig. 3 has the form[10]

$$\frac{d\sigma(x, Q^2, z)}{dx\, dy\, dz} \propto \frac{1}{2}\left[1 + (1-y)^2\right](1-z)^2 + \frac{4}{9}(1-y)F_\pi(Q^2). \tag{34}$$

Note that the high twist term discussed here contributes only to the structure function $\bar{H}_2$. A test of Eq. (34) requires examining data on $eN \to e'\pi X$ for large z and verifying whether there is a contribution to $\sigma(x, Q^2, z)$ which is proportional to $(1-y)/Q^2$. Tests made with neutrino and antineutrino data have shown encouraging results,[34-36] but much higher statistics are desirable over a broad range of Q^2.

5. Nuclear Dependence of $H_i^{A,h}\,(eA \to e'hX)$

Models[1] have been proposed to explain the nuclear (A) dependence of the fully inclusive structure functions $F_i^A(x, Q^2)$. In all approaches deep inelastic scattering occurs from quark and antiquark constituents. The approaches differ in the manner in which the constituents are grouped into color singlet degrees of freedom within a nucleus. These models provide expectations for the A dependence of the quark and antiquark densities, $q^A(x, Q^2)$ and $\bar{q}^A(x, Q^2)$.

If factorization is invoked, then *all* of these models of the nuclear dependence of $F_2^A(x, Q^2)$ lead to the expectation that at sufficiently large Q^2 the A dependence of the semi-inclusive structure function is expressed as

$$H_2^{A,h}(x, Q^2, z) = \sum_f e_f^2 x\Big[q_f^A(x, Q^2) D_{h/f}(z, Q^2) + \bar{q}_f^A(x) \bar{D}_{h/f}(z, Q^2)\Big]. \tag{35}$$

The only dependence on A resides in $q^A(x, Q^2)$ and $\bar{q}^A(x, Q^2)$ which are the measured parton densities of a nucleus.

In the remainder of this section I will comment briefly on further implications of the pion exchange model developed at Argonne.[12] It begins with the basic hypothesis that a nucleus is a *bound system of A nucleons plus an indefinite number of mesons.* The mesons are associated with nuclear binding. The structure functions (and hence the quark distributions) of the nucleons and mesons are not affected by the nuclear medium. They are the same as those measured on free nucleons and mesons.

The many-body bound state wave function of the nucleus is expressed in terms of the light-front momenta of the constituent nucleons and mesons. Fractions of the light-front momentum of the nucleus carried by nucleons and mesons are defined. These are fractions per nucleon, denoted x_π for π's, and x_N for nucleons. Number densities per nucleon of mesons and nucleons are also defined, $f_\pi^A(x_\pi)$ and $f_N^A(x_N)$, and computed from the bound state wave function. The mean number of pions per nucleon is given by the integral $\int f_\pi^A(x_\pi)\, dx_\pi = \langle n_\pi^A \rangle$. Use of light-front dynamics guarantees that the number densities are invariant under longitudinal Lorentz boosts.

In the pion exchange model, the fully inclusive structure function of a nucleus, per nucleon, $F_2^A(x, Q^2)$ is expressed in terms of the structure functions $F_2^N(x, Q^2)$ and $F_2^\pi(x, Q^2)$ measured on unbound nucleons and pions:

$$F_2^A(x, Q^2) = \int_x f_\pi^A(x_\pi) F_2^\pi\left(\frac{x}{x_\pi}, Q^2\right) dx_\pi + \int_x f_N^A(x_N) F_2^N\left(\frac{x}{x_N}, Q^2\right) dx_N. \tag{36}$$

Analogous expressions may be derived for the quark and antiquark densities per nucleon, $q^A(x, Q^2)$ and $\bar{q}^A(x, Q^2)$, as well as for the gluon density $G^A(x, Q^2)$. For example,

$$q^A(x, Q^2) = \int_x f_\pi^A(x_\pi) q^\pi\left(\frac{x}{x_\pi}, Q^2\right) dx_\pi + \int_x f_N^A(x_N) q^N\left(\frac{x}{x_N}, Q^2\right) dx_N. \tag{37}$$

According to the pion exchange model calculations, $\langle n_\pi^{\mathrm{Fe}} \rangle = 0.095$, meaning that in an Fe nucleus, there are on average 5 to 6 pions from which deep inelastic scattering occurs. The mean momentum per nucleon carried by those pions is $\langle x_\pi^{\mathrm{Fe}} \rangle = 0.052$. The "books are balanced" in the sense

that momentum lost to nucleons through binding, $\langle x_N^A \rangle < 1$, is carried by exchange pions. The average nucleon momentum $\langle x_N^A \rangle = 1 - \langle x_\pi^A \rangle \simeq 0.95$. This average nucleon momentum may be related to the mean one-nucleon separation energy observed in the reaction $(e, e'p)$. As shown in Fig. 4, the pion exchange model provides a unified description of $R_{\rm EMC}(x)$ for all x. The value of $\langle n_\pi^A \rangle$ controls the size of the enhancement of $R_{\rm EMC}(x)$ above unity at small x, whereas $\langle x_\pi^A \rangle$ controls the shape and size of the depression below unity for intermediate x. In the model, there is a modest change of $\langle n_\pi^A \rangle$ with A. For Al, Fe, and Au, $\langle n_\pi^A \rangle = 0.089$, 0.095, and 0.114.

Without further approximations, the pion exchange model may be used to obtain a convolution formula for semi-inclusive structure functions per nucleon:

$$\bar{H}_i^{A,h}(x,Q^2,z) = \int_{x_\pi > x} dx_\pi f_\pi^A(x_\pi) \bar{H}_i^{\pi,h}\left(\frac{x}{x_\pi}, Q^2, z\right) + \int_{x_N > x} dx_N f_N^A(x_N) \bar{H}_i^{N,h}\left(\frac{x}{x_N}, Q^2, z\right). \quad (38)$$

This equation expresses the semi-inclusive structure function of a nucleus as the incoherent sum of the semi-inclusive structure functions of the nucleon and pion constituents of the nucleus. The pion and nucleon densities, $f_\pi^A(x_\pi)$ and $f_N^A(x_N)$ are unchanged from the fully inclusive case.

Structure functions $\bar{H}_i^{N,h}(x,Q^2,z)$ are those measured on a deuteron target. The structure functions $\bar{H}_i^{\pi,h}(x,Q^2,z)$ would require experiments on a pion target: $e\pi \to e'hX$. In the fully inclusive case, it was possible to construct the functions $q^\pi(x,Q^2)$ and $F_2^\pi(x,Q^2)$ used in Eqs. (36) and (37) from measurements of pion induced massive lepton pair production $\pi N \to \mu\bar{\mu}X$. I know of no similarly direct way to obtain the function $\bar{H}^{\pi,h}(x,Q^2,z)$ which enters Eq. (38). Therefore, in order to extract specific predictions from Eq. (38), the x and z dependences of $\bar{H}^{\pi,h}$ would have to be modeled. In this sense, Eq. (38) is less predictive than Eq. (36).

One particularly interesting contribution to $eA \to e'\pi X$ is associated with elastic scattering from pions bound in the nucleus. This term is described in the next section.

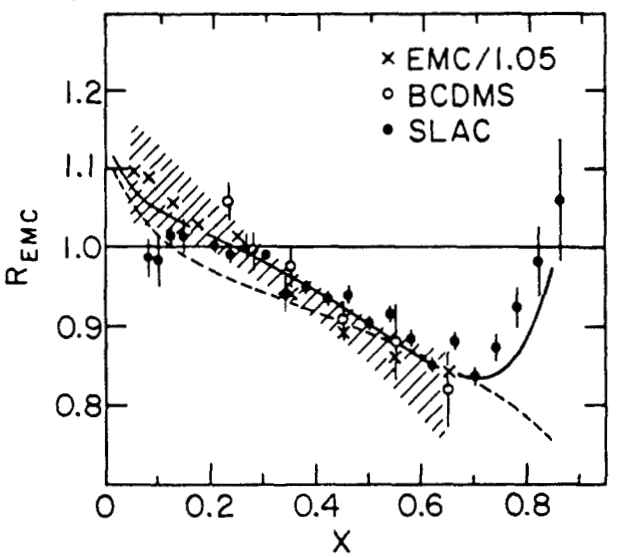

Figure 4: A compilation of data published prior to 1986 on the ratio of structure functions $R_{\rm EMC}(x,Q^2) \equiv F_2^{\rm Fe}(x,Q^2)/F_2^D(x,Q^2)$ for deep inelastic electron and muon scattering. Shown are published results from the EMC Collaboration (Ref. 2), divided by 1.05, as well as data from the BCDMS Collaboration (Ref. 4), and from SLAC experiments (Ref. 3). The shaded band indicates the EMC group's estimate of experimental systematic uncertainties. The solid curve is calculated from the pion exchange model of Ref. 12. The dashed curve shows the expectation of Q^2 rescaling (Ref. 37) with $Q^2 = (200x + 10)$ GeV^2 appropriate for the kinematics of the EMC data.

6. Special Term $e\pi \to e'\pi$

In this section I consider briefly the possibility of elastic scattering from a constituent pion in the nucleus.[38,39] In the deep-inelastic limit, this subprocess provides the following specific contributions[39] to $\bar{H}_i^A$:

$$\bar{H}_1^{A,\pi}(x,Q^2,z) = 0 \quad (39)$$

$$\bar{H}_2^{A,\pi}(x,Q^2,z) = \delta(1-z)F_\pi^2(Q^2)\int_{x_\pi > x} dx_\pi f_\pi^A(x_\pi)\delta\left(\frac{x}{x_\pi} - 1\right) = \delta(1-z)x f_\pi^A(x) F_\pi^2(Q^2). \quad (40)$$

Since the pion electromagnetic form factor, $F_\pi(Q^2)$, falls as Q^{-2} at large Q^2, this special contribution to $eA \to e'\pi X$ decreases as Q^{-4}. However, if it could be identified it would allow a direct measurement of the pion momentum density $xf_\pi(x)$ in nuclei. The characteristic signatures of the contribution are the delta function, $\delta(1-z)$, in Eq. (40) and the Q^{-4} dependence.

If Eq.(40) is integrated over x, one obtains

$$\int \bar{H}_2^{A,\pi}(x,Q^2,z) = \delta(1-z)\langle x_\pi^A \rangle F_\pi^2(Q^2). \quad (41)$$

Recall that $\langle x_\pi^A \rangle$ is the mean momentum per nucleon carried by constituent pions in the nucleus.

A high twist Q^{-4} contribution of the form of Eq. (40) is also expected for scattering from a free proton, $ep \to e'\pi X$, and is therefore included in the function $\bar{H}_2^{N,\pi}(x,Q^2,z)$ which appears in Eq. (38). To proceed experimentally towards the identification of the special term in Eq.(40), it would be necessary to begin with precise measurements with a deuteron target to determine the full Q^2 dependence of $\bar{H}_2^{N,\pi}(x,Q^2,z)$ at large z. The special term in Eq.(40) could then be determined from the difference

$$\bar{H}_2^{A,\pi}(x,Q^2,z) - \int_{x_N > x} dx_N f_N^A(x_N)\bar{H}_2^{N,\pi}\left(\frac{x}{x_N}, Q^2, z\right).$$

Of practical concern for the identification of the special term are:

i. Since the pion must exit the nucleus without being absorbed, does the term survive?

ii. Is the term large enough to stand out above various backgrounds?

The concept of "color transparency"[26,40,41] suggests that the final pion will indeed emerge unscathed from the nucleus at large enough Q^2. Exclusive reactions such as $e\pi \to e'\pi$ are dominated at large Q^2 by contributions from the valence Fock state of the pion, $|q\bar{q}\rangle$. The valence state has small transverse separation of the constituents and therefore negligible hadronic interactions. Correspondingly, a large momentum transfer exclusive reaction can occur deep within a nuclear target without any elastic or inelastic initial or final state interaction. In addition to $e\pi \to e'\pi$, aother example would be $\pi A \to \pi p(A'-1)$. To obtain a rough estimate of the expected background to $e\pi \to e'\pi$, I adopt Eq.(19) for the contribution to single pion electroproduction from "conventional sources". Since the $e\pi \to e'\pi$ signal is prominent only at large z, Eq.(33) can be used for the fragmentation function, with $A = 1$. Summing over the charges of pions, and integrating over all x and $0.9 < z < 1$, I obtain

$$\int_0^1 dx \int_{0.9}^{1.0} dz \bar{H}_2^{A,\pi}(x,Q^2,z) = \frac{1}{3}\int_0^1 F_2^A(x,Q^2)dx \int_{0.9}^{1.0} dz F_\pi(Q^2), \tag{42}$$

valid for values of Q^2 such that the high twist term in Eq.(33) is dominant at large z. Since $\int F_2^A(x,Q^2)dx \simeq 0.5(5/18)$, I derive a signal to background ratio of

$$r^A \equiv \frac{\sigma(\text{special term})}{\sigma(\text{background})} \simeq 200\langle x_\pi^A\rangle F_\pi(Q^2). \tag{43}$$

The mean momentum per nucleon carried by pions is computed[12] to be $\langle x_\pi^{Fe}\rangle \simeq 0.05$, and I approximate[33] $F_\pi(Q^2)$ by $F_\pi(Q^2) \simeq (1+Q^2/0.4\ \text{GeV}^2)^{-1}$. Correspondingly, $r^{Fe} > 1$ for $Q^2 \lesssim 3\ \text{GeV}^2$.

This computation indicates that when an integral is made over all x, the contribution of the special term exceeds that of conventional sources of single pions as long as $Q^2 \lesssim 3\ \text{GeV}^2$. An experiment therefore looks feasible. However, at least two reservations should be stated. First, the restriction $Q^2 \lesssim 3\ \text{GeV}^2$ is in conflict with the assumption of the deep inelastic limit. A more thorough computation of the structure functions, Eqs. (39) and (40) should be made with non-asymptotic terms retained in the kinematics. Second, since experiments are done at fixed x or over a limited interval in x, a more relevant estimate of the signal to background ratio would be obtained by comparing Eqs. (19) and (40) at fixed x rather than after an integral is done over all x.

7. Summary and Conclusions

Some of the points made in this paper include:

- There are four independent structure functions for $eA \to e'hX$. To separate them at fixed x and Q^2, it is necessary to study the ϕ, p_T, and $y(=\nu/E)$ dependences of the cross section.
- Values of $W_X^2 = Q^2(1-x)/x \gtrsim 50\ \text{GeV}^2$ are required for clean separation of quark and target fragmentation effects in the data and unambiguous extraction of fragmentation functions $D(z,Q^2)$ for the full range of z. Values of $W_X \gtrsim 5$ GeV may be adequate if attention is restricted to $z \gtrsim 0.2$.
- In the region $z > 0$, factorization is the statement that the structure functions may be expressed as a sum of terms each having the form $q(x,Q^2)D(z,Q^2)$.
- Study of the nuclear A dependence of fragmentation as a function of Q^2, ν, x, and z will provide information on the breaking of factorization and on the dynamics of parton and hadron interactions in nuclear matter.
- Interesting high twist contributions to the quark fragmentation function $D_{\pi/q}(z,Q^2)$ may be extracted by studying the behavior of $D_{\pi/q}(z,Q^2)$ at large z and modest Q^2.
- The pion exchange model developed to interpret the A dependence of inclusive structure functions, $F_2^A(x,Q^2)$, leads to specific convolution formulas for the semi-inclusive structure functions $\bar{H}_2^{A,h}(x,Q^2,z)$.
- A special term, $e\pi \to e'\pi$, in which scattering occurs coherently from pions bound in nuclei provides a distinct contribution to $eA \to e'\pi X$. Identification of this contribution would allow a direct measurement of the pion momentum distribution in nuclei, $f_\pi(x_\pi)$.

Acknowledgment

I have benefitted from numerous discussions with Dr. Fritz Coester at Argonne.

References

1. For a recent review of data and interpretations, see E. L. Berger and F. Coester, Argonne report ANL-HEP-PR-87-13, to be published in Ann. Rev. of Nucl. Part. Sci. **37**, (1987).
2. J. J. Aubert *et al.*, Phys. Lett. **123B**, 275 (1983).
3. A. Bodek *et al.*, Phys. Rev. Lett. **50**, 1431 (1983), and **51**, 534 (1983); R. G. Arnold *et al.*, Phys. Rev. Lett. **52**, 727 (1984).
4. G. Bari *et al.*, Phys. Lett. **163B**, 282 (1985); A. C. Benvenuti *et al.*, CERN-EP/87-13, Phys. Lett., to be published.
5. N. Schmitz, Acta Phys. Pol. **B11**, 913 (1980).
6. European Muon Collaboration, M. Arneodo *et al.*, Z. Phys. **C31**, 1 (1986); J. J. Aubert *et al.*, Z. Phys. **C31**, 175 (1986); M. Arneodo, *et al.*, Nucl. Phys. **B258**, 249 (1985); M. Arneodo *et al.*, Z. Phys. C , (1987).
7. R. P. Feynman, *Photon-Hadron Interactions* (W. A. Benjamin, Reading, Mass., 1972).

8. J. D. Bjorken, Lectures at International Summer Inst. on Theoretical Physics, Hamburg, 1975, *Current Induced Reactions*, edited by J. G. Körner, G. Kramer, and D. Schildknecht (Springer-Verlag, 1976), p. 93.

9. G. Altarelli, R. K. Ellis, G. Martinelli, and S.-Y. Pi, Nucl. Phys. **B160**, 301 (1979).

10. E. L. Berger, Phys. Lett. **89B**, 241 (1980) and Z. Phys. **C4**, 289 (1980).

11. E. L. Berger, S. J. Brodsky, and G. P. Lepage in *Proceedings of the Drell-Yan Workshop*, Fermilab, 1982, edited by E. L. Berger, P. Malhotra, R. Orava, and H. Thacker, (Fermilab, 1982) p. 187. See also E. L. Berger and S. J. Brodsky, Phys. Rev. **D24**, 2428 (1981).

12. E. L. Berger, F. Coester, and R. Wiringa, Phys. Rev. **D29**, 398 (1984); E. L. Berger and F. Coester, Phys. Rev. **D32**, 1071 (1985); E. L. and Coester, F. in *Quarks and Gluons in Particles and Nuclei*, ed. by Brodsky, S. and Moniz, E. (World Scientific, Singapore, 1986), p. 255.

13. See, for example, E. L. Berger, Nucl. Phys. **B85**, 61 (1975).

14. J. L. Siegrist *et al.*, Phys. Rev. **D26**, 969 (1982); G. Hanson *et al.*, Phys. Rev. **D26**, 999 (1982).

15. DESY-Cornell Collaboration, G. Drews *et al.*, Phys. Rev. Lett. **41**, 1433 (1978).

16. R. D. Field and R. P. Feynman, Nucl. Phys. **B136**, 1 (1978).

17. R. Blankenbecler and S. J. Brodsky, Phys. Rev. **D10**, 2973 (1974); S. J. Brodsky and J. F. Gunion, Phys. Rev. **D17**, 848 (1978).

18. H. Georgi and H. D. Politzer, Phys. Rev. Lett. **40**, 3 (1978).

19. R. Cahn, Phys. Lett. **78B**, 269 (1978).

20. See, for example, A. Harindranath, K. Lassila, and J. Vary, Iowa State University report, 1986.

21. M. Derrick *et al.*, Phys. Lett. **164B**, 199 (1985); D. Bender *et al.*, Phys. Rev. **D31**, 1 (1985).

22. European Muon Collaboration, J. J. Aubert *et al.*, Phys. Lett. **160**, 417 (1985); M. Arneodo *et al.*, Phys. Lett. **150B**, 458 (1985); M. Arneodo *et al.*, Phys. Lett. **145B**, 156 (1984).

23. FNAL-Serpukhov-Moscow-Michigan Collaboration, J. P. Berge *et al.*, Nucl. Phys. **B203**, 1 (1982).

24. G. T. Bodwin, Phys. Rev. **D31**, 2616 (1985); J. C. Collins, D. E. Soper, and G. Sterman, Nucl. Phys. **B261**, 104 (1985).

25. A. Bialas and T. Chmaj, Phys. Lett. **133B**, 241 (1983); A. Bialas, Z. Phys. **C26**, 301 (1984); A. Bialas, Acta Phys. Polon. **B11**, 475 (1980); A. Bialas and E. Bialas, Phys. Rev. **D21**, 675 (1980) and Phys. Rev. **D20**, 2854 (1979).

26. A. H. Mueller in *Quarks, Leptons, and Supersymmetry*, Proceedings of the XVII Rencontre de Moriond, 1982, edited by J. Tran Thanh Van (Editions Frontieres, France), p. 13.

27. European Muon Collaboration, A. Arvidson *et al.*, Nucl. Phys. **B246**, 381 (1984).

28. MIT-SLAC collaboration, L. S. Osborne *et al.*, Phys. Rev. Lett. **40**, 1624 (1978).

29. J. P. Berge *et al.*, Phys. Rev. **D18**, 3905 (1978).

30. H. Deden *et al.*, Nucl. Phys. **B198**, 365 (1982).

31. Fermilab-Cracow-Michigan State-Univ. of Washington collaboration, L. Hand *et al.*, Acta Phys. Polon. **B9**, 1087 (1978).

32. To obtain Eq. (33), I begin with Eq. (6) of the first paper cited in Ref. 10. I then set $\langle p_T^2 \rangle = 0.4$ GeV^2. Noting next that the pion's electromagnetic form factor $F_\pi(Q^2)$ is measured (Ref. 33) to be approximately $(1 + Q^2/0.4 \text{ GeV}^2)^{-1}$, I replace $\langle p_T^2 \rangle / Q^2$ by $F_\pi(Q^2)$. For further discussion of the normalization of the high twist contribution to the longitudinal structure function in terms of $F_\pi(Q^2)$, see Ref. 11.

33. C. J. Bebek, *et al.*, Phys. Rev. **D13**, 25 (1976).

34. BEBC-WA59 Collaboration, P. J. Fitch *et al.*, Z. Phys. **C31**, 51 (1986).

35. M. Haguenauer *et al.*, Phys. Lett. **100B**, 185 (1981).

36. D. Allasia *et al.*, Phys. Lett. **124B**, 543 (1983).

37. F. E. Close, R. G. Roberts, and G. C. Ross, Phys. Lett. **129B**, 346 (1983).

38. F. Güttner, G. Chanfray, H. J. Pirner and B. Povh, Nucl. Phys. **A429**, 389 (1984).

39. E. L. Berger and F. Coester, in preparation.

40. G. Bertsch, S. J. Brodsky, A. S. Goldhaber, and J. G. Gunion, Phys. Rev. Lett. **47**, 297 (1981).

41. S. J. Brodsky, XIII International Symposium on Multiparticle Dynamics, 1982, edited by W. Kittel, W. Metzger, and A. Stergiou (World Scientific, 1982), 963.

EXPERIENCE WITH A WARM GAS JET TARGET FOR NUCLEAR PHYSICS

Andrew S. Hirsch, Physics Department, Purdue University,
West Lafayette, IN 47907

Abstract: A room temperature pulsed internal gas jet target has been used in the main ring at both FNAL and the Brookhaven AGS in order to study proton-nucleus collisions. We have produced ultra-thin targets in the range of 1-100 ng/cm^2 using a variety of pure and mixed gases.

Introduction

The viability of a gas jet target situated in the main accelerator ring has been demonstrated in a series of experiments conducted at both FNAL and the AGS at BNL. Our primary objective in these experiments has been to study proton-nucleus collisions, and to this end we have used a variety of noble gas targets mixed with molecular hydrogen. This paper summarizes our several thousand hours of experience with the gas jet.

In 1975, a feasibility study of a room temperature gas jet target for use in Fermilab's main ring was undertaken by Frank Turkot and Paul Mantsch.[1] A gas jet target built in the U.S.S.R. by the Dubna Laboratory had been in use in the Internal Target Area at FNAL since 1972. This target utilized liquid He both to cool the gas injected into the vacuum chamber and to cryopump the gas after it had passed through the beam. It was hoped that in developing a room temperature gas target, many of the complexities encountered in operating the cooled jet could be avoided.

From the experimental point of view, several features were deemed important: 1) a variable range of target thickness from 1 ng/cm^2 to 100 ng/cm^2, 2) a jet pulsing time at least 10% or 300 msec of the acceleration period, 3) a transverse dimension of the jet approximately equal to the horizontal size of the beam, 4) a density of gas not in the jet proper 1/1000 of that in the jet, 5) good access to the interaction region for detectors, 6) continuous operation with good reliability, 7) a design which permitted the installation of a spare nozzle in about 1 hour. Of course, accelerator operation imposes constraints on any potential gas jet target situated in the main ring. Scheduled access is usually limited to once per week at most. The attenuation of the beam must be small (< .1%) per jet pulse, and the extraction efficiency of the beam from main ring unaffected by the jet operation.

The de Laval Nozzle

The nozzle chosen for use at Fermilab was a 100 μm diameter de Laval nozzle (fig. 1) When a gas initially at rest in the entrance chamber under pressure escapes through such a nozzle, in general, two possibilities arise. The first is that the pressure in the flow decreases in the converging entry section up to the throat and increases in the diverging exhaust section of the nozzle. The flow remains subsonic throughout. This occurs when the receiver pressure remains above a certain value, P_2 (fig. 2).

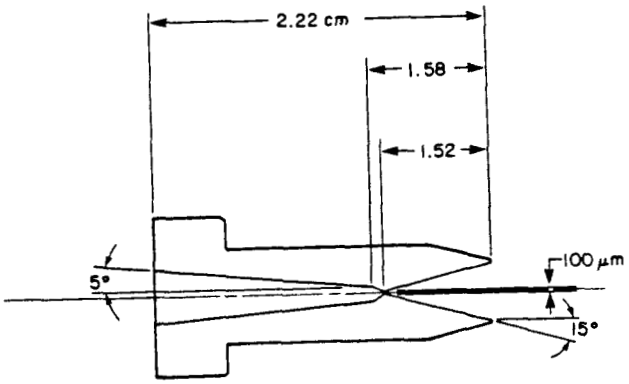

Fig. 1: de Laval Nozzle

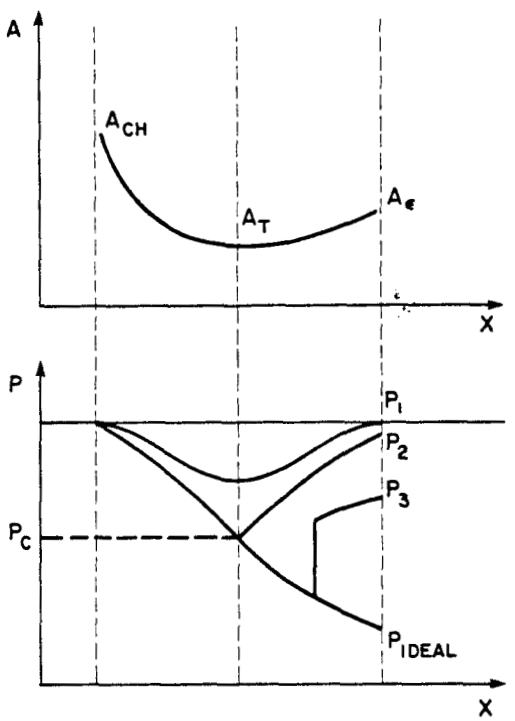

Fig 2: Area and Pressure as a function of distance along the nozzle

At P_2, the pressure at the throat achieves its critical value and is given by

$$P_c = P_i \left(\frac{2}{\gamma + 1} \right)^{\frac{\gamma}{\gamma - 1}} \qquad (1)$$

where γ is the ratio of specific heats and P_i is the inlet pressure. When the receiver pressure falls below the value P_2, the other possibility occurs; the pressure in the flow decreases up to the throat, as before, but now becomes just sonic at the throat. The flow up to the throat is not affected by further decreasing the receiver pressure. In the diverging exhaust section of the nozzle, the pressure continues to drop. If ideal flow is to be achieved, the receiver pressure must be matched to the pressure in the flow at the nozzle exit. Otherwise, the adjustment to the receiver pressure is made via a shock front. This behavior is summarized in figure 2. Under proper conditions, the adjustment to the receiver pressure will occur several centimeters outside the nozzle. This is the regime in which the nozzle was operated in our experiments.

Approximating the flow using a one-dimensional gas dynamics model that assumes an ideal gas in steady-state isentropic flow, we can find a relation among the parameters of interest, namely the density in the jet when its radius is R, the radius r, of the nozzle at its throat, the pressure, P_i, at the inlet, and the temperature, T_o of the gas at the inlet. (fig. 3)

$$\rho = \left(\frac{r}{R}\right)^2 \left(\frac{P_i M}{C\,T_o}\right)\left(\frac{2}{\gamma+1}\right)^{\frac{1}{\gamma-1}}\left(\frac{\gamma-1}{\gamma+1}\right) \qquad (2)$$

M is the molecular weight of the gas and C is the molar gas constant. The gas flow through the nozzle is given by

$$Q = \pi r^2 P_i \left(\frac{2}{\gamma+1}\right)^{\frac{1}{\gamma-1}} \left(\frac{2\gamma}{\gamma+1}\right)\left(\frac{C}{MT_o}\right)T_t \qquad (3)$$

where T_t is the temperature of the gas in the target box. We have measured the throughput of both a 100 and 150 μm nozzle by injecting a known quantity of helium gas into the nozzle. As shown in figure 4, the agreement with eq. (3) is quite satisfactory.

Measurement of the density profile of the jet can be made using the technique of hot wire anemometry. This technique, when used to measure a single component gas, gives reasonable agreement with the predicted results based on eq. (2). Typically, the measured values are about 70% of the predicted. Measurements performed on a 100 μm de Laval nozzle gave a linear relation between the jet full width at half maximum (fwhm), 2R, and the distance Z from the nozzle. At inlet pressures above about 40 psia using hydrogen, the FWHM is independent of the the inlet pressure and is approximated by

$$2R = 0.16Z + 0.4 \qquad (4)$$

where both R and Z are in mm. At pressures below 40 psia, there is a transition to a wider profile. At 35 psia,

$$2R = 0.38Z + 0.25 \qquad (5)$$

The target thickness, $2R\rho$, can now be expressed in terms of the inlet pressure and the distance from the nozzle.

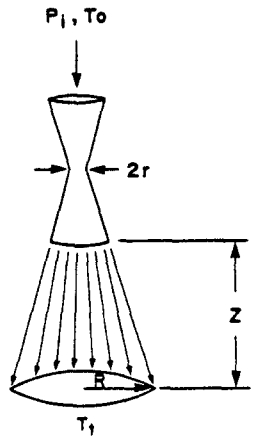

Fig. 3: de Laval Nozzle Schematic

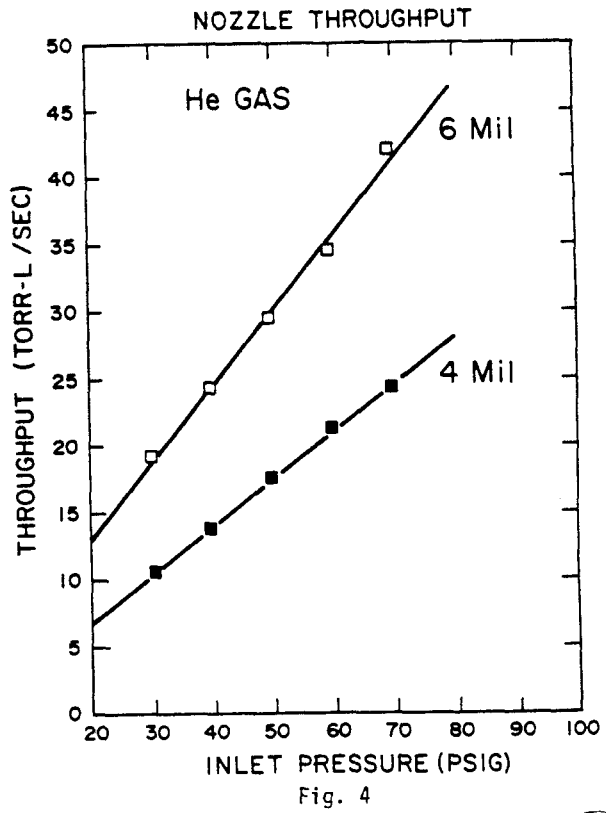

Fig. 4

The Jet Housing and Target Box

The de Laval nozzle was contained within a jet housing, shown in figure 5, which was situated above the target chamber. The housing was isolated from the target box by means of a 12 in. vacuum gate valve. During operation, the nozzle was positioned via remote control in both the vertical and horizontal planes by maximizing the beam-jet interaction as measured by the p-p elastic scattering from the hydrogen component of the target gas. At BNL, the nozzle opening was 3.8 cm above the nominal beam center line. Horizontal motion of the jet was ±0.5 in. along a line at 45° with respect to the incident beam direction. Inlet gas pressure was typically about 25 psig for all gases used. At pressures much lower, a suitable jet was not formed, whereas at higher pressures, radiative beam losses became a problem. The inlet valve shown in figure 5 was actually an electrically operated solenoid located inside the vacuum immediately before

the nozzle. When the solenoid opens, the gas is forced through the nozzle and forms a conically shaped jet within 10 ms. When the solenoid is closed to end the jet firing cycle, a small amount of gas is left between the valve and the nozzle. To aid in producing a sharp end to the jet and to help main ring vacuum recover, a small 75 liter buffer volume at 1 μm Hg was connected to the nozzle through a second 'exhaust' solenoid valve. This valve was opened 20 ms after the inlet valve closed and remained open for 200 ms in order to remove the residual gas.

A collection cone with an opening diameter of 5.0 cm was located below the jet and approximately 3.8 cm below the nominal beam position. Approximately 80% of the gas in the jet was captured by the cone which led to a 1000 liter buffer volume maintained at high vacuum by two unbaffled 5600 l/s oil diffusion pumps (DP). The remaining 20% of the gas escaped into the main ring target box and was pumped away by the main ring vacuum system, discussed below.

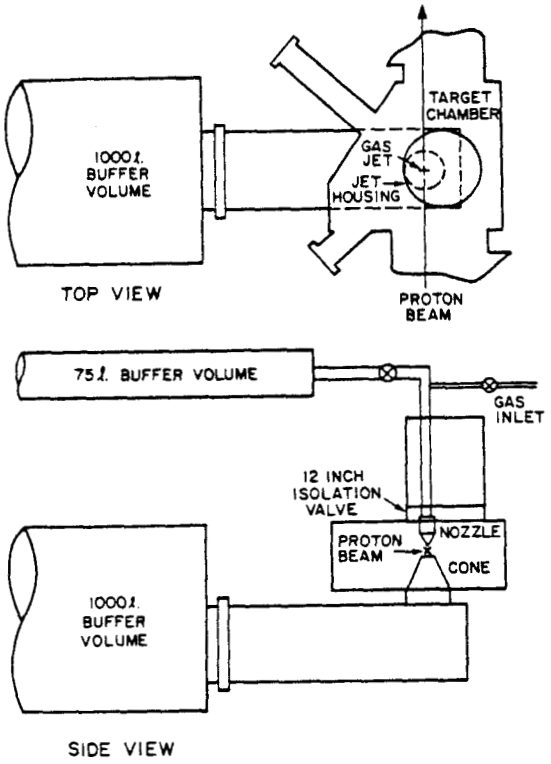

Fig. 5: Target box and Housing Jet

The Vacuum System and Jet Gating Electronics

The pressure rise due to the 20% of the gas which escaped capture by the buffer volume posed a threat to both the circulating beam and to our detectors. Hence, it was essential to contain the pressure fluctuations each time the jet was fired, and to return quickly to ambient vacuum levels.

At FNAL, the long straight sections facilitated the installation of the target box and additional pumps along the beam line. The layout at FNAL is shown in figure 6. Two 10 in. DPs, each 4000 l/s, were located on the target box. Additionally, there were three upstream and two downstream DPs on the main ring and at the ends of the straight section there were two ion pumps upstream and one ion pump downstream. Table 1 indicates the maximum pressures encountered at each pump during a typical pulse and compares these values with the corresponding ambient vacuum readings.

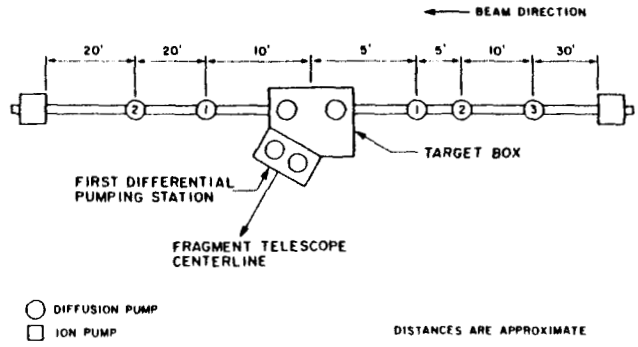

Fig. 6: FNAL Beam Line

Table 1
Pressure fluctuations at various locations in the FNAL vacuum system (see Fig. 6).

Location	Peak (Torr)	Recovery (Torr)
IP downstream	2×10^{-8}	6×10^{-9}
2nd DP downstream	1×10^{-7}	5×10^{-8}
1st DP downstream	4×10^{-6}	1×10^{-7}
Buffer Volume	3.5×10^{-4}	1×10^{-7}
Target Box	1.5×10^{-6}	5×10^{-7}
1st DP upstream	2.5×10^{-7}	1×10^{-7}
2nd DP upstream	7×10^{-8}	1×10^{-7}
3rd DP upstream	9×10^{-8}	6×10^{-8}
IP upstream	1×10^{-8}	4.5×10^{-9}

Installing the jet at the AGS required that all of the up and downstream pumping be accomplished within the eight feet between bending magnets. To this end, up and downstream of the central target chamber two end boxes of 200 l total volume were added (fig. 7) Each end box was pumped on by a 5600 l/s 10 in. DP with a cold water baffle. This cut the

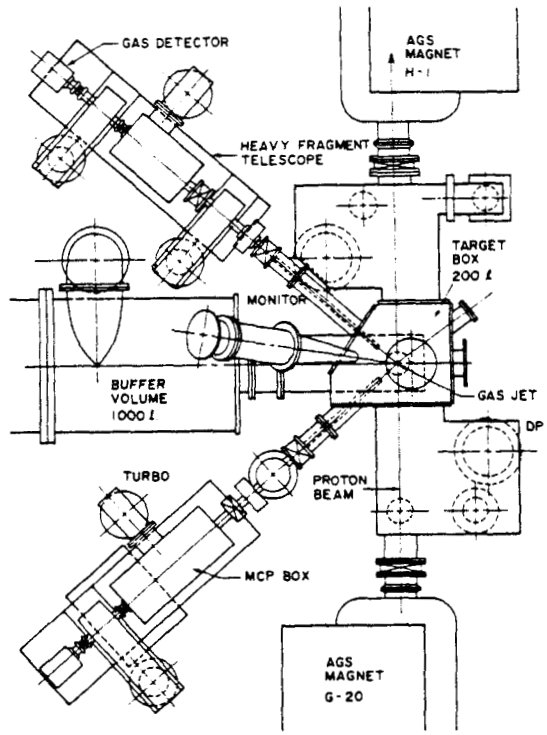

Fig. 7: BNL Detector Schematic

effective pumping speed in half but kept oil out of the main ring. Each end box was followed by a differential pumping chamber which further reduced the pressure rise as it travelled down the main ring beam pipe. Each differential chamber was pumped on by two baffled 750 l/s 6 in. DPs. Any gas getting past the differential pumping chambers entered the main ring vacuum system. During normal pulsing, the pressure fluctuation was damped to normal after about 40 feet. Table 2 contains the vacuum levels for a typical pulse at the AGS.

Table 2
Pressure fluctuations at various locations in the AGS vacuum system (see Fig. 7).

Location	Peak (Torr)	Recovery (Torr)
Upstream target box	5×10^{-6}	1.3×10^{-6}
Downstream target box	7×10^{-6}	7×10^{-7}
Central target box	4×10^{-6}	9×10^{-7}
Buffer volume	1×10^{-5}	2.8×10^{-6}
TEL1 1st DP	5.2×10^{-7}	5.2×10^{-7}
TEL1 MCP Box	3.8×10^{-6}	3.8×10^{-6}
TEL3 1st DP	1×10^{-7}	1×10^{-7}
TEL3 MCP Box	7×10^{-7}	7×10^{-7}

The entire vacuum system was monitored via cold cathode discharge gauges (DG) on all high vacuum boxes ($<10^{-5}$ Torr) and by thermocouple gauges (TC) located on each fore and rough pump and on the foreline on the low pressure side of each DP. All gauge readings were displayed in the operations trailer. Each gauge controller had trip sets which were fed into a central interlock box. In the event the vacuum rose above the trip point, the appropriate valves would be closed, DPs shut down, and the jet turned off.

The operation of the jet and vacuum systems was conducted from the operations trailer some 40 m away from the internal target. The jet was positioned, first vertically, then horizontally, by means of digital counter-comparators to some nominal preset position. A "jet scan" could then be performed by changing the horizontal position until the maximum p-p elastic counting rate was found. The timing of the jet firing was referenced to a clock signal provided by the accelerator. This signal, referred to as T_o represents the start of the acceleration cycle. Figure 8 shows schematically the gating electronics with times for a typical accelerator cycle. The gating signals were displayed on a CRT along with the beam intensity, the magnetic field ramp, the target box vacuum, and the horizontal and vertical beam position. A typical display is shown in figure 9. The jet timing parameters used during data acquisition are summarized in table 3.

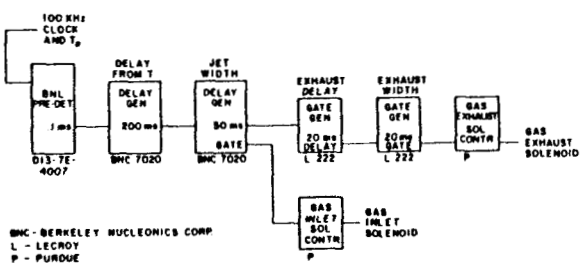

Fig. 8: Gating Electronics

Table 3
Typical times for the operation of the gas jet at FNAL and BNL.

Occurrence	Time after T_o at FNAL	Time after T_o at AGS (ms)
Gas valve opens	2.00	200
Gas valve closes	3.00	250
Evacuation valve opens	4.05	270
Evacuation valve closes	5.05	470

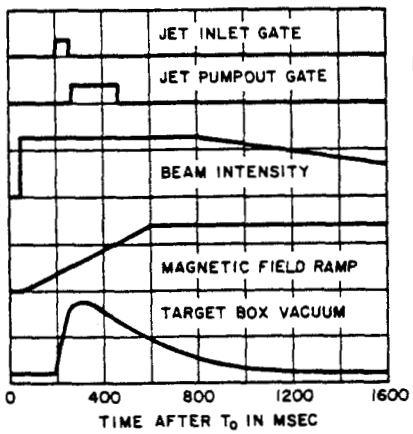

Fig. 9: CRT Display of Gating Signals

The Monitor Telescope and Jet Density Profile

Our primary objective has been the study of proton-nucleus collisions. In particular, we have been interested in the production of heavy nuclear fragments which emergy from the interaction between high energy (>1 GeV) protons and heavy nuclear targets, such as neon, argon, krypton, and xenon. One might expect that a supersonic jet target could be made from each of these gases. This is true, except that as the atomic weight of the gas increases, the input pressure must be increased in order to form a jet which has a reasonable profile. At the same time, the target thickness becomes so high that it causes significant beam losses. For this reason we used mixtures of molecular hydrogen and the above noble gases. These mixtures are presented in table 4. The use of the mixed gas target allowed us to normalize the heavy fragment data using the proton-proton elastic cross section.

The kinematics of p-p elastic scattering gives the following result for the relation between the recoil kinetic energy and the angle between this proton and the incident beam direction:

$$T(\theta) = \frac{2Mc^2\cos^2\theta}{((E+Mc^2)/(E-Mc^2)) - \cos^2\theta} \qquad (6)$$

where E is the total energy of the incident proton and M is the mass of the proton. The appropriate choice of θ will give recoil energies in a range that is manageable for silicon surface barrier detectors. At both FNAL and the AGS, θ was close to 85°. Over the incident energy range at the AGS, the recoil energy given by eq. (6) necessitated two two monitor arrays. These were located at 84.8° and inclined out of the plane defined by the AGS main ring by 30° and 34°. These telescopes were designated M4 and M5 respectively. The detector thicknesses were chosen to cover the range of 5 to 18 MeV in M4 and 8 to 28 MeV

Table 4
Target gas mixtures at FNAL and BNL

FNAL target gases	BNL target gases
10% xenon-90% hydrogen	1% xenon-99% hydrogen
10% krypton-90% hydrogen	3% xenon-97% hydrogen
20% krypton-80% hydrogen	100% hydrogen
25% argon-75% hydrogen	
60% neon-40% hydrogen	
100% methane	
100% hydrogen	

in M5. All detectors had an active area of 50 mm^2 with thicknesses listed in table 5. Because the passage of the beam through the jet caused both visible and ultra-violet radiation to be emitted from the jet, a 2.2 cm diameter 1360 $\mu g/cm^2$ nickel foil was placed between each monitor telescope and the jet to shield the detectors. The visible light was a useful indicator that the jet was working and was monitored by a TV camera stationed at a quartz window on the target chamber.

Table 5
Monitor silicon surface barrier detector thickness at BNL

Detector	Thickness (μm)
M4DE	200
M4E	2000
M4V	1000
M5DE1	500
M5DE2	2000
M5E	2000
M5V	1000

The monitor telescope housing was isolated from the target box by a gate valve. This enabled the monitor to be let up to atmosphere without disturbing the target box vacuum.

In figure 10, we display data from the high energy monitor M5, for incident beam momentum 13.9 < P_{inc} < 15.1 GeV/c, and a 50 ms jet of H_2 at 25 psig. The p-p elastic cross section in this region varies slowly with beam energy and is about 6.5 mb/sr at 84.8°. In order to extract the target thickness of hydrogen, we have modeled the jet density distribution as a Gaussian,

$$\rho(X) = \rho_o e^{-(X-X_o)^2/2\sigma_x^2} \qquad (7)$$

where ρ_o is the peak density and the parameter X_o is the displacement of the jet centroid from the nominal beam-jet intersection point. Since, according to eq. (6), to each recoil kinetic energy there corresponds a unique scattering angle, one can treat each energy bin of the recoiling proton as sampling a different portion of the jet density distribution, as shown in figure 11. Thus, the density distribution becomes

$$\rho(\phi) \propto e^{-(\phi-\phi_o)^2/2(\sigma_\phi/\cos\phi_o)^2} \qquad (8)$$

where, $\phi = \frac{\pi}{2} - \theta$, $\sigma_\phi/\cos\phi_o = \sigma_x/D$ and D is the -jet detector distance.

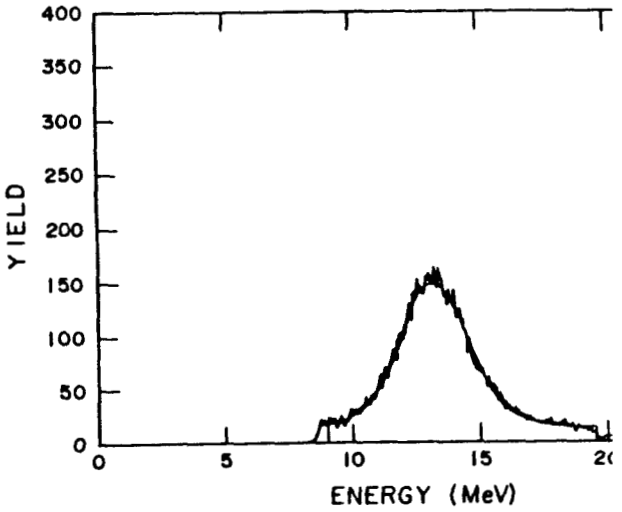

Fig 10a: p-p Elastic Peak

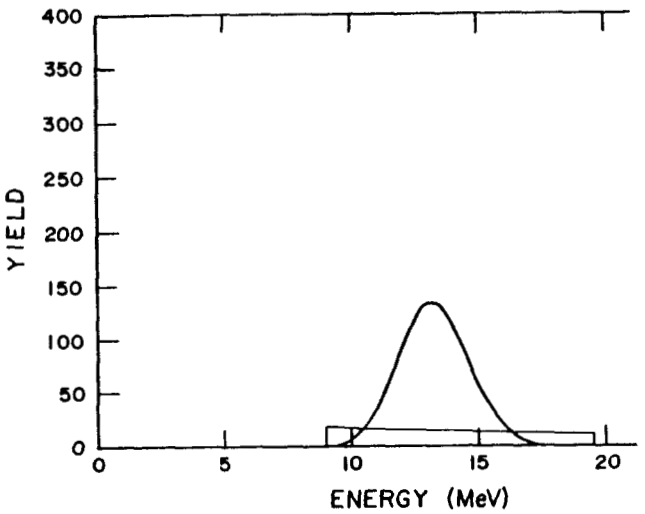

Fig. 10b: p-p Elastic and Background Contributions

In addition to the jet profile, we have added an empirical background contribution to account for scattering from residual gas in the target box of the form

$$A + BT + CT^2 \qquad (9)$$

where T is the detected proton's kinetic energy. We have fit the data according to the above procedure and show both the total fit and the separate contributions of the jet and background in figure 10. The target thickness is found by integrating eq. 7 over the variable X. After correcting the data for multiple scattering losses, about 20%, this yields a target thickness of $(2.5 \pm 0.2) \times 10^{15}$ atoms/cm^2 and a fwhm of 11.8 + 0.1 mm. These results lie in between those predicted on the basis of eqs. (2), (4), and (5) with Z = 38 mm. This is quite reasonable since at 25 psig we have not yet made the transition to the narrow jet profile. Further details concerning the monitor array and fitting procedures can be found in references 2 and 3.

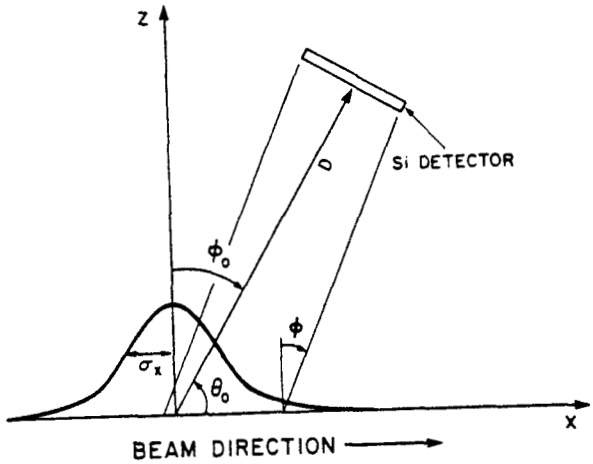

Fig. 11: p-p Elastic Geometry

The Fragment Telescopes

Heavy nuclear fragments emerging from high energy p-nucleus collisions typically have energies between 1 and 2 MeV per nucleon. Reaction products extend down to virtually zero kinetic energy. Thus, it is important that one use a thin target in order to limit the energy lost via ionization. In addition, one must design a low mass fragment detection telescope in order to determine the mass, charge, and energy over a wide range of fragment types and energies.

The fragment telescope at FNAL, shown schematically in figure 12, was located at a scattering angle of 34° and was attached to the first differential pumping station. Micro-channel plates, MCP, were used to provide fast timing signals, following the design of Zebelman, et al.[4] Since these detectors require a vacuum of less than 5 x 10^{-5} Torr to ensure their long-term operation, they were housed in aluminum boxes which could be vacuum isolated from the rest of the system. A turbomolecular pump (450 l/s) maintained the vacuum in this portion of the detector telescope.

The telescope terminated in a gas ionization chamber. An unsupported 3/4 in. diameter polypropylene window, 80 $\mu g/cm^2$ thick separated the aluminum boxes at high vacuum from the interior of the gas detector which was at 20 Torr. The flight path though the gas, P-10, was 11.11 cm. There was enough diffusion of the gas through the thin window so that it was necessary to have a diffusion pump between the gas detector window and the last MCP. A fast closing valve was inserted as well to protect the timing detectors in the event of a window rupture. The experimental apparatus was operated for several thousand hours during the course of testing and data acquisition. No catastrophic failures occurred and no detectors were lost due to vacuum system failure.

The fragment telescope was supported by an aluminum frame which was attached at its back end to a remotely controlled mechanical driving mechanism. In addition, a pivot point employing a flexible vacuum coupling located in the front of the telescope near the target box enabled the telescope to move horizontally and vertically ± 2 in. Once the jet position had been established by maximizing the counting rate in the monitor telescope, the fragment telescope was then driven until its counting rate was maximized.

As an example of the data acquired with this

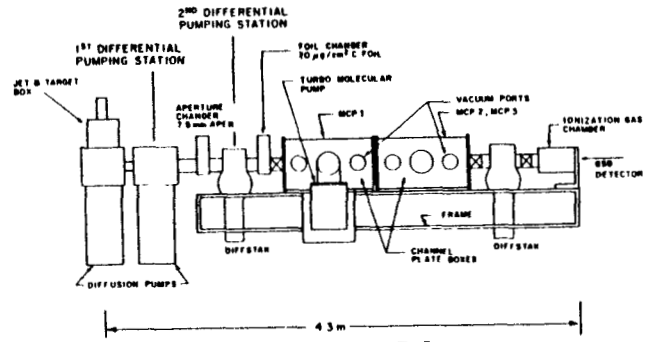

Fig. 12: Fragment Telescope

apparatus[5], we show the aluminum masses in figure 13. The flight of the fragments was between the first MCP (START) and the surface barrier detector (STOP) in the ionization chamber. Corrections were made for the energy and multiple scattering losses. The excellent mass resolution permitted the measurement of fragment kinetic energy spectra to quite low energies. Some typical spectra are shown in fig. 14.

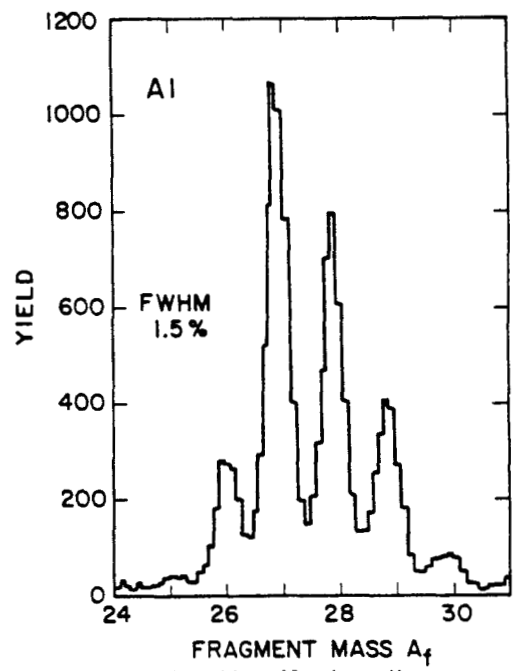

Fig. 13: Aluminum Masses

Conclusion

We have described the operation of a supersonic gas jet which has been used in several experiments at different national laboratories. The internal target has been proven to be flexible enough to permit adaptation to the different physical constraints encountered. The unique feature of the gas jet is its operation in the accelerator's main ring, where multiple traversals by the beam result in an effective target thickness comparable to that of a foil target. The ability to pulse the jet over the entire acceleration cycle, allows one to measure the energy dependence of the cross section of interest, while the ability to pulse mixed gases makes normalization of the data possible.

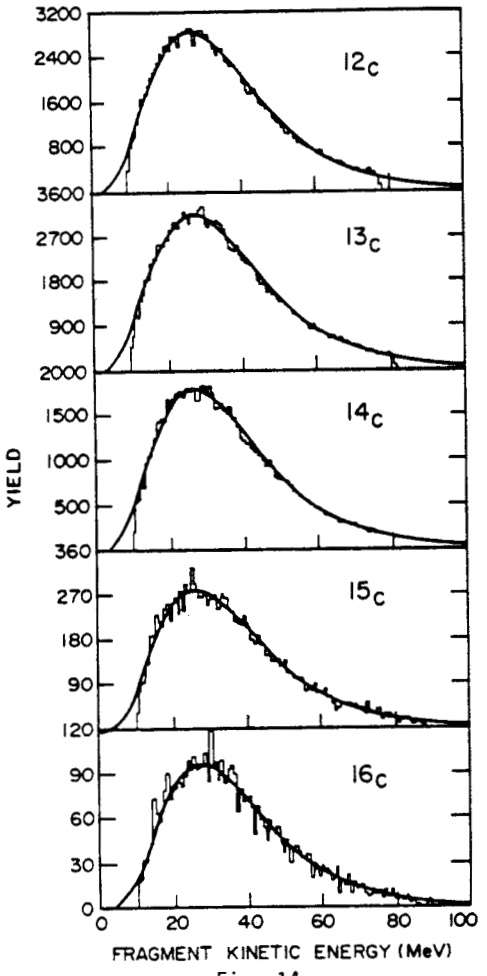

Fig. 14

References

1. D. Gross, P. Mantsch, and F. Turkot, FNAL Report TM-534-0710.0 (January 1975). P. Mantsch and F. Turkot, FNAL Report TM-582-0170.0 and FNAL Report TM-586-0710.0 (June 1975).

2. T. C. Sangster, Ph. D. Thesis, Purdue University (1986).

3. M. Mahi, Ph. D. Thesis, Purdue University (1986).

4. A. M. Zebelman, et al., Nucl. Instr. and Meth. 141, 443 (1977).

5. J. E. Finn, Ph. D. Thesis, Purdue University (1982).

POSSIBILITIES FOR POLARIZED INTERNAL TARGETS

R. D. McKeown
W. K. Kellogg Radiation Laboratory
California Institute of Technology
Pasadena, CA 91125

An important feature of experiments with internal targets in storage rings is the possibility of using thin polarized gas targets. Various methods of polarizing different nuclei are under development, and suitable target thicknesses appear quite feasible. A survey of techniques is presented with a discussion of advantages, disadvantages and possible problems that will need to be addressed.

Introduction

Many experiments in electronuclear physics benefit from the use of polarized targets. Often there are amplitudes that cannot be extracted by other methods, and the existence of interference effects in spin dependent quantities allows better access to small amplitudes. These features of polarized targets have been discussed by others at this workshop, so I will concentrate on the target technology itself.

The use of polarized targets in electron scattering experiments was pioneered at SLAC[1], and improvements in the technique have been recently reported by the Bonn group[2]. These polarized hydrogen targets contain hydrogen (or deuterium) in beads of alcohol or ammonia at low temperature (≈ 0.1°K). A large magnetic field (typically 5 Tesla) is applied to produce electronic polarization. Application of microwaves at a resonant frequency induces polarization of the protons (or deuterons). The protons become highly polarized, but tensor polarization of deuterium is low. Although the protons are highly polarized, only a small fraction ($< 20\%$) of the nucleons in the target are actually polarized due to the presence of heavier nuclei in the beads. This reduces the measured asymmetry which makes the experiments correspondingly more difficult. The high magnetic field causes problems in deflecting the incident and/or scattered particles. (The detailed extraction of small amplitudes requires accurate determination of scattering angles and careful alignment of the spin direction with respect to particle momenta.) In addition, the targets become radiation damaged when the incident beam current is greater than a few nanoamperes, so that the full beam intensity cannot be utilized.

In contrast, the internal targets are of high purity, high polarization, and will not suffer from radiation damage. The holding field is usually in the range of 10-100 Gauss, which simplifies the problem of particle deflection. The type and degree of polarization is easily varied so that, for example, tensor polarization is as easy as vector polarization to achieve. Of course, the main disadvantage is the very thin target thickness, but this can be offset by the use of a storage ring with high circulating current.

Table I summarizes the basic beam parameters of the two facilities most likely to be utilized in the near future. Also included in the table is the estimated maximum target thickness allowed in the ring. Note that a thin ($10\mu g/cm^2$) carbon foil corresponds to $6 \times 10^{18}/A$ atoms/cm^2, so we should consider windowless, differentially-pumped gas targets.

For definiteness, I will consider the nucleon cross-section at $Q^2 = 1(\mathrm{GeV}/c)^2$ as a reference cross-section for rate estimates. (This cross-section is at the boundary between the PEP energy range and the MIT-Bates range.) Then we roughly find that the cross-section per nucleus is given by

$$\frac{d\sigma}{d\Omega} \lesssim 2.5 \times 10^{-33} E^2 A \frac{\mathrm{cm}^2}{\mathrm{sr}}, \qquad (1)$$

where E is the incident beam energy. For a solid angle of 10 msr (0.01 sr) at $E = 2$GeV the cross-section becomes

$$\sigma \lesssim 1 \times 10^{-34} A \mathrm{cm}^2. \qquad (2)$$

To obtain a rate of 0.1 Hz (10^4 counts per day) then requires a luminosity of $L \gtrsim 10^{33}/A$ cm^2/sec, and assuming a beam current of 40mA the target thickness must be

$$n_t \gtrsim 4 \times 10^{15}/A \text{ atoms/cm}^2. \qquad (3)$$

I will use the reference value of $10^{15}\mathrm{cm}^{-2}$ as a goal for target thickness. Of course, some experiments will require more or less, but this is usually within an order of magnitude of the required thickness for experiments that have been considered recently.

Table I. Relevant Storage Ring Parameters

		PEP	Bates PSR
Energy (GeV)		4–18	0.3–1.0
Current (mA)		> 20	40
Max. Target Thickness	$A \leq 6$	$6 \times 10^{15}/A$	$10^{19}/A$
(atoms/cm^2)	$A = 40$	6×10^{13}	2×10^{17}

I will survey the development of hydrogen and ^{3}He targets. Certainly other targets will be feasible (such as optically pumped alkali vapors), but these are the ones of most common interest and have a broader range of applicability in the field.

Hydrogen Targets

I will discuss three types of polarized hydrogen targets which are relevant to internal target designs. Each could be used as either a proton or deuteron target.

The first technique has been under development for many years: the atomic beam[3]. A schematic is shown in fig. 1. A dissociator is used to form an atomic beam of H atoms, which is passed through a sextupole magnet yielding atomic (but not nuclear) polarization in a strong magnetic field. Polarization is transferred to the nucleus by inducing RF transitions of various types. The resulting beam of $\sim 5 \times 10^{11}/\mathrm{cm}^3$ could be used to form a target by intersection with the electron beam

Figure 1. Polarized hydrogen atomic beam apparatus

of $n_t \sim 5 \times 10^{12}/\text{cm}^2$. This falls short of our goal by about a factor of 100, and two methods are being explored to try to increase the density: (a) cooling the H beam[4], and (b) storing the H atoms in a bottle[5]. Cooling the beam slows the atoms so they spend more time in the path of the electron beam and increases the acceptance of the sextupole magnet. Cooling to 20°K should give about a factor of 50 improvement in density, but this has not been achieved in practice. The storage bottle is being developed at the Univ. of Wisconsin and they have had some success recently. The problem is that after several wall collisions, an H atom is likely to be depolarized or recombine to form a molecule. In order to reach $n_t \sim 10^{15}/\text{cm}^2$ one will need to develop wall coatings that allow $10^3 - 10^4$ wall collisions without loss of polarization. The Wisconsin group has recently achieved 120 bounces and hopes for further improvements[6].

Another technique which is currently under development at Argonne[7] is the spin-exchange method, shown schematically in fig. 2. Dissociated hydrogen is introduced to a cell containing a small amount ($\sim 1\%$) of potassium. The potassium is polarized by optical pumping with a dye laser, and transfers polarization to the hydrogen by spin-exchange collisions. The Argonne group expects to achieve a polarization rate of $\sim 5 \times 10^{16}$/sec with 100 milliwatts of laser power. This feed rate is equivalent to the best atomic beam available, and one could expect to increase the laser power to several watts. If this is achieved, the demand on the wall coatings could be reduced to the point where the existing coatings may be sufficient. The present status is that the Argonne group has just observed a polarization signal for the first time[8], and is proceeding to make improvements.

An interesting new technique has been proposed by Kleppner[9], and is being used to develop a target for the AGS at Brookhaven. The basic idea is sketched in fig. 3. Dissociated ultra-cold H (0.5°K) is expelled by a very large ($\sim$ 8Tesla) magnetic field. The resulting beam would be well focussed and monochromatic, with an estimated output density about a factor of 100 greater than a conventional atomic beam. RF transitions would then be used to create high nuclear polarization. The technique requires quite a bit of cryogenic equipment and a superconducting magnet, but certainly looks quite promising at the moment.

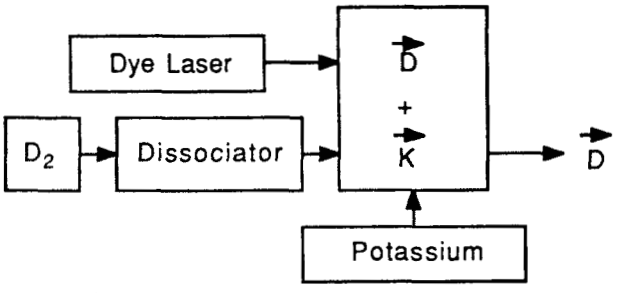

Figure 2. Polarized deuterium using spin exchange

^{3}He Targets

A polarized ^{3}He target can be used essentially as a polarized neutron target. The two protons are predominantly coupled to spin zero, so that the nuclear spin is primarily the neutron spin. Thus, measurement of a spin observable selects the neutron with only small corrections for the protons, which can be calculated accurately with Fadeev techniques[10]. Two techniques are employed to polarize ^{3}He, and both have been improved markedly in the last few years.

The first method is being developed by Chupp at Harvard and McDonald at Princeton[11], and is shown in fig. 4. The ^{3}He is in a cell with a small amount of rubidium and about 20% nitrogen. The rubidium is optically pumped with a dye laser and transfers spin to ^{3}He by spin exchange collisions. The Rb is optically thick to facilitate efficient angular momentum transfer, but this causes the phenomenon of "radiation trapping",

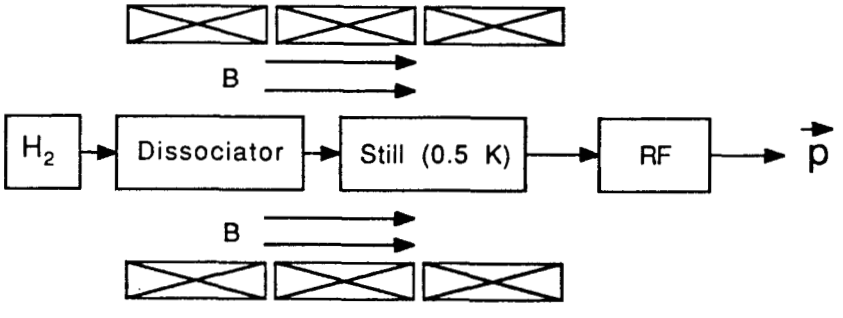

Figure 3. Ultracold polarized hydrogen apparatus

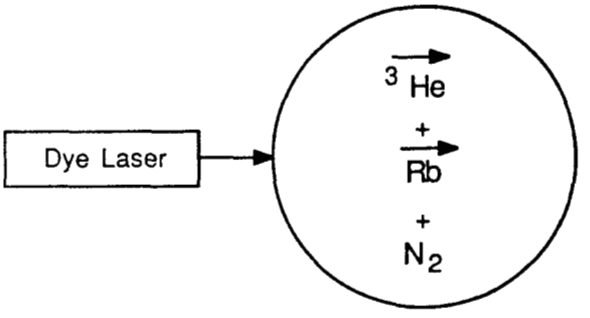

Figure 4. Polarized ^{3}He by spin exchange with Rb.

where re-emitted photons are absorbed leading to saturation of polarization at low values (the absorbed secondary photons depolarize atoms on the way out). The cure is to add the nitrogen as a buffer gas so that the Rb collisionally de-excites, eliminating the secondary photons. The presence of nitrogen is again a nuisance as it was for external hydrogen targets, but perhaps this is a soluble problem. In addition, the feed rate is low, but this may also be improved. Note that no bottle problem exists for ^{3}He since, being a noble gas, wall collisions are not severely depolarizing.

Another technique, shown in fig. 5, has been developed by Leduc and Laloe at L'Ecole Normale Superieur in Paris[12]. Our group at Caltech is presently adapting this technique to build realistic targets for use in electronuclear physics experiments[13]. In this technique, a small population of metastable triplet state ^{3}He atoms is optically pumped by a laser. The pumped atoms collide with ground state atoms and exchange electronic states leaving a polarized nucleus in an atomic ground state. Gradually, angular momentum is transferred to completely polarize the ground state population. The polarization rate with present laser technology is $\sim 10^{17}$/sec, and the ^{3}He is pure. This appears at present to be a very appropriate method for internal target use.

The Bottle and Effects of the Electron Beam

Most of the target designs discussed above require the use of a storage bottle to hold the gas in order to generate the appropriate target density. The typical bottle is shown in fig. 6. It consists of a 10 cm long cell with gas at $10^{14}/\text{cm}^3$ and two long tubes (length l and radius a) to provide an impedance to gas flow and allow the beam to pass through. In the molecular flow limit (mean free path long compared to a) one can express the tube conductance, F, as[14]

$$F = \frac{5 \times 10^{16}/\text{sec}}{10^{14}/\text{cm}^2}, \\ = \frac{K\bar{v}}{4}\pi a^2, \tag{4}$$

where $K \approx \frac{8}{3}\frac{a}{l}$, $\bar{v} = 1.5 \times 10^4\sqrt{T/A}$ cm/sec (thermal velocity), and we have assumed a feed rate of 10^{17} atoms/sec into the bottle which is at temperature T degrees Kelvin. For typical values of $A = 3$, $l = 30$cm, and $T = 300°$, one computes that the tube radius must be $a = 0.36$cm. The tube radius is the sensitive parameter, as the conductance goes as a^3. One can also estimate the mean holding time in the bottle as 0.01-0.1 sec which yields the number of wall collisions as $10^3 - 10^4$.

I will consider two possible sources of depolarization by the electron beam: ionization and magnetic field effects. The ionization rate is easily computed for minimum ionizing particles at 40mA intensity by assuming $\sim$ 30eV/ionized atom is required. This yields the result 1.5×10^{14}/sec, which is much less than the typical feed rates of $\sim 10^{17}$. This does not seem to be a problem.

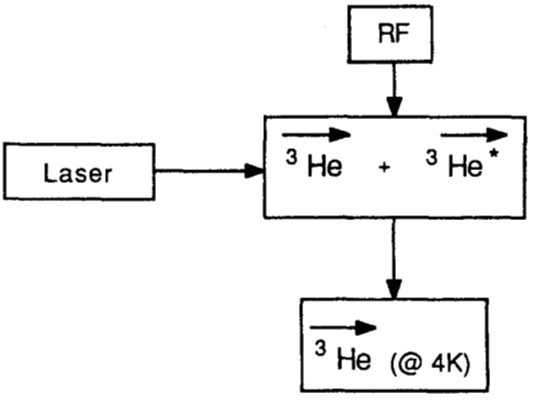

Figure 5. Polarized ^{3}He by Optical Pumping of Metastables

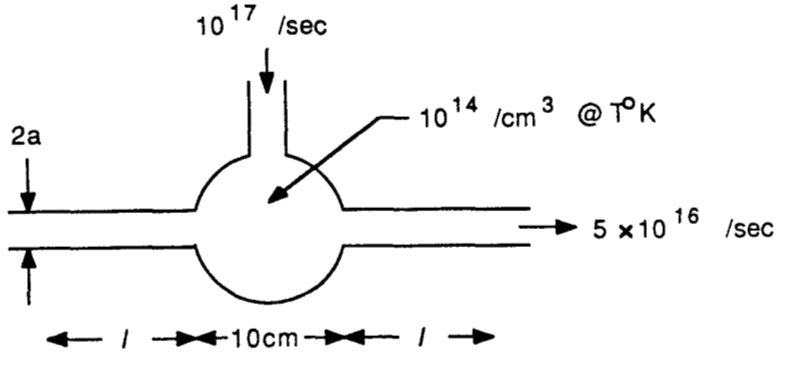

Figure 6. Bottle design for polarized gas target

The magnetic field of the beam is a rather subtle issue. We consider a hydrogen target, and a pulsed beam structure with pulse length τ and peak current I_p. The peak magnetic field in the vicinity of the beam is B_p and occupies about 10^{-4} of the target volume (this gives the number of affected atoms). If

$$B_p \gtrsim B_0 \tag{5}$$

(B_0 is the holding field) *and*

$$\tau \gtrsim (\gamma_B B_p)^{-1} \tag{6}$$

(γ_B is the Bohr frequency 1.7×10^7rad/G/sec), then there can be significant depolarization. The atoms will precess about the randomly oriented B_p by many radians within the affected volume. Thus the target will be depolarized in $\sim 10^4$ beam pulses. If $B_p \ll B_0$, the spins will only precess about B_0 with little depolarization. If $\tau \ll (\gamma_B B_p)^{-1}$, then an atom only precesses a small amount during the beam pulse, and then precesses about B_0, so a random walk takes place, and the depolarization is not severe.

At PEP with 40 mA beam, $B_p \sim 5$kG and $\tau \sim 10^{-10}$sec, so that a hydrogen target would be depolarized in $\sim 10^{-3}$sec (this calculation assumes 3 bunch operation). If the beam is spread out in hundreds of bunches, the peak magnetic field is reduced by ~ 100 and the target will retain its polarization. At Bates, where one only encounters the microstructure, the beam pulse is short compared to a rotation time so very little depolarization will occur. For noble gas targets such as ^{3}He, the frequency of spin precession is a factor of ~ 2000 smaller and these effects are not anticipated to be a problem.

Summary

In summary, it appears that several viable target technologies can be applied to the polarized internal target problem. Densities of $10^{15}/\text{cm}^2$ seem quite feasible by several methods for H, D, ^{3}He, and other types of polarized targets. Many experimental groups are presently working on the construction of realistic targets and it seems likely that in the next year or two they will achieve the goals outlined here.

The depolarization due to the electron beam can be a problem when peak currents are high for long beam pulses. However, it appears that by spreading the beam over many bunches, the problem can be handled adequately. Nevertheless, one should consider these effects carefully in designing specific experiments.

Finally, it seems that with the anticipated target technology developments outlined here, and the very important physics issues that can be addressed by using that technology, more consideration should be given to the availability of appropriate facilities. The Bates PSR upgrade proposal explicitly provides for generation and maintenance of longitudinal polarization of the electrons at the interaction region in the ring. A detailed study of the requirements for a similar facility at PEP has not been carried out. B. Norum has worked on various schemes for maintenance of longitudinal polarization[15], but more work and some engineering need to be done to really assess the feasibility of these experiments at PEP. I hope that this issue will be addressed in the near future so that optimal utilization of these various target designs can become a reality at both facilities.

References

1. V. W. Hughes and J. Kuti, Ann. Rev. Nucl. Part. Sci. **33**, 611(1983).

2. K. H. Althoff *et al.*, "Radiation Resistance of Ammonia at 1 Kelvin and 2.5 Tesla" in *Proceedings of the* 4$^{\text{th}}$ *International Workshop on Polarized Target Materials and Techniques*, 1984, pp. 23-32.
3. W. Haeberli, AIP Conf. Proc. No. 128, American Instituite of Physics (New York) 1985, p. 251.
4. W. Gruebler, "Polarized Atomic Beams for Targets", in the *Proceedings of the Workshop on Polarized Targets in Storage Rings*, 1984, pp. 223-248.
5. W. Haeberli, Helvetica Physica Acta **59**, 597(1986).
6. W. Haeberli, private communication.
7. M. C. Green, "Design of a Tensor Polarized Deuterium Target Polarized by Spin Exchange with optically pumped Na", in the *Proceedings of the Workshop on Polarized Targets in Storage Rings*, 1984, pp. 307-342.
8. R. Holt, private communication.
9. D. Kleppner, AIP Conf. Proc. No. 80, American Instituite of Physics (New York) 1982, p. 138.
10. B. Blankleider and R. M. Woloshyn, Phys. Rev **C29**, 538 (1984).
11. T. Chupp, private communication.
12. M. Leduc *et al.*, Nuclear Science Appl. **1**, 1 (1983).
13. R. G. Milner, R. D. McKeown, and C. E. Woodward, to be published in Nucl. Instr. Meth.; R. G. Milner, in these proceedings.
14. S. Dushman and J. M. Lafferty, *Scientific Foundations of Vacuum Technique*. New York: J. S. Wiley and Sons, 1962, ch. 2, p. 91.
15. B. Norum, in these proceedings.

A LARGE ACCEPTANCE MAGNETIC SPECTROMETER FOR CEBAF

Bernhard A. Mecking

CEBAF
12070 Jefferson Avenue
Newport News, Virginia 23606

Abstract

A large acceptance magnetic spectrometer for the investigation of electron- and photon-induced nuclear reactions at CEBAF is described.

I. Introduction

The scientific program for the CEBAF 4 GeV electron accelerator aims at studying the structure and the motion of the nuclear constituents. The experimental equipment that has been proposed consists of focusing magnetic spectrometers with relatively small acceptances ($\Delta\Omega \simeq 10^{-3} \cdot 4\pi$, $\Delta p/p \simeq 10\%$) but high momentum resolution ($\Delta p/p \lesssim 10^{-4}$) and a large acceptance spectrometer. In the following report, the physics motivation for a large acceptance detector, the general design criteria and technical details of the detector will be discussed.

II. Physics Motivation

Electron scattering experiments have provided most of what we know about the structure of nuclei. However, our knowledge is limited to the electromagnetic structure of ground states and excited states of nuclei (explored in (e,e') experiments) and to some aspects of the nuclear single-particle structure (explored in (e,e'p) experiments). Very little is known about the many-body aspects of the nucleus, like e.g. the structure of bound nucleons, the origin of short-range correlations or the propagation of meson or nucleon resonances in the nuclear medium. The reason for this limitation is largely due to the technical features of the available experimental facilities:

a) The low duty-cycle of existing electron accelerators limits coincidence experiments to a narrow kinematical region where a sufficient signal-to-noise ratio can be achieved. It also makes the operation of large acceptance detectors inefficient because their counting rates are limited by the instantaneous background rates.

b) High accuracy in charged particle detection can only be achieved in small acceptance magnetic spectrometers.

Important technical developments have changed this picture

a) Electron accelerators with 100% duty-cycle are being built.

b) The quality and versatility of large acceptance detectors has improved dramatically.

A large acceptance detector will be required for the detection of multiple particle final states and for measurements at limited luminosity. Examples will be given for these experiments:

1. Multiple Particle Final States

For reactions involving several particles in the final state, high detection efficiency and a model-free analysis of the data can only be achieved by using a detector with a wide coverage of the angular and energy range for all outgoing particles. Examples for reactions which are of special interest for CEBAF are:

a) Hadronic final states in inclusive electron scattering off nuclei. Single arm electron scattering and (e,e'p) coincidence experiments have generated puzzles which can only be solved by a detailed investigation of the hadronic final state. Using a large acceptance detector, a bias-free investigation can be carried out by triggering on the scattered electron only. In the off-line analysis, the inclusive scattering cross section can then be decomposed into its hadronic channels. With increasing energy loss for the electron, the following phenomena can be studied:

(1) Electron scattering at large negative y (y= momentum component of the struck nucleon parallel to the direction of the virtual photon $\vec{q}$) yields higher cross sections than expected from standard nuclear models. The excess cross section can be explained by high momentum components in the nuclear wave function (→ emission of a single nucleon) or by interaction of the virtual photon with quark clusters[1] (→ emission of nucleon pairs or nucleon clusters like deuterons etc.). These two possibilities can be distinguished by detecting the hadronic final state.

(2) Quasi-free electron scattering off bound nucleons (requiring the hadronic final state to contain a recoiling nucleon around the direction of $\vec{q}$). A long-standing problem is the failure of the Coulomb sum rule to account correctly for the number of protons in the nucleus. This has been interpreted as a change of the nucleon form factor in the nuclear medium or as evidence for a direct interaction of the virtual photon with a six-quark bag.

(3) Multi-nucleon emission (requiring the hadronic final state to contain ≥2 nucleons). Two nucleon emission is assumed to be responsible for filling the dip between the quasi-free peak and the Δ-peak; there should also be strength in the Δ-region due to Δ-excitation with subsequent Δ-N interaction.

(4) Production and propagation of non-strange (Δ and higher nucleon resonances) and strange (Λ, Σ and their excited states) 3-quark objects in nuclei (requiring the hadronic final state to be a πN, ηN, $\pi\pi N$, KA etc. system in the appropriate mass range). Modifications of the properties of these resonances in the nuclear medium can be studied.

(5) Deep inelastic electron scattering. The aim of this program is to study the hadronization of the struck quark in the region of large momentum and energy transfer and to understand how the inclusive cross section is built up out of individual hadronic channels.

Good particle identification for multiple particle final states down to very small angles ($\theta \lesssim 5°$) is important for this program.

b) Photo- and electro-excitation of the higher nucleon resonances. The harmonic oscillator quark model with QCD motivated additions (like a one-gluon exchange term) predicts, in addition to the known nucleon resonances, many states which have not been observed. A plausible explanation[2] is that these states decouple from the πN elastic channel and can, therefore, not be observed in elastic πN scattering. Since, on the other hand, the photocoupling is still strong, photoexcitation becomes the only available formation mechanism. Promising decay channels are:

$$\gamma N \to N^* \to \pi \Delta \to \pi \pi N$$
$$N^* \to N \rho \to \pi \pi N$$
$$N^* \to N \omega \to \pi \pi \pi N$$

c) Photo- (and electro-) excitation of vector mesons: $\gamma N \to V N$ ($V = \rho, \omega, \phi$). An important goal of this program is to measure the γ-V coupling constant to get information on the hadronic content of the photon[3] and its variation with Q^2. In addition, the vector meson coupling to the nucleon can be determined. In boson exchange models of the nucleon-nucleon interaction, this quantity is of fundamental importance for the short range part of the NN-interaction.

d) Hyperon production and interaction: $\gamma N \to K \Lambda (\Sigma)$ The basic cross sections and coupling constants for these reactions have to be known for the analysis of the electromagnetic excitation of hypernuclei. Using the outgoing kaon to determine the Λ kinematics, a tagged low intensity hyperon beam can be generated. The production rates are large enough so that the decay and the interaction of the produced hyperon can be studied in the reactions:

(1) $\Lambda p \to \Lambda p$ (elastic scattering)
Because of its short decay length, the interaction of low momentum Λ's is best studied in the production target. Using the $\gamma p \to K^+ \Lambda$ reaction for Λ production, about 500 Λ scattering events can be observed per day in a large acceptance spectrometer.

(2) $\gamma d \to K^+ \Lambda n$
This reaction allows also to study the ΛN interaction. Especially interesting is the search for long-lived S=-1 dibaryons; the masses of these objects have been predicted to be around the Σ-cusp[4].

(3) Radiative hyperon decay: $\Lambda^*(1520) \to \gamma \Lambda$ and $\Lambda^*(1520) \to \gamma \Sigma$.
Using a tagged photon beam, about $5 \cdot 10^5$ $\Lambda^*(1520)$ can be produced per day. The radiative decay width yields a sensitive test of the quark structure of the system.

e) Exclusive photoreactions on few-body systems

$$\gamma d \to N N \pi \qquad\qquad \gamma\, {}^3\mathrm{He} \to p p n$$
$$\to \Delta \Delta \to N N \pi \pi \qquad\qquad \to \pi \text{ (3N)}$$

The basic properties of bound 3-quark systems are best studied in few-body nuclei because the nuclear structure can be calculated exactly (at least in the framework of a non-relativistic potential model). Interesting questions are the off-shell behavior of the γNN^* vertex, the structure of the N^*N interaction, the existence of dibaryons[5] and of 3-body forces[6] in ^{3}He.

f) Interaction parameters of unstable particles.
The measurement of the A-dependence of total production cross sections for unstable particles will determine their total hadronic cross sections. In contrast to hadronic production reactions, the electromagnetic production offers the big advantage that the interaction of the incident projectile is so weak that the A-dependence of the cross section can be interpreted directly in terms of the interaction of the produced particle. Especially interesting is a comparison of the hadronic interaction of the η(549) and η'(958) which are supposed to be different mixtures of the same SU(3) states. The large η' mass is attributed to a sizeable exotic (gluonic or hybrid) component; this should show up as a difference in the hadronic behavior of η and η'[7].

A comprehensive study of the reactions b) - e) requires the use of polarized beams (longitudinally polarized electrons, linearly and circularly polarized photons) and polarized targets (polarized protons, vector- and tensor-polarized deuterons).

2. Limited Luminosity

The luminosity (target density • beam intensity) limitation can be due to the target or due to the beam.

a) Limitation due to the beam intensity.
Experimental programs using secondary particle beams (real γ, μ, π, K) need large acceptance coverage to collect sufficient count rate, independent of the number of particles in the final state. Especially important are tagged photon beam experiments where the intensity has to be limited to $\simeq 10^7$ tagged γ/sec to keep accidental coincidences small.

b) Limitation due to the use of a polarized target.

(1) Polarized solid state hydrogen and deuterium targets.
For present solid state polarized targets (ammonia or deuterated ammonia) the luminosity has to be kept low ($\simeq 10^{33} \mathrm{cm}^{-2}\mathrm{sec}^{-1}$ for tensor-polarized deuterium, $\simeq 10^{35} \mathrm{cm}^{-2}\mathrm{sec}^{-1}$ for polarized hydrogen) in order to avoid a reduction of the polarization due to beam heating and radiation damage.

(2) Polarized gas targets.
The disadvantages of polarized solid targets (high magnetic fields, nuclear background, low temperatures, limited to hydrogen and deuterium) can, in principle, be avoided by using a low density polarized gas target in combination with a high intensity electron beam. A dedicated electron storage ring would clearly be ideal for this program. However, the rapid progress in gas target technology will make experiments in the CEBAF external electron beam possible.

Compared to a storage ring, polarized gas target experiments in an external beam will have lower luminosity. However, there are also some important advantages:

a) No difficulties to achieve longitudinal electron polarization.
b) Modest vacuum requirements → less differential pumping will be required.
c) Greater flexibility in the arrangement of the experimental apparatus.
d) Since the beam passes through the target only once, small beam losses are acceptable → thin

windows or very small diameter openings for bottle targets can be used.

These features should also make it possible to achieve higher target density than in a storage ring. A minimum density of $\simeq 10^{15}$ atoms/cm^2 is necessary to give reasonable counting rate. At this luminosity ($\simeq 10^{30} cm^{-2} sec^{-1}$), the combination of a polarized gas target and a large acceptance spectrometer will be useful for the investigation of reactions induced by quasi-real photons.

For ^{3}He, the densities already reached [8),9)] give a luminosity of several $10^{32} cm^{-2} sec^{-1}$. This luminosity is high enough to allow for an extensive nuclear physics program especially with a large acceptance detector. Polarized ^{3}He targets can be used to investigate the structure of the 3-body system or as a source of polarized neutrons. The following experiments are of special interest:

(a) $^3\vec{He}(\vec{e},e'n)pp$ to determine the electric form factor of the neutron G_e^n.

(b) $^3\vec{He}(\vec{e},e'\Delta^0)pp$ to determine the C2/M1 ratio for the $n \to \Delta^0$ transition.

III. General Design Considerations

A large acceptance detector that is suitable for a broad range of photonuclear experiments using electron and photon beams should have the following properties:

1. Homogeneous coverage of a large angular and energy range for charged particles (magnetic analysis), photons (total absorption counters) and possibly neutrons.

2. Good momentum and angular resolution (→ magnetic analysis for charged particles).

3. Good particle identification properties in the momentum range of interest (→ combination of magnetic analysis and time-of-flight).

4. No transverse magnetic field at the beam axis (to avoid sweeping e^+e^--pairs into the detector).

5. No magnetic field in the target region to provide for the installation of polarized (solid state or gaseous) targets requiring their own guiding field or other complicated equipment (cryogenic or track sensitive targets, vertex detectors etc.).

6. Symmetry around the beam axis to facilitate triggering and event reconstruction.

7. Large $\int B \cdot dl$ for forward going particles to account for the Lorentz-boost.

8. High luminosity and count rate capability. The detector should operate in the difficult background environment encountered in electron scattering experiments. The background caused by a tagged bremsstrahlung photon beam ($N_\gamma \simeq 10^7$/sec) is much lower and will give no additional constraints.

9. Open geometry for the installation of a long time-of-flight path for neutron detection.

The consequences of these requirements for the choice of the magnetic field configuration have been studied. Transverse dipole, longitudinal solenoidal and toroidal fields have been considered. In all cases, the target has been assumed to be inside the magnetic field volume. The results are summarized in table I. To fulfill requirements #2 and #3, a large $\int B \cdot dl$ and a long time-of-flight (ToF) path is necessary. This can be achieved by all field configurations. The transverse dipole field is ruled out by #4 in combination with #8; it also violates #6. The solenoid which has become the standard magnetic field configuration at e^+e^- colliders violates requirements #5, #7 and #9; therefore, it has to be ruled out. The only configuration that fulfills all requirements is the toroidal magnetic field. Since the ϕ-range for magnetic analysis is limited due to the coils, the detection efficiency for high multiplicity (> 4) final states will be low. However, in view of the present CEBAF program, it seems to be more important that the detector will be capable to complement the standard spectrometer set-up instead of trying to specialize it for high multiplicity reactions.

IV. The Large Acceptance Detector

The solution that has been proposed for the CEBAF Large Acceptance Spectrometer (LAS) is a superconducting toroidal magnet equipped with drift chambers, scintillation counters and shower counters. A description of the main features of the LAS will be given below.

1. Toroidal Magnet

The toroidal magnet consists of 8 coils arranged around the beam line to produce essentially a magnetic field in ϕ-direction. The size, field strength and coil shape were determined on the basis of the physics requirements (see table II for details). A perspective view of the magnet is shown in fig. 1, the coil shape is given in fig. 2. Each superconducting coil is embedded in a rigid coil case (about 4 meter long and 2 meter wide). Details of the coil layout, construction and protection have been worked out during the Workshop on CEBAF Spectrometer Magnet Design and Technology [10)]. The coils are housed in individual cryostats to facilitate manufacturing, assembly and testing. For the magnetic field calculations, the finite size of the coil was simulated by adding up the contributions of 4 discrete conductor loops (as indicated in fig. 2). The r-dependence of the magnetic field is given in fig. 3 for different z-positions. In a cylinder of 50 cm diameter around the axis the magnetic field is ≤10 Gauss. As demonstrated in fig. 4, the field lines are essentially circles (corresponding to a pure ϕ-field) with important deviations close to the coils. Figure 5 gives the integral over the ϕ-component of the field as a function of the particle emission angle θ. For forward going particles, the integral is about twice as high as for particles going sideways.

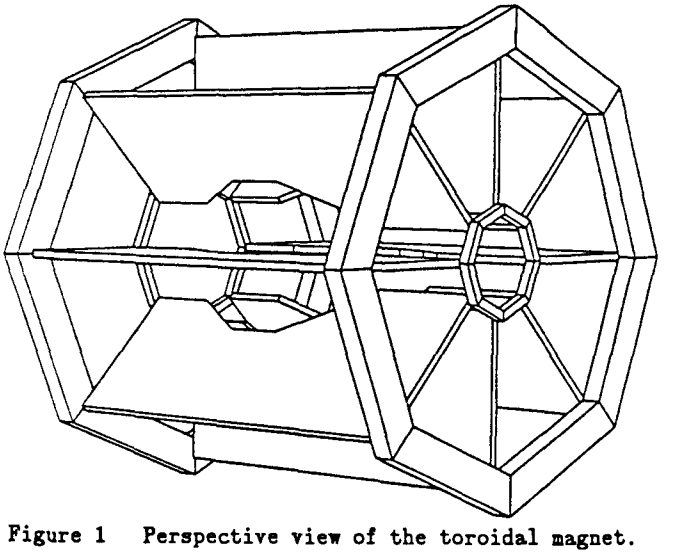

Figure 1 Perspective view of the toroidal magnet.

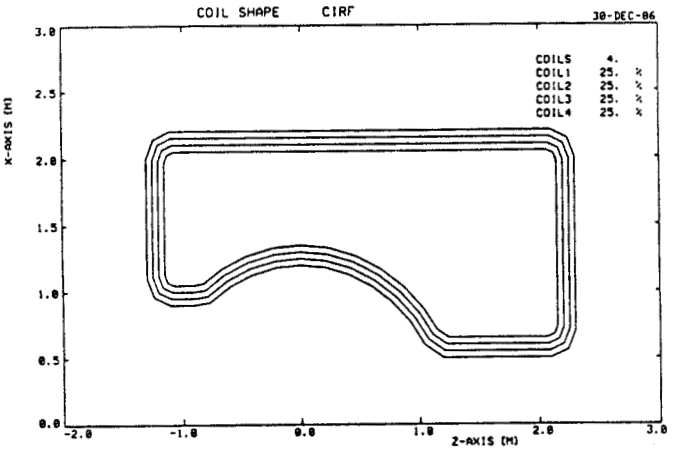

Figure 2 Coil shape. The superconductor is represented by 4 individual current loops.

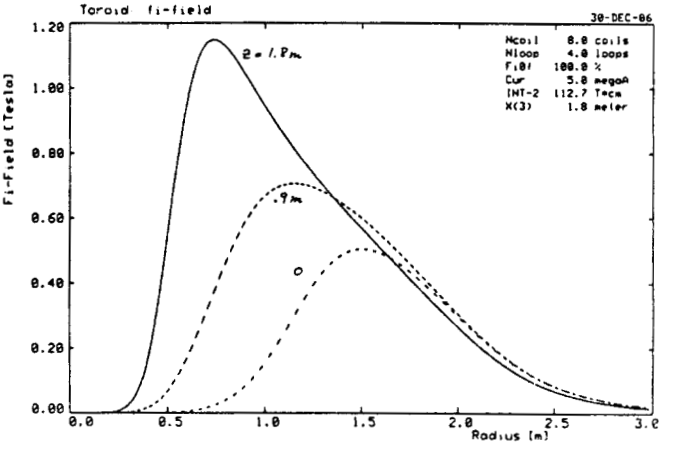

Figure 3 Radial dependence of B_ϕ for z=0, 0.9 m and 1.8 m (z=0 corresponds to the target position) and ϕ=0 (corresponding to the mid-plane between two coils).

The inner section of the coil is circular to avoid transverse (in ϕ-direction) motion of those outgoing particles that do not form a 90° angle with the conductor. This is demonstrated in fig. 6a for a rectangular coil shape (the current has been adjusted to make the total bend angle the same as for the circular coil). The transverse deflection depends on the angles θ (relative to the axis), ϕ (azimuthal angle) and on the particle momentum and polarity. The resulting loss of events will be difficult to correct. By using a circularly shaped coil, the angle of incidence can be kept normal to the coil, independent of θ. As shown in fig. 6b, the transverse particle motion is very much reduced.

2. Particle detection system

The proposed particle detection system consists of drift chambers to determine the track of charged particles, scintillation counters for the trigger and for time-of-flight, and shower counters to detect photons. A side view of the detection system is given in fig. 7, a cut in the target region in fig. 8. Note that all 8 segments are individually instrumented to form 8 independent magnetic spectrometers. This will facilitate track reconstruction in a large background environment.

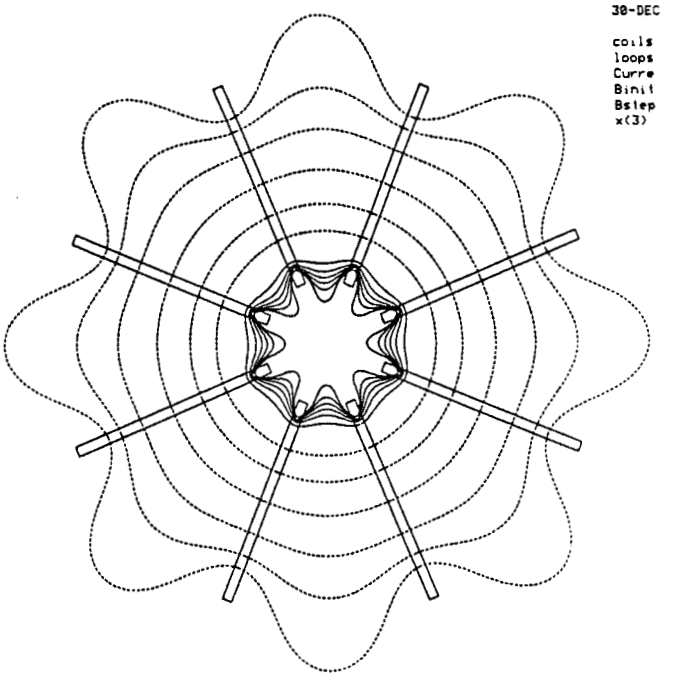

Figure 4 Field lines (giving the direction of the magnetic field) for z=1.8m (forward part of the magnet.

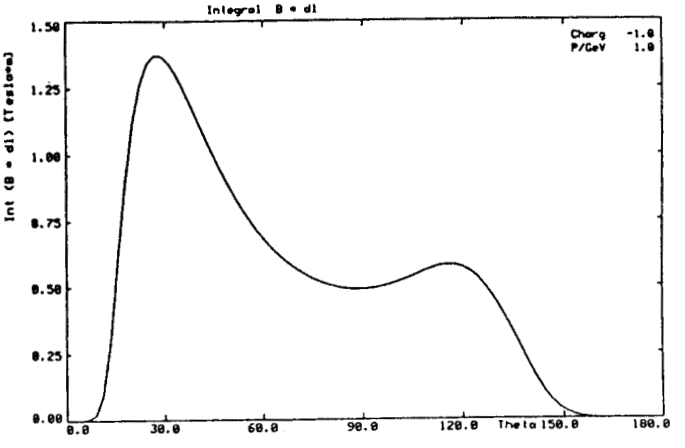

Figure 5 θ-dependence of the integral $\int B_\phi \cdot dr$. θ is the particle emission angle relative to the axis; the target has been assumed to be at z = 0 m. Particle momentum 1 GeV/c.

2.1 Tracking chambers

Charged particles are tracked by planar wire chambers. Each planar chamber consists of 4 layers of sense wires stretched in ϕ-direction. The position of the hit along the sense wire will be determined by charge division.

2.2 Scintillation Counters

The outer planar drift chambers are completely surrounded by scintillation counters. The barrel counters consist of 8•8 counters, each about 400 cm long, 20 cm wide, and 5 cm thick. The counters are viewed by 2" phototubes at both ends for improved timing and position resolution. The endcaps are covered by 8•4 pie-shaped counters, each viewed by one photomultiplier. Because of the high rate, the

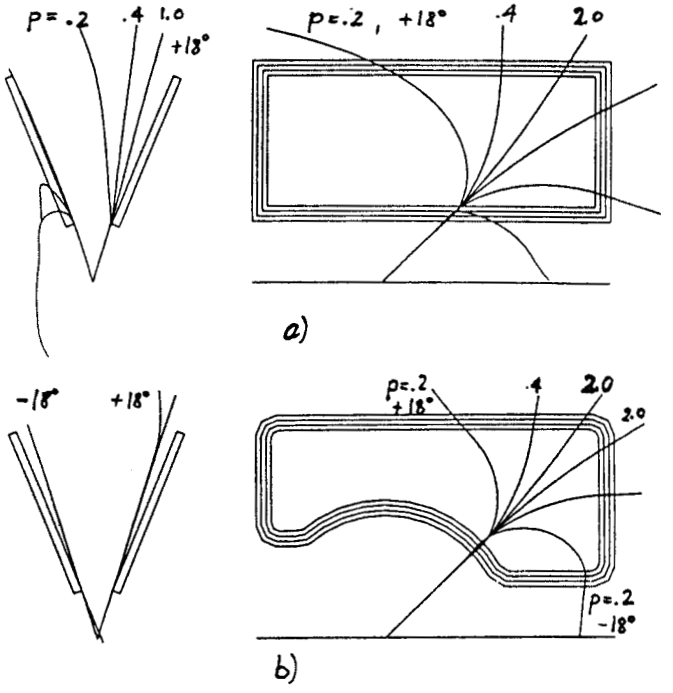

Figure 6 Transverse particle deflection in toroidal magnets for particles with θ=40°, p= 0.2, 0.4 and 2.0 GeV/c and ϕ=±18° (ϕ=0 corresponds to the mid-plane).
a) rectangular coil shape. Particles that are deflected away from the axis by the ϕ-component of the field are bent back to the mid-plane; particles that are deflected away towards the axis are bent towards the coils and are lost.
b) coil with a circular inner section. Note that there is no transverse motion at inner edge of the coil.

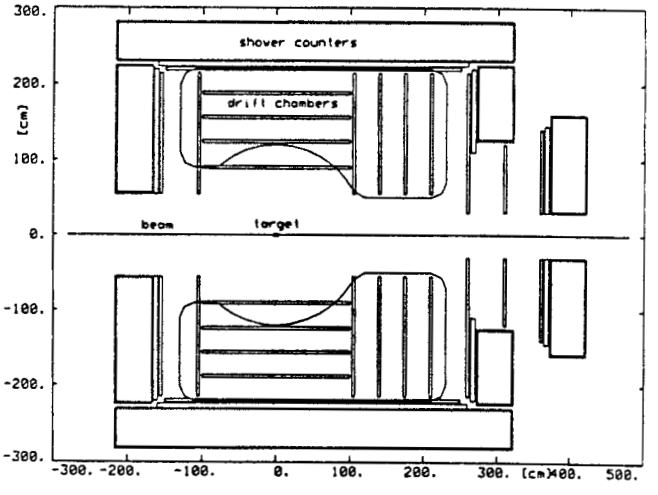

Figure 7 Transverse view of the particle detection system.

forward endcap counters are split into two rings: one ring at large and one at small angles. The scintillation counters serve the double purpose of providing the trigger and the time-of-flight information. Also, a fraction of the high energy neutrons (≃5%) will interact in the scintillation counters and will thus be detected.

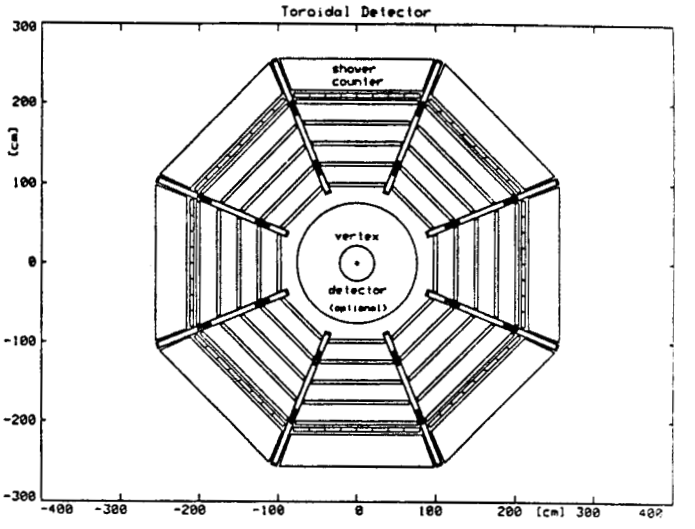

Figure 8 View of the detection system in the direction of the beam for z=0 (target position).

2.3 Shower Counter

The detector is surrounded by shower counters for the detection of showering particles like high energy photons from the decay of hadrons like π^0, η, η' etc. Due to the size and the weight of the counter (≃80 m^2, ≃100 tons), inexpensive materials and construction techniques have to be used (e.g., a sandwich of lead plates interleaved with active material like scintillators or gas detectors). The expected energy resolution is $\sigma/E_\gamma \leq .13/\sqrt{E_\gamma(\text{GeV})}$.

3. Maximum Luminosity

In an electron beam, the main background is caused by electron-electron scattering and wide angle bremsstrahlung. At a luminosity of $10^{33}\text{cm}^{-2}\cdot\text{sec}^{-1}$, the rate of Møller scattered electrons is estimated to be of the order of $5\cdot10^{7}\text{sr}^{-1}\cdot\text{sec}^{-1}$. Since the energies are low, the electrons are bent back even by the small magnetic fringe field. A fraction of the electrons will, however, radiate photons that will subsequently generate spurious signals in the chambers. The total integrated flux of photons due to wide angle bremsstrahlung has been estimated to be of the order of $10^{6}\text{sr}^{-1}\cdot\text{sec}^{-1}$ (luminosity $10^{33}\text{cm}^{-2}\cdot\text{sec}^{-1}$, E_o = 2 GeV, ^{12}C target, all photons above 10 keV). Compared to these electromagnetic background rates, the hadronic rates are nearly negligible. The total rate of electrons scattered into the angular range $15°\leq\theta\leq150°$ due to hadronic processes is less than 1000/sec. The total hadron rate (mainly produced by by quasi-real photons) is ≃$5\cdot10^{4}$/sec. On the basis of these counting rate estimates and also due to past operating experience of a large acceptance detector at an electron accelerator[11], one can expect that the detector can be operated at a luminosity of ≃ $10^{33}\text{cm}^{-2}\cdot\text{sec}^{-1}$ (corresponding to a 1 μA electron beam on a 1 mg/cm^2 target).

There will be no difficulties to operate the detector at tagged photon beam intensity (≃$10^{7}\gamma$/sec). (At this photon beam intensity, the hadronic production rate is about the same as in electron beam

with a luminosity of $10^{32}cm^{-2}sec^{-1}$; however, due to the lack of Møller scattered electrons the background rate is much lower.)

4. Track Resolution

The track resolution has been calculated taking the position resolution of the chambers and multiple scattering into account. The momentum resolution $\Delta p/p$ for known vertex position is shown in fig. 9 for 1 GeV/c particles as a function of the particle emission angle θ. The momentum resolution reaches 0.6 % in the forward direction; in the central part, it drops to 1.5 % due to the decreasing $\int B \cdot dl$. For known vertex position, $\Delta p/p$ is dominated by multiple scattering; therefore, it is nearly constant in the whole momentum range of interest. The initial angle can be determined with an uncertainty $\Delta\theta \leq 1$ mrad for 1 GeV/c particles (2 mrad for 0.2 GeV/c).

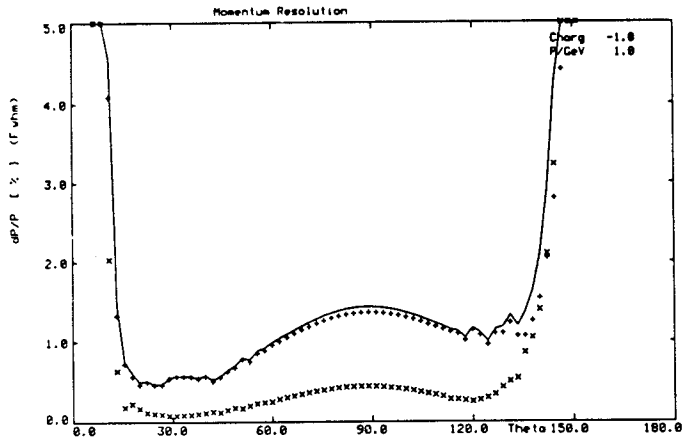

Figure 9 Momentum resolution $\Delta p/p$ (FWHM) as a function of the particle emission angle θ for p = 1 GeV/c. The vertex is assumed to be known.
- x contribution of the chamber position resolution
- \+ multiple scattering contribution
- — sum of both contributions.

5. Particle Identification

The combination of momentum and time-of-flight (a time resolution of $\Delta\tau$=200 psec (sigma) was assumed) gives clean particle identification over a wide momentum range. In the forward direction, pions can be separated from kaons up to 1.5 GeV/c, the limit for kaon/proton separation is 2.5 GeV/c. π/e, π/μ and μ/e separation can be achieved by using the pulse height in the shower counter in addition.

6. Acceptance

Using a Monte Carlo technique, random multiple particle events were generated to determine the acceptance. Examples for single events as they would be reconstructed and displayed on-line by the detector single-event display are presented in figs. 10 and 11. For the calculation of the acceptance, the θ-range of the detector was taken to be $15° \leq \theta \leq 150°$, 20% of the ϕ-range was assumed to be obstructed by the coils. In addition, cuts in the kinetic energy of the emitted particles were applied to account for detection thresholds: $T_\pi \geq 40$ MeV and $T_p \geq 50$ MeV. For the process $\gamma + p \rightarrow F35(1975) \rightarrow \pi^- + \Delta^{++} \rightarrow \pi^- \pi^+ p$ about 60% of the all $\pi^- \pi^+ p$ events are accepted if only θ and T_{min} cuts are used. The addition of the ϕ-cuts reduces the total detection efficiency to 30%.

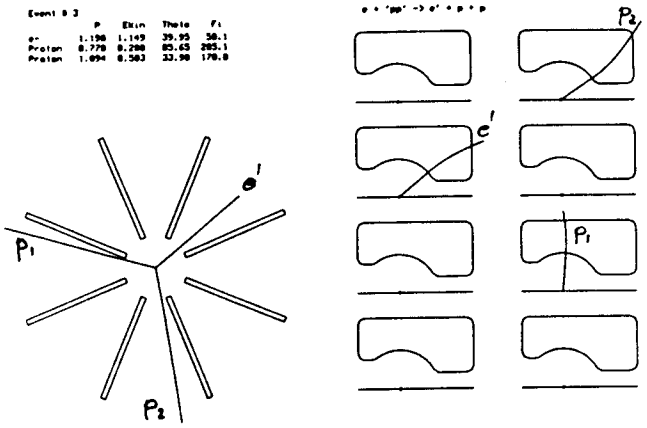

Figure 10 Single event display for a Monte Carlo generated event from the reaction (e,e'pp). E_o = 2 GeV, θ_e =40°. The left hand side of the display shows a view of the event in the direction of the beam, the r.h.s. presents the tracks in the 8 individual segments.

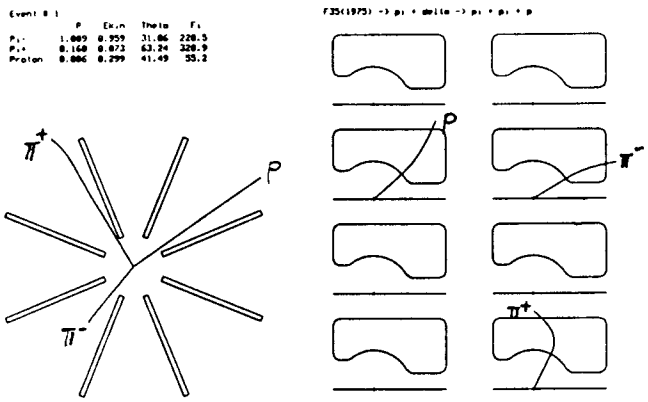

Figure 11 Single event display for a Monte Carlo generated event from the reaction γ p → $N^* \rightarrow \pi^- \Delta^{++} \rightarrow \pi^- \pi^+$ p induced by real photons. E_γ = 1.6 GeV.

7. Counting Rate Examples

a) (e,e'X)
The counting rate for have been estimated for $^{12}C(e,e')$ at E_o =2 GeV and θ_e =15°. A luminosity of $10^{32}cm^{-2}sec^{-1}$ (per nucleon) and 80% ϕ-coverage have been assumed. The total rate of electrons scattered into the angular interval 14°-16° and the energy interval (1.3-2.0) GeV is ≃100/sec.

b) photon induced reactions
Combining a tagged photon beam with an intensity of 10^7 γ/sec and a hydrogen target of 0.5 g/cm² (≃7 cm liquid) results in a total hadronic production rate of ≃400 events/sec (E_o= 2 GeV, σ_{tot}= 140 μb).

8. Layout of End Station B

The detector will be located in end station B. A possible layout of the end station is shown in fig. 12. End station and beam dump are fully shielded to allow for experiments using a high intensity beam on a thin gas target (also to allow for a second high

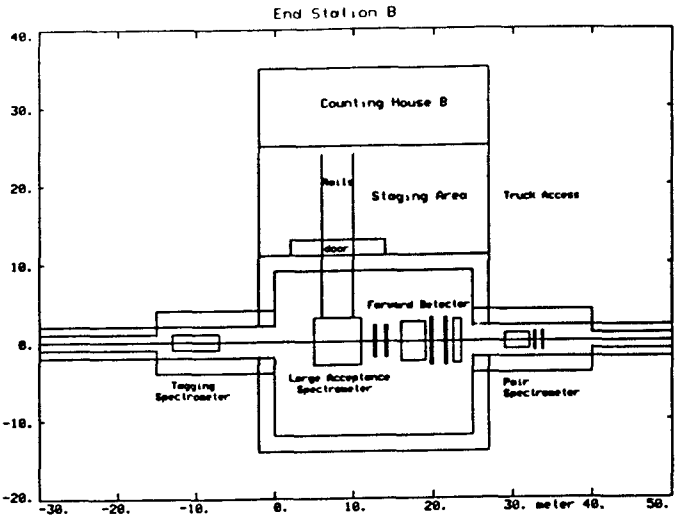

Figure 12 Proposed layout of the low intensity end station B.

intensity experiments in this area). The detector can be moved on rails into an adjacent staging area for extended service. For photon experiments, a vertically deflecting tagging spectrometer is located in an enlarged tunnel section.

V. Summary

A large acceptance magnetic spectrometer has been proposed for the investigation of electron- and photon-induced nuclear reactions at CEBAF. The magnetic field is generated by eight toroidal coils. Charged particles are tracked using scintillation counters and drift chambers; high energy photons are detected by shower counters. The spectrometer will be indispensable for the investigation of multiple particle final states from (e,e'X) reactions and from the decay of excited $q\bar{q}$ and qqq-states. In addition, it will provide the highest possible counting rate for experiments in which the luminosity is limited due to low target density or low beam intensity.

References

1) H.J. Pirner et al., Phys. Rev. Lett. 46 (1981) 1376.

2) N. Isgur, Proc. of the 1984 CEBAF Summer Workshop, Newport News, Virginia, ed. by F. Gross and R. R. Whitney, p. 199

3) T.H. Bauer et al., Rev. of Mod. Physics, 50 (1978) 261

4) M.E. Sainio, AIP Conf. Proc. 150 (1986) 886

5) M.P. Locher et al., Adv. in Nucl. Phys., Vol. 17 (1986) 47

6) I. Sick, Lecture Notes in Physics 260 (1986) 42

7) F. Lenz, Nucl. Phys. B279 (1987) 119

8) R.D. McKeown and R.G. Milner, 1985 CEBAF Summer Study, RPAC I, p. 12-45

9) R.G. Milner et al., private communication, submitted to Nucl. Instr. and Meth.

10) P.G. Marston: Report of the Working Group on the Large Acceptance Spectrometer, Proc. of the Workshop on CEBAF Spectrometer Magnet Design and Technology, Newport News, April 1986, ed. by J. Mougey and P. Brindza

11) L.A. Ahrens et al., Nucl. Instr. Meth. 173 (1980) 537.

Table I: Evaluation of magnetic field configurations for a large acceptance spectrometer to be used for electron- and photon-induced reactions

(+ denotes advantage, - drawback)

	Dipole	Solenoid	Toroid
Large solid angle	(+)	+ +	(+)
No transverse field	- -	+	+
No field at the target	- -	- -	+
Symmetric configuration	-	+ +	+
Open mechanical structure	(+)	-	+
Large $\int B \cdot dl$ at small angles	+	- -	+
High luminosity capability	-	+	+

Table II: Design considerations for the toroidal magnet

1) Size

time-of-flight path required for particle identification via momentum and β

$L \geq 2$ m for particles going sideways

$L \geq 3$ m for particles going forward

→ diameter $\simeq$ 4 m, total length $\simeq$ 4 m

2) Field level

a) small destabilizing forces

b) momentum resolution $\Delta p/p \simeq 1$ %

→ $\int B \cdot dl \simeq .5$ T·m → Amp·turns $\simeq 5 \cdot 10^6$

3) Number of coils

a) 4-fold symmetry for polarised target experiments
→ 4, 8, 12, ...

b) low obstruction of the ϕ-range due to the coils
→ 8 coils

4) Coil shape

a) no transverse focusing/defocusing effects due to r-and z-components of the field
→ circular inner coil shape

b) large $\int B \cdot dl$ in the forward direction
→ asymmetric coil shape with longer forward part